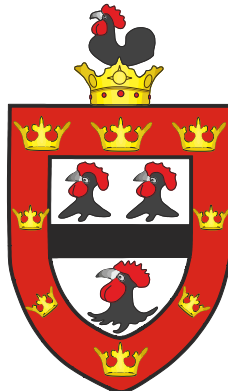


Bleed in Axial Compressors

Samuel David Grimshaw

Jesus College



A dissertation submitted for the degree
of Doctor of Philosophy

Whittle Laboratory
Department of Engineering
University of Cambridge
February 2014

Bleed in Axial Compressors

Samuel David Grimshaw

Summary

In axial compressors for aero-engines and land-based gas turbines, “bleed flow” is removed part-way through the machine for use in combustor and turbine cooling and for stage matching of the compressor during operation at off-design conditions. Bleed systems comprise of a bleed slot, plenum chamber and off-take ducts. Depending on the configuration of these components bleed extraction from the main annulus flow can be circumferentially uniform or non-uniform on the lengthscale of the circumference. The bleed rates of interest in this study are representative of design operating conditions and vary between 0 and 6.2%.

The first aim of this thesis is to provide a conceptual understanding of the effect of uniform and non-uniform bleed on the main annulus flow and how this affects the performance of a downstream compressor stage, including its operating range. The second aim is quantify the effect of bleed rate and bleed system configuration on loss in the bleed system. Single-stage axial compressor rig tests and CFD calculations are employed to meet these aims.

Circumferentially uniform bleed extraction is shown to have a small effect on the spanwise distribution of flow upstream and downstream of the bleed slot. With limited spanwise redistribution of the mainstream flow, pressure rise and efficiency characteristics, for different bleed rates, collapse towards one line when plotted against stage inlet flow coefficient. The small changes in spanwise distribution with bleed do, however, reduce incidence at the rotor tip by up to 1 degree and this improves operating range by up to 3.8% as bleed rate is increased.

Non-uniform bleed extraction leads to a circumferential distribution of flow coefficient and flow angle upstream and downstream of the bleed slot. The resultant distribution of rotor incidence at stage inlet causes operating range to reduce by up to 4.9% compared to uniform bleed extraction at the same bleed rate. The circumferential distribution of bleed in the slot is used as a proxy for the non-uniform flow at stage inlet and the loss of operating range caused by non-uniform bleed is found to correlate with the “peak sector-averaged bleed non-uniformity”. This new parameter takes inspiration from the $DC(\theta_{crit})$ method used to characterise stagnation pressure inlet distortion tests.

For uniform bleed, CFD shows that 67% of bleed system loss occurs in the bleed slot, 25% in the plenum chamber and 8% in the off-take duct. A loss coefficient is defined which is found to be constant within $\pm 1.1\%$ for the uniform bleed rates tested and increases as bleed system non-uniformity increases. For different configurations this loss coefficient is shown to correlate with slot velocity cubed.

Declaration

The research presented in this dissertation was conducted at the Whittle Laboratory in the Cambridge University Engineering Department between October 2009 and February 2014. This dissertation is my own work and contains nothing which is the outcome of work done in collaboration with others, except as specified in the text and Acknowledgements. None of the work presented in this dissertation has been submitted to any other University or Institution for any other qualification. This dissertation contains approximately 47,900 words and 135 figures.

Sam Grimshaw

February 2014

Publication

Grimshaw, S.D., Pullan, G. & Walker, T. Bleed-Induced Distortion in Axial Compressors. Paper to be presented at the ASME Turbo Expo 2014, Düsseldorf. Recommended for publication in the *ASME Journal of Turbomachinery*.

Acknowledgements

I am greatly indebted to everyone who has shared their knowledge, encouraged, and kept me going, all the way through this project and I would like to take this opportunity to thank them.

First and foremost I wish to thank my supervisor Dr Graham Pullan. I am very grateful to have been Graham's student and feel lucky that he gave me the opportunity to return to Cambridge and the Whittle Laboratory to undertake this work. Graham has given his time generously and I have learnt a great deal from him about turbomachinery and how to approach a research project. The other members of staff at the Whittle Laboratory have provided valuable advice and in particular I would like to thank Dr Ivor Day, Dr Tom Hynes and Dr John Longley for sharing their expertise with me. I am also grateful to Prof. Ed Greitzer for his shrewd advice which has helped to focus this work.

The experimental aspects of this work would not have been possible without the support of the Whittle Lab technicians. I would especially like to thank Stefan Waterson who has always been on hand to drill another hole or make one more piece for the rig. Data acquisition was made far easier thanks to the LabVIEW codes and advice provided by Dr Anna Young. Also, my thanks go to Zoe Bignell and Neil Houghton who performed the initial work to incorporate a bleed system into the design of the rig.

For the computational work I am indebted to the staff of the High Performance Computing Service at Cambridge University who work around the clock to provide an outstanding supercomputer resource. I would also like to thank Dr Tobias Brandvik for his work on the Turbostream code and James Taylor who has helped me a great deal with CFD meshing and post-processing.

I am very fortunate to have been sponsored by Mitsubishi Heavy Industries. As well as providing funding, their interest in the project and technical support have been invaluable. I would like to thank in particular Dr S. Aoki, Dr S. Uchida, T. Walker, R. Mito and J. Iwatani.

Away from work, I have spent much of my time playing hockey and socialising with the magnificent Cambridge University Hockey Club and I would like to thank everyone in CUHC for providing so many great memories. I'd also like to thank my wonderful girlfriend, Katie, who has provided love and support every step of the way.

Finally, and most importantly, I want to thank my Mum, who taught me never to give up, and my Dad who continues to be my greatest inspiration. Thankyou.

Contents

1	Introduction	1
1.1	Industrial Gas Turbines for Power Generation	1
1.2	Compressor Bleed	4
1.3	Motivation and Approach	5
1.4	Contribution of the Work	8
1.5	Layout of Thesis	8
2	Literature Review	13
2.1	Introduction	13
2.2	Circumferentially Uniform Bleed	13
2.3	Circumferentially Non-uniform Bleed	21
2.4	Compressor Stall	22
2.5	Inlet Distortion	24
2.6	Summary and New Work	26
3	Experimental Methods	40
3.1	Introduction	40
3.2	Compressor Rig Details	40
3.3	Measurement Techniques	46
4	Computational Methods	60
4.1	Introduction	60
4.2	Computational Codes	60
4.3	Mesh Generation	61
4.4	Procedure	62
4.5	Post-processing	63
4.6	Validation	64
4.7	Summary	68
5	Uniform Bleed	79
5.1	Introduction	79
5.2	Pressure Rise and Flow Field	79
5.3	Stall	83
5.4	Efficiency	84

5.5	Conclusions	87
6	Non-uniform Bleed	98
6.1	Introduction	98
6.2	Passage-averaged Analysis	99
6.3	Pitch-averaged Analysis	105
6.4	Efficiency	110
6.5	Conclusions	114
7	CFD	138
7.1	Introduction	138
7.2	Circumferentially Uniform Bleed	138
7.3	Circumferentially Non-uniform Bleed	145
7.4	Conclusions	149
8	Non-uniform Bleed and Stall	169
8.1	Introduction	169
8.2	Flow Coefficient at Stall	169
8.3	Circumferential Distribution of Bleed	170
8.4	Characterisation of Bleed Non-uniformity	171
8.5	Effect of Bleed Non-uniformity on Operating Range	172
8.6	Conclusions	173
9	Conclusions and Future Work	179
9.1	Introduction	179
9.2	Uniform Bleed	179
9.3	Non-uniform Bleed	180
9.4	Non-uniform Bleed and Stall	182
9.5	Suggestions for Future Work	182
References		185

Nomenclature

Latin Symbols	Description	Equation Reference
A	Cross Sectional Area of Main Annulus Flow	
R_{bl}	Bleed Rate	3.9
c	Chord	
c_x	Axial Chord	
C_{p0}	Inlet Stagnation Pressure Correction Factor	3.7
$DC(\theta_{crit})$	Inlet Distortion Coefficient	2.1
h_0	Stagnation Enthalpy	
K	Inlet Mass Flow Calibration Factor	3.5
\dot{m}	Mass Flow Rate	
P	Static Pressure	
P_0	Stagnation Pressure	
r	Radius	
Re	Reynolds Number	
U	Midspan Blade Speed	
V	Absolute Velocity	
V_x	Axial Velocity	
V_r	Radial Velocity	
V_t	Circumferential Velocity	
V_s	Local Radial Velocity in Slot	
Y_p	Bleed System Loss Coefficient	5.3 (Experiment), 7.2 (CFD)

Greek Symbols	Description	Equation Reference
α	Flow Angle (Absolute Frame of Reference)	
α_{rel}	Flow Angle (Rotor Relative Frame of Reference)	
β	Non-uniform Bleed Loss Parameter	6.2
$\eta_{overall}$	Overall Efficiency	3.12 (Experiment), 4.2 (CFD)
η_{stage}	Stage Efficiency	3.14 (Experiment), 4.4 (CFD)
$\Delta\eta_{bleed}$	Loss in efficiency due to bleed flow loss	5.1 (Experiment), 7.1 (CFD)
θ	Sector Size (in degrees)	
μ	Dynamic Viscosity	
ρ	Density	
τ	Motor Torque	
ϕ_{rig}	Rig Inlet Flow Coefficient	3.3
ϕ_{stage}	Stage Inlet Flow Coefficient	3.4
ψ_{t-s}	Total-to-static Pressure Rise Coefficient	3.1
ψ_{s-s}	Static-to-static Pressure Rise Coefficient	3.2
Ω	Rotational Speed	
κ	Reduced Frequency	6.1

Subscripts for Locations

$[]_{in}$	Calibrated Inlet Value
$[]_{rig}$	Rig Inlet
$[]_{stage}$	Stage Inlet
$[]_{pr}$	Probe Value
$[]_{bl}$	Exit of Bleed System
$[]_{bl,loc}$	Local value in Bleed Slot
$[]_{CV,in}$	Control Volume Inlet
$[]_{CV,exit}$	Control Volume Exit

Chapter 1

Introduction

1.1 Industrial Gas Turbines for Power Generation

Global electricity demand grew by over 70% between 1990 and 2009 from 9,711 TWh to 16,747 TWh [1]. Figure 1.1 includes historic data and the International Energy Agency's (IEA) projections until 2035 for three scenarios: Current Policies, New Policies and the 450 Scenario¹. The figure shows electricity demand increasing at between 2.0% and 2.7% per annum until 2035 depending on the scenario. Power generators are expected to meet this increase in demand while also addressing the challenge of reducing CO₂ emissions. In its fifth assessment report, published in 2013, the Intergovernmental Panel on Climate Change (IPCC) [2] states that “Warming of the climate system is unequivocal... it is extremely likely that human influence has been the dominant cause of the observed warming since the mid-20th century... [and] continued emissions of greenhouse gases will cause further warming and changes in all components of the climate system.” Figure 1.2 shows that global emissions of CO₂ (the most significant man-made greenhouse gas) increased by nearly 40% between 1990 and 2009 and that in 2009 power generation accounted for over 40% of these emissions. National and international policy makers are working to regulate greenhouse gas emissions, e.g. UK Climate Change Act 2008 [3], EU Emissions Trading System [4] and the United Nations Framework Convention on Climate Change (UNFCCC) Kyoto Protocol [5]. However, the IEA predicts that even with New Policies (its central scenario), emissions will continue to rise, reaching 36.4 Gt in 2035 which leads to an emissions trajectory consistent with a long term global temperature increase of more than 3.5°C. To achieve an average warming of only 2°C, global emissions will have to follow the much more challenging 450 Scenario shown in Fig 1.2.

¹ The *Current Policies Scenario* includes all policies in place and supported through enacted measures as of mid-2011. The *New Policies Scenario* includes policies in the Current Policies Scenario and other broad policy commitments and plans that have been announced but not yet enacted. The *450 Scenario* sets out an energy pathway that is consistent with a 50% chance of meeting the goal of limiting the increase in average global temperature to 2°C compared with pre-industrial levels, i.e. an emissions trajectory consistent with stabilisation of the greenhouse-gas concentration at 450 parts per million [1].

Power generators, therefore, have to address the combined challenges of reducing CO₂ emissions while still meeting increased demand for electricity; gas-fired power plants using industrial gas turbines are an important part of the solution. Figure 1.3 shows historical data and the IEA's projections for total electricity generation up to 2035. The figure also shows generation from gas-fired power stations. In all three of the IEA's future scenarios (including the low carbon 450 Scenario) the amount of gas-fired generation increases compared with today. In terms of installed capacity of gas-fired generation the IEA predicts an increase from 1298 GW in 2009 to 2185 GW in 2035 in the New Policies Scenario (2333 GW in the Current Policies Scenario, 2111 GW in 450 Scenario). This results in an increase on average of 34.1 GW per year (39.8 GW per year in Current Policies Scenario, 31.3 GW per year in 450 Scenario). Much of this predicted increase is due to rapid growth in developing countries, such as China and India.

There are four reasons for the predicted continued growth of gas-fired power generation: availability of gas, low cost of electricity from combined cycle gas turbine (CCGT) plants, efficiency of CCGT plants, and flexibility.

Availability of gas. Predicted gas resources up to and beyond 2035 are ample to meet demand and estimates of their magnitude are growing. In particular the estimated size of unconventional gas resources, which include those from coal beds (coalbed methane), low-permeability reservoirs (tight gas) and shale formations (shale gas) has increased. These unconventional resources are now estimated to be of a similar size to conventional recoverable resources and in total there is an estimated 250 years of production at 2010 levels [1]. In the shorter term, the recent increase in shale gas production in North America is expected to be repeated in other markets around the world, notably China and Australia.

Cost of generation. Gas-fired power plants produce low cost electricity compared to other types of power generation. Table 1.1 provides projected levelized² costs for electricity produced by different types of power plant entering service in the US in 2018. CCGT power plants have the lowest overall levelized cost at 65.6 \$/MWh [6].

Efficiency. CCGT plants are more efficient and emit less CO₂ per kWh of electricity produced than any other fossil fuel powered generation [7]. Table 1.2 gives the efficiency and carbon intensity for several different generation technologies and fuels. CCGT power plants are more efficient than open cycle gas turbines or steam cycle turbines because the high temperature exhaust from the gas turbine is used to boil water in a steam cycle. Improved efficiency, coupled with the lower carbon

² Levelized cost is a convenient summary measure of the overall competitiveness of different generating technologies. It represents the per-kWh cost of building and operating a generating plant over an assumed financial life and duty cycle

content of natural gas compared to coal, leads to reduced CO₂ emissions per kWh of electricity produced. The IEA predict that generation from CCGT plants will increase from 2600 TWh in 2009 to almost 4900 TWh in 2035 [1]. Natural gas is also cleaner to burn than coal and hence makes a much smaller contribution to local air pollution; an important consideration, especially in developing economies like India and China.

Flexible generation. The fourth reason for the continued use of gas-fired generation is its role in future electricity generation networks which include intermittent sources such as wind or solar power. An electrical power network has to be in balance, with electricity generation matching consumption. While balancing can be achieved through export, import, and with some control on the consumption-side, it is most common for the supply side to adapt to demand. The introduction of intermittent sources such as wind or solar power makes supply side management more challenging as the output can vary significantly over short time-scales. These variations are also hard to predict and schedule for accurately. Non-intermittent generators in the network must, therefore, be able to respond to changes in generation from the intermittent sources. Table 1.3 provides data which illustrates the flexibility of several conventional power generation technologies. Pumped storage plants provide the most responsive generation type but of the other technologies, CCGT plants are the most flexible. The combination of a load gradient of 4% per minute and a relatively quick start up (less than 1.5 hours from warm conditions) make CCGT plants suitable for load-following, a characteristic which will become increasingly important as the penetration of renewable energy sources increases [8].

All of this means that gas-fired power stations are likely to remain a key part of the global energy mix for at least the next twenty-five years. Improving the performance of industrial gas turbines is therefore an important undertaking. Purely in terms of fuel burn, a 1% increase in efficiency across all of the world's gas-fired power stations would reduce global CO₂ emissions in 2035 by 32 million tonnes per year³. Another important area for improvement is in making industrial gas turbines easier and cheaper to maintain. Operations and maintenance (O&M) costs represent a significant portion of the costs of running a power plant: for a CCGT plant O&M forms the second largest cost category (after fuel costs) and consumes around 7% of cash flow over the life of the plant [9]. Design changes which make gas turbines easier to maintain can therefore reduce operating costs. Lost revenue due to maintenance (scheduled or unscheduled) is not counted as an O&M cost but is

³ Assume average CCGT power station produces 355gCO₂ / kWh and open cycle gas turbine power station produces 485gCO₂ / kWh [7]. 1% efficiency increase therefore reduces CO₂ emissions by 3.55gCO₂ / kWh and 4.85 gCO₂ / kWh respectively. Total gas-fired generation in 2035 projected as 7923 TWh with 62% from CCGT.

also related to the maintainability of a power plant's equipment. The cost to an operator of lost revenue can be twice the cost of performing repairs to return the unit to service [9] so reducing the time needed for maintenance, by improving the design of the gas turbine, can lead to significant costs savings.

1.2 Compressor Bleed

Industrial gas turbines require the extraction of “bleed air” from the compressor to perform a variety of tasks. These include cooling for high-temperature engine components such as the combustor, early stage turbine blades and discs, pressurisation for drum cavities and bearing chambers, and stage matching for the compressor at off-design conditions and machine start-up (also known as handling bleed). The bleed air is normally taken from the mid-to-rear stages of the compressor. Bleed air is removed from the main annulus flow through slots or one-per-passage holes in the casing and is collected in an axisymmetric plenum chamber. The bleed air leaves the plenum chamber via a small number (typically four) of off-take ducts. For machine start-up and part-speed conditions, handling bleed rates can be as high as 20% of the main annulus flow but under normal operating conditions bleed rates are typically between 0% and 6%. A typical Mitsubishi Heavy Industries (MHI) gas turbine is shown in Fig 1.4. This figure also shows a meridional cross section of part of the compressor in which the bleed slot, plenum chamber and off-take duct are labelled.

The geometry of the casing bleed slot or holes is either axisymmetric or periodic on the length scale of a blade pitch. Some extraction geometries result in large variations in bleed rate on the length scale of a blade pitch (e.g. casing holes within a stator passage) but the bleed can still be classified as uniform if variations on the circumference length scale are small. After passing through the casing and into the plenum chamber the bleed air flow becomes non-axisymmetric as the air is drawn off through discrete off-take ducts. The flow is then periodic on a length scale of the order of the circumference, i.e. depending on the number and location of the off-take ducts. Gomes et al. [10], use an annular cascade to show that the non-axisymmetric nature of the bleed system causes a circumferentially non-uniform static pressure at the hub below the bleed slot. This distortion in the main annulus passage flow has the potential to affect compressor performance and so the non-axisymmetric configuration of the bleed system should be considered in bleed system design.

The axial location of the bleed slots or holes is determined by the air pressure required for the different applications. It is desirable from a cycle efficiency point-of-view to extract air from as far forward in the compressor as possible, so that work is not ‘wasted’ in compressing air that will subsequently be extracted into the bleed system. The axial position of bleed holes or slots is a compromise between cycle-efficiency and the pressure demands of the applications the air is required

for. In terms of the bleed system design it is therefore important to minimise any stagnation pressure loss through the bleed system [11].

1.3 Motivation and Approach

1.3.1 Problem statement

A desire to cut component cost or weight, or to decrease the time needed for maintenance, encourages the designer to reduce both the size of the bleed system plenum chamber and the number of off-take ducts. Each of these changes, however, will increase the circumferential non-uniformity of the bleed flow. Non-uniform bleed extraction will cause a distortion in the main annulus flow and the pressure drop through the bleed system may also be increased. The purpose of this work is to establish the connection between bleed, both uniform and circumferentially non-uniform, and compressor and bleed system performance. The bleed rates studied are those used at design operating conditions, i.e. between 0% and 6.23%. In this work bleed is classified as uniform when circumferential variations in bleed extraction are small on a length scale of the order of the compressor circumference.

1.3.2 Research questions

It is helpful to split the investigation into three broad questions and then divide each of these into specific research questions which can be addressed:

1. What is the effect of circumferentially uniform bleed on compressor and bleed system performance?
 - (a) How do different rates of uniform bleed affect compressor pressure rise and efficiency characteristics?
 - (b) What is the effect of different rates of uniform bleed on the compressor flow field?
 - (c) How is the stagnation pressure loss through the bleed system affected by different rates of uniform bleed?
2. What is the effect of circumferentially non-uniform bleed on compressor and bleed system performance?
 - (a) How does circumferentially non-uniform bleed extraction affect the compressor pressure rise and efficiency characteristics and, in particular, what is the effect on operating range?
 - (b) What effect does non-uniform bleed extraction have on the compressor flow field around the annulus?

- (c) How is the stagnation pressure loss through the bleed system affected by different non-axisymmetric bleed system configurations?
3. Is there a connection between circumferentially non-uniform bleed and compressor operating range?
- (a) How is the stalling flow coefficient of the compressor affected by different non-axisymmetric bleed system configurations?
 - (b) Can non-uniform bleed distributions be characterised to connect bleed non-uniformity with the reduction in compressor operating range?

1.3.3 Approach

The effect of bleed on compressor performance is investigated with a low-speed test compressor and Computational Fluid Dynamics (CFD). A configurable bleed system allows bleed rate, plenum chamber size and off-take duct number and location to be changed so that bleed can be extracted at varying bleed rates and with a circumferentially uniform or non-uniform distribution. The responses to the research questions have been grouped into three parts: main annulus flow field and compressor operating range, compressor efficiency and bleed system loss, and CFD. Each of these has their own approach and these are discussed below.

Main annulus flow field and compressor operating range. The questions relating to the flow field and compressor operating range are approached in three steps. First, the effects of different rates of uniform bleed on compressor performance are studied. Bleed will be close to uniform in many real machines and it is therefore useful to understand the effect of uniform bleed extraction. This step also provides a bridge towards understanding non-uniform bleed where the rate of bleed varies circumferentially around the annulus. Second, the results from one non-uniform bleed configuration (small plenum, one off-take duct, bleed rate of 4.14%) are studied in detail to develop a conceptual picture of the influence of non-uniform bleed on the main annulus flow field. Particular attention is paid to the flowfield at stage inlet as this influences the operating range of the downstream compressor stage. In the final step non-uniform bleed distributions measured in the bleed slot for over 30 bleed system configurations provide a proxy for the flow field at stage inlet and are used to characterise the effect of non-uniform bleed on the operating range of the downstream stage.

In general, in a real machine (as shown in Fig. 1.4), bleed is extracted from an embedded stage of an axial compressor. Of interest is the stability of the stage immediately downstream of the bleed. If the compressor is throttled and the flow into the rotor reduced sufficiently, the compressor will stall either via “modes” (if the stage reaches the peak of its total-to-static pressure rise characteristic) or “spikes” (if stall occurs, due to high rotor incidence, on the negative slope of the characteristic). In

common with similar machines in real applications, the test compressor in the current work exhibits spike-type stall inception so that rotor incidence determines when the stage stalls.

To simplify the problem the geometry considered is a single stage compressor with a bleed slot immediately upstream. Typical of the mid-to-rear stages where bleed is generally employed, the test compressor used in this report has a high hub-to-tip radius ratio of 0.75. This means that bleed extraction, at the rates typical of design operating conditions, results in low meridional curvature of the streamsurfaces in the main annulus flow. The investigation of the compressor flow field, for both uniform and non-uniform bleed, is therefore first addressed with a passage-averaged approach which disregards spanwise variations. This simplifies the analysis while retaining the key features of the flow's response to bleed. For uniform and non-uniform bleed, spanwise distributions of the flow are then studied to provide further details for the conceptual picture of the effect of bleed on the main annulus flow and compressor performance.

Non-uniform bleed extraction through the slot will result in a circumferentially non-uniform distribution of incidence on to the downstream rotor. It is noted here that the link between bleed extraction distribution and stage inlet incidence distribution will be different when stages are present upstream of the bleed (for example, the static pressure distortion created by the non-uniform bleed would cause the upstream stage to deliver a non-uniform total pressure). However, the connection between the circumferential distribution of incidence entering the downstream stage and the operating range of the downstream stage - the area of interest here - does not depend on the presence of stages upstream of the bleed slot.

Compressor efficiency and bleed system loss. The overall efficiency of the experimental rig depends on the efficiency of the downstream stage and the losses incurred by the flow passing through the bleed system. In this work these effects are split and studied separately.

Changes to the efficiency of the downstream stage are due to changes in the main annulus flow field caused by the bleed extraction, i.e. spanwise and circumferential redistribution of the flow. Efficiency characteristics for the downstream stage are measured and compared for uniform and non-uniform bleed system configurations with different bleed rates.

Bleed system loss occurs as the bleed flow passes through the bleed slot, the plenum chamber and the off-take duct. In the experimental work the stagnation pressure in the off-take duct is measured so that the total loss incurred by the flow passing through the bleed system can be determined. A loss coefficient is defined for the bleed flow and this is used to quantify the effect of changes in uniform bleed rate and compressor operating point on the bleed system loss. For non-uniform bleed extraction the loss coefficient is used to characterise the effect of different bleed system configurations on the loss in the bleed system. It is proposed that the loss in the bleed system with

non-uniform bleed is proportional to bleed slot velocity cubed and a parameter incorporating this using local bleed distribution measurements is correlated with the bleed system loss coefficient.

CFD. CFD calculations are performed which model the experimental compressor with uniform and non-uniform bleed. The effect of uniform bleed on the main annulus flow can be modelled with a single passage calculation with bleed extracted from the top of the bleed slot. These calculations run quickly enough for characteristics to be calculated for all the uniform bleed rates tested experimentally. In order to calculate flow in the bleed system with a large plenum chamber and four off-take ducts, a quarter annulus calculation is required. A full annulus calculation is used to study non-uniform bleed caused by a single off-take duct and a small plenum chamber. These calculations require much more computational resource and are therefore only run at one operating point with a bleed rate of 4.1%.

The calculations performed are validated against experimental measurements so that the CFD methods used in the current work can be used with confidence in future studies of compressor bleed. CFD calculations including the plenum chamber and off-take duct are also used to expand on the experimental measurements by providing a means to study the flow, and the associated losses, in the bleed system.

1.4 Contribution of the Work

The work provides a qualitative description of the compressor flow field with uniform and non-uniform bleed and a quantitative connection between non-uniform bleed distribution and the change in stability margin of a downstream compressor stage. The effects of uniform bleed rate and non-axisymmetric bleed system design on downstream stage efficiency and bleed system loss are also presented. Finally, CFD calculations of uniform and non-uniform bleed are validated against experimental measurements and the flow in the bleed system is described qualitatively.

1.5 Layout of Thesis

This thesis is organised as follows: Chapter 2 provides a review of published literature on compressor bleed and also considers relevant papers relating to inlet distortion and stall. In Chapters 3 and 4 the experimental and computational methods used in this work are described.

The results of the uniform bleed tests are presented in Chapter 5. Here, the effects of varying uniform bleed rate on compressor pressure rise and efficiency characteristics, the compressor flow field and bleed system loss are studied.

In Chapter 6 the effect of a non-axisymmetric bleed system configuration on the compressor flow field is investigated. Passage-averaged and pitch-averaged analyses of the flow are presented as well as the effect of this particular non-uniform bleed distribution on compressor operating range. The effect of different bleed system configurations on downstream stage efficiency and loss in the bleed system is also studied.

Chapter 7 consists of the CFD results for calculations which model uniform and non-uniform bleed. The CFD is validated against the experimental measurements and then used to investigate loss in the bleed flow and to provide a qualitative description of the flow in the bleed system.

In Chapter 8 a method for characterising non-uniform bleed is introduced and used to link the non-uniform bleed distributions with the change in operating range of the downstream stage. Finally, conclusions and suggestions for further work are discussed in Chapter 9.

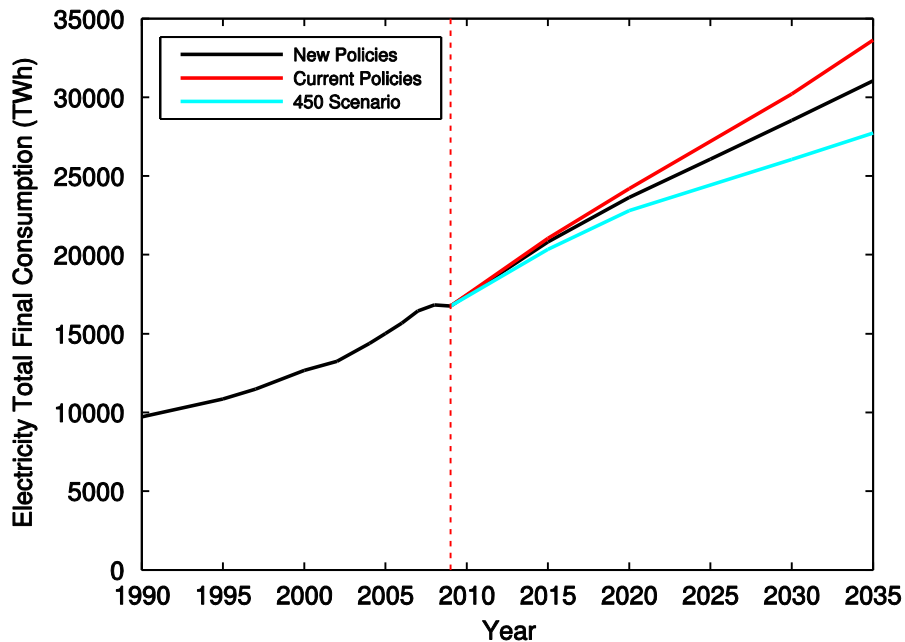


Figure 1.1: Historic and projected total final electricity consumption for three IEA scenarios [1].

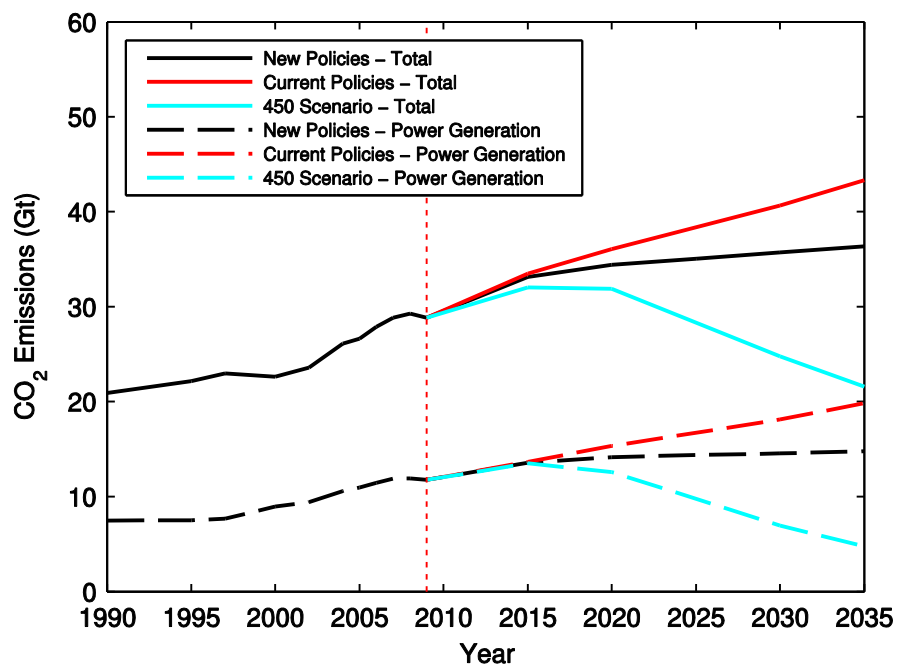


Figure 1.2: Historic and projected global CO₂ emissions from all sources and from power generation for three IEA scenarios [1].

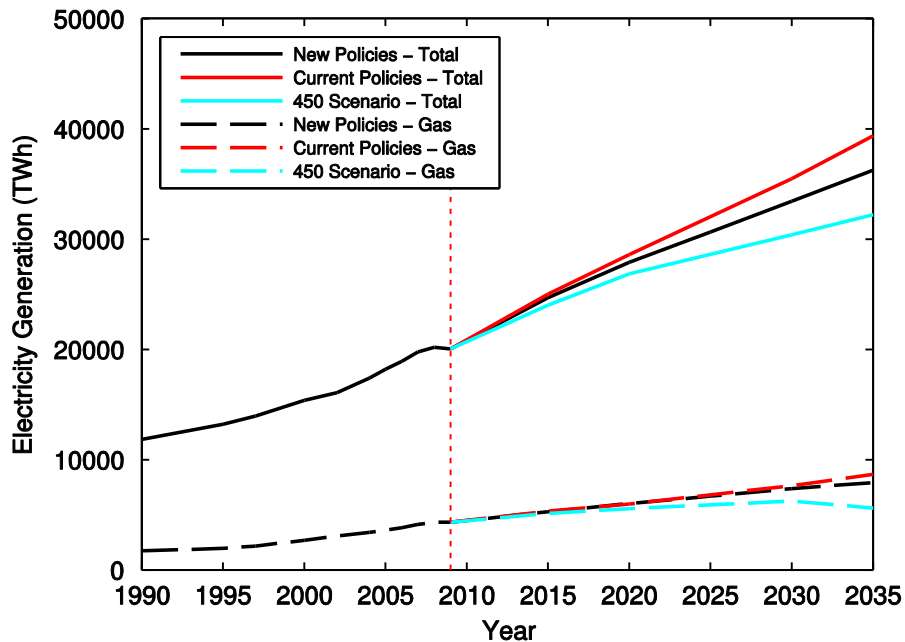


Figure 1.3: Historic and projected electricity generation from all sources and from gas-fired power stations [1].

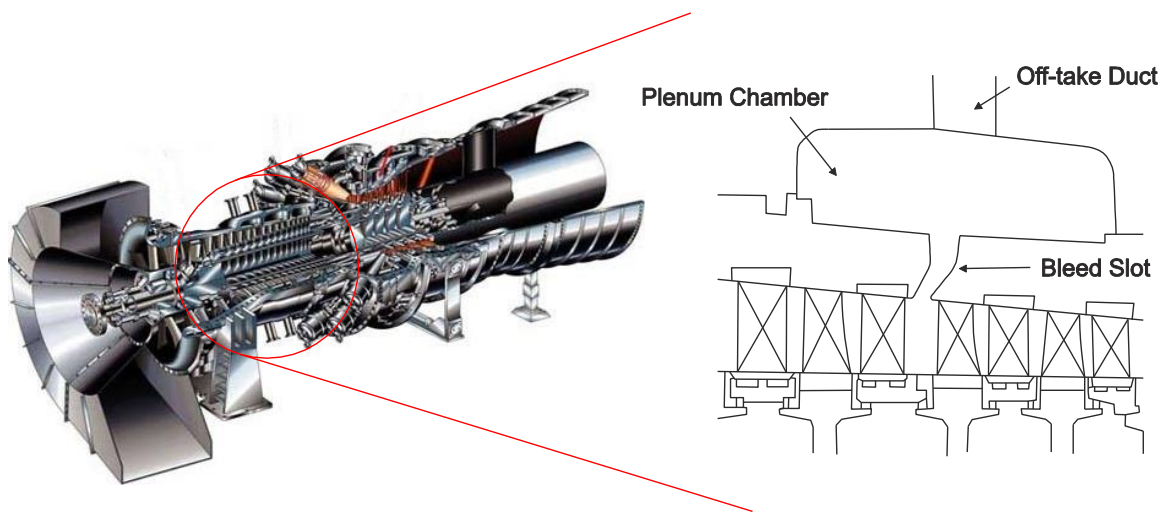


Figure 1.4: Mitsubishi Heavy Industries (MHI) M501G gas turbine and meridional cross section showing bleed slot, plenum chamber and off-take duct.

Type of Power Plant	US average leveled costs in 2011\$ / MWh
Conventional coal	100.1
Advanced coal with carbon capture and storage	135.5
Combined cycle gas turbine (CCGT)	65.6
Nuclear	108.4
Geothermal	89.6
Biomass	111.0
Wind – onshore	86.6
Wind – offshore	221.5
Solar PV	144.3
Solar thermal	261.5
Hydroelectric	90.3

Table 1.1: US average leveled cost in 2011\$/MWh for different types of power plant entering service in 2018 [6].

Type of Power Plant	Thermal efficiency %	gCO ₂ / kWh
Pulverised coal combustion (subcritical and supercritical)	35 – 44	830 – 990
Integrated gasification combined cycle (IGCC) coal plant	42 – 52	592 – 862
Gas turbine open cycle	30 – 40 (size dependent)	413 – 557
CCGT	55 – 62	340 – 370

Table 1.2: Efficiency and CO₂ emissions of fossil fuel fired power generation systems [7].

Type of Power Plant	Start-up time “cold”	Start-up time “warm”	Load gradient change	Minimum shutdown time	Minimum possible load
Nuclear	~40h	~40h	~5%/min	-	50%
Hard coal-fired	~6h	~3h	~2%/min	-	40%
Lignite-fired	~10h	~6h	~2%/min	-	40%
CCGT	<2h	<1.5h	~4%/min	-	<50%
Pumped Storage	~0.1h	~0.1h	~40%/min	~10h	~15%

Table 1.3: Flexibility of conventional power generation technologies [8].

Chapter 2

Literature Review

2.1 Introduction

The literature review chapter begins by studying research into the effect of uniform bleed. This includes CFD studies and experimental cascade tests which investigate the interaction of bleed with the main passage flow and downstream stages. Some of these studies also consider the flow in the bleed system. The chapter then goes on to review experimental work which considers the effects of circumferentially non-uniform bleed on full annulus flow in an annular cascade. Finally, the review also includes the key literature on stall inception and inlet distortion and draws links between these and both uniform and non-uniform bleed.

2.2 Circumferentially Uniform Bleed

In this work bleed is classified as uniform when circumferential variations in bleed are small on a length scale of the order of the compressor circumference. This means that though some extraction geometries result in large variations in bleed rate on a blade pitch length scale (e.g. casing holes within a stator passage) the bleed can still be classified as uniform if variations on the circumference length scale are small. Most of the literature concerning bleed slot design and performance assumes (either implicitly or explicitly) that the bleed is uniform over a length scale of the circumference. This simplifies rig design and reduces computational cost for CFD calculations while still highlighting some of the key flow mechanisms relating to the interaction between the bleed and main passage flow.

The first part of this section reviews work which investigates the interaction of bleed extraction with the main passage flow. The second section looks at work done to investigate the effect of uniform bleed extraction on downstream stages. The third section reviews work which relates to losses in the bleed system. Finally a summary is presented and the key areas which the current work aims to address are highlighted.

2.2.1 Effect of uniform bleed on main passage flow

The simplest way to model bleed in a 3-D Navier-Stokes CFD calculation is to add a boundary condition on the surface through which the air is to be bled. Bleed boundary conditions can either specify a constant mass flow through the surface or set a pressure and allow air to bleed through the surface. The main benefit of the boundary condition bleed model is that it simplifies the mesh generation process and reduces computational cost compared to fully meshing the casing bleed slot or hole and/or the plenum chamber and off-take duct. However, as the work reviewed below shows, interactions between the bleed flow and the main annulus flow are not captured accurately.

Conan and Savarese's work [12] on bleed airflow modelling in jet engine compressors employs a 3-D Navier-Stokes CFD code with simple boundary conditions at the casing wall to represent the bleed holes or slot in a one-stage compressor. The authors recognise that this is a simplification and that explicit calculation of the flow in the bleed cavity gives more detailed flow patterns. However, the simple boundary condition method is retained in order to minimise computational costs. The work considers two cases; one with bleed holes and the other with an axi-symmetric bleed slot just upstream of a rotor row. The bleed slot case is more relevant as it is positioned in a similar location to the bleed slot in the current work. It is this case that is reviewed here. Two different boundary conditions were tested. Model A imposes a uniform flow rate normal to the bleed surface and Model B imposes a static pressure on the bleed surface which is numerically adjusted to obtain the required bleed rate. The bleed rate is set at 8.4% of the incoming mass flow rate. This is quite a high bleed rate for a design operating condition and its effect is expected to be greater than that observed for the maximum bleed rate of 6.23% tested in the current work. Models A and B are compared with a 0% bleed rate case and a through-flow prediction. The hub-to-tip ratio is not reported, however, the blades modelled are representative of those found in the mid stages of the compressor so the hub-to-tip ratio is expected to be similar to that in the current work.

Figure 2.1 shows the blade passages and bleed slot boundaries and Fig. 2.2 shows the Mach number and static pressure profiles upstream and downstream of the slot. The spanwise flow profiles show that for both boundary condition models, upstream of the bleed slot the static pressure near to the casing wall (outer 25% of span) is reduced and therefore the flow is accelerated in this region. Downstream of the slot the bleed reduces the Mach number in the main annulus flow. This is because the bleed slot removes air from the flow and mass continuity means that the flow velocity must reduce. Near the casing, where the bleed has been extracted, the reduction in Mach Number is around 0.05 and near the hub it is around 0.025 showing that there is some spanwise redistribution of the flow due to bleed. This differs from the through-flow analysis where mass is removed uniformly from the passage so that the change in Mach number across the span, with bleed, is uniform. The difference in spanwise profiles between the through-flow calculation and Models A and B is quite small – this

suggests that the spanwise redistribution of the flow due to bleed at the casing is small. Whether this spanwise redistribution of the flow is enough to significantly alter the performance of the downstream stage is not investigated in this piece of work.

Wellborn and Koir [13] investigate a bleed slot just upstream of the rotor leading edge with a fully meshed slot. They show that the flow field can be “quite complex, with severe axial, radial and circumferential flow gradients”. Figure 2.3 shows the variation in tangential, radial and axial velocity at the interface between the slot and the primary flow with 0% bleed, calculated using a three-dimensional CFD solver.

For this case, where the net bleed flow is 0%, there are still strong velocity gradients, especially towards the back of the slot. It also shows how, even with an axisymmetric bleed slot, the flow can be circumferentially non-uniform on the length scale of a blade pitch. These complex flow fields led Wellborn and Koir to undertake a study which compares different models for bleed extraction. A CFD model with a constant mass flux boundary condition is compared with a model which includes a fully-meshed slot geometry. In this case the slot was located over the rotor tip from 25% to 50% axial chord. Figure 2.4 shows isentropic Mach number distributions at 95% span on the rotor blade for the different modelling techniques. The blade surface pressure distributions show that the constant mass flux extraction model predicts only a small change in blade loading. The full mesh model, however, predicts a complex flow structure created by the bleed extraction and Wellborn and Koir conclude that the bleed slot should be fully meshed for the rest of the study. Changes to the predicted performance of the compressor, due to the different bleed models, are not discussed in the paper.

Elmendorf et al. [14] model a 15-stage compressor in a steady, single blade passage CFD calculation which includes an axisymmetric bleed slot. The bleed rate is not specified. Figure 2.5 shows that the pitchwise-averaged total temperature in the outer 30% of span is reduced downstream of the slot compared to upstream. This is because the high total temperature boundary layer fluid on the outer casing is removed by the bleed slot resulting in a reduction in low-momentum, high loss fluid at the casing downstream of the slot.

The most in depth study of bleed flow mechanisms to date was conducted by Leishman [15]. His PhD thesis built upon work by Bowman [16] conducted at the Whittle Laboratory at Cambridge University. Leishman’s work answers Conan and Saverese’s call for “more precise experimental data” [12] by including a detailed experimental investigation of a cascade rig with bleed, as shown in Fig. 2.6. The rig’s flexible design meant that many different bleed geometries could be tested; these included various circular holes, an axisymmetric bleed slot and a variety of more complex geometries combining the holes and slot with different inlet ramps. The position of the circular holes in the stator passage could be varied to investigate how the bleed extraction varies over blade pitch length scales. The work also follows the conclusions of Wellborn and Koir and uses a three-dimensional Reynolds

averaged Navier-Stokes solver to model the full cascade geometry including the bleed slot or hole, and plenum chamber.

By modelling both the blade passage and bleed system geometry Leishman was able to investigate how different configurations changed the impact of bleed on the main passage flow and on bleed system performance (i.e. pressure recovery through bleed slot or hole). Leishman et al. [17] describe the effects of bleed through circular bleed holes. These were situated on the casing within the stator blade passage and the blade passage aerodynamics discussed are therefore not directly applicable to the current work. However, some of the more general observations are relevant. The authors conclude that the interaction of bleed extraction with the main passage flow primarily involves inviscid, pressure-driven phenomena. They show that CFD calculations can accurately predict the experimental results and agree with Wellborn and Koiri that CFD calculations should model the full bleed system geometry to reproduce the complex flow structures within the bleed slot and the interaction with the primary flow correctly.

The second paper by Leishman et al. [18] is more relevant to this work as it includes a study of an axisymmetric bleed slot. The stator blade and slot are shown in Fig. 2.7. Figure 2.8 shows measured contours of stagnation pressure loss in the main passage, downstream of the slot and Fig. 2.9 shows pitchwise-averaged loss coefficient and flow angle downstream of the slot. In both plots bleed air is being extracted from the lower endwall, i.e. at span = 0%. Figures 2.8 and 2.9(a) show that the stagnation pressure loss is not changed between the baseline case (i.e. clean wall, no bleed) and the case where there is a slot with 0% bleed rate. This lack of interaction is also demonstrated in Fig. 2.9(b) which shows that the flow angle is not affected by the slot with 0% bleed rate. However, it can be seen that as the bleed rate is increased, the extraction of high-loss end wall boundary layer fluid into the bleed slot reduces the stagnation pressure loss near to the lower end wall. On the upper end wall, Figure 2.8 shows that the blade suction-surface corner separation is increased. This is because bleed extraction draws air into the bleed slot and streamlines in the main passage curve towards the bleed slot. This spanwise redistribution of flow results in the blade near the endwall, opposite the bleed slot, being more highly loaded and hence the corner separation is increased. Near to the lower endwall (up to about 10% span) Fig. 2.9(b) shows that the cases with bleed are under turned relative to the baseline data; this is in the region where the endwall boundary layer has been removed. From 10% to 35% of span bleed causes the flow to be slightly over turned and for the rest of the span the cases with bleed are under turned as the size of the separation at the upper endwall increases.

Leishman's work on axisymmetric slots is particularly useful because simple flow mechanisms are suggested to explain the results; the same flow mechanisms should be present in the current work. Leishman and Cumpsty [11] also clearly lay out the restrictions of their linear cascade tests; in particular they note that the effects of bleed on compressor stalling characteristics and on the

downstream rotor performance are not considered. These open questions are important to a designer and the current work addresses them by using a rotating compressor rig with a stage downstream of a bleed slot.

2.2.2 Effect of bleed on downstream stages

Only a small number of studies have investigated the effect of bleed flow on a downstream blade row. As discussed above, Wellborn and Koir [13] show that bleed slots should be fully meshed in CFD to capture the complex flow structures that they generate. Following the initial modelling work, the study goes on to investigate the impact of bleed slot position and bleed rate on the peak efficiency of a compressor. Included in the work is a configuration with the bleed slot on the casing just upstream of a rotor row, i.e. in a similar location to the current work. Wellborn and Koir point out the similarities between bleed slots and a shrouded stator cavity and refer to several studies which show that shroud leakages can significantly affect the main annulus flow [19, 20, 21]. Bleed slots also affect the main annulus flow, as shown by Elmendorf et al [14] and Leishman [15], and are therefore expected to change the performance of the downstream blade row. Wellborn and Koir aim to improve compressor efficiency by bleeding high entropy air out of the primary flow. CFD calculations show that with a bleed rate of 5% there is a negative effect on the peak efficiency of the compressor and bleed system of -1.0% points compared to a baseline case with no bleed slot. For this result the losses in the bleed slot are included in the efficiency calculation. With a definition for efficiency which does not include the loss in the bleed slot, a small improvement in efficiency of +0.25% points is achieved. Wellborn and Koir explain that the change in efficiency is small because of the dominance of the rotor tip clearance flow near the casing. Bleed extraction at the rates tested (up to 5%) do little to alter the tip clearance flow. For the case where the bleed slot is upstream of the rotor, the incoming vorticity field is changed but the tip clearance flow and the associated loss still occur at nearly the same level as in the smooth wall configuration.

The CFD results in Wellborn and Koir [13] also show that with a fixed exit flow rate (i.e. adjusted for bleed) the spanwise axial velocity distribution downstream of the rotor is unaffected by increased bleed rate from 1% to 5%. This can be seen in Fig. 2.10. Unfortunately the paper does not show the spanwise distribution of flow downstream of the bleed slot (just upstream of the rotor) but it does show that downstream of the rotor at least, the spanwise distribution of the flow is not affected by increased bleed rate. Also the study does not discuss the link between the change in upstream flow field, caused by bleed extraction, and stall.

Gümmer et al. [22] use CFD to study the effect of bleed on compressor performance. The types of bleed slot investigated are different to that in the current work; first a small bleed (1%) extracted over the rotor tip is modelled and second, a number of different bleed holes in the stator passage, similar to Leishman [17] are investigated. Although these cases are different to the axisymmetric,

interstage bleed slot in the current work it is relevant to note the effect that they have on the main passage flow and compressor performance. Figure 2.11(a) shows that bleed extraction over the rotor tip reduces the loss coefficient downstream of the rotor in the outer 30% of span although the effect that this has on efficiency is not quantified. Gümmer et al also show that a tailored hole on the casing in the stator passage can reduce the loss coefficient downstream of the stator. This is shown in Fig. 2.11(b). The impact of bleed on the operating range and stall point of the compressor is not considered.

Di Mare et al. [23] conducted a computational study which includes steady and unsteady calculations to assess the effect of bleed flows on flutter and forced response in axial compressors. A ramped bleed slot with bleed rates of 3.6% (design) and 20% (handling) is investigated. The study focuses on the aeromechanical response of the blades but some observations relating to the effect of bleed extraction on the flow and on compressor performance are made. Steady CFD calculations are performed at different operating points to form pressure rise characteristics and these show that increasing bleed rate from 3.6% to 20% moves the downstream rotor operating point up and to the left on its characteristic: the normalised mass flow function reduces by 0.08 and the normalised pressure ratio increases by 0.025. It is shown that there is an increase in incidence onto the rotor row downstream of the bleed slot with increased bleed; this is consistent with the increase in pressure rise across the rotors. This is a useful result as it is believed to be the only published work that considers the effect of bleed on the operating point of a compressor, however, the impact that this has on the stall point is not discussed.

2.2.3 Bleed system flow and losses

Wellborn and Koir [13] predict a small increase in efficiency with increased bleed rate if the bleed slot flow is not accounted for in the calculation of efficiency. However, with bleed flow included, the overall efficiency is shown to reduce with increased bleed rate. This reduction in efficiency is due to loss generated in the bleed system; this section reviews work related to this topic.

Elmendorf et al. [14] include the bleed slot in their CFD mesh and Fig. 2.12 shows that the flow separates from the upstream face of the slot and causes a region of ‘blockage’ in the slot passage. Most of the bleed flow is extracted towards the back of the slot. This finding agrees with the work of Mossman and Randall [24] and Dennard [25]. Mossman and Randall’s work on the shape of air intakes for military aircraft shows that the pressure recovery through the intake is maximised when the angle at which the air intake is inclined to the main flow is as small as possible. Dennard found that the flow separates around the sharp “leading edge” of the intake but a more axially inclined upstream wall provides a surface for the flow to reattach to, reducing the separated flow and hence the blockage in the passage. Following the same argument, intakes with long walls were also found to give better pressure recovery. Bleed slots, which are similar in form and function to these air intakes, should

therefore be inclined towards the axial direction and be long enough for the flow to reattach. However, in a compressor both the slot angle and length of bleed slot are constrained by the space provided by other components. The geometry of the bleed slot in the study by Elmendorf et al. is typical of this constraint and is quite similar to the bleed slot investigated in the current work.

The work by Leishman et al. [18] also considers the flow in the bleed system. CFD calculated contours of radial velocity at 50% of the radial depth of the slot are shown in Fig. 2.13. At entry to the slot the flow separates at the inlet edge and causes flow to re-circulate back towards the primary flow (red contours represent flow from the slot back towards the passage). Most of the flow passes through the slot near to its downstream face. The separated flow is described as “similar to a trapped vortex with the axis of rotation in the pitchwise direction”; it is the same type of separation as observed by Wellborn and Koir [13] and Elmendorf [14] and it causes a significant portion of the slot to be blocked. This reduces the pressure recovery through the bleed system. Figure 2.13 shows that the bleed air enters the slot nearly uniformly across the blade passage although in the blade wake, where the flow has less axial momentum, the bleed slot separation is smaller and the flow is more evenly distributed across the slot.

These observations give a qualitative description of the flow in an axisymmetric bleed slot but Leishman et al. [18] also provide bleed characteristics for various bleed slot geometries which are shown in Fig. 2.14. The bleed pressure coefficient C_p is defined as $(P_s - P_{sI}) / (\frac{1}{2}\rho V_{ref}^2)$ where P_s is the average static pressure measured in the plenum chamber, P_{sI} is the inlet freestream static pressure, ρ is the inlet freestream density and V_{ref} is the inlet freestream velocity. Figure 2.14 shows that the bleed pressure coefficient drops as the bleed mass flow rate increases. It is explained that this is because with increased bleed, the bleed air is accelerated to higher velocities as it enters the bleed slot.

Leishman et al. [18] also test slots with different radius sizes on the bleed slot inlet edge. Figure 2.14 shows how the new slot geometries are defined and the bleed characteristics for various different inlet edge profiles. With increasing bleed rate, the drop in bleed pressure coefficient is dependent on the radius of the inlet edge. It is explained that there is less bleed pressure loss with increased inlet radius because the flow acceleration around the corner is reduced, reducing the flow separation and blockage and hence lowering the velocity of the flow in the slot.

Gomes et al. [10] investigate non-axisymmetric bleed system configurations using an annular cascade and configurable bleed system; the conclusions of this work in relation to non-uniform bleed are discussed in Section 2.3. However, their conclusion that “the main part of the pressure loss occurs within the bleed slot and by the abrupt expansion of the flow into the plenum chamber” is relevant here. They show that there is a flow separation within the bleed slot, a swirling secondary flow within the plenum chamber and flow separations and secondary flows within the off-take ducts.

The work also presents the effect of bleed rate on the stagnation pressure loss through the bleed system, shown in Fig. 2.15. \mathcal{Q} is defined as $(P_{01} - P_{obl}) / (P_{01} - P_1)$ where P_{01} and P_1 are the stagnation and static pressures measured in the main flow upstream of the bleed slot and P_{obl} is the average stagnation pressure in the off-take duct. The configuration tested has a large plenum chamber (cross sectional area 5000mm^2) and two off-take ducts separated by 90 degrees. The results show that for bleed rates below 6% \mathcal{Q} is between 1 and 1.08 and as bleed rate is increased \mathcal{Q} increases. The loss in stagnation pressure, for the bleed rates tested, is equal to between 1 and 1.5 dynamic heads of the mainstream flow. A similar measurement is performed in the current work, however, the flow through the bleed system is considered in a separate control volume to the mainstream flow which passes through the downstream compressor stage. As such, the dynamic head used to normalise the stagnation pressure loss through the bleed system is taken from the mainstream flow which is extracted, rather than the entire mainstream flow.

The work reviewed shows that the bleed system loss is dependent on the separation in the bleed slot, the expansion of the bleed flow into the plenum chamber, the flow field in the plenum chamber, and the flow in the off-take ducts. The experimental rig in the current work allows the total stagnation pressure in the off-take duct to be measured so that a loss coefficient for the bleed system can be calculated. CFD is then used to quantify the loss in the different components of the bleed system, i.e. in the bleed slot, plenum chamber, and off-take duct.

2.2.4 Summary

Even taken together, the work reviewed above gives an incomplete picture of the impact of circumferentially uniform bleed on compressor performance. Leishman's work provides detailed experimental and CFD results showing the interaction between stationary blades and a bleed slot but does not include downstream stages. Wellborn and Koiri's work investigates the effect of bleed on a downstream rotor row with CFD but details of the changes to the main passage flow due to the bleed extraction are limited. Gümmer et al. use CFD to study the effect of bleed specifically tailored to improve the main passage flow but their work doesn't consider the effect of bleed on the operating range of the compressor. Only in Di Mare's study is the effect of bleed on operating point explicitly considered and this is not taken forwards to consider the effect of bleed on compressor stall. Indeed, the topic of bleed and compressor stall is believed not to have been reported in the literature at this time. The current work addresses this open question. Elmendorf, Leishman, Wellborn and Koiri and Gomes all show that there is a large separated region in the bleed slot and this reduces the bleed system's pressure recovery and increases loss. Gomes also shows that loss through the bleed system increases with bleed rate and provides a qualitative description of the structure of the flow field in the plenum chamber and off-take ducts. The current work is well suited to studying the losses in the bleed

system, both with the experimental measurements and CFD calculations, and the effect of different uniform bleed rates is investigated.

2.3 Circumferentially Non-uniform Bleed

The work reviewed above assumes that air is bled through an axisymmetric bleed slot or bleed holes which result in uniform bleed extraction on the length scale of the circumference. In a real industrial gas turbine, however, air is bled into a plenum chamber and then removed by discrete off-take ducts. The discrete ducts mean that the flow rate through the slot varies around the compressor and so the effect on the primary flow is non-uniform in a circumferential direction. The positioning of the ducts and the size and shape of the plenum chamber also become important aspects of design when discrete off-take ducts are considered.

Gomes et al. [10] carried out experimental studies using an annular cascade with a row of stator blades upstream of a bleed system. The bleed system consisted of a bleed slot inclined at 45° to axial, a plenum chamber and off-take ducts. The bleed system was designed to be configurable so the shape of the bleed slot, size of plenum chamber and number and circumferential position of the off-take ducts, could be changed. Figure 2.16 shows the experimental setup and also shows the location of the static pressure measurements. In addition, a pneumatic probe is used to determine pressure losses and velocity components within the off-take ducts and oil film visualisations and 3-D Doppler-Global-Velocimetry are used to further understand the flow field in the plenum chamber.

In the main passage flow, a circumferentially non-uniform pressure distribution is shown at the hub of the main passage flow. Figure 2.17 shows the static pressure coefficient measured at the hub below the slot. $C_{p,h}$ is defined as $(P_h - P_{in}) / (P_{o,in} - P_{in})$ where P_h is the static pressure at each hub location and P_{in} and $P_{o,in}$ are the static pressure and stagnation pressure, respectively, measured in the main passage flow upstream of the bleed slot. The pressure at the hub is sensitive to the position of the bleed off-take ducts and this effect is enhanced with the smaller plenum chamber. Gomes et al. [10] briefly comment on this “higher inhomogeneity in the core flow” and state that it might have a negative effect on compressor aerodynamics. They also go on to suggest that the non-symmetric influence on the primary flow can be reduced by changing the shape of the plenum chamber. An increased outer plenum radius, near the ducts is suggested to make the flow field in the plenum chamber and primary flow more uniform.

A qualitative description of the flow in the bleed system is also provided. A swirling secondary flow is shown to be set up within the plenum chamber and flow separations and secondary flows are also present in the off-take ducts. Gomes and Schwarz [26] investigate these effects in more detail and show that changes in the plenum flow field depend on the bleed rate and the number and position of

the off-take ducts. For a configuration with two ducts spaced 90 degrees apart, two counter rotating vortices remain stable for about 210° of the circumference. Close to the ducts however the flow field changes due to the suction from the off-take ducts and stable vortices are no longer observed in the plenum chamber.

The work by Gomes [10, 26] focuses mainly on the flows within the bleed system and there is limited analysis of the effect of non-uniform bleed on the main passage flow. Also, as with Leishman's work, the experimental set-up does not include a stage downstream of the bleed slot so the impact of non-uniform extraction on compressor performance cannot be assessed. In the current work the experimental set up and full annulus CFD calculations enable the impact of non-uniform bleed extraction on a downstream compressor stage to be investigated for the first time. The effect of different plenum chamber sizes and off-take duct configurations on bleed system loss is also studied using the experimental rig.

2.4 Compressor Stall

All the work reviewed thus far has studied the effect of bleed at a stable compressor operating point. It is also extremely important to understand the impact that bleed has on compressor stall; however, to date, no work has been published directly linking bleed and stall. This section therefore provides a brief review of the key literature on stall and stall inception and where possible highlights areas that might be influenced by bleed.

Stenning [27] describes the normal operation of a compressor as “essentially steady and axisymmetric, apart from the blade-to-blade pressure variations and the small scale unsteadiness associated with the moving pressure and velocity fields of the rotors.” However, as the mass flow rate through the compressor reduces, and the pressure rise increases (at a fixed rotational speed), there becomes a point where compressor operation becomes unstable. This is shown by the compressor performance map in Fig. 2.18. The transition from stable to unstable operation at varying speeds are joined together with a ‘stall line’. To the left of this line, the flow is no longer steady: self-induced flow distortions may rotate around the annulus and/or large axial oscillations of mass flow may occur. These instabilities were first categorized by Emmons et al. [28] with rotating disturbances in a blade row called “stall” and large axial instabilities called “surge”. Both instabilities cause large, unsteady stresses on the compressor and surge in particular can lead to the interruption of the combustion process. The stall line, therefore, represents a limit to the safe operation of the machine and should be avoided. Often, however, the region of maximum efficiency occurs close to the stall line and it is therefore extremely important to be able to predict the onset of instability and, if possible, move it away from the most efficient operating point.

Having been distinguished from surge, stall can be split into two types. In “full-span” stall the whole blade span is stalled and usually there is one large, rotating stall cell. In “part-span” stall only part of the blade span stalls and the rest of the blade operates normally. In this case there are usually several small stall cells rotating around the blade row at any given time. Day et al. [29] show that stage loading and the proportion of the annulus blocked by the stall cell(s) are important factors in determining whether full-span or part-span stall occur. In general low hub-to-tip ratio blades, such as aero-engine fans, display part-span stall while several studies [29,30] show that compressors with high hub-to-tip ratio blades, like those investigated in the current work, can exhibit either full-span or part-span stall.

The process of moving from steady, stable compressor flow to unsteady, stalled flow is called stall inception. There are two recognised stall inception mechanisms, “modes” and “spikes”, and much work has been done to understand them. Moore and Greitzer [31] use linear stability theory to propose that modal waves would precede stall and these waves were first observed in a compressor by McDougall [32]. The modal waves are perturbations in velocity, seen around the entire circumference of the compressor, which grow over tens of revolutions and eventually cause the breakdown of the flow into rotating stall. This is shown in schematic form in Fig. 2.19(a).

The second stall inception mechanism, called a “spike”, was observed by Day [33] and investigated further by Camp and Day [34]. In this mechanism a small number of blades stall in the tip region causing a spike to appear on a rotor blade passing pressure signal. This happens without any modal perturbations occurring. The stalled blades cause a three-dimensional disturbance which passes from blade to blade and propagates around the annulus of the compressor in the rotor frame of reference. In its early stages the spike only effects two or three blades and is confined to the tip region but it rapidly grows and develops into a rotating stall cell within a few revolutions. This is shown in schematic form in Fig. 2.19(b). Camp and Day also found that spikes are most likely to occur if the compressor stalls on the negatively sloped part of the total-to-static pressure rise characteristic while modal stall is more likely to occur if the gradient of the characteristic at stall was zero.

In Pullan et al. [35] CFD calculations, corroborated with experiments, show that spikes are caused by a flow separation at the rotor leading edge resulting from high incidence. As the flow separates, a vortex is shed from the leading edge and convects towards the pressure surface of the adjacent blade. This approaching vortex triggers separation in the adjacent blade and so the spike propagates.

Why a compressor should stall with one mechanism and not the other is still not fully understood. Work by Dickens [36] suggests that spanwise location of blockage might be related to the stall mechanism and Simpson and Longley [37] show that restaggering stator blades or changing the inlet flow profile could change the stalling mechanism. Simpson and Longley suggest that this is

because the changes to the compressor alter the spanwise loading distribution on the rotor blades causing the flow breakdown to move, for example, from tip to hub and the stall mechanism to therefore change from spikes to modes.

Despite all the work carried out, of which the above is only a brief summary, it is still not possible for a designer to reliably predict whether a compressor will stall with modes or spikes or at what flow coefficient or pressure rise. It is therefore extremely difficult to predict what effect bleed will have on compressor stall, though some useful observations can be made. For circumferentially uniform bleed, Di Mare et al. [23] show that increasing bleed rate moves the operating point of a downstream stage to the left as the mass flow in the primary flow is reduced. If bleed extraction does not affect spanwise flow distribution, i.e. the bleed is removed uniformly across the span, one would expect characteristics plotted with pressure rise against flow coefficient at stage inlet (i.e. downstream of the bleed slot) to be the same for different bleed rates and for stall to occur at the same stage inlet flow coefficient. However, if the spanwise flow is redistributed by the bleed extraction the downstream stage will operate with a different inlet profile and the stage inlet stalling flow coefficient may change. Indeed, if the redistribution is large then the spanwise loading distribution may vary enough to change the mechanism for stall inception, as observed by Simpson and Longley [37]. These ideas are examined in Chapter 5 (experimental tests) and Chapter 7 (CFD) where the effect of varying uniform bleed rate on compressor performance is investigated.

2.5 Inlet Distortion

A non-uniform circumferential distribution of bleed extraction through the bleed slot or bleed holes results in a circumferential variation in the main passage flow entering the downstream stage. The stage therefore operates on different parts of its characteristic around the annulus in a similar way to a compressor subjected to inlet distortion. Figure 2.20 shows how a stall line is moved due to distorted inlet flow.

Before going on to review the relevant literature it is worth noting that most inlet distortion studies are concerned with a circumferential and/or radial variation in stagnation pressure. In the current work a one stage compressor with an upstream bleed slot is tested. In this case the flow entering the stage, just downstream of a slot with non-uniform circumferential bleed extraction has a circumferentially non-uniform static pressure field and a uniform stagnation pressure field. This is because the suction from the discrete off-take duct causes a non-uniform static field but between rig inlet and stage inlet there is little change in stagnation pressure so the stagnation pressure dsitribution is circumferentially uniform. Both stagnation pressure and static pressure distortion result in a non-uniform velocity flow field, however, so work related to inlet distortion is still relevant to the current

work. Another difference is that bleed in a real machine is extracted between embedded blade rows with relatively high hub-to-tip ratios in the mid-to-rear sections of the compressor whereas inlet distortion studies, by definition, focus on the inlet to the first stage of a compressor where hub-to-tip ratios are lower.

The parallel compressor model, first attributed to Pearson and McKenzie [39], provides a simple, idealised approach for understanding the effects of inlet distortion. Figure 2.21 shows how the parallel compressor model works. The flow is split into two sectors which have the same static pressure but different stagnation pressures and axial velocities. The pressure rise characteristic for each sector is assumed to be the same as the characteristics of the whole machine with uniform flow. The figure shows that with a distorted inlet flow this simple model predicts a loss of pressure rise. This is due to the shape of the characteristic curve; the averaged performance of the two sectors will always be below the operating point for uniform flow at the same overall flow coefficient.

The parallel compressor model has also been used to help understand the impact of distortion on compressor stability. Figure 2.21 shows that as the compressor is throttled the low stagnation pressure sector will reach the stall point on the characteristic before the equivalent operating point for uniform flow. This explains why a compressor operating with inlet distortion has a reduced operating range as shown in Figure 2.20. However, as research into inlet distortion progressed, inadequacies of the parallel compressor theory became apparent. Reid's tests [38] with distortions of varying circumferential extent are shown in Fig. 2.22. They show that regions of distortion have little effect on compressor operating range below a critical sector angle, θ_{crit} , and that the extent of individual sectors is more important than the total area of the distorted flow. Although these studies investigate inlet stagnation pressure distortions, similar changes to the velocity field, and hence to compressor operation, are expected if the circumferential distribution of bleed extraction is altered by changing the size of plenum chamber and/or number and location of off-take ducts.

The observations made by Reid led to the definition of a distortion parameter $DC(\theta_{crit})$ [40]. $DC(\theta_{crit})$ is widely used in distortion studies and gives a measure of how severe the stagnation pressure drop of the most distorted sector of angle θ_{crit} is below the mean stagnation pressure. It is defined as:

$$DC(\theta_{crit}) = \frac{\overline{P_0}|_{360} - \overline{P_0}|_{\theta_{crit}}}{\frac{1}{2}\rho U^2} \quad (2.1)$$

where $\overline{P_0}|_{360}$ is the mean stagnation pressure around the annulus, $\overline{P_0}|_{\theta_{crit}}$ is the mean stagnation pressure in a sector of size θ_{crit} which has the lowest stagnation pressure, ρ is the density and U the midspan blade velocity. Figure 2.23 shows the correlation between loss of surge pressure ratio and the

$DC(\theta_{crit})$ distortion coefficient for eight different compressor designs with different levels of distortion and operating at different engine speeds [40].

The $DC(\theta_{crit})$ method is used to characterise stagnation pressure inlet distortions and as such is of little use in the current work where the distortion is believed to be in the static pressure field. However, the idea of using a critical sector angle to characterise a circumferentially non-uniform flow remains relevant. The method developed in Chapter 8 to characterise non-uniform bleed draws heavily on the $DC(\theta_{crit})$ approach.

2.6 Summary and New Work

The work reviewed above can be considered in terms of the research questions framed in Chapter 1. For circumferentially uniform bleed the literature review demonstrates that there is a spanwise redistribution of the flow downstream of a bleed slot or hole and that this is affected by bleed rate. Questions remain, however, about the effect of bleed on the performance of a downstream stage; how does the bleed rate affect the spanwise flow distribution? How does a change in spanwise distribution affect compressor pressure rise and efficiency characteristics and how is the operating range affected? These questions are addressed in Chapter 5 (experiments) and Chapter 7 (CFD).

For circumferentially non-uniform bleed, Gomes et al. [10] show that the non-axisymmetric design of the bleed system, i.e. off-take duct number and location, cause a non-uniform static pressure field in the main annulus flow. However, questions about the effect of this non-uniform flow on a downstream compressor stage are not answered in the work reviewed above. The work in Chapter 6 (experiment) and Chapter 7 (CFD) addresses the following open questions: How does circumferentially non-uniform bleed extraction affect the main annulus flow upstream and downstream of a bleed slot? How does the non-uniform flow field affect a downstream stage in terms of its pressure rise (both annulus-averaged and locally), efficiency, and operating range?

Leishman [15] investigated how changes in bleed rate, and bleed slot and bleed hole geometry affect the stagnation pressure loss through the bleed system. However, this work was only able to consider circumferentially uniform bleed (on the lengthscale of the circumference) and did not include an off-take duct in the bleed system geometry. The work in Chapter 5 (experiments) investigates the effect of bleed rate on overall bleed system loss and in Chapter 7 (CFD) the breakdown of this loss in the different components of the bleed system is presented. The work in Chapter 6 studies the effect of non-axisymmetric bleed system configurations on stagnation pressure loss through the bleed system.

There is no work published on the effect of circumferentially non-uniform bleed on compressor operating range. However the links drawn in the literature review between bleed induced distortion

and inlet distortion lead to a hypothesis that increased bleed non-uniformity will lead to a loss in downstream stage operating range. The work in Chapter 8 tests this hypothesis and uses the critical sector angle approach, borrowed from the inlet distortion literature, to characterise the effect of circumferentially non-uniform bleed.

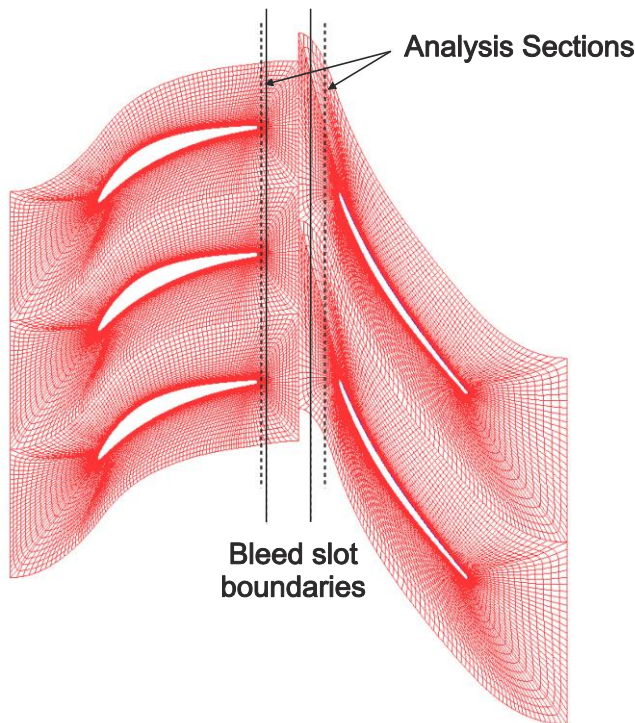


Figure 2.1: Blade passage and bleed slot mesh for Conan and Savarese's interstage bleed slot CFD calculation [12].

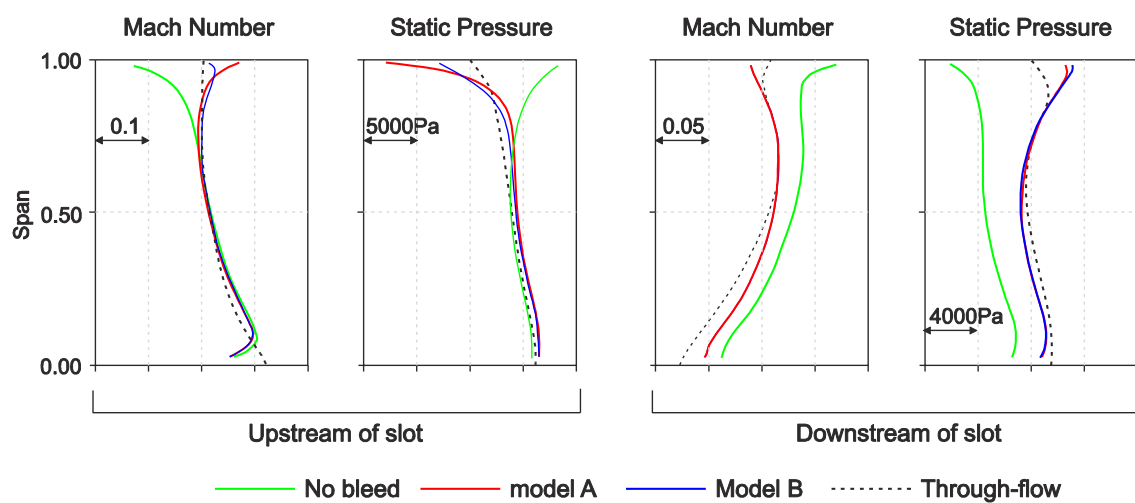


Figure 2.2: Spanwise Mach number and static pressure profiles upstream and downstream of bleed slot [12].

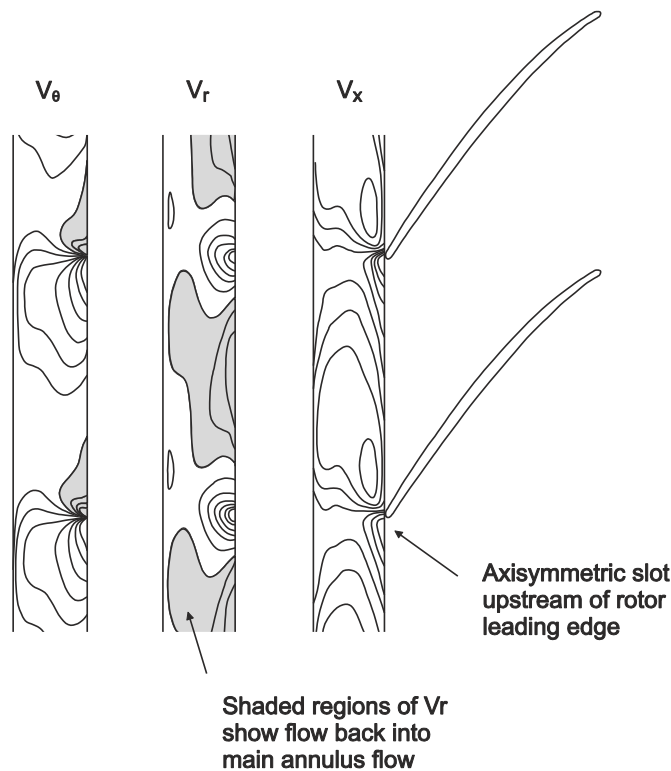


Figure 2.3: Velocity contours at bleed slot entrance with 0% bleed. Shaded regions denote negative velocities [13].

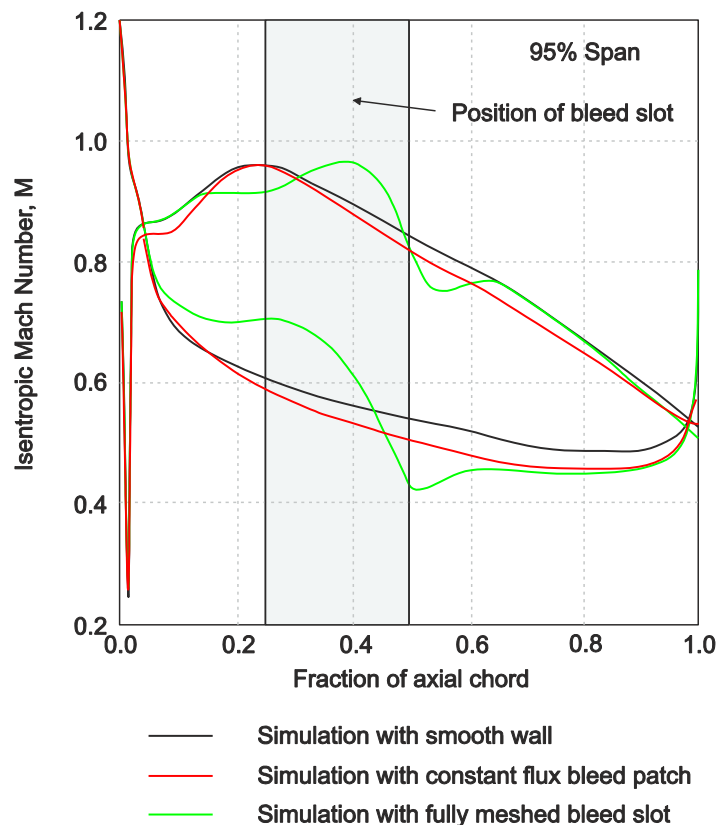


Figure 2.4: Blade surface Mach number distribution at 95% span [13].

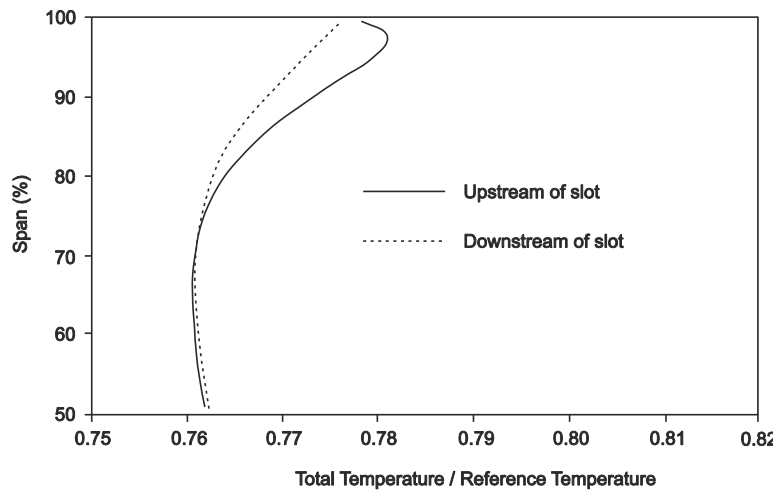


Figure 2.5: Effect of bleed on total temperature upstream and downstream of an axisymmetric bleed slot [14].

1. Inlet b'layer traverse plane at $0.75Cx$
2. Interchangeable sidewall
3. 2D CDA low-speed aerofoils
4. Adjustable tailboards
5. Downstream traverse plane at $1.25Cx$
6. Bleed holes machined into sidewall
7. Top/bottom b'layer suction box
8. Perforated wall for b'layer suction
9. Cascade sidewall

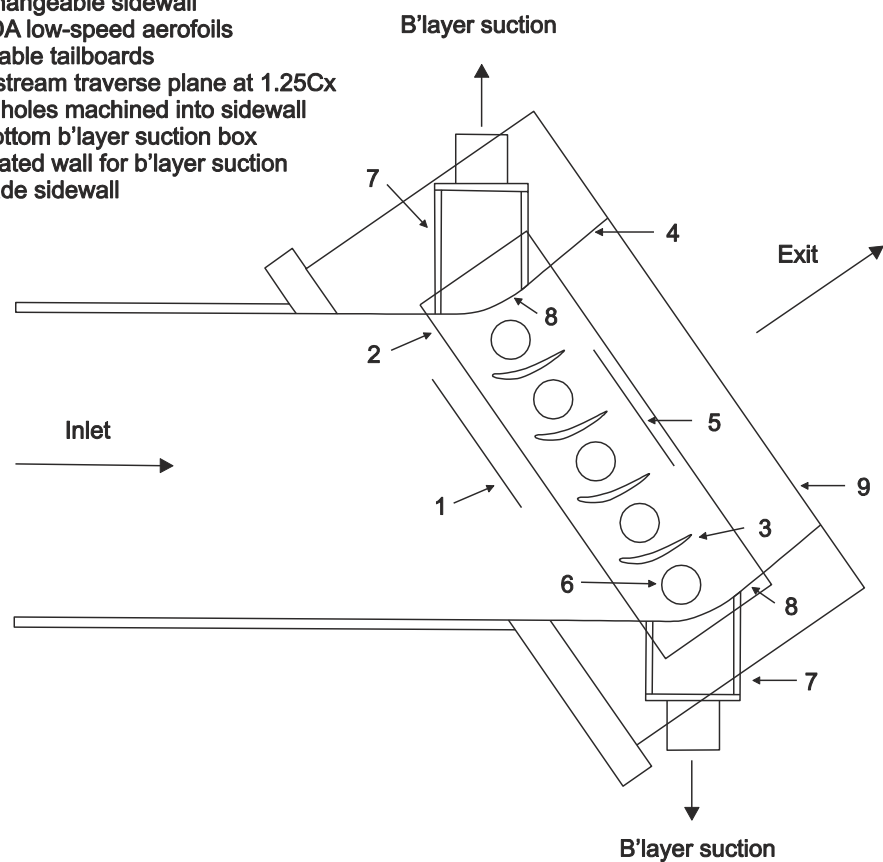


Figure 2.6: Linear cascade rig with bleed holes [17].

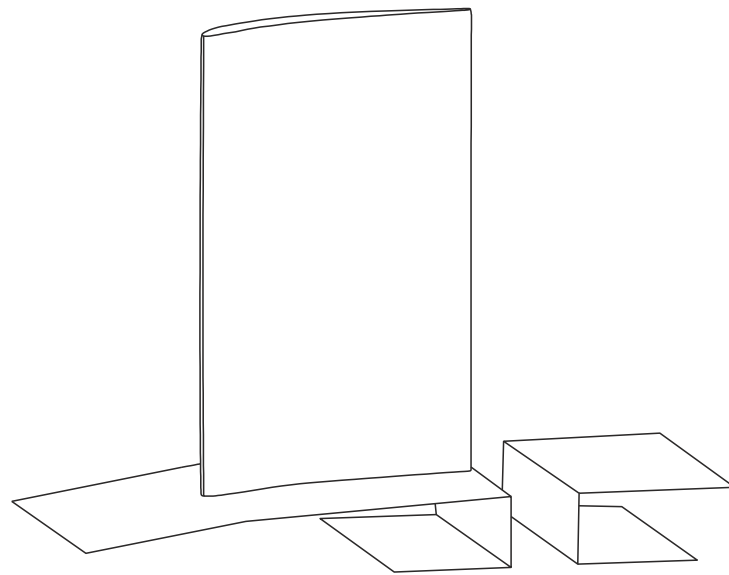


Figure 2.7: Stator blade and axisymmetric slot [18].

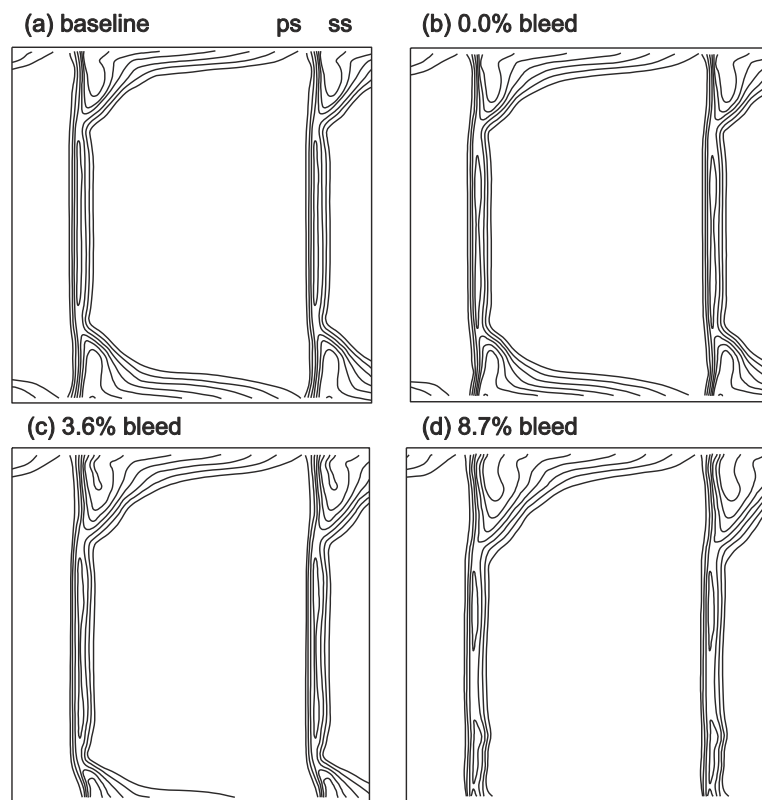


Figure 2.8: Measured contours of stagnation pressure loss downstream of bleed slot (minimum stagnation pressure loss coefficient contour 0.1; contour increment 0.1) [18].

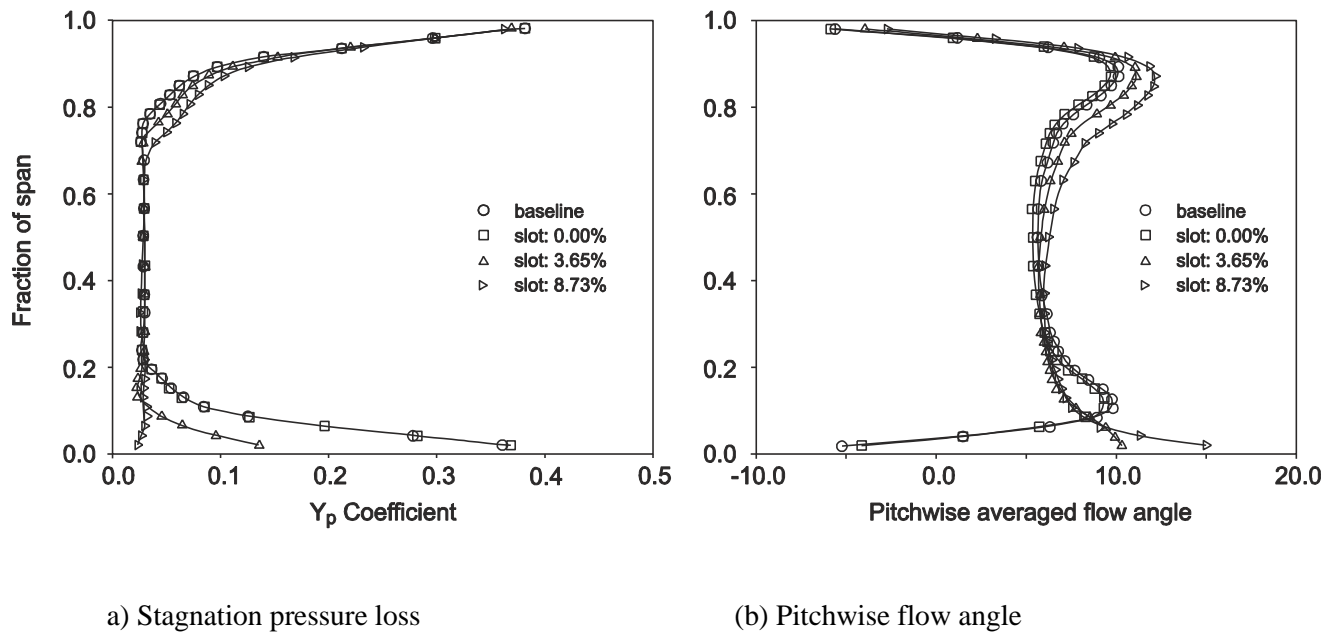


Figure 2.9: Measured pitchwise-averaged profiles of flow downstream of bleed slot [18].

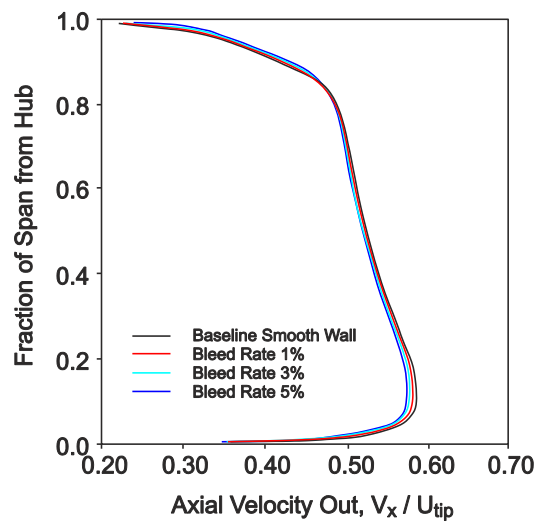


Figure 2.10: Spanwise distributions of axial velocity downstream of the rotor for varying bleed rates [13].

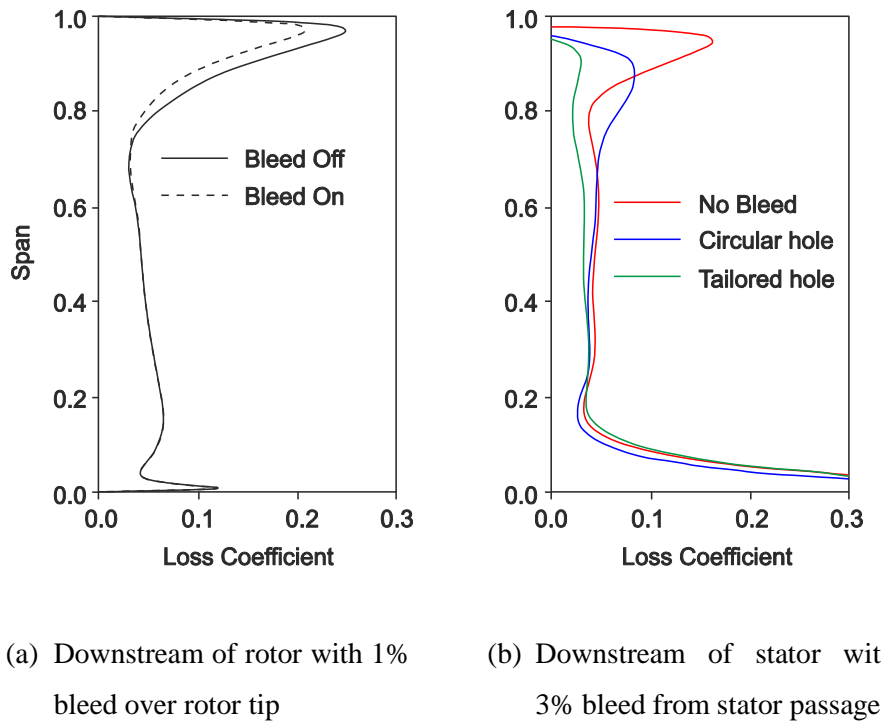


Figure 2.11: Pitchwise-averaged loss coefficient downstream of blade row [22].

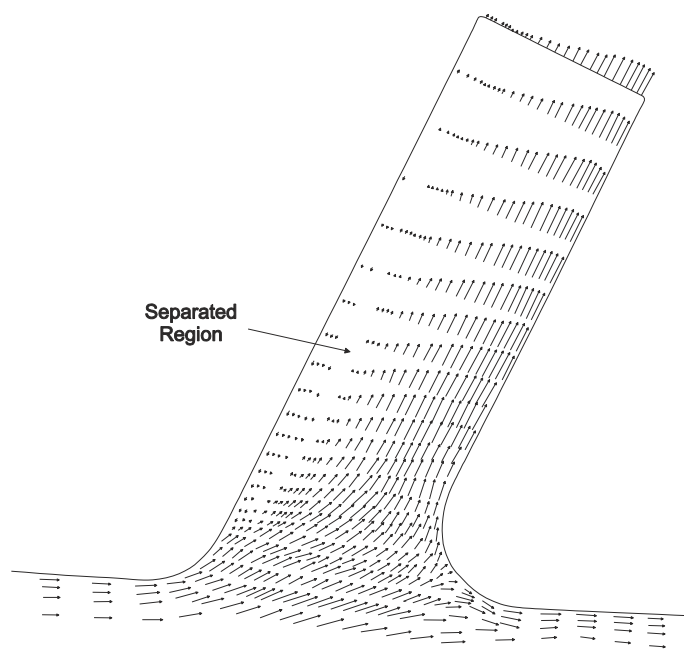


Figure 2.12: Meridional view of bleed slot showing velocity vectors calculated using CFD [14].

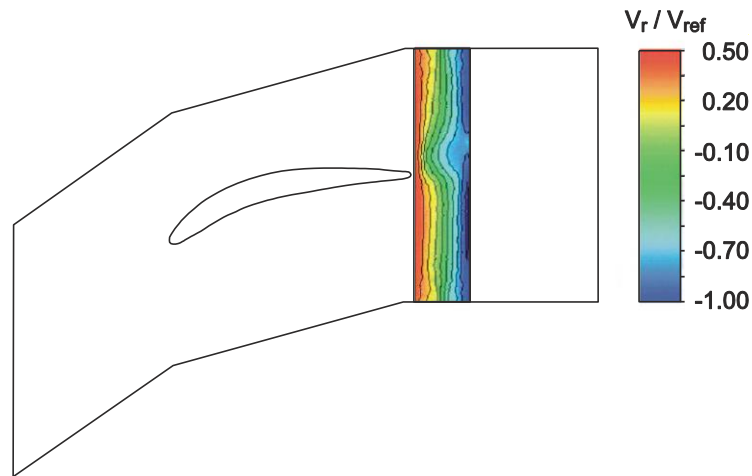


Figure 2.13: CFD calculated contours of radial velocity inside the slot with 8% bleed rate [18].

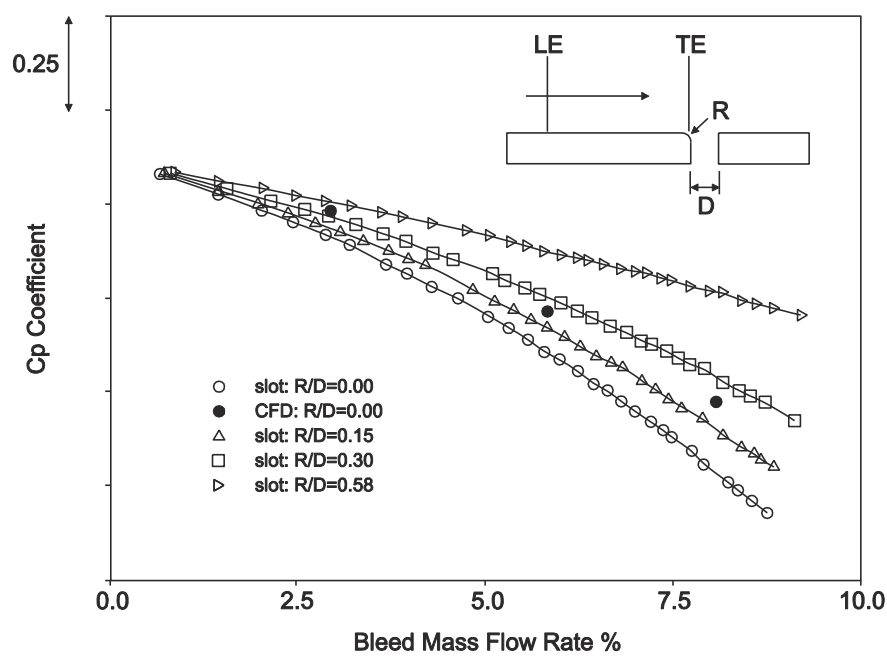


Figure 2.14: Bleed characteristics for downstream axisymmetric slots with varying inlet-edge fillets [18].

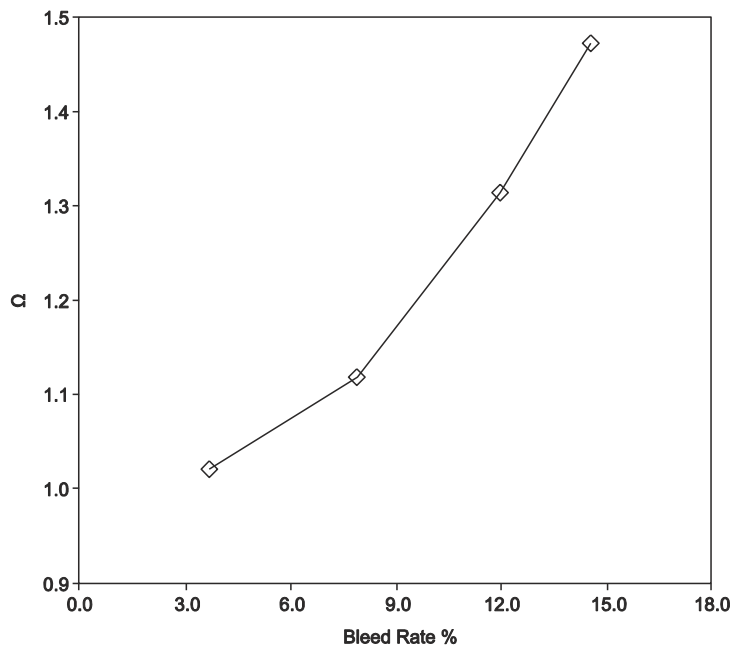


Figure 2.15: Bleed system loss coefficient against bleed rate [10].

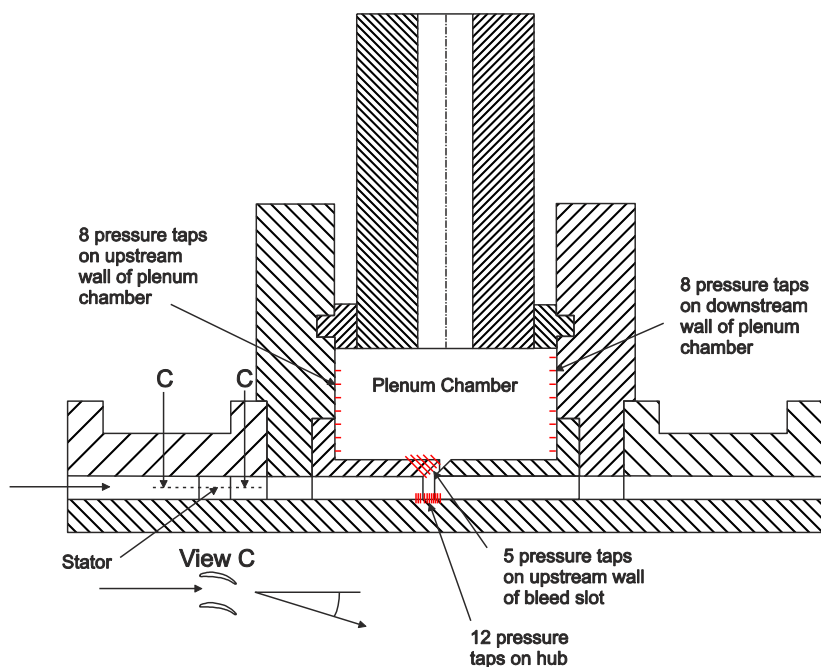


Figure 2.16: Detailed view of test section with instrumentation [26].

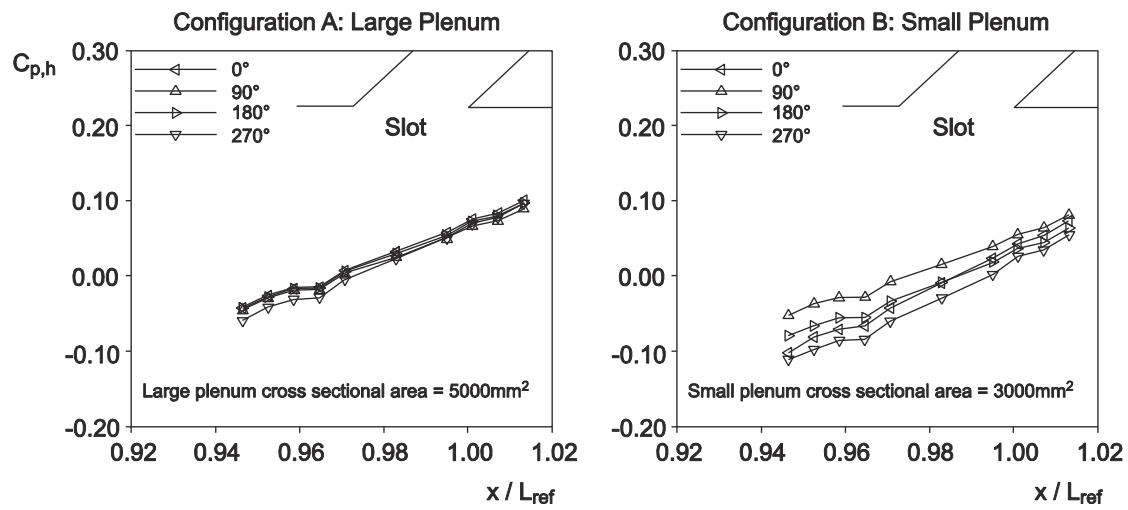


Figure 2.17: Static pressure coefficient at different locations on the hub for bleed rate of 12% [10].

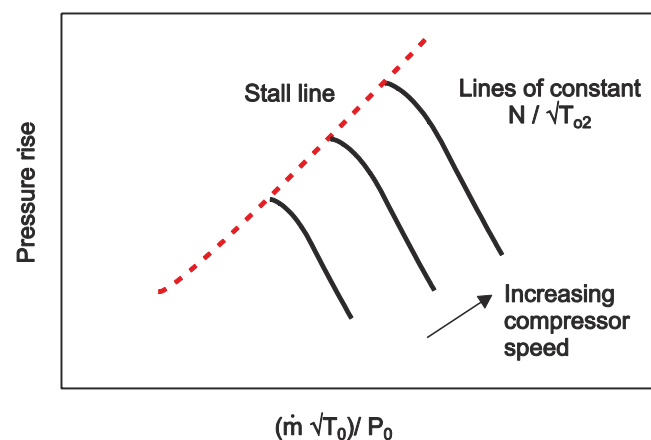


Figure 2.18: Compressor performance map [27].

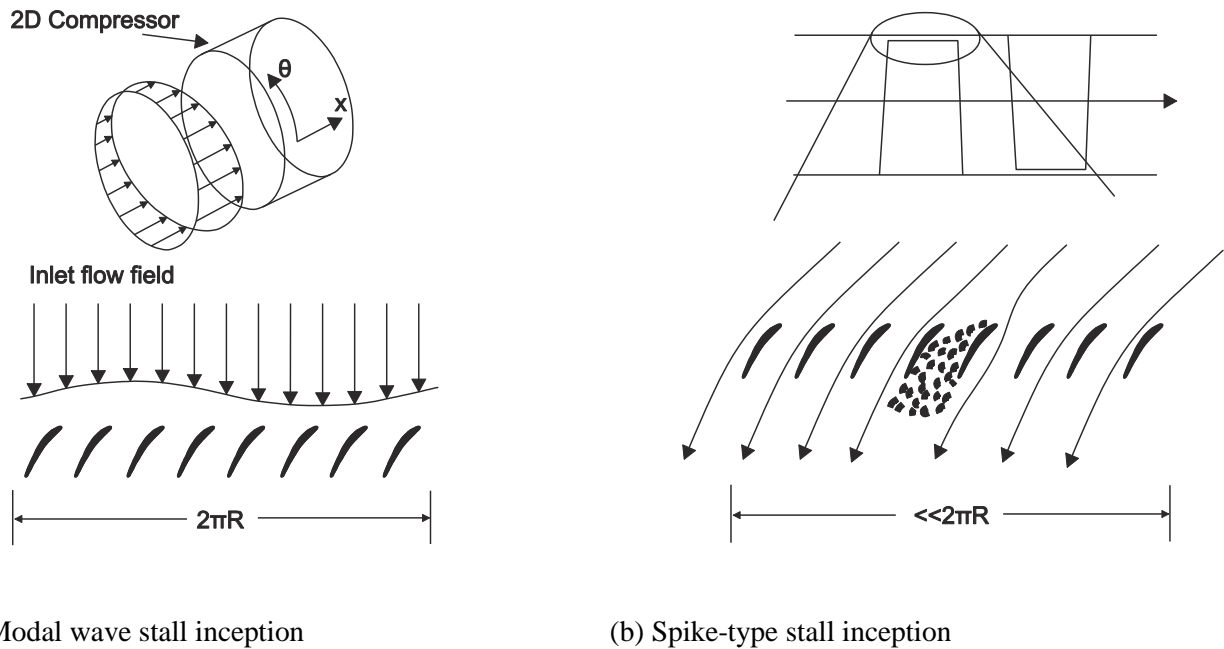


Figure 2.19: Schematic of modal wave and spike-type stall inception (Courtesy of J.P. Longley/I. J. Day).

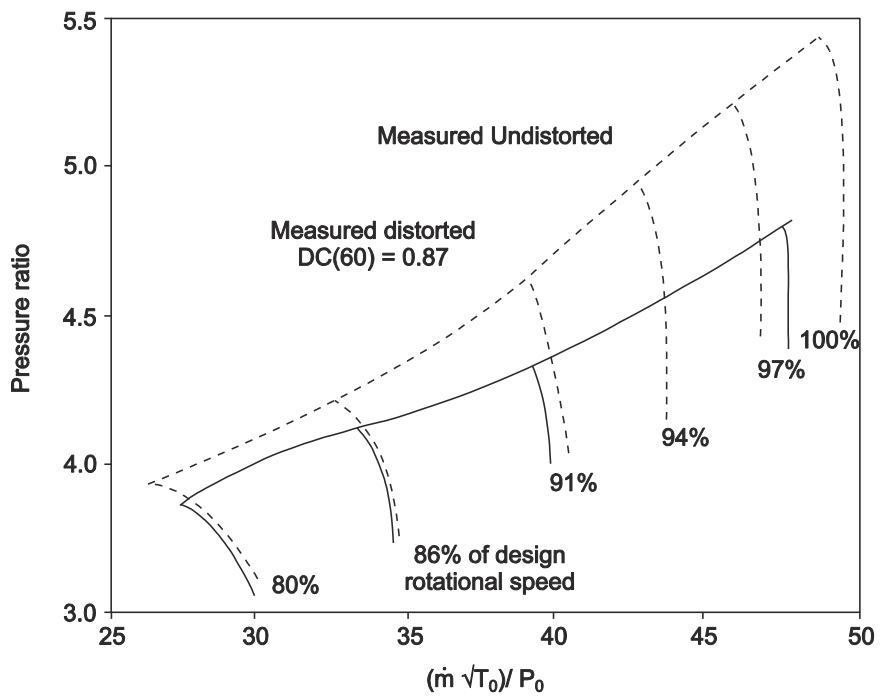


Figure 2.20: Loss of compressor performance due to inlet distortion [38].

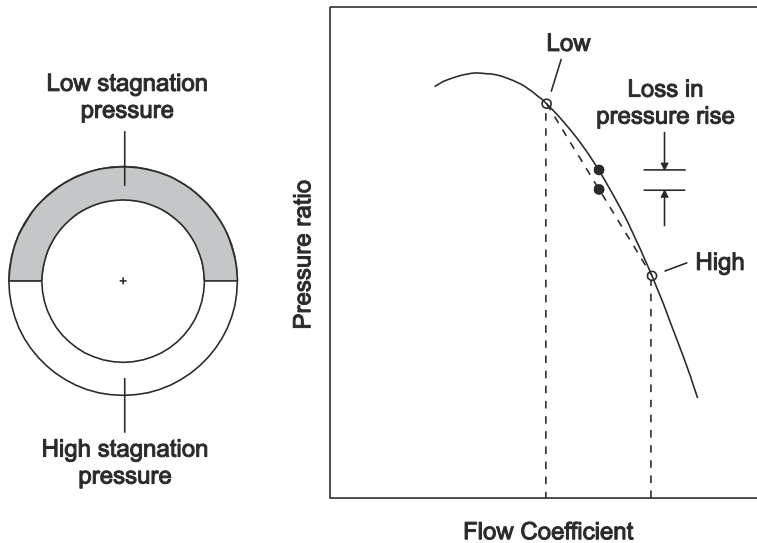
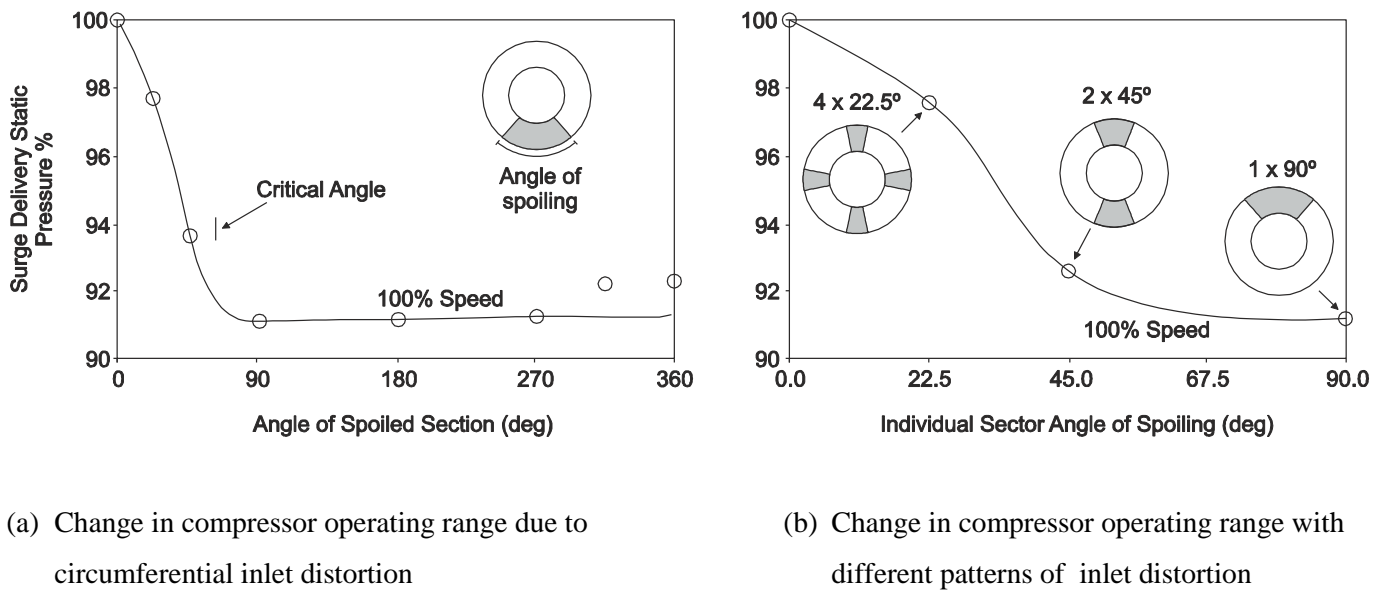


Figure 2.21: Parallel Compressor Model [39].



(a) Change in compressor operating range due to circumferential inlet distortion

(b) Change in compressor operating range with different patterns of inlet distortion

Figure 2.22: Effect of inlet distortion sector size on compressor operating range [38].

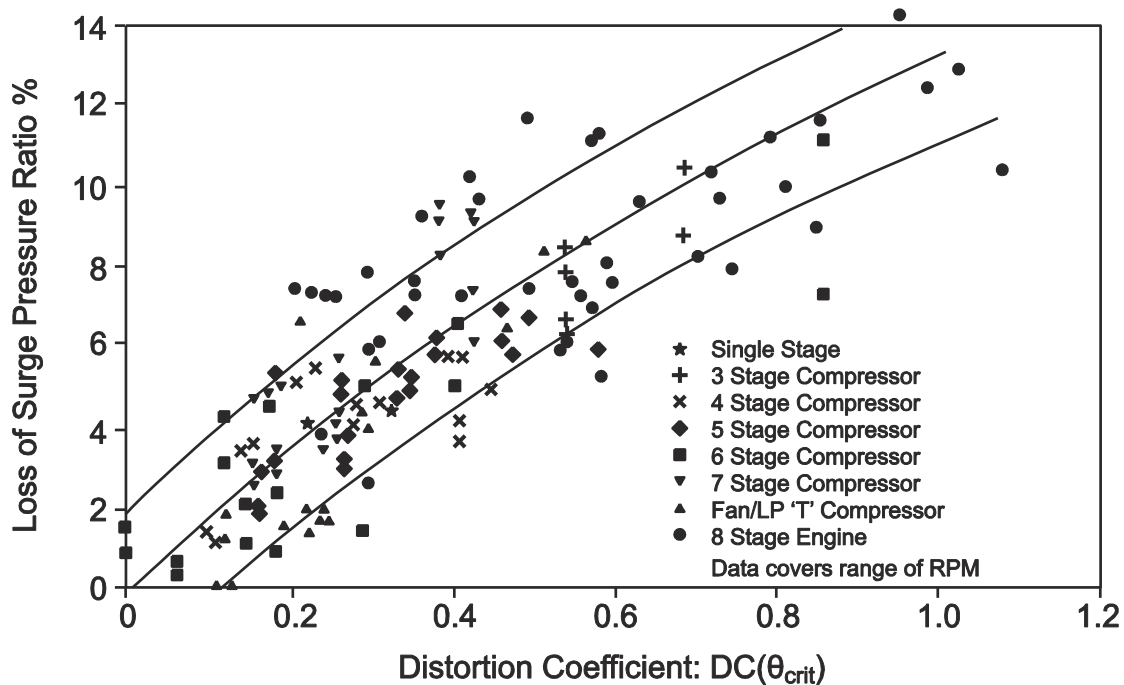


Figure 2.23: Correlation between $DC(\theta_{crit})$ and loss in surge pressure ratio [40].

Chapter 3

Experimental Methods

3.1 Introduction

This chapter describes the experimental methods that were used to investigate the impact of bleed on compressor performance. The first section introduces details of the annulus and blading, the overall layout of the Whittle Laboratory Red Compressor, and the design of the bleed system. The second section describes the various measurement techniques and experimental equipment that were used to investigate compressor performance, the compressor flow field, and bleed system loss.

3.2 Compressor Rig Details

This section gives details of the main annulus and blading, describes the overall layout of the rig, and presents the bleed system design including how the bleed system configuration can be changed.

3.2.1 Blading

The main annulus flow path consists of a parallel casing and hub with radius 0.254m and 0.1905m respectively, a row of 60 IGVs and a compressor stage comprising a row of 58 rotor blades and a row of 60 stator blades.

Blade design. The blades are designed by Mitsubishi Heavy Industries (MHI) to be a low speed representation of the blading in the intermediate pressure section of an industrial gas turbine compressor. The design was constrained by the rotational speed of the rig, the hub and casing diameters, the number of blades in each row and the axial envelope that each blade has to fit in. The IGV and stator blades are cantilevered from the casing; the IGV tips are adjacent to the stationary nose cone and the stator tips are adjacent to the rotating rotor hub. The axial spacing between the IGVs and rotors is 146.0mm or 6.1 rotor midspan axial chords at the casing. The rotors and stators are spaced by 19.4mm or 0.8 rotor midspan axial chords at the casing. Table 1 shows aerodynamic data for the blades.

Hub-to-tip radius ratio	0.75
Design $\phi = V_x/U$	0.43
Design $\psi_{t-s} = (P_2 - P_{01}) / (\frac{1}{2}\rho U^2)$	0.48
Tip speed Mach number	0.23
Rotor Re = $(\rho V_{rel} c) / \mu$	1.6×10^5
Rotor tip gap	1.7% c_x (= 0.4 mm)
Rotor blade count	58
Stator blade count	60
Casing Diameter	0.508m

Table 1: Data for Whittle Laboratory Red Compressor with MHI blades.

Blade manufacture and installation. The blades are vacuum cast using semi-rigid silicon moulds and are made from a urethane plastic. The blades are fitted to the rig using a jig which sets each blade at the correct stagger angle to within ± 0.2 degrees of the specified angle. Once fitted the blade tips are machined to the correct length. The nominal tip gap for all three rows of blades is 0.40mm or 1.3% IGV midspan axial chord, 1.7% rotor midspan axial chord, 1.0% stator midspan axial chord or 0.63% of span. A dial gauge is used to clock the casing rings concentric with a variation of ± 0.05 mm so the tip gaps vary between 0.35mm and 0.45mm or between 0.55% and 0.71% of span. This range of tip gap size was confirmed using a feeler gauge.

3.2.2 Overall layout of rig

The compressor studied in this project is a one-stage axial-flow, low-speed, vertical-axis compressor with inlet guide vanes (IGVs). It is located in the Whittle Laboratory at the University of Cambridge. This section presents the casing and hub designs, the drive systems used to power the compressor, the inlet section, and the throttle. A photograph of the rig, showing the compressor and bleed system, is shown in Fig. 3.1. Figure 3.2 shows a cross section of the working section of the compressor and bleed system.

Casing Design. The compressor casing is constructed from stacked aluminium rings which allow the rig to be assembled and dis-assembled easily. The casing rings just upstream of the compressor stage form a bleed slot and the upper section of the compressor is supported on six equi-spaced struts which extend across the bleed slot passage. These struts are cylindrical with a diameter of 13 mm and are labelled in Figure 3.2. They are set back from the entrance to the slot in order to minimise their impact on the main annulus flow.

A typical experimental traverse set up requires a circumferential slot to be machined in the compressor casing so that a measurement probe can be traversed in circumferential and radial directions. However, with the bleed system in place, access to the casing upstream and downstream of the slot, and downstream of the rotors, is difficult. The position of the plenum chamber means that the traverse probe has to be supported and controlled from a considerable distance from the compressor (over 0.3m) and would also have to pass through slots in the plenum walls, as well as through a slot in the casing. Slots in the plenum wall would cause a large leakage flow area and could significantly affect the flow in the bleed system. It was decided, therefore, that the probe should pass through radial holes in the plenum chamber rather than circumferential slots.

To allow area traverses downstream of the IGVs the casing and IGVs are rotated relative to the stationary probe. Figure 3.2 shows the location of the bearings that allow the casing and IGVs to rotate. The section of casing which rotates is also labelled. Six spacer bars are fixed to the stationary rings below the rotating casing section and these are fixed to a non-rotating flange above the IGV ring. This set up fixes the position of the non-rotating rings relative to each other and the spacer bars give the correct axial spacing so that the casing rings can turn smoothly on the axial thrust bearings. The rotating casing rings are positioned using a dial gauge to ensure they are concentric with the rest of the compressor and three eccentric cam follower bearings are used to secure this position. The gaps between the rotating and stationary casing rings are sealed with rubber v-seals as shown in Fig. 3.2. The seals are lubricated with grease to reduce friction and help reduce leakage.

The rotating casing allows area traverses to be performed with a probe fixed in a circumferential position at the following locations: upstream of the IGVs, downstream of the IGVs (i.e. at rig inlet), upstream of the slot, downstream of the slot (i.e. at stage inlet) and downstream of the rotors. Access for these traverses is provided by slots in the casing upstream and downstream of the IGVs and with radial holes cut through the plenum chamber and bleed slot rings. Downstream of the stators the plenum chamber does not obstruct the casing and an area traverse can be performed by changing the circumferential position of the probe. Figure 3.3 shows the rig working section in cross section with the various traverse holes and slots labelled. At stage inlet the space between the bleed slot and the rotor row is limited. The head of the probe therefore traverses a plane that is 2.5 mm upstream of the rear face of the bleed slot. This is not an ideal location and its effect on the results is discussed and accounted for in Chapters 5 and 7.

Rotating the IGVs relative to the stators and the off-take ducts introduces ‘clocking’. Clocking occurs when wakes formed by upstream stationary blade rows convect through the flow and interact with downstream stator rows and wakes. Gundy-Burlet & Dorney [41] show with CFD that efficiency can vary by as much as 0.8% by clocking two stator rows with respect to each other. In the current work the casing and IGVs are only rotated for area traverses at rig inlet, upstream of the slot, at stage

inlet and downstream of the rotors. For all other tests including the traverses downstream of the stators the casing is not required to rotate and the rings are fixed in the same datum location. For the area traverses listed, however, clocking might affect the results so a short study was undertaken. The compressor was run at a fixed throttle position with a bleed rate of 0% and the rotating casing was moved from -3 to +3 degrees (i.e. one IGV pitch) relative to the datum position in 1 degree intervals. The operating point for each clocked position was measured and plotted on a total-to-static pressure characteristic as described in Section 3.3.1. Figure 3.4 shows that the operating point changes as the IGV rings are clocked. The difference in rig inlet flow coefficient between the clocked positions one pitch apart (i.e. at -3 degrees and +3 degrees) is only 0.02%. The change in rig inlet flow coefficient between the -3 degree position and 0 degree position is 0.10% and the change in total-to-static pressure rise coefficient is 0.29%. It is concluded that for the current work the effect of clocking on the area traverses is negligible.

For area traverses where the casing is rotated, the IGVs also move relative to the off-take ducts. However, any non-uniformity caused by bleed from discrete off-take ducts should occur over a length scale which is comparable to the distance between them, i.e. for four off-take ducts, quarter of the circumference of the casing, ~400mm. During the area traverse the blades will only move over one blade pitch which has a length scale of ~30mm. This difference in length scale means that the movement of the IGVs relative to the off-take ducts will not change the flow through the IGVs significantly. Overall, it can be concluded that the effects of clocking and the movement of the blades relative to the off-take ducts do not significantly affect the results obtained by the area traverses.

Rotor disc design. The rotor discs are supported on a table fixed to the rotor shaft; the height of this table can be adjusted to set the axial location of the rotor row. The lower rotor disc (with rotor blades attached) sits on this table and stacked on top of this are spacer discs. Eight bolts secure all of the discs to the shaft table and a further eight caphead bolts are used to fix the discs together. The rotor is balanced by attaching two small weights to the inside wall of the upper spacer disc. The weights are moved circumferentially until the vibration, measured by a vibration meter fixed to the casing wall, is reduced to a minimum.

Drive system. The compressor can be driven with a variable-speed electric motor drive or a fixed-speed, soft start electric motor drive. The soft start drive was installed because the variable speed drive causes severe electrical noise which particularly effects torque and unsteady pressure measurements. All tests reported in this thesis are run with a shaft speed of $49.8\text{Hz} \pm 0.2\%$, driven with the fixed-speed drive.

Inlet and flow conditioning. Air enters the compressor through an inlet section which includes a filter, a honeycomb flow straightener and plenum. The air then passes through an inlet contraction consisting of a bell mouth casing and non-rotating nose cone.

Throttle design. The throttle is located 350mm (9 midspan stator axial chords) downstream of the stators. It consists of two cylindrical, metal sheets which have three equally spaced holes. The outer sheet fits as a sleeve over the inner and can be rotated so that the holes move relative to each other (like a shutter) to control the exit flow.

3.2.3 Bleed system

The bleed system consists of five components: firstly, air is bled from the primary flow through the axisymmetric casing slot. This bleed air passes from the slot into the axisymmetric annular plenum chamber and from here the air is extracted through one or more off-take ducts. The off-take ducts are attached to orifice plates which measure bleed mass flow rate and finally the air passes through vacuum pumps which provide the suction to draw air through the bleed system.

Slot design and location. The bleed slot is designed by MHI and is representative of a typical slot found in the mid stages of an industrial gas turbine. Figure 3.5 shows a cross section of the casing rings that form the bleed slot, the key dimensions of the slot and the location of the slot relative to the downstream rotor row. In non-dimensional terms the 4.3mm gap between the slot downstream face on the casing and rotor leading edge is 18% of rotor midspan axial chord.

The bleed slot is shaped as a diffuser in an attempt to achieve some pressure recovery. This slot shape is a compromise, however, between aerodynamic design and the limited axial space in which it can be positioned. The slot is “kinked” to make the inlet angle to the slot closer to axial and the leading edge of the slot also has a radius. As discussed in the literature review, these design features are an attempt to reduce the separation and subsequent blockage that occur as air enters the slot. Optimising the shape of the bleed slot is not in the scope of the current work and the shape of the bleed slot remains the same for all of the work described in this thesis.

Plenum chamber design. The plenum chamber assembly is designed so that it can be easily changed. Three sizes of plenum chamber are tested and these are shown in Figure 3.6. The large plenum chamber is formed from sheet metal and is representative of the size and shape of the plenum used in an industrial gas turbine. Figure 3.6(a) shows a cross section of the large plenum chamber and the casing rings to which it is attached. The outer wall of the plenum chamber can be removed to allow access inside the plenum and to allow the blocks for the medium and small plenum chambers to be inserted (see below). The figure also shows how the tubes from the static pressure tappings are taken along the outside of the casing and out of holes in the plenum walls. Leakage through these holes is prevented with silicon sealant. For traverses, probes pass through an aluminium block which is located with respect to the casing by four dowel pins. This ensures that the probe is positioned accurately so that it passes without interference through the plenum chamber, and the casing rings,

into the passage. Joints between the sheet metal and the casing rings are sealed with silicon sealant and foam tape is used to seal the join between the plenum walls and the outer face.

Figure 3.6(b) and 3.6(c) show how the medium and small plenum chambers are formed. Four quarter annulus blocks, made from modelling board, are inserted into the sheet metal plenum chamber. These blocks form either the medium or small plenum chambers and include off-take duct holes which sit under the off-take ports on the outer face of the sheet metal plenum. Small notches are cut in the blocks to accommodate the pressure tapping tubes and unsteady pressure transducer cables (see Section 3.3.5) and these notches are sealed with foam. This design makes it possible to switch between plenum chamber sizes without disassembling the annulus walls or compressor blades.

Off-take ports and ducts. The number of off-take ducts is another key variable in the current work and the rig has been designed with sixteen equally spaced off-take ports available. When not in use these ports are blocked with bungs so that they do not act as resonant chamber and so there is no leakage. The off-take ports and ducts have an internal diameter of 80mm although this reduces to 60mm for the off-take holes cut into the medium and small plenum blocks. The sixteen available off-take ports allow a variety of different off-take duct configurations to be tested. In this study these are: four ducts equi-spaced, two ducts with the ducts positioned from 22.5 degree to 180 degrees apart, and one duct. Area traverses investigating non-uniform bleed can also be performed by moving the duct locations relative to the fixed traverse location.

Orifice plates. The orifice plates' design and operation is based on International Standard EN ISO5167; more information on their operation is given in Section 3.3.2. Orifice plates are mounted in four long, straight pipes with 1710mm (30 orifice diameters) length upstream and 460mm (8 orifice diameters) length downstream. When four off-take ducts are in use each pipe is connected directly to an off-take duct allowing the bleed mass flow rate to be measured and controlled independently in each duct. For operation with one off-take duct a plenum box is used to attach the four orifice plate pipes to a single duct. Similarly, for two off-take ducts two plenum boxes are used to attach two orifice plate pipes to a duct.

Vacuum pumps and control valves. Four vacuum pumps provide the suction required to draw air through the bleed system. These are attached to the downstream end of an orifice plate pipe. The mass flow rate through the off-take ducts is controlled by the power setting on the vacuum pumps (coarse control) and by flow control valves in place between the orifice plate pipes and the vacuum pumps (fine control).

3.3 Measurement Techniques

A number of techniques are used to measure the effect of bleed on compressor performance, on the compressor flow field, and on the loss through the bleed system. These techniques provide pressure rise and efficiency characteristics, overall and local bleed mass flow rates, area traverses of the flow field, and unsteady pressure measurements of the rotor blade passing signal. This section describes the techniques and the instrumentation required.

3.3.1 Pressure rise characteristics

Pressure rise and flow coefficients. The change in pressure across the compressor is non-dimensionalised to give the following pressure rise coefficients:

$$\psi_{t-s} = \frac{P_2 - P_{01}}{\frac{1}{2}\rho U^2} \quad (3.1)$$

$$\psi_{s-s} = \frac{P_2 - P_1}{\frac{1}{2}\rho U^2} \quad (3.2)$$

where subscript 2 is the downstream location, subscript 1 is the upstream location, subscript 0 represents stagnation conditions, P is pressure, U is the midspan blade speed, and ρ is the density of air at the upstream location.

The flow coefficient at rig inlet (i.e. downstream of the IGVs) is defined as:

$$\phi_{rig} = \frac{V_{x,in}}{U} = \frac{\dot{m}_{in}}{\rho A U} \quad (3.3)$$

and the flow coefficient at stage inlet (i.e. downstream of the bleed slot) is defined as:

$$\phi_{stage} = \frac{\dot{m}_{in} - \dot{m}_{bl}}{\rho A U} \quad (3.4)$$

where $V_{x,in}$ is the one-dimensional area-averaged axial velocity at inlet, \dot{m}_{in} is the calibrated inlet mass flow (see below), \dot{m}_{bl} is the bleed mass flow, ρ is the density of the flow at the axial location where the coefficient is defined and A is the cross-sectional area of the main annulus flow.

Static and stagnation pressure measurements. For the static pressure measurements there are eight equally spaced static pressure tappings located on the casing wall at the following locations: in the parallel section of the inlet, upstream of the IGVs, downstream of the IGVs, upstream of the slot, downstream of the slot, downstream of the rotors and downstream of the stators. For overall pressure rise characteristics each set of eight pressure tappings are connected together using manifolds and a pneumatically averaged static pressure is measured. In addition to the static pressure tappings, four Pitot tubes are located in the compressor inlet and these are pneumatically averaged and recorded to give an inlet stagnation pressure.

Inlet density and rig speed. Three equally spaced thermocouples are mounted in the parallel section of the inlet. The inlet static pressure is calculated from the atmospheric pressure, recorded by a digital barometer close to the rig, and the gauge pressure of the pneumatically averaged inlet static tappings. The average of the three temperature measurements and the inlet static pressure are used to calculate the inlet density. The rig speed is measured using a tachometer mounted on the rotor shaft and this is used to calculate the midspan blade speed.

Inlet calibration. The inlet mass flow is found by performing a radial traverse upstream of the IGVs (see Section 3.3.4). For characteristics it is inconvenient to have to perform a traverse every time the inlet flow coefficient is required. Instead, the traverse-measured mass flow is compared with the difference between the inlet stagnation pressure and the inlet static pressure to form a non-dimensional calibration factor, K , as described by Dunkley [42] and defined as:

$$K = \iint \frac{\rho_{pr} V_{x,pr}}{\sqrt{\rho_{in}(P_{0,in} - P_{in})}} dA \quad (3.5)$$

where ρ_{pr} and $V_{x,pr}$ are the density and axial velocity measured by the five hole probe, $P_{0,in}$ and P_{in} are the stagnation pressure and static pressure measured by the inlet Pitot tubes and pressure tappings in the inlet section and ρ_{in} is the inlet density. This calibration can then be applied to the inlet stagnation and static pressure difference, while running a characteristic, to provide the calibrated inlet mass flow, \dot{m}_{in} :

$$\dot{m}_{in} = \sqrt{\rho_{in}(P_{0,in} - P_{in})} K \quad (3.6)$$

A correction factor C_{p0} is calculated which links the stagnation pressure measured by the inlet Pitot tubes and that measured by a five hole probe area traverse at rig inlet, i.e. downstream of the IGVs. C_{p0} is defined as:

$$C_{p0} = \frac{P_{0,in} - \overline{P_{opr}}}{P_{0,in} - P_{in}} \quad (3.7)$$

so that the calibrated rig inlet stagnation pressure, $P_{0,rig}$ is:

$$P_{0,rig} = P_{0,in} - (P_{0,in} - P_{in})C_{p0} \quad (3.8)$$

where $P_{0,in}$ and P_{in} are as above and $\overline{P_{opr}}$ is the mass-averaged stagnation pressure from the area traverse. A similar stagnation pressure calibration is performed with area traverses at stage inlet which are used to give stage inlet total to stage exit static pressure rise.

These calibration factors are particularly important for matching experimental data with CFD results as changes in K and C_{p0} shift the experimental compressor characteristic left and right or up and down respectively. In order to measure the inlet mass flow accurately as much of the end wall

boundary layers are traversed as possible by touching the probe onto the (stationary) hub and casing (see Section 3.3.4). The remaining end wall boundary that cannot be traversed has been modelled by setting velocities to zero, stagnation pressure to the same value as static pressure and all other quantities to the same value as recorded at the traverse point closest to the wall. After repeating the radial traverses upstream of the IGVs four times, the averaged value for K is 0.12524 with a variation over these repeats of $\pm 0.2\%$. C_{p0} at rig inlet was found to be 0.0603 with variation $\pm 1.5\%$.

Recording characteristics. Pressure rise characteristics are generated by closing the exit throttle to reduce the mass flow and thereby change the pressure rise across the compressor. Pressure rise characteristics can be measured continuously as the compressor is throttled (see, for example, Camp and Day [34]). However for the current work, the bleed extraction means that this is not possible. The bleed rate is required to be constant across the compressor operating range where bleed rate is defined as:

$$R_{bl} = \frac{\dot{m}_{bl}}{\dot{m}_{in}} \quad (3.9)$$

Throttling the compressor changes the bleed rate so characteristics in the current work are made up of discrete operating points and the bleed rate is adjusted to the required fraction of mainstream mass flow at each of these. 20 measurements are taken at each operating point and averaged in the post processing. Measurements are only recorded if the bleed rate is within $\pm 0.5\%$ of its specified target. For more details on bleed measurement see Section 3.3.2. Repeated experiments show that at $\phi_{rig} = 0.43$, rig inlet to stage exit $\Delta P_{t,s}$ is repeatable within ± 0.0015 , i.e. $\pm 0.3\%$.

Stall measurements. To measure the stall point the characteristic has to be recorded continuously and as discussed above the bleed rate cannot be kept constant as the compressor is throttled. The change in bleed rate can be minimised by setting the bleed rate for the last stable operating point as close to the stall point as possible. In practice it is possible to set the bleed rate at a flow coefficient within 1.4% of the stall point and the bleed rate is then maintained to within 0.1% points of its target when the compressor stalls. The pressure transducer only logs data at 2.5 Hz (see Section 3.3.6) so to ensure that the stall point is measured accurately the compressor is throttled at a rate of change of flow coefficient of around 0.001 per second. At this rate of throttling the change in flow coefficient between measurements is around 0.1% just before stall. The accuracy of the measured stalling flow coefficient is improved by recording ten stall events, back to back, and calculating the average stalling flow coefficient and pressure rise (the standard deviation of a typical set of ten stalling flow coefficients is 0.15%).

In order to change the plenum chamber size the bleed system is disassembled and rebuilt. It is found that after these “builds” the stalling stage flow coefficient of the compressor with a bleed rate of 0% can change by ± 0.003 ($\pm 0.75\%$). It is assumed that the stall point of the 0% bleed case should be

constant, independent of the bleed system configuration. The reason for the change is not known but it is hypothesised that the change in stall point is due to small changes in the compressor geometry, caused by the rebuild. The stalling flow coefficients for a particular build are therefore recorded relative to the 0% bleed rate case for that build and then adjusted to a datum 0% bleed rate case. This allows the same case (i.e. same bleed rate, plenum chamber size and number and location of off-take ducts), tested during two different builds to have a stalling stage flow coefficient repeatable to ± 0.001 ($\pm 0.25\%$).

3.3.2 Bleed measurements

This section describes how the total bleed rate extracted through the bleed system is measured with orifice plates and the local bleed rate through the bleed slot is measured with 16 pairs of static tappings and stagnation pressure probes.

Orifice plates. Orifice plates are designed and operated in line with International Standard EN ISO5167. The system works by measuring the pressure drop across the orifice plate and from this the mass flow rate can be calculated. The pressure upstream and downstream of the orifice plate are measured by four static pressure tappings in the pipe walls which are connected together with a manifold, pneumatically averaged and recorded. The density of the bleed air is also required. Temperature is measured by a thermocouple mounted in the pipe downstream of the orifice plate and the pressure is calculated from the digital barometer and the gauge pressure measured by the tappings downstream of the orifice plate. When one or two off-take ducts are in use a plenum box is used to connect the orifice plate pipes to the off-take duct(s) and the mass flow rates measured by each orifice plate are summed to give the overall bleed rate through the off-take duct(s).

Circumferential bleed rate measurement. In the current work it is important to know the circumferential distribution of the bleed flow in the slot. This is a key measurement which allows bleed non-uniformity to be quantified and characterised. The measurement is performed using 16 equally spaced pairs of static pressure tappings and stagnation pressure probes located in the bleed slot. Figure 3.7 is a cross section of the casing rings which form the bleed slot and it shows the location of the static pressure tapping and stagnation pressure probe. The probe holes' centreline is located only 3mm above the downstream face of the slot. This is because the flow separates off the upstream wall of the slot and most of the bleed air passes along the downstream face, making this the most effective location to measure the stagnation pressure. The stagnation pressure probes can also be rotated and for each measurement taken the probes are nulled so that the total pressure measured is at a maximum. The probes therefore face into the direction of the flow and these flow angles are recorded. The stagnation pressure probe used is a simple cylinder, sealed at one end, with a hole in. This type of probe is used in favour of a Pitot probe because it has a poor tolerance to flow angle. This

means that the probe can be nulled more accurately because the measured stagnation pressure drops off more quickly when it is not pointing into the flow.

The local bleed rate measurement is made by using the pressure difference between the tapping and the probe to measure the local bleed mass flow rate. To do this the pressure differences are calibrated against known mass flow rates, which are obtained by extracting circumferentially uniform bleed through the bleed slot. It is assumed that the bleed is circumferentially uniform when the bleed system consists of a large plenum chamber and four off-take ducts. This assumption is supported by the results in Fig. 3.8 which show the circumferential variation in static pressure coefficient in the bleed slot. The static pressure coefficient is defined as the static pressure at each tapping minus the average of the 16 tappings, divided by $\frac{1}{2}\rho U^2$. The cases shown are for bleed rates of 4.14% at $\phi_{stage} = 0.43$ for the large plenum chamber, four off-take duct case and the small plenum chamber, one off-take duct case. The static pressure coefficients in the slot vary by less than ± 0.004 for the large plenum, four duct case whereas this variation is between -0.15 to +0.03 for the small plenum, one duct case. From this it can be assumed that the bleed extraction through the slot is uniform on the length scale of a circumference for the large plenum, four off-take duct cases.

The pairs of tappings and probes are calibrated against uniform bleed rates from 0% to 10% so that each pair has its own calibration line mapping non-dimensional pressure difference to non-dimensional local bleed rate. To measure the distribution of circumferentially non-uniform bleed the total pressure probes are re-nulled, the angles recorded and the pressure difference for each tapping and probe pair measured. The calibration is then used, along with the flow angle, to calculate the local radial bleed rate through the slot at each of the 16 circumferential locations. The limitation of the method is that for strongly non-uniform bleed flows the local bleed rate exceeds the calibration bleed rates and an extrapolation has to be performed. Despite this, the integrated bleed mass flow rate obtained using the probes is within 20% of the bleed rate measured by the orifice plates for 97% of cases and within 10% for 60% of the cases.

3.3.3 Efficiency characteristics

The total to static isentropic efficiency is defined as:

$$\eta = \frac{Power_{isentropic}}{Power_{actual}} \quad (3.10)$$

and for a case with 0% bleed:

$$\eta = \frac{\dot{m}_{in} U^2 \left(\psi_{rig,t-s} + \frac{\phi_{rig}^2}{(\cos \alpha_{exit})^2} \right)}{2\tau\omega} \quad (3.11)$$

where ρ is the inlet density, A is the cross sectional area of the main passage flow, ϕ_{rig} is the rig inlet flow coefficient, U is the midspan blade speed, $\psi_{rig,t-s}$ is the total-to-static pressure coefficient as defined in Equation 3.1 from rig inlet to stage exit, α_{exit} is the passage-averaged yaw angle downstream of the stators, τ is the motor torque, and ω the rotor speed.

A calibrated strain gauge is used to measure the torque reaction of the motor mounted in a freely-rotating gimballed frame. The yaw angle downstream of the stator is measured with area traverses (described in Section 3.3.4) for a number of different operating points. The passage-averaged yaw angle increases by 2.8 degrees over the operating range of the compressor and the value used for the efficiency characteristic is interpolated from the measurements at different operating points. The other measurements are required for the pressure rise characteristics and are described in Section 3.3.1.

For cases with bleed the flow from rig inlet to a point in the off-take duct must also be considered and the calculation for overall efficiency becomes:

$$\eta_{overall} = \frac{\dot{m}_{in} U^2 \left(\psi_{rig,t-s} + \frac{\phi_{stage}^2}{(\cos \alpha_{exit})^2} \right) - \dot{m}_{bl} U^2 \left(\psi_{rig,t-s} + \frac{\phi_{stage}^2}{(\cos \alpha_{exit})^2} \right) + \dot{m}_{bl} U^2 \Delta P_{0,bl}}{2\tau\omega} \quad (3.12)$$

where:

$$\Delta P_{0,bl} = \frac{P_{0,bl} - P_{0,in}}{\frac{1}{2}\rho U^2} \quad (3.13)$$

The bleed mass flow rate, \dot{m}_{bl} , is measured with orifice plates as described in Section 3.2. The bleed stagnation pressure, $P_{0,bl}$, is measured 140mm (1.75 off-take duct diameters) into the off-take duct with a five-hole Pitot tube rake, shown in Figure 3.9. In this location the stagnation pressure loss due to the flow passing through the slot, plenum chamber and off-take duct entrance is included. For cases where more than one off-take is used it is assumed that the stagnation pressure in all of the off-take

ducts is the same. The five Pitot tubes in the rake are connected together with a manifold and pneumatically averaged.

The efficiency of the stage downstream of the bleed slot is defined as:

$$\eta_{stage} = \frac{m_{in} U^2 \left(\psi_{stage,t-s} + \frac{\phi_{stage}^2}{(\cos \alpha_{exit})^2} \right)}{2 \tau \omega} \quad (3.14)$$

where ϕ_{stage} is the stage inlet flow coefficient, $\psi_{stage,t-s}$ is the total-to-static pressure coefficient as defined in Equation 3.1 from stage inlet to stage exit.

The additional information required to form efficiency characteristics is recorded at the same time as the pressure rise characteristic data. This results in an efficiency characteristic which is made up of discrete operating points. Repeated experiments show that the overall efficiency measurements are repeatable within $\pm 0.1\%$ points.

3.3.4 Area traverses

A five hole probe is used to measure stagnation pressure, static pressure, yaw angle and pitch angle at the locations shown in Fig. 3.3 in Section 3.2.1. The probe head is 2mm in diameter with holes perpendicular to the probe head faces as recommended by Dominy and Hodson [43]. The probe used is shown in Figure 3.10.

Traverse gear. The probe is fixed in a yawing mount and this is mounted on a radial traverse gear. Both degrees of freedom are driven by computer-controlled stepper motors although during traverses, the yaw angle of the probe remains fixed. This assembly can be moved axially, using a manually operated traverse gear, so that all traverse locations can be accessed. For area traverses located at rig inlet, upstream of the slot, at stage inlet and downstream of the rotors, the upper casing rings and IGVs are rotated as described in Section 3.2.1. This motion is driven by a third computer-controlled stepper motor. For traverses downstream of the stators the entire traverse gear assembly is moved manually in a circumferential direction and secured at 0.3 degree intervals using a dowel pin.

Five hole probe measurements. The probe is calibrated in a steady-flow wind tunnel between +30 and -30 degrees in the yaw and pitch directions at intervals of 2 degrees. The calibration is automated and the probe is fixed in the yaw mounting exactly as it is when mounted on the compressor traverse gear. Upstream of the IGVs a radial traverse with 31 radial points is used to measure the flowfield and the results of these tests are used to provide the inlet calibration, K , as described in Section 3.3.1. At the other locations area traverses are required to resolve the wakes from upstream stationary blades. These traverses are performed with 21 radial and 21 circumferential points. The radial points are clustered towards the endwalls and the circumferential points are equally spaced. The clearance between the probe head and the end walls is 0.5mm so that the centre of the

probe head traverses from 1.5mm to 62.0mm span or 2.4% to 97.6% span. At each location the probe is set at a fixed yaw angle which points approximately into the flow direction. This ensures that the measurements stay in range of the calibration.

Settling and measurement time. At each measurement point a 1 second settling time is included after the probe is moved. This value was selected after the following test was performed: A pressure rise was applied, via a T-piece, to the probe and to a piece of tube 20mm long, both connected to separate channels on the pressure transducer. The probe was connected to the pressure transducer with its normal tubing of length ~3m. The pressures were logged and the response of the probe and the short tube are shown in Figure 3.11. The probe responds less than 0.5 seconds after the short tube showing, therefore, that the 1 second settling time is sufficient.

The pressure transducer provides pressure measurements at a frequency of 2.5 Hz. For each traverse location, three output measurements are taken from each channel and these are averaged and recorded. The data is logged automatically and only recorded if the bleed rate is within 0.5% of its target and the flow coefficient is within 0.1% of its target. In the cases where area traverses were repeated they typically gave passage-averaged flow coefficients within 0.5% of each other.

3.3.5 Unsteady pressure measurements

Six Kulite 5 psi high frequency pressure transducers, spaced equally around the casing, are mounted just upstream (13% of axial chord at tip) of the rotor leading edge. They are used to study the rotor blade passing signal. The transducers are fixed in 2.9mm diameter metal tubes for protection and to make them easier to handle. These tubes are mounted so that the transducers are flush with the casing wall. Calibration is performed with a vacuum pump and steady-state pressure transducer. For all measurements in the current work the signal is amplified without filtering and then logged at 80 kHz by the data acquisition card. This sample rate gives 26.7 data points per blade passing. The output is logged continuously with a buffered logging system. 1 second of data is recorded to file when stall occurs with 0.5s recorded before the stall event and 0.5s after. The stall event is detected when a stall cell causes the voltage signal of one of the transducers to rise above a pre-determined level.

3.3.6 Data acquisition and analysis

The pressure measurements for the characteristics, bleed measurements, area traverses, and five-hole probe and unsteady pressure transducer calibrations are recorded on one of three Scanivalve DSA 16-channel pressure scanners. Atmospheric pressure in the lab is measured with a digital barometer and temperature measurements are taken with K-type thermocouples and recorded using a digital sensor. The unsteady pressure measurements, motor torque and rotor shaft speed are acquired using a National Instruments data acquisition card. The data logging is controlled by LabVIEW which

performs real-time analysis of the data so that the experiments can be monitored. LabVIEW also controls the stepper motors which move the traverse gear and writes the raw data to file for post-processing with MATLAB.

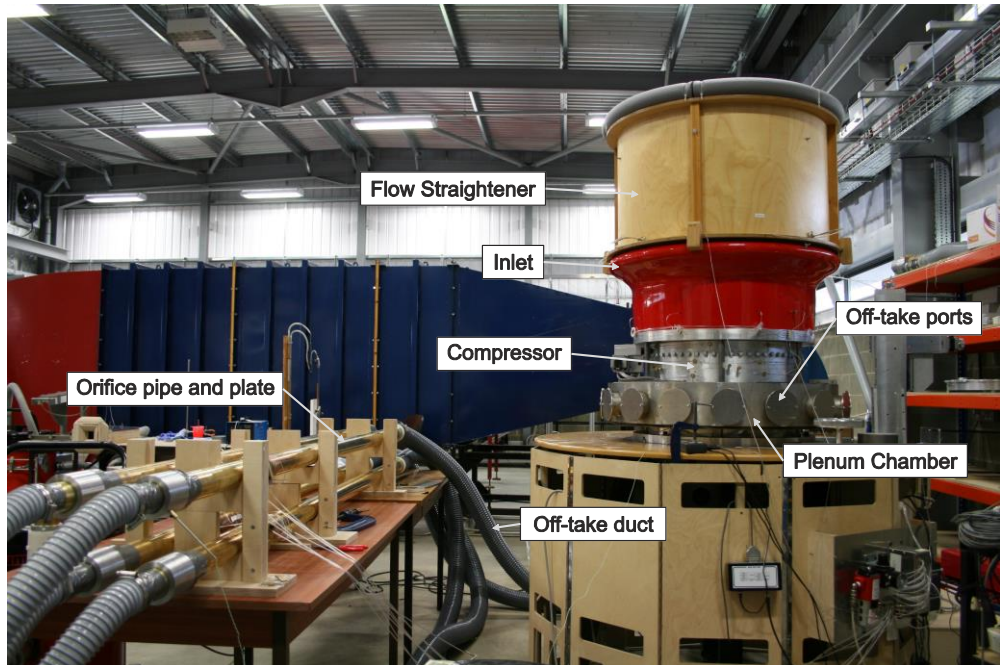


Figure 3.1: Photo of compressor rig and bleed system.

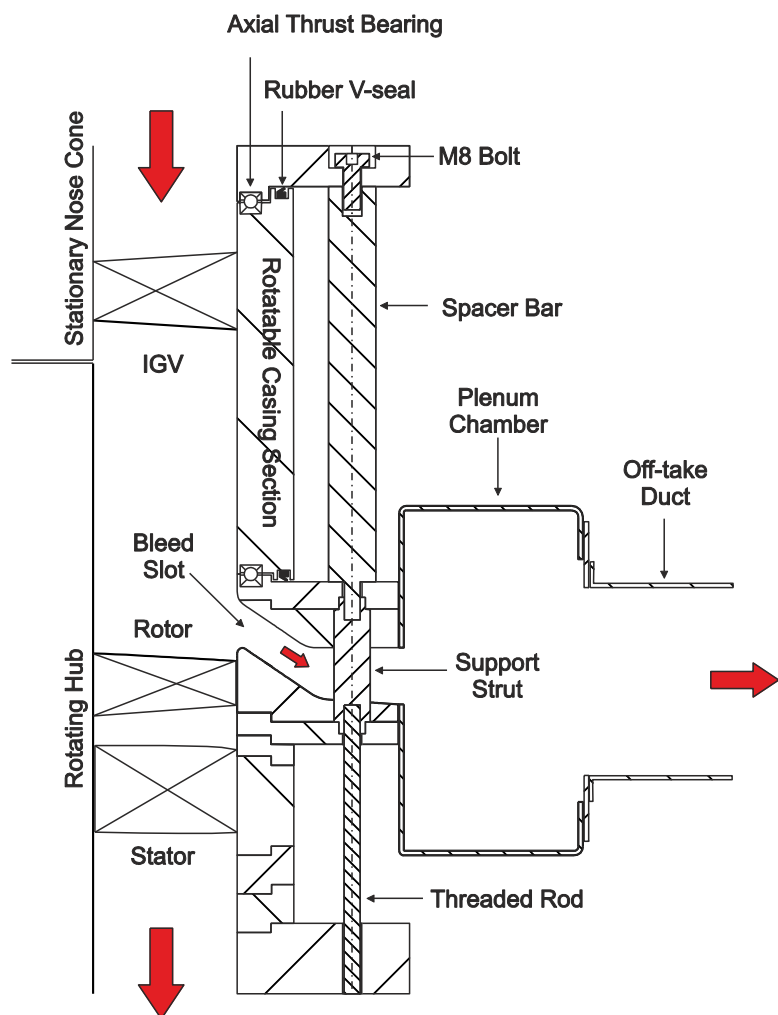


Figure 3.2: Cross section of the working section of compressor rig.

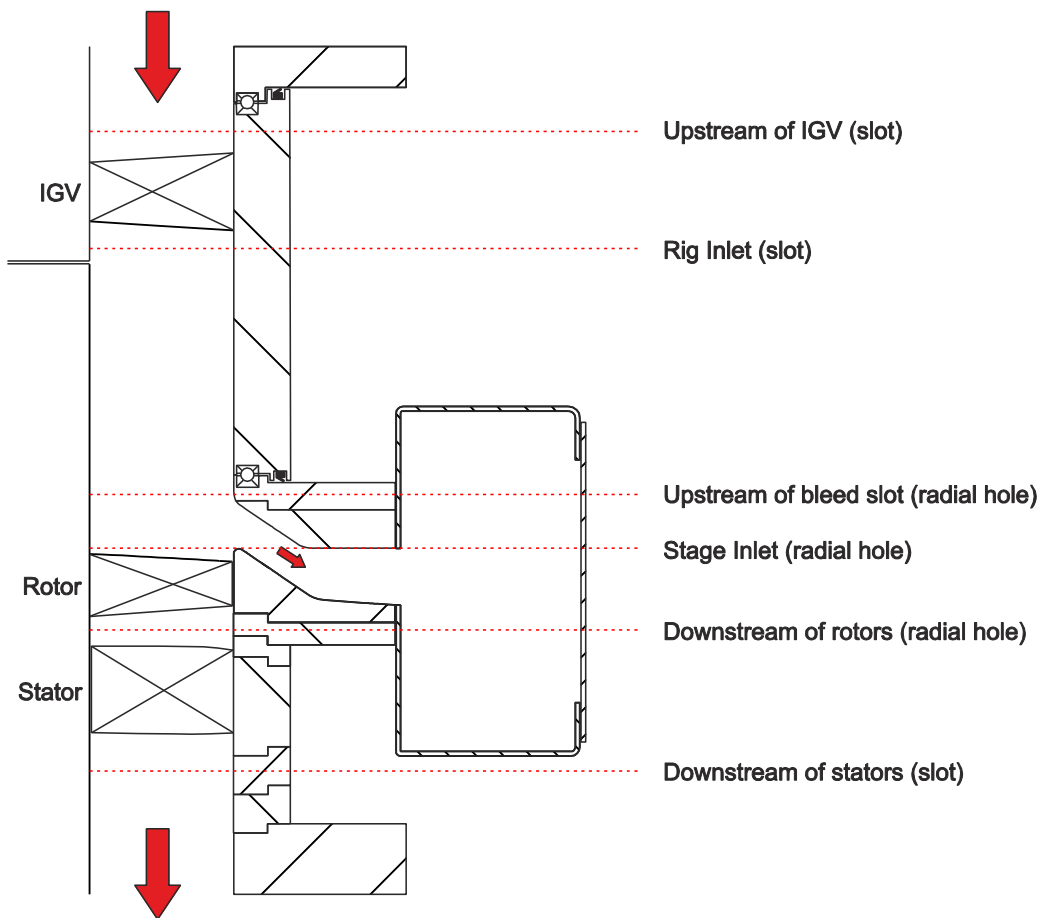


Figure 3.3: Cross section of working section of compressor rig showing traverse locations.

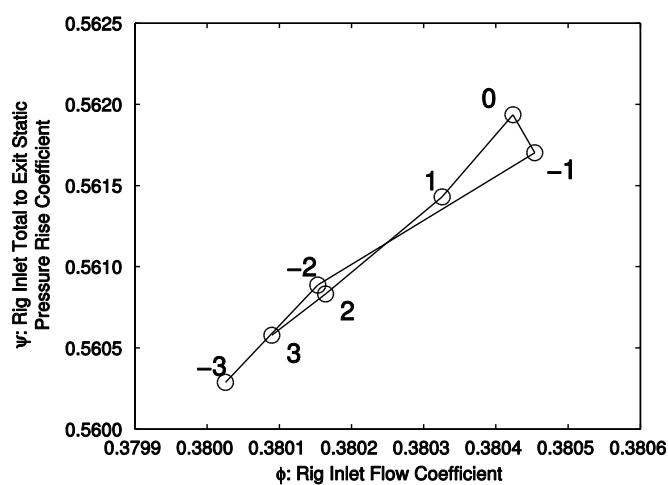


Figure 3.4: Total-to-static pressure rise against rig inlet flow coefficient for varying clocked positions.

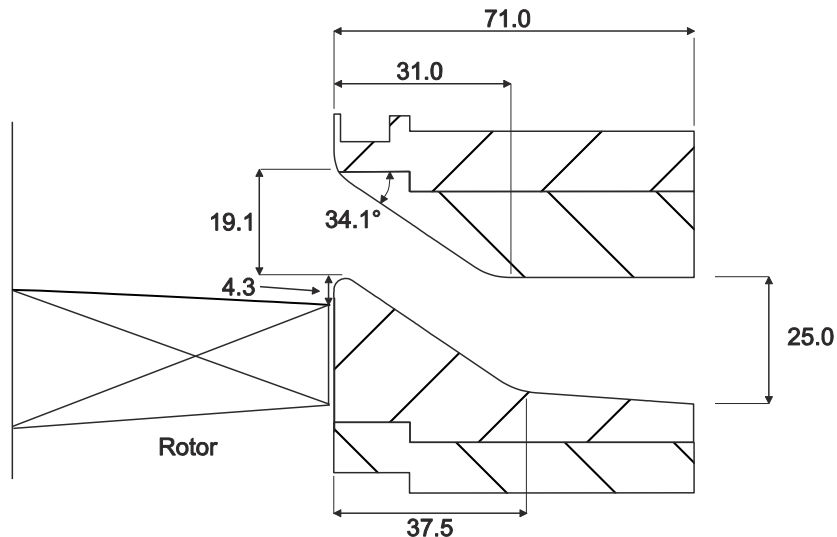
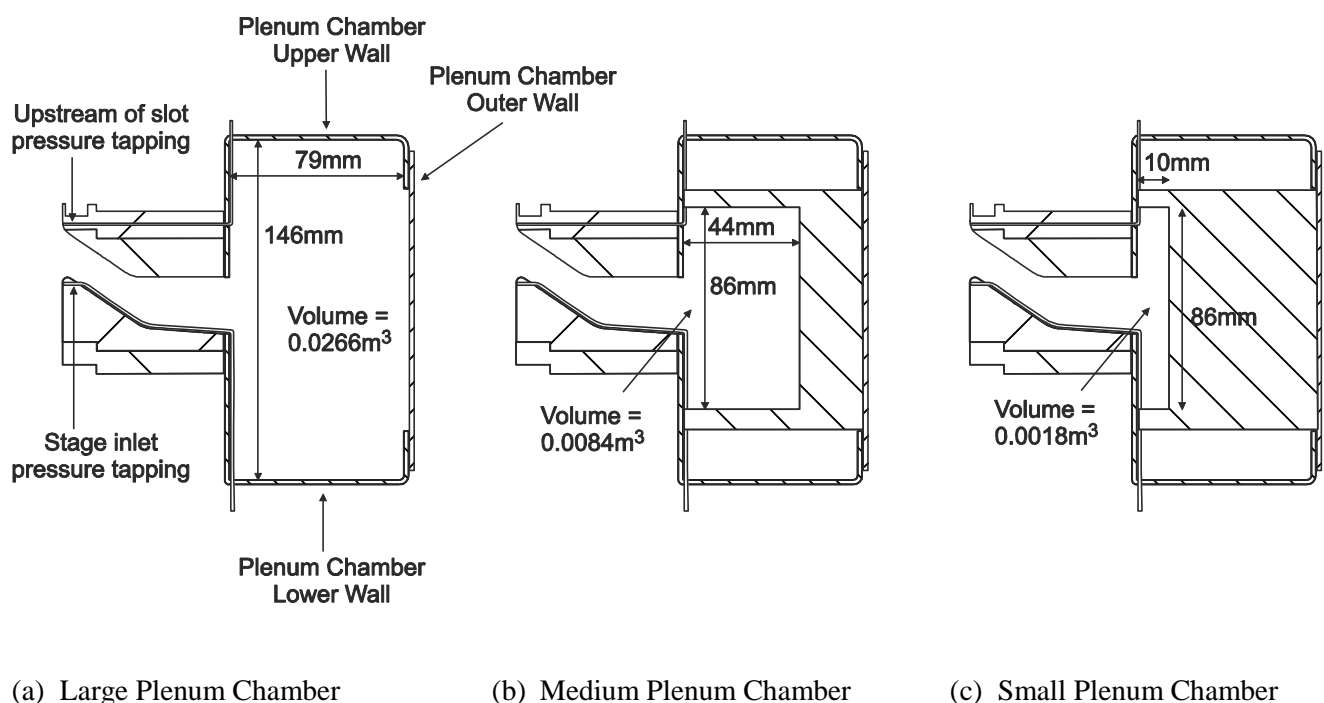


Figure 3.5: Cross section of casing rings which form the bleed slot. All dimensions in mm.



(a) Large Plenum Chamber

(b) Medium Plenum Chamber

(c) Small Plenum Chamber

Figure 3.6: Cross section of plenum chamber assembly showing different plenum chamber sizes.

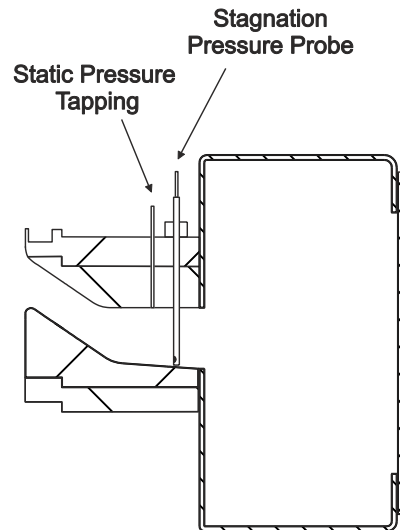


Figure 3.7: Cross section of bleed slot and plenum chamber showing stagnation pressure probe and static pressure tapping for local bleed rate measurement.

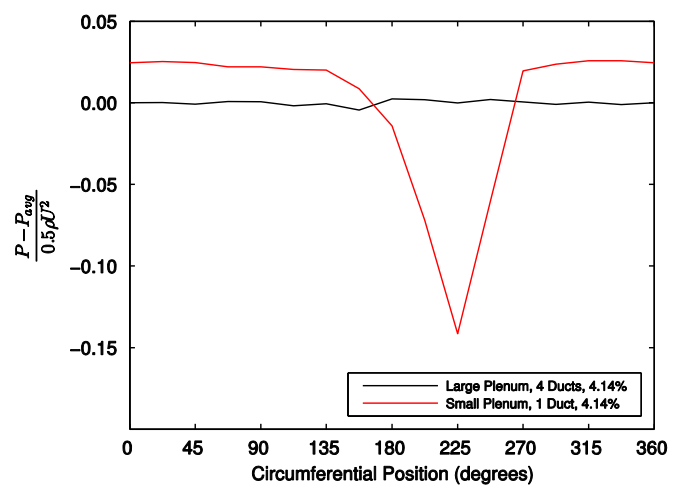


Figure 3.8: Circumferential variation in local static pressure in the bleed slot for large plenum chamber, four off-take duct case and small plenum chamber, one off-take duct case with bleed rates of 4.14%.

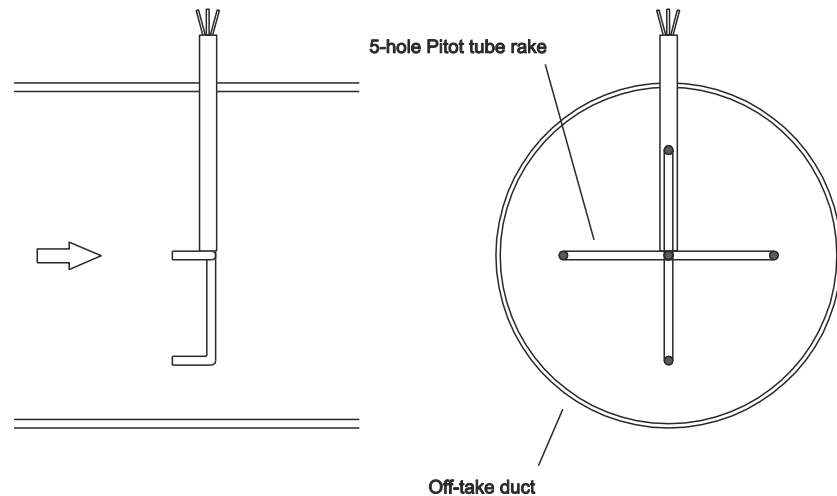


Figure 3.9: Diagram of 5-hole Pitot tube rake in off-take duct.

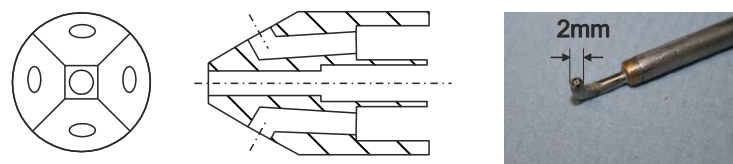


Figure 3.10: Diagram and photograph of five hole probe [43].

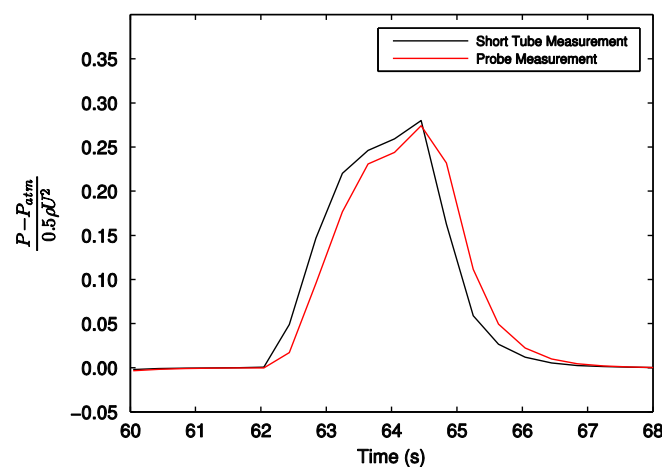


Figure 3.11: Comparison of short tube and five hole probe response to pressure rise.

Chapter 4

Computational Methods

4.1 Introduction

Computational Fluid Dynamics (CFD) is used to model the flows associated with the compressor rig and bleed system described in Chapter 3. The aim is to use CFD to capture flow features measured in the rig and to provide a tool which can further investigate the flow in ways that cannot be achieved experimentally. This chapter describes the CFD solver, Turbostream, employed throughout the current work. The meshes and procedure employed and post processing methods are then presented. Finally, validation of these CFD methods is provided with comparisons to the two-dimensional solver MISES and with experimental measurements.

4.2 Computational Codes

Turbostream is based on the latest version of TBLOCK and has been implemented to run on Graphics Processing Units (GPUs) instead of the traditional Central Processing Unit (CPU). TBLOCK, developed by Denton, is a finite volume, three dimensional Reynolds-averaged Navier Stokes (RANS) flow solver which uses the ‘SCREE’ scheme solution algorithm [44]. TBLOCK derives from earlier solvers, MULTIP and UNSTREST, and is suitable for modelling both main annulus flow and secondary flow paths such as those through the bleed slot, plenum chamber and off-take ducts. A more detailed description of TBLOCK is given by Klostermeier [45]. Turbostream makes use of GPU’s massively parallel architecture and allows an order of magnitude improvement in calculation speed compared to CFD solvers running on traditional CPUs. In order to take advantage of GPUs’ superior performance the TBLOCK solver has been completely rewritten; the underlying physical model, however, remains largely unchanged [46].

Turbostream uses a dual time-stepping algorithm for unsteady calculations [47] and in this study all runs are performed with 72 physical time steps per blade passing period. All calculations are performed using the Spalart-Allmaras turbulence model [48], the boundary layers are set to be fully turbulent and at solid boundaries a slip condition is applied with wall functions. The Spalart-Allmaras model is a one equation eddy viscosity model that solves a transport equation for turbulent viscosity;

it is widely used in industry and academia. All calculations in this study assume ideal gas properties and a Prandtl number equal to one.

4.3 Mesh Generation

The mesh models the geometry of the experimental rig described in Chapter 3. A number of different meshes have been generated to study different aspects of compressor bleed. The first part of this section describes a single blade passage mesh with bleed slot which is used to study the effects of circumferentially uniform bleed. The second part describes two multi-passage meshes, one modelling a large plenum chamber and four off-take ducts, the other with a small plenum chamber and one off-take duct. These are used to study loss through the bleed system and circumferentially non-uniform bleed.

4.3.1 Single passage mesh

The meshes were generated using Autogrid, a commercially available, multi-block, structured mesh generator. The blade row meshes have an H-O-H topology and the tip gaps are modelled with two blocks which have an O-H topology. The mesh has 121 spanwise points with 21 points in the tip gap. $Y+$ values are less than 8 everywhere. The blade-to-blade mesh for the rotor is shown in Fig. 4.1. The bleed slot mesh and how it is attached to the blade passage is shown in Fig 4.2.

For calculations investigating circumferentially uniform bleed only a single passage mesh with bleed extracted from the top of the bleed slot is required. For the unsteady, single passage calculations the rotor and stator pitch must be equal so the number of rotors is set as 60 (instead of 58 as in the experiment) to match the number of stators. Figure 4.3 shows the computational domain for the single blade passage mesh with bleed slot. This mesh has approximately 3.6×10^6 cells.

4.3.2 Multi-passage mesh

The blade passage mesh used for the single passage calculations is copied in a circumferential direction to produce the mesh for the multi-passage calculations. Two multi-passage meshes have been generated. The first is a mesh with fifteen blade passages, i.e. a quarter annulus section, bleed slot, large plenum chamber and one off-take duct. This mesh is an extension to the single passage, uniform bleed calculations. The bleed extraction through the slot is still circumferentially uniform on the length scale of a circumference, but the flow in the plenum chamber and off-take duct can now be investigated. With one off-take duct in a quarter annulus section the bleed system geometry models that of the rig with the large plenum chamber and four off-takes. To match the rotor and stator pitch for the unsteady calculation the compressor is again modelled with 60 stators and 60 rotors. The large plenum chamber and off-take duct are modelled with an O-H topology which ensures a good quality

mesh. The computational domain for the quarter annulus case is shown in Fig. 4.4. This mesh has approximately 67×10^6 cells.

The second multi-passage mesh generated is full annulus with the correct number of rotors and stators modelled. The mesh includes the bleed slot, the small plenum chamber and one off-take duct. The topology used to mesh the off-take duct and small plenum chamber is the same as that used for the large plenum chamber. This mesh has approximately 250×10^6 cells.

4.4 Procedure

4.4.1 Boundary conditions

The inlet stagnation pressure boundary condition is set to equal the spanwise distribution measured experimentally upstream of the IGV's. The measured spanwise distributions of inlet yaw and pitch, upstream of the IGV, are 0 degrees \pm 1 degree and are therefore set to zero for the calculations. The total temperature at inlet is specified as uniform. The inlet to the computational domain is ten midspan axial rotor chords upstream of the IGV leading edge compared to the traverse location on the rig which is 38% of midspan axial rotor chord upstream of the IGV. To ensure that the stagnation pressure profile in the calculation matches the measured profile in the experiment a zero skin friction condition is applied to the hub and casing walls upstream of the traverse location. This stops the endwall boundary layers from developing between the computational domain inlet and the location of the experimental traverse.

The exit boundary condition is set by specifying the hub static pressure and using simple radial equilibrium to obtain the variation with radius. The exit passage includes a converging nozzle section which starts nine midspan axial rotor chords downstream of the stators. This allows the pressure behind the compressor to vary with mass flow while the pressure at exit of the computational domain, downstream of the nozzle, is fixed. The static pressure behind the compressor (and hence the compressor operating point) is set according to the exit static pressure boundary condition and the matching of the compressor and nozzle characteristics [49].

For the single passage calculations the bleed flow is extracted from the top of the bleed slot using a bleed patch through which bleed mass flow is specified. For the cases with the plenum chamber and off-take duct the bleed flow is extracted from the top of the off-take duct.

4.4.2 Running an unsteady calculation

The increased speed of Turbostream allows for all of the calculations in this work to be run unsteady. This is done because unsteady calculations provide a better match to the experimental measurements than steady calculations (see Section 4.6.2). The process for running an unsteady

calculation is as follows: a steady calculation is run with satisfactory convergence typically obtained in 50,000 time steps. With two NVIDIA K20 GPUs these calculations take approximately two hours to run. The unsteady calculation is restarted from the converged steady solution and run for 120 blade passings (i.e. two revolutions). If there is bleed flow present the bleed patch mass flow is updated to match the target bleed rate and the calculation is run for a further 30 blade passings. The bleed readjustment procedure is repeated until a solution with the correct bleed rate (within $\pm 0.1\%$ points of the target bleed rate) is obtained. The calculation is then run for a final 60 blade passings and an output file obtained for the time average of the last 30 blade passings. Typically the inlet mass flow varies at the rotor blade passing frequency by less than $\pm 0.3\%$. Using two NVIDIA K20 GPUs, 60 blade passings (i.e. one revolution) takes approximately nine hours to run.

4.4.3 Running unsteady calculations for a compressor characteristic

Single passage unsteady CFD calculations have been used to generate compressor characteristics. Instead of starting from a steady solution each new calculation is restarted from the solution obtained for the previous operating point. The exit static pressure is “ramped up” from the previous value to the new value over the first 30 blade passings to provide a smooth transition between the operating points. At each operating point the same procedure as described above is used to set the bleed rate. Near stall the convergence history of the solution is checked to test whether the final operating point is stable. A solution is defined as stable if it has a constant inlet mass flow within $\pm 0.3\%$ over the last 30 blade passings. If the solution has not yet converged on a constant operating point but is tending towards one, the solution is run for a further 60 blade passings. At the point where the calculation will no longer produce a stable unsteady solution, i.e. the mass flow and pressure rise are falling and do not tend towards a constant operating point, the compressor is said to have stalled.

4.5 Post-processing

The unsteady CFD calculations are time-averaged over the last 30 blade passings and the solution is “cut” in the same locations as the measurement planes on the rig. For flow coefficients and pressure rise characteristics the flow properties are analysed in the same way as they are measured in the experiment, i.e. inlet total pressures are passage-averaged while exit static pressures are taken as pitchwise-averaged values at the casing, similar to a static pressure tapping in the experiment. This means that Equations 3.3 and 3.4 can be used to calculate CFD rig inlet flow coefficient and stage inlet flow coefficient, and Equation 3.1 is used for CFD rig inlet to stage exit total-to-static pressure rise and stage inlet to stage exit total-to-static pressure rise.

Compressor efficiency is given by:

$$\eta = \frac{Power_{isentropic}}{Power_{actual}} \quad (4.1)$$

For the CFD calculations the actual power is given by the increase in stagnation enthalpy in the compressor and bleed system and the isentropic power is calculated in the same way as it is for the experimental measurements. The definition for overall compressor efficiency with bleed, used for the CFD calculations, is therefore:

$$\eta_{overall} = \frac{\dot{m}_{in}U^2\left(\psi_{rig,t-s} + \frac{\phi_{stage}^2}{(\cos\alpha_{exit})^2}\right) - \dot{m}_{bl}U^2\left(\psi_{rig,t-s} + \frac{\phi_{stage}^2}{(\cos\alpha_{exit})^2}\right) + \dot{m}_{bl}U^2\Delta P_{0,bl}}{\dot{m}_{exit}(h_{0,exit} - h_{0,in}) + \dot{m}_{bl}(h_{0,bl} - h_{0,in})} \quad (4.2)$$

where:

$$\Delta P_{0,bl} = \frac{P_{0,bl} - P_{0,in}}{\frac{1}{2}\rho U^2} \quad (4.3)$$

α_{exit} is the passage-averaged yaw angle downstream of the stator row, \dot{m}_{exit} is the mass flow out of the compressor, $h_{0,in}$ is the mass-averaged stagnation enthalpy at rig inlet, and $h_{0,exit}$ is the mass-averaged stagnation enthalpy at exit. The bleed mass flow rate, \dot{m}_{bl} , bleed stagnation pressure, $P_{0,bl}$, and bleed stagnation enthalpy, $h_{0,bl}$, are calculated from radial cuts either at the top of the bleed slot (for the single passage calculations) or in the off-take duct at the same location as the five-hole Pitot tube rake in the rig (for the multi-passage calculations). The other variables are required for the pressure rise characteristics.

The efficiency of the stage downstream of the bleed slot is defined as:

$$\eta_{stage} = \frac{\dot{m}_{in}U^2\left(\Delta P_{stage,t-s} + \frac{\phi_{stage}^2}{(\cos\alpha_{exit})^2}\right)}{\dot{m}_{exit}(h_{0,exit} - h_{0,in}) + \dot{m}_{bl}(h_{0,bl} - h_{0,in})} \quad (4.4)$$

The term for the actual power is the same as in Equation 4.2. This is so that the CFD stage efficiency can be compared with that from the experimental measurements where the actual power term, obtained from the motor torque and rotor speed, cannot be split up.

4.6 Validation

This section provides two types of validation for the CFD methods used in this work. First the two-dimensional flow over the midspan blade profile predicted by Turbostream is compared with that from a well-established 2D code. Second, the steady and unsteady CFD predictions of the 0% bleed rate case are compared with experimental data.

4.6.1 Validation with MISES

The calculations undertaken in the current work assume fully turbulent boundary layers at all locations in the computational domain. The validity of this assumption is tested using MISES [50] which couples a two-dimensional Euler solver with an integral boundary layer solver and which can predict laminar and turbulent boundary layers as well as transition. In order to compare the solutions from the two solvers, the midspan blade profiles for the rotors and stators are meshed as two-dimensional cascades and run as steady and unsteady calculations in Turbostream. The inlet flow conditions are matched to those for the design operating point with a bleed rate of 0%. Young [51] found that freestream turbulent intensity in a rig similar to the one in the current work varied from 1.0% to 2.0%. The MISES cases were therefore run with freestream turbulence levels of 0.5%, 1.0%, 3.0%, and with fully turbulent boundary layers for comparison.

Figure 4.5 shows a comparison of Turbostream and MISES calculations of pressure distribution over the midspan profile of the rotor and stator blades and Table 4.1 compares outlet flow properties. For the midspan rotor case, Table 4.1 shows that the exit flow conditions of the MISES calculations do not vary significantly with different levels of freestream turbulence. However, with a fully turbulent boundary layer, the MISES prediction of Mach number and loss coefficient increase and the exit flow angle becomes more negative. The steady and unsteady Turbostream calculations match each other closely. They also match the MISES calculation with fully turbulent boundary layers: Mach numbers differ by 0.0004 (+0.3%), flow angle by 0.15 degrees and loss coefficient by 0.0029 (+7.4%). Figure 4.5(a) also shows a close match between the fully turbulent MISES and Turbostream calculations. Compared to the MISES calculations with freestream turbulence of 1.0%, the unsteady Turbostream calculation has an exit Mach number increased by 0.0014 (+1.1%), reduced flow turning by 0.52 degrees and increased loss coefficient of 0.0121 (+40.6%). Figure 4.5(a) shows that the differences between the Turbostream calculations and MISES calculations with boundary layer transition are due to laminar flow from 0% to 30% of axial chord and a separation bubble from 30% to 40% of axial chord on the suction surface. The close agreement in the outlet flow between the fully turbulent MISES calculation and the Turbostream calculations show that the mismatch in pressure profiles, seen in Fig. 4.5(a) close to the blade trailing edge, has little impact on the exit flow.

For the stator, Table 4.1 shows that the Mach Numbers and exit flow angles are similar for all the cases tested but, as with the rotor, the loss coefficient is higher for the cases with fully turbulent boundary layers. Figure 4.5(b) shows that the pressure profiles with and without boundary layer transition differ due to a separation bubble present from 30% to 45% of axial chord on the suction surface.

In summary, the main difference between the solutions is that MISES predicts a separation bubble and boundary layer transition on the suction surface of both blades. This only has a small effect on exit Mach Number and flow angle but the blade loss coefficient is increased by up to 40.6%.

4.6.2 Validation with experimental data

Pressure rise and flow field. Figure 4.6 shows experimental and CFD calculated rig inlet to stage exit total-to-static pressure rise characteristics for the compressor with 0% bleed rate. Between $\phi_{rig} = 0.50$ and $\phi_{rig} = 0.41$ both steady and unsteady solutions match the experimental characteristic well. At $\phi_{rig} < 0.40$ the steady calculations do not converge and the last point plotted is not fully converged after 100,000 steps: inlet mass flow is decreasing and residuals are beginning to increase. At $\phi_{rig} < 0.41$ the unsteady CFD calculation of the pressure rise characteristic under predicts the measured pressure rise for a given flow coefficient. However, the solutions in this region (from $\phi_{rig} = 0.41$ to $\phi_{rig} = 0.36$) are stable, i.e. the predicted mass flow is steady in time at the end of the calculation. At $\phi_{rig} > 0.41$ the unsteady CFD predicts the experimental pressure rise slightly better than the steady calculations. Below $\phi_{rig} = 0.41$ the unsteady calculations do not match the experimental pressure rise well, however, the steady calculations will not converge at these operating points. From these results it is concluded that the unsteady calculations give a better prediction of the compressor characteristic than steady calculations.

To understand why the unsteady CFD provides a better prediction than steady CFD and why the calculated characteristic does not match the experiments at low flow coefficients, axial cuts are taken in the CFD solutions at rig inlet, downstream of the rotor and downstream of the stator and compared with experimental area traverses at two different operating points. Figure 4.7 shows that the steady and unsteady CFD predictions at rig inlet (i.e. downstream of the IGV) match the experimental results well at both operating points. Downstream of the rotor, Fig. 4.8(a) shows that the pitchwise-averaged flow coefficient above 40% span, calculated with steady and unsteady CFD calculations agrees to within 0.015 of the experimental measurements. Below 30% span the measured spanwise flow coefficient profile shows that there is a rotor hub corner separation; neither the steady nor unsteady CFD calculations capture the size and shape of this separated region of flow. Figure 4.8(a) also shows that the unsteady CFD yaw angle relative to the rotor blade agrees to within 0.5 degrees with the experimental measurement except in the region of the corner separation. The steady CFD calculation predicts a rotor relative yaw angle between one and two degrees more negative across the span. This means that less turning is done through the rotor row and this is consistent with the pressure rise in Fig. 4.6 being lower for the steady CFD calculation than the experiment or unsteady calculation.

Downstream of the stator, at $\phi_{rig} = 0.43$, Fig. 4.9(a) shows that above 50% span both the steady and unsteady CFD flow coefficient and yaw angle profiles agree well with experimental

measurements. At $\phi_{rig} = 0.38$, however, the unsteady CFD spanwise distribution of flow coefficient does not match the measured profile in the lower 50% of span. Although the steady calculation appears to match the experiment more closely it should be noted that this calculation is not converged and the solution shown here is not stable. At lower flow coefficients the hub separation from the rotor and the stator are a significant part of the flow field. These separations are large, unsteady phenomena and the steady calculation becomes unable to predict a stable, steady solution and hence will not converge. The unsteady calculation is able to model the unsteady nature of the separations and so can still produce a stable solution. However, the flow in this region is sensitive to shear layer modelling at the edge of the separation and the accuracy of the calculation is limited by the turbulence model. This explains why below $\phi_{rig} = 0.41$ the pressure rise characteristic predicted by the CFD does not match the experimental measurements and at $\phi_{rig} = 0.38$ there is a 0.033 (5.9%) difference in pressure rise coefficient.

Efficiency. The experimentally measured overall efficiency characteristic for 0% bleed rate is compared with the unsteady CFD calculations in Fig. 4.10. Over most of the operating range the CFD calculated value is below the measured efficiency. The CFD calculated peak efficiency is 0.78% points less than the measured peak efficiency. At $\phi_{rig} = 0.38$ this difference has increased to 3.54% points. This finding is consistent with the result from the MISES validation that fully turbulent blade boundary layers, used in Turbostream calculations, result in more blade profile loss and hence reduced efficiency. However, the shapes of the characteristics also do not match and there are other issues in addition to the two-dimensional blade profile loss. At flow coefficients below $\phi_{rig} = 0.41$ the CFD calculated efficiency drops more quickly than the measured efficiency. As with the reduced pressure rise, this is due to rotor and stator hub corner separations being larger in the CFD calculation than measured experimentally. At $\phi_{rig} > 0.46$ the CFD calculated efficiency is higher than the measured value and the efficiency reduces less quickly with increased flow coefficient. The reason for this is not known though a relevant limitation with the experimental measurements is the use of exit static pressure on the casing and exit flow angle to calculate exit stagnation pressure. This method is also used to post-process the CFD, however, the exit static pressure on the casing is sensitive to changes in blockage downstream of the stator. This may differ between the CFD and experiment due to differences in the size of hub separation, leading to differences in measured and CFD calculated efficiency.

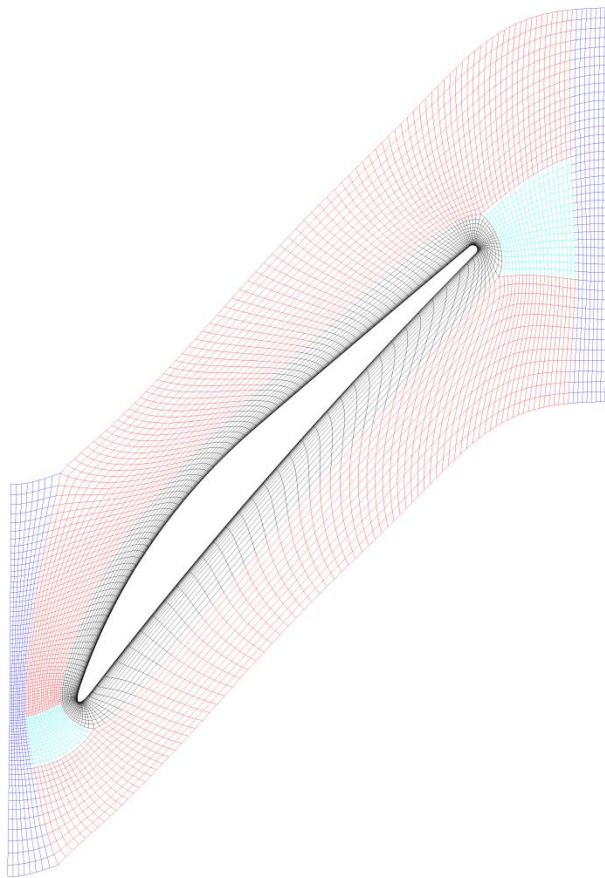
These results show that unsteady single passage calculations can adequately model the compressor flow field and pressure rise above $\phi_{rig} = 0.41$ with a bleed rate of 0%. At lower flow coefficients converged solutions are obtained from unsteady CFD calculations but the pressure rise is under predicted due to the details of the rotor and stator hub separation not being captured by the CFD. This means that the unsteady CFD method described in this chapter can be extended to

investigate the effect of circumferentially uniform bleed with single passage calculations and circumferentially non-uniform bleed with multi-passage calculations. The results obtained should quantitatively match the experimental results near to the design operating point and qualitatively match trends, such as the change in pressure rise due to bleed, below $\phi_{rig} = 0.41$. The CFD calculated efficiency characteristics do not match well with the experimental measurements. The compressor efficiency results presented in Chapter 7 will therefore focus on the computed changes in efficiency with bleed rate, rather than the absolute values predicted.

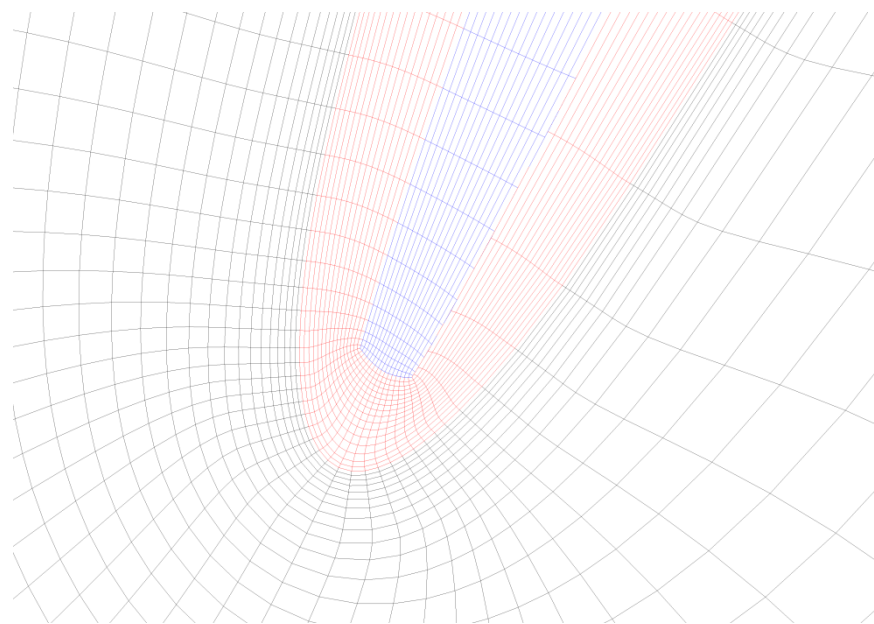
4.7 Summary

This chapter is summarised as follows:

1. The Turbostream flow solver is used because of its speed. It allows single passage, unsteady calculations to be undertaken in a reasonable time so that the full operating range of the compressor can be investigated at several different bleed rates. Turbostream also allows large, quarter annulus and full annulus calculations to be performed so that the flow in the bleed system and circumferentially non-uniform bleed extraction can be modelled.
2. MISES calculations of the rotor and stator midspan profiles predict a separation bubble and boundary layer transition on the blade suction surface. Despite this, Turbostream calculations of the midspan profiles, which assume fully turbulent boundary layers, agree well with the exit Mach numbers and flow angles predicted by MISES. The Turbostream calculated blade profile loss, however, is increased by up to 40.6% due to the fully turbulent boundary layers.
3. For the compressor with 0% bleed rate, the unsteady calculations match the total-to-static pressure rise characteristic well for $\phi_{rig} > 0.41$. For flow coefficients below this, however, the unsteady CFD under predicts pressure rise because the rotor and stator hub separation sizes are exaggerated by the CFD. For 0% bleed rate, the CFD calculations predict peak efficiency 0.78% points below the measured value; the shape of the measured and computed efficiency characteristics also do not match. This is due to differences in blade profile loss and rotor and stator hub separation size.



(a) Midspan rotor mesh showing block topology including O-mesh (in black)



(b) Close up of rotor leading edge mesh at casing including tip gap O-mesh (in red) and H-mesh (in blue)

Figure 4.1: Blade-to-blade view of rotor mesh.

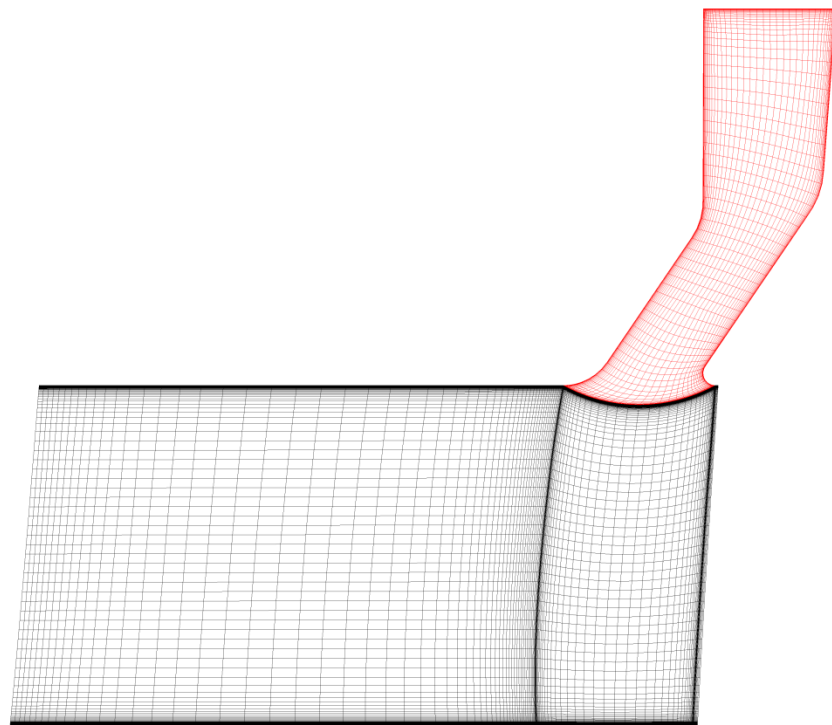


Figure 4.2: Meridional view of main passage mesh between rig inlet and stage inlet (in black) and slot mesh (in red).

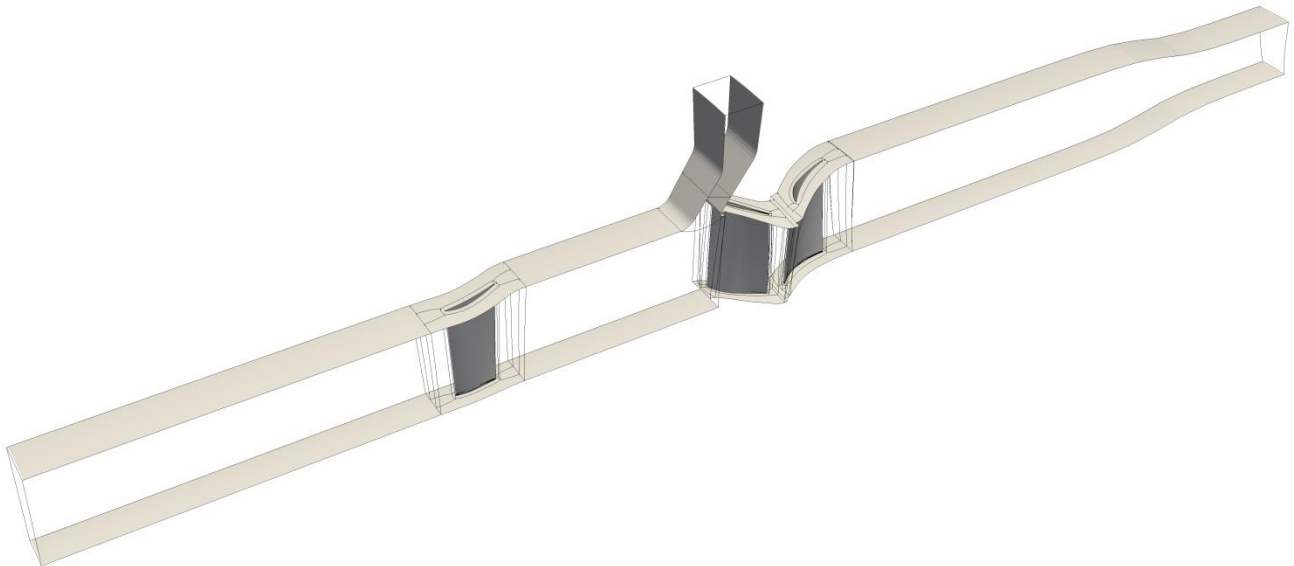


Figure 4.3: Computational domain for single passage calculation with walls and blades shaded.

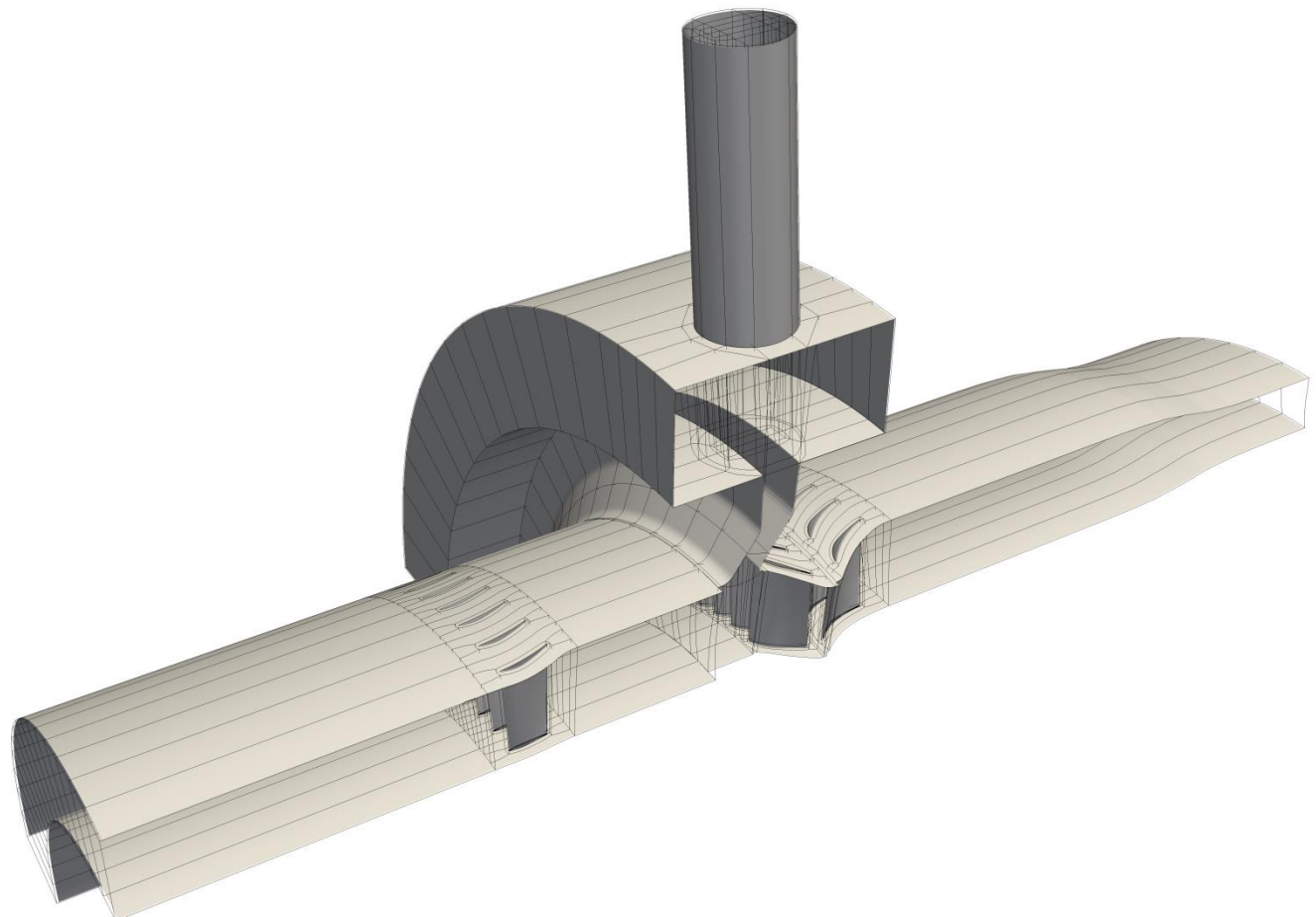
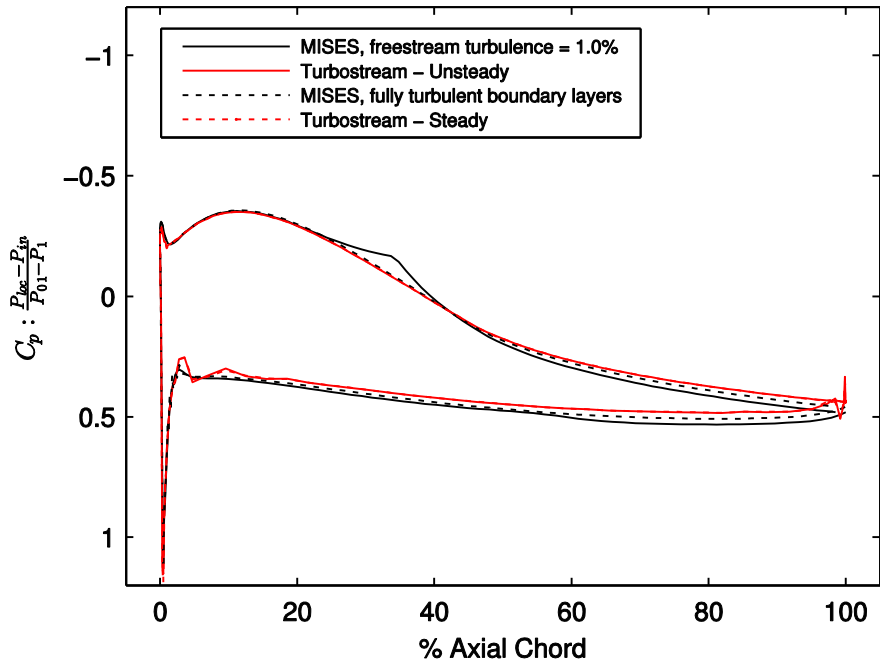
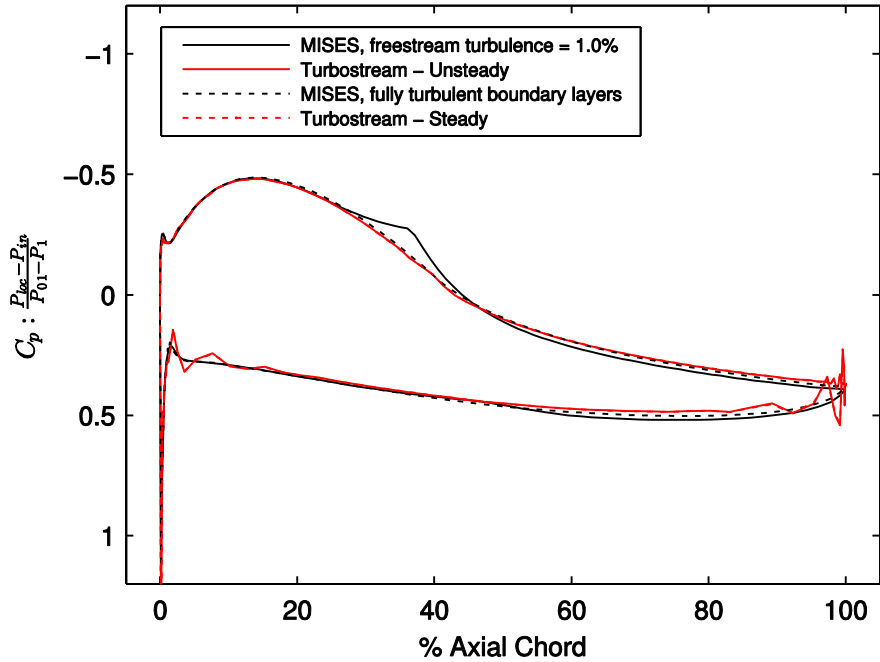


Figure 4.4: Computational domain for quarter annulus calculation with large plenum and off-take duct. Walls and blades are shaded.



(a) Rotor midspan pressure profiles



(b) Stator midspan pressure profiles

Figure 4.5: Turbostream and MISES blade surface pressure profiles.

	Mach Number	Flow angle (degrees)	Loss coefficient ¹
Rotor			
Inlet flow conditions (same for all calculations)	0.1939 (Reynolds number = 159,240)	-62.71	
Turbostream – Steady	0.1290	-47.05	0.0412
Turbostream – Unsteady	0.1290	-47.04	0.0419
MISES with freestream turbulence = 0.5%	0.1279	-46.63	0.0305
MISES with freestream turbulence = 1.0%	0.1276	-46.52	0.0298
MISES with freestream turbulence = 3.0%	0.1276	-46.50	0.0298
MISES with fully turbulent boundary layers	0.1286	-46.89	0.0390
Stator			
Inlet flow conditions (same for all calculations)	0.1344 (Reynolds Number = 129,560)	48.45	
Turbostream – Steady	0.0934	18.13	0.0379
Turbostream – Unsteady	0.0934	18.18	0.0393
MISES with freestream turbulence = 0.5%	0.0934	18.18	0.0335
MISES with freestream turbulence = 1.0%	0.0933	18.28	0.0302
MISES with freestream turbulence = 3.0%	0.0933	18.13	0.0303
MISES with fully turbulent boundary layers	0.0935	18.53	0.0375

Table 4.1: Comparison of outflow properties for Turbostream and MISES calculations.¹ Loss coefficient for these calculations is defined as:

$$\text{Loss Coefficient} = \frac{P_{0in} - P_{0exit}}{P_{0in} - P_{in}}$$

where pressure quantities are mass averaged at inlet and exit measurement planes.

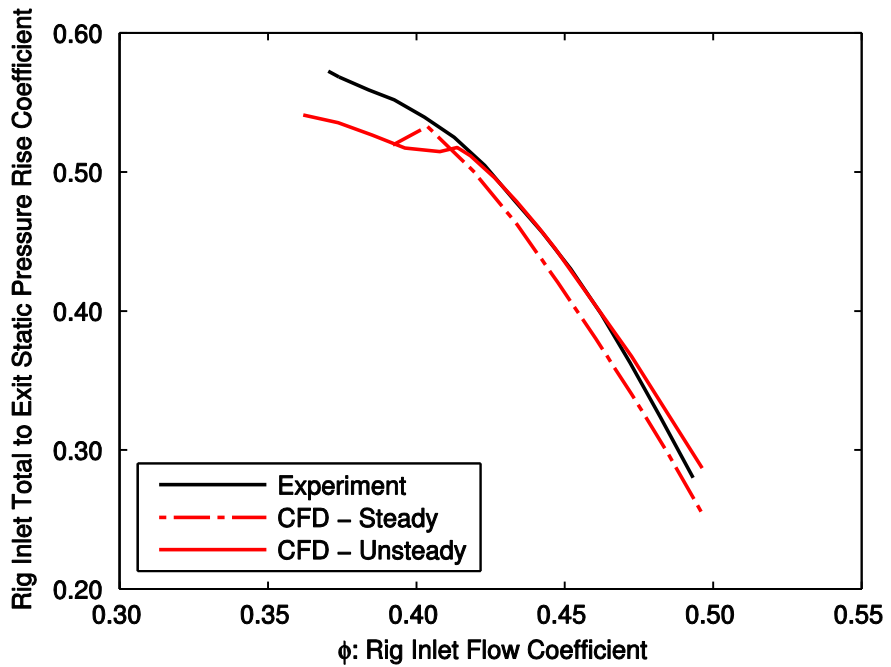


Figure 4.6: Experimental measurements and CFD calculations for rig inlet to stage exit total-to-static pressure rise characteristic with 0% bleed rate.

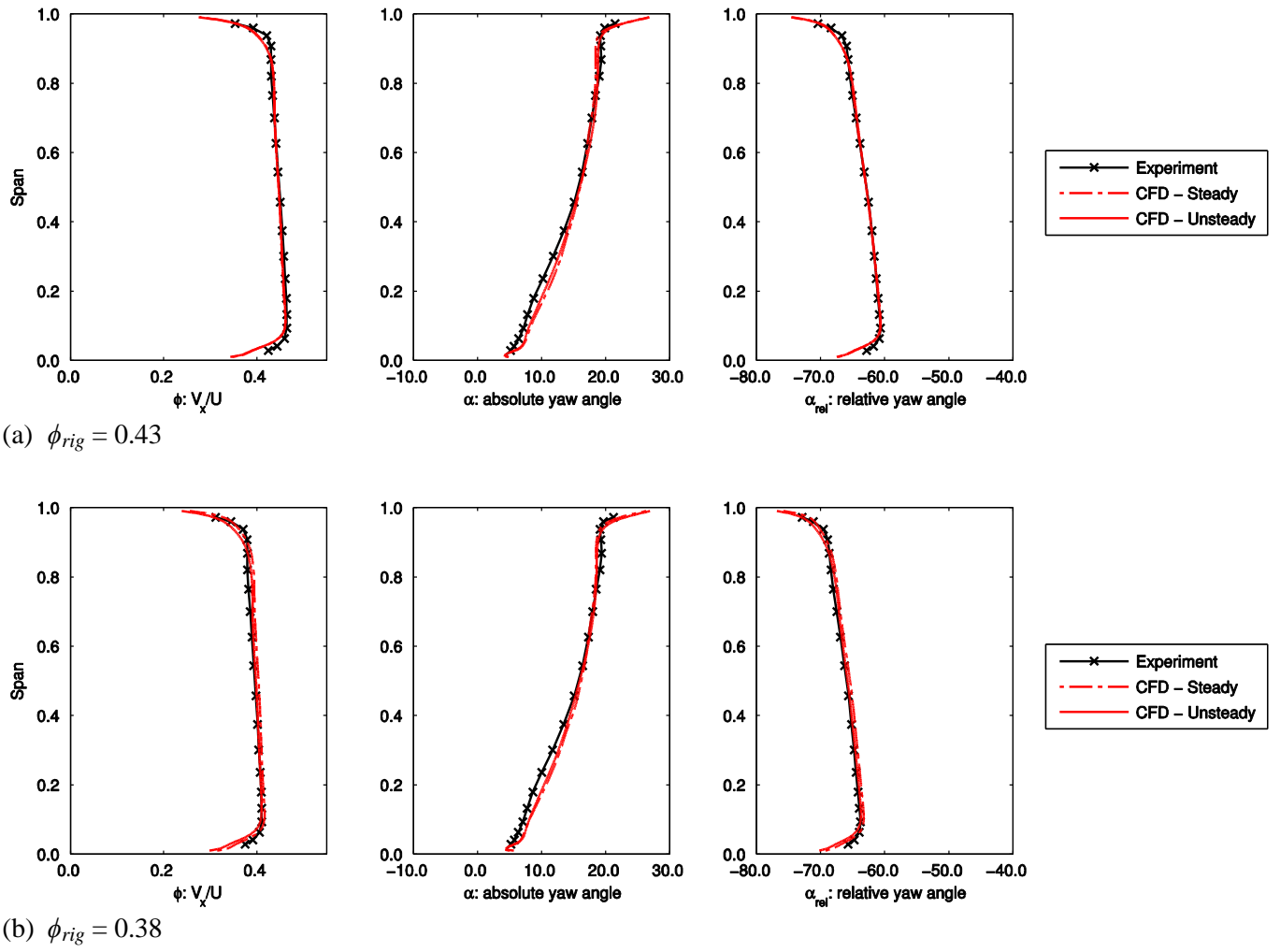
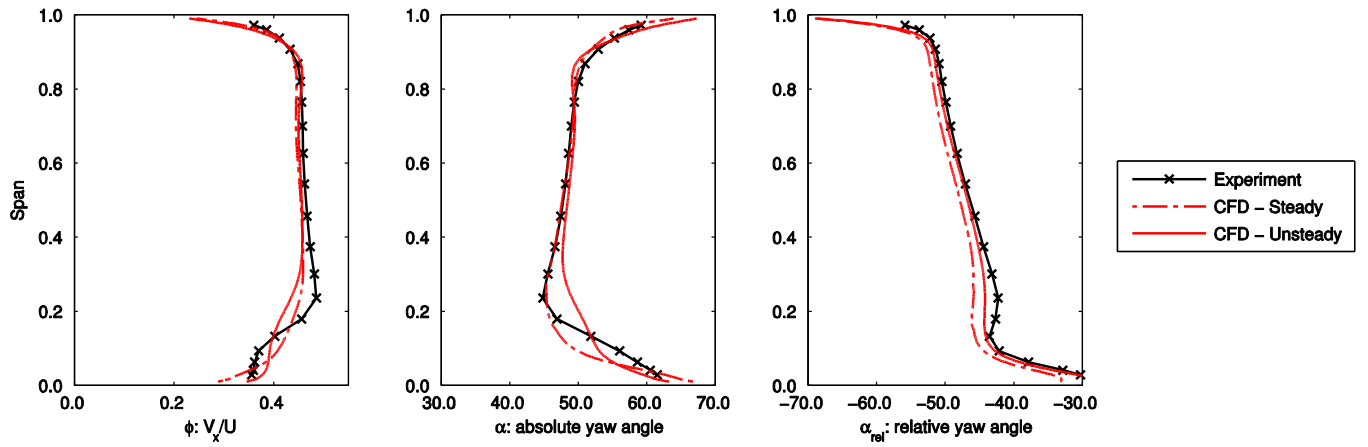
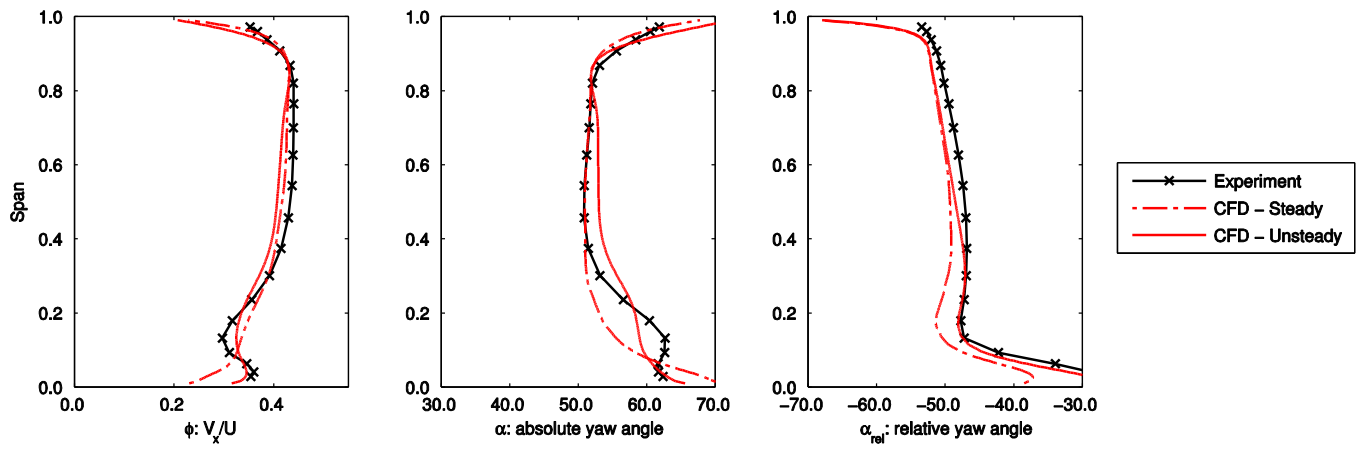


Figure 4.7: Experimental measurements and CFD calculations of pitchwise-averaged flow coefficient and flow angles at rig inlet, with 0% bleed rate.

(a) $\phi_{rig} = 0.43$ (b) $\phi_{rig} = 0.38$ **Figure 4.8:** Experimental measurements and CFD calculations of pitchwise-averaged flow coefficient and flow angles downstream of rotor row, with 0% bleed rate.

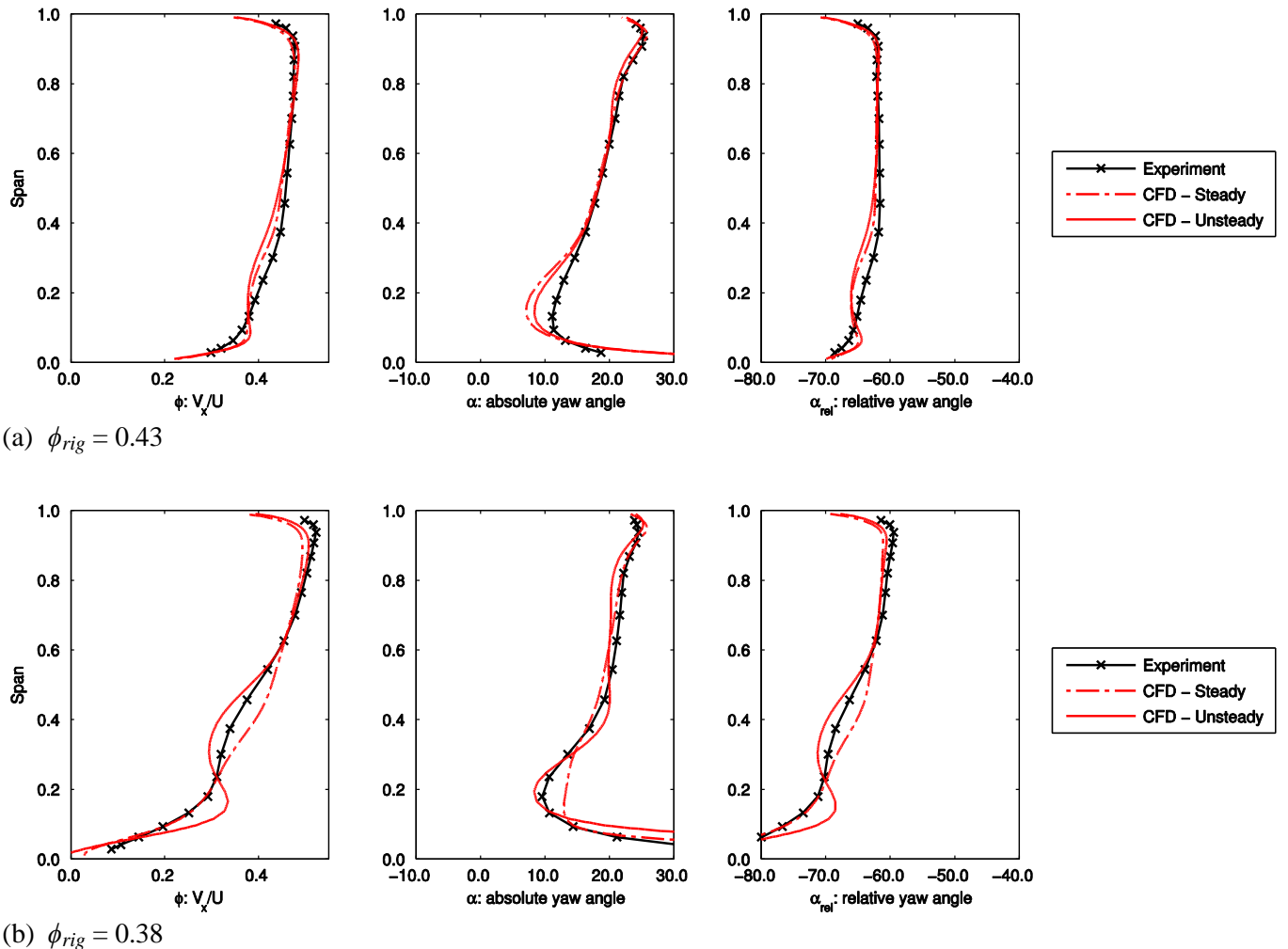
(b) $\phi_{rig} = 0.38$

Figure 4.9: Experimental measurements and CFD calculations of pitchwise-averaged flow coefficient and flow angles downstream of stator row, with 0% bleed rate.

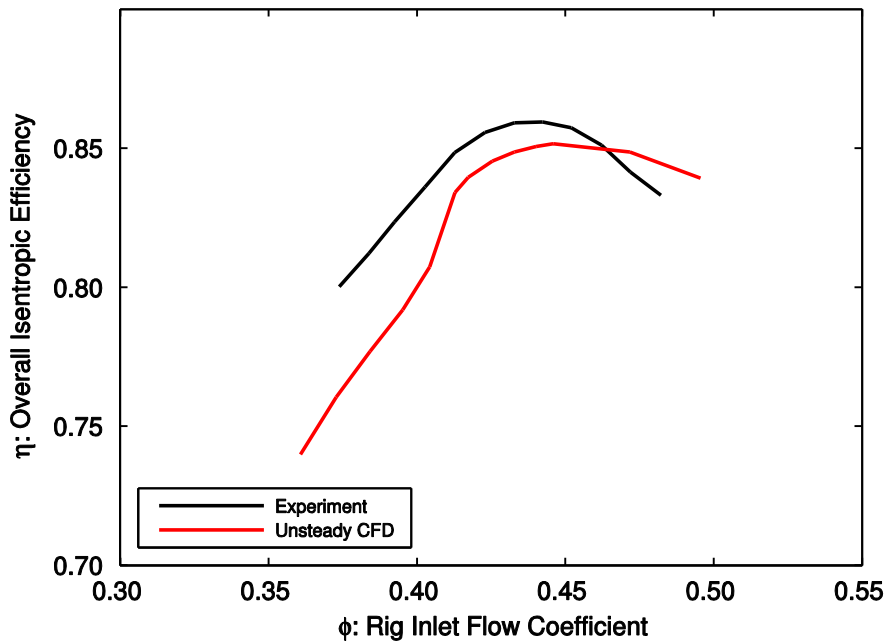


Figure 4.10: Experimental measurement and CFD calculations for efficiency characteristic with 0% bleed rate.

Chapter 5

Uniform Bleed

5.1 Introduction

This chapter investigates the effect of varying the rate of circumferentially uniform bleed on compressor performance. The compressor bleed system on the experimental rig is set up with the large plenum chamber and four equally spaced off-take ducts; this provides circumferentially uniform bleed as described in Section 3.3.2. There are two reasons for studying circumferentially uniform bleed. The first is that bleed extraction will be close to uniform in many machines. It is important, therefore, to understand how changes to the main annulus flow, caused by uniform bleed extraction, affect compressor performance and how changes in bleed rate affect the flow in the bleed system. The second motivation is that an understanding of the effects of uniform bleed provides a stepping stone to the discussion of circumferentially non-uniform bleed in later chapters.

The results in this chapter are divided into three sections: the first investigates the effect of bleed rate on compressor pressure rise and flow field, the second section examines the effect of bleed rate on operating range and the third section studies compressor efficiency and bleed system loss.

5.2 Pressure Rise and Flow Field

In this section uniform bleed rate is varied from 0% to 6.23% and experimental pressure rise characteristics and area traverses are studied. The first part of the section characterises the response of the compressor with passage-averaged flow properties. This is a useful concept for simplifying the analysis of uniform bleed and also helps in understanding the effects of non-uniform bleed in later chapters. The second part is a pitch-averaged analysis which looks in detail at the change in spanwise flow distribution, caused by varying bleed rate.

5.2.1 Passage-averaged analysis

Figure 5.1 shows the rig inlet to stage exit total-to-static pressure rise plotted against rig inlet flow coefficient for cases with bleed rates of 0%, 2.07%, 4.14% and 6.23%. Figure 5.1 shows that as bleed rate is increased the total-to-static pressure rise increases for a given rig inlet flow coefficient.

This is because increased bleed rate reduces the flow rate downstream of the bleed slot. This moves the stage operating point to the left on its characteristic so that the pressure rise is increased.

Figure 5.2 shows the same cases as Figure 5.1 but plotted with stage inlet to stage exit total-to-static pressure rise against stage inlet flow coefficient. The characteristics now collapse towards a single line, although for a given stage inlet flow coefficient there is a slight reduction in pressure rise as bleed rate is increased. Note also that differences are apparent in the stage inlet flow coefficient at stall for varying bleed rates.

To help understand these passage-averaged results assume that the bleed upstream of the compressor causes no spanwise variation to the main passage flow. Changing the bleed rate changes the flow coefficient at inlet to the stage and because there is no spanwise variation in the flow, the compressor responds according to its pressure rise characteristic, just as it would if throttled. In this idealised case the pressure rise characteristics for different bleed rates collapse onto each other when plotted with stage inlet flow coefficient (i.e. downstream of the bleed) and will have the same stall point. In comparison, the experimental results show that with a bleed rate of 6.23%, at $\phi_{stage} = 0.43$, the stage total-to-static pressure rise is reduced by only 2.5%. The stage inlet stalling flow coefficient is reduced by 3.8%; this beneficial change in operating range is examined further in Section 5.3. The effect of bleed rate on the pressure rise characteristic is captured well enough with the passage-averaged analysis for the approach to be used in Chapter 6 to simplify the analysis of circumferentially non-uniform bleed.

5.2.2 Pitch-averaged analysis

The second part of this section investigates the effect of varying bleed rate on the spanwise distribution of flow through the compressor. Area traverses have been performed at two operating points: $\phi_{stage} = 0.43$ and $\phi_{stage} = 0.38$.

Rig inlet. Figures 5.3 and 5.4 show the pitch-averaged spanwise profiles at rig inlet (i.e. downstream of the IGVs) at $\phi_{stage} = 0.43$ and $\phi_{stage} = 0.38$. Both figures show that upstream of the slot the pitch-averaged flow coefficient increases with increased bleed rate. This is because the traverses were performed at a fixed stage inlet flow coefficient, so from Equation 3.10 it can be seen that as bleed rate is increased the rig inlet mass flow, and hence rig inlet flow coefficient, increases. The change in flow coefficient is uniform across the span. This is because there is no spanwise redistribution of the flow at this location. This observation is supported by the plots of V_r/U which indicate that there is no significant radial component of velocity. The spanwise distributions of absolute yaw angle are unaffected by change in bleed rate because there is no circumferential static pressure gradient. The stagnation pressure coefficient, at both operating points, is unaffected by increased bleed rate at this axial location.

Upstream of slot. The spanwise distributions of flow, just upstream of the slot, with varying uniform bleed rate and $\phi_{stage} = 0.43$ and $\phi_{stage} = 0.38$ are shown in Figs. 5.5 and 5.6. Because this measurement station is upstream of the bleed slot the flow coefficient increases with bleed rate for the same reason as at rig inlet. However, at this location, the flow coefficient in the outer 30% of span increases more than the rest of the span and this effect increases with bleed rate. The redistribution of flow occurs because the streamlines in the meridional plane, near the casing, are being drawn into the bleed slot and this causes streamlines across the rest of the span to move upwards. This effect can also be seen in the plot of V_r/U where the radial component of velocity increases as bleed rate is increased. The absolute yaw angle and stagnation pressure coefficient are not affected by increased bleed rate.

Stage inlet. Figures 5.7 and 5.8 show spanwise distribution of flow at inlet to the stage, i.e. downstream of the bleed slot, at $\phi_{stage} = 0.43$ and $\phi_{stage} = 0.38$. At this location the passage-averaged flow coefficient varies by less than 0.8% across the four cases; this is expected because the traverses are performed at a fixed stage inlet flow coefficient. However, as bleed rate is increased there is a trend for the pitch-averaged flow coefficient from 70% to 95% span to reduce and that over the lower 70% to increase. At the last measurement location at 97.6% span, the 0% bleed case has a lower flow coefficient than the cases with bleed. Similar qualitative changes in the spanwise distribution of flow coefficient are observed by Leishman [15, Fig. 4.23(c)] downstream of an axisymmetric bleed slot. The reason for the redistribution of flow is that the air drawn into the bleed slot leaves a deficit of flow near to the casing. The stream tubes across the rest of the span therefore experience a static pressure gradient and curve upwards. At the stage inlet measurement location the pressure gradient caused by the bleed extraction is still influencing the flow, redistribution is still occurring and the deficit of flow near the casing and extra flow across the rest of the span are still present. The plot of V_r/U shows that near the casing the radial component of velocity is greatest as flow is drawn into the bleed slot; this trend increases as bleed rate is increased. Across the rest of the span the radial component of velocity also increases with bleed rate as the stream tubes curve further upwards. The spanwise distribution of radial velocity coefficient also highlights the non-ideal location of the traverse plane in relation to the bleed slot, discussed in Section 3.2.2. Radial velocity is still increasing close to the casing because the traverse plane is upstream of the rear face of the bleed slot and flow is being drawn past the probe head into the slot.

The spanwise distribution of stagnation pressure coefficient shows that near to the casing the stagnation pressure increases as bleed rate is increased. This effect is observed by Leishman et al. [18] as discussed in Section 2.2.1 and occurs because some of the high loss casing boundary layer is removed by the bleed extraction. This also explains why close to the casing (at the last spanwise measurement location) the flow coefficient for the case with 0% bleed rate is lower than for the cases

with bleed - some of the low velocity fluid in the casing boundary layer is removed, meaning that the flow coefficient close to the casing increases with bleed rate.

The plot of yaw angle in the absolute frame in Figs. 5.7 and 5.8 show that in the outer 30% of span flow angle increases with bleed rate. This is because the circumferential velocity component is not affected by uniform bleed extraction but in the outer 30% of span, the axial velocity is reduced as bleed rate is increased and yaw angle in the absolute frame is therefore increased. Together, the spanwise redistribution of flow coefficient and yaw angle result in a change in the flow angle in the rotor frame of reference. The plot of relative yaw angle shows that up to 70% of span there is an increase in rotor relative yaw angle (i.e. rotor incidence is reduced) with increased bleed rate. This is because the flow coefficient in this region increases with bleed rate and the absolute yaw angle is unaffected. Above 95% span there is also an increase in relative yaw angle with bleed rate. This is due to flow coefficient in this region increasing with bleed rate because the low velocity casing boundary is removed. Overall, therefore, there is an increase in passage-averaged yaw angle in the rotor frame of reference, at a fixed stage inlet flow coefficient, as bleed rate is increased. For an increase in bleed rate from 0% to 6.23%, at $\phi_{stage} = 0.43$, the increase in passage-averaged rotor relative yaw angle is 0.49 degrees and for $\phi_{stage} = 0.38$ it is 0.34 degrees. This reduces the rotor loading and shifts the stage pressure rise characteristic down, as seen in Fig. 5.2. The effect of rotor incidence on compressor operating range is investigated in Section 5.3.

Downstream of rotor row. Pitch-averaged, spanwise distributions of flow downstream of the rotor row at $\phi_{stage} = 0.43$ and $\phi_{stage} = 0.38$, are shown in Figs 5.9 and 5.10. At both operating points the spanwise distributions of flow coefficient, radial velocity coefficients and flow angles do not change with increased bleed rate. The stagnation pressure coefficient reduces slightly across the entire span as bleed rate is increased; this is consistent with the reduced pressure rise observed in Fig. 5.2. The flow coefficient plot in Fig. 5.9 shows a rotor hub corner separation up to 25% of span. As the compressor is throttled this separation increases and in Fig. 5.10, at $\phi_{stage} = 0.38$, it can be seen to extend up to 40% of span. Contours of flow coefficient and the pitch-averaged spanwise flow coefficient distribution, downstream of the rotor row, for fixed rig inlet flow coefficient, $\phi_{rig} = 0.43$, are shown in Fig. 5.11. With a fixed rig inlet flow coefficient the rotor hub corner separation grows as bleed rate is increased because the flow coefficient at stage inlet is reduced.

Downstream of stator row. Figures 5.12 and 5.13 show pitch-averaged, spanwise distributions of the flow downstream of the stator row at $\phi_{stage} = 0.43$ and $\phi_{stage} = 0.38$. Similar to the traverses downstream of the rotor, the flow coefficient, radial velocity coefficient and flow angles are not affected by bleed rate while stagnation pressure coefficient is reduced slightly. The stator hub corner separation increases as the compressor is throttled. This reduces the pitchwise-averaged flow coefficient near the hub and redistributes flow towards the casing. Figure 5.14 shows contours of flow

coefficient and the pitch-averaged spanwise flow coefficient distribution, downstream of the stator row for a fixed rig inlet flow coefficient, $\phi_{rig} = 0.43$. As bleed rate is increased, the stage inlet flow coefficient reduces and the stator hub corner separation grows.

5.2.3 Summary

This section shows that a passage-averaged analysis, where spanwise variation of the flow is ignored, provides a reasonable conceptual picture of the effect of uniform bleed rate on the downstream stage pressure rise characteristic; as expected from the passage-averaged approach the pressure rise characteristics collapse towards a single line. The small reduction in pressure rise with bleed rate, and the change in stage inlet stalling flow coefficient cannot be explained with the passage-averaged approach. Instead, a spanwise analysis of the main passage flow is required. This shows that the flow upstream and downstream of the bleed slot is redistributed by the bleed extraction, reducing the rotor incidence at stage inlet. The area traverses also show that increasing the bleed rate with a fixed rig inlet flow coefficient causes the rotor and stator hub corner separations to grow.

5.3 Stall

In this section the effect of varying the rate of uniform circumferential bleed on the stall inception mechanism and compressor operating range are investigated. Bleed rates of 0%, 2.07% 4.14% and 6.23% are tested and unsteady pressure measurements, pressure rise characteristics and area traverses are studied near to and at stall.

5.3.1 Stall inception mechanism

With a bleed rate of 0% the compressor stalls via spike-type stall inception. Figure 5.15 shows the unsteady pressure on the casing 13% of axial rotor tip chord upstream of the rotor at six equally spaced locations. The typical spike-type inception pattern can be seen whereby the static pressure in the stationary frame (i.e. on the casing) first spikes upwards and is then immediately followed by a downward spike. Pullan et al. [35] show that the upward spike in static pressure is due to a “blocked” passage caused by a separation at the rotor leading edge. The downward spike in pressure is then caused by a vortex which is shed from the leading edge of the next rotor blade as it separates. This disturbance initially has a small circumferential extent and only affects two or three blade passages; it propagates around the annulus at 77% of rotor speed. As the disturbance propagates it grows so that more blade passages are affected. After about four rotor revolutions the disturbance has grown into a stall cell which rotates at 53% of rotor speed. The same spike-type stall inception mechanism is observed for the other bleed rates tested.

5.3.2 Effect of bleed rate on operating range

Figure 5.16 shows the rig and stage inlet stalling flow coefficients against bleed rate for circumferentially uniform bleed. If there was no spanwise redistribution of the flow by the bleed extraction, the stalling stage inlet flow coefficient would remain constant. The figure shows, however, that stage inlet stalling flow coefficient reduces (the operating range improves) by 3.8% as bleed rate is increased from 0% to 6.23%. This result shows that the flow mechanisms linking uniform bleed rate and the stall point of a downstream stage are not captured by the passage-averaged approach.

For spike-type stall inception Pullan et al [35] show that the initial small disturbance recorded in the unsteady pressure measurements is caused by a flow separation from the suction surface of the rotor near its tip. This separation is caused by high incidence of the flow onto the rotor in the tip region. Figure 5.17 shows the yaw angle in the rotor relative frame, at stage inlet from 90% to 100% of span at a stage inlet flow coefficient, $\phi_{stage} = 0.38$ (close to stall). In this region, the 0% bleed rate case has a more negative relative yaw angle and hence a greater rotor incidence; at 97% the rotor incidence is 1 degree greater than for the cases with bleed. This result is consistent with the 0% bleed case stalling at a higher flow coefficient than for the cases with bleed. Increased rotor incidence triggers earlier separation in the tip and this leads to stall at a higher stage inlet flow coefficient.

At this point the limitations of these measurements should be pointed out. The area traverses are performed at a location which is still affected by the slot flow and so the rotor relative yaw may change before the flow reaches the inlet to the stage. Also, the measurements are taken at $\phi_{stage} = 0.38$, rather than at the point at which stall occurs. Despite these limitations it seems reasonable to conclude that the change in stall point is determined by the local effect of bleed on rotor tip incidence.

5.3.3 Summary

At all bleed rates tested the compressor stalls with the spike-type stall inception mechanism. As bleed rate is increased the operating range of the downstream stage improves. The cases with bleed have an improved operating range because the bleed extraction leads to reduced rotor incidence in the critical region of flow near the rotor tip.

5.4 Efficiency

The effect of varying the rate of circumferentially uniform bleed on compressor efficiency and loss in the bleed system is described in this section. First, the effects of bleed rate on overall efficiency characteristics are studied and then the overall efficiency is broken down into stage efficiency and loss through the bleed system.

5.4.1 Overall efficiency of rig

Figure 5.18 shows the overall efficiency of the compressor rig, defined in Equation 3.12, for varying bleed rate, plotted against rig inlet flow coefficient. These efficiency characteristics are offset because, for a given rig inlet flow coefficient, the stage inlet flow coefficient changes with bleed rate. Figure 5.19 shows the overall efficiency characteristics plotted against stage inlet flow coefficient. The peak efficiencies now line up between $\phi_{stage} = 0.43$ and $\phi_{stage} = 0.44$ and there is a reduction in peak overall efficiency as bleed rate is increased; for a bleed rate of 6.23% the peak overall efficiency is reduced by 2.2% compared to the case with a bleed rate of 0%.

5.4.2 Stage efficiency

To understand the change in efficiency it is helpful to separate the efficiency of the compressor stage and the loss of efficiency due to the bleed system. Figure 5.20 shows that stage efficiency, defined in Equation 3.15 and plotted against stage inlet flow coefficient, collapses towards a single line for varying bleed rate. Figure 5.21 shows the peak overall and peak stage efficiencies plotted against bleed rate. The peak stage efficiency increases by 0.19% points with an increase in bleed rate from 0% to 2.07%. The peak stage efficiency then reduces by 0.46% as bleed rate is increased from 2.07% to 6.23%. These small changes in stage efficiency agree well with the simplified picture of the compressor, where changes in spanwise flow distribution due to bleed extraction are ignored.

The repeatability of the efficiency measurements is given as $\pm 0.1\%$ in Section 3.3.3 so there does appear to be a small measurable reduction in stage efficiency as bleed rate is increased to 6.23%. Like the reduction in pressure rise with bleed, this is due to a spanwise redistribution of the flow by the bleed extraction and can only be captured with a pitch-averaged analysis. The increase in efficiency between the cases with bleed rates of 0% and 2.07% falls just within the range of experimental error. If it is a real effect it could be explained by the reduction in casing boundary layer thickness, discussed in Section 5.2.2. A similar effect is reported by Wellborn & Koir [13] and is discussed in Section 2.2.2.

5.4.3 Bleed system loss

The difference in peak stage efficiency and peak overall efficiency for the case with a bleed rate of 6.23% is 2.6% points. In order to separate the loss in the bleed flow from the rest of the main annulus flow, a control volume is defined as shown in Fig. 5.22. The inlet to this control volume is at the traverse location upstream of the bleed slot and its lower boundary is defined by the captured stream tube which separates the main annulus flow through the downstream stage from the bleed flow. The change in overall efficiency caused by the bleed system losses is defined as:

$$\Delta\eta_{bleed} = \frac{\dot{m}_{bl}U^2\Delta P_{0,CV,bl}}{2\tau\omega} \quad (5.1)$$

where \dot{m}_{bl} is the bleed mass flow, U is the midspan blade speed, τ is the motor torque, ω the rotor speed and $\Delta P_{0,CV,bl}$ is defined as:

$$\Delta P_{0,CV,bl} = \frac{P_{0,bl} - P_{0,CV,in}}{\frac{1}{2}\rho U^2} \quad (5.2)$$

where, $P_{0,bl}$ is the stagnation pressure in the off-take duct and $P_{0,CV,in}$ is the mass-averaged stagnation pressure at inlet to the control volume. $P_{0,CV,in}$ is calculated from the characteristic measurements using a correction factor $C_{p0,bl}$ which is derived from the area traverses upstream of the bleed slot. This is similar to the correction factor for rig inlet stagnation pressure which is calculated using Equation 3.7 and applied to the characteristic measurements using Equation 3.8. The difference is that the correction is applied to the area traverse above the height of the captured stream tube. The spanwise position of this stream tube is calculated by integrating mass flow down from the casing until the bleed mass flow is obtained.

Figure 5.23 shows the change in efficiency due to the bleed system plotted against stage inlet flow coefficient for varying bleed rate. For a given stage inlet flow coefficient the loss in efficiency increases with increased percentage bleed rate. Also, for a given percentage bleed rate, the loss in efficiency decreases as the compressor is throttled because the absolute bleed rate (in kg/s) through the bleed system is reduced.

Loss is expected to occur in each of the components of the bleed system, i.e. in the bleed slot, plenum chamber and off-take duct. In Chapter 7, a CFD model of the compressor and bleed system is used to calculate, and compare, the loss in each of these parts of the bleed system. However, given the experimental measurements obtained in the current work, only the overall bleed system loss can be studied here. A loss coefficient for the flow passing through the bleed system control volume is defined as:

$$Y_p = \frac{P_{0,CV,in} - P_{0,bl}}{(P_0 - P)_{CV,in}} \quad (5.3)$$

where $(P_0 - P)_{CV,in}$ is the mass-averaged dynamic head at inlet to the control volume and is calculated from the characteristic data with a correction factor, derived using the same method as $P_{0,CV,in}$. Figure 5.24 shows that Y_p is constant across the operating range within ± 0.01 ($\pm 1.1\%$). It is also constant for the different bleed rates tested with the average loss coefficient across the operating range, $\overline{Y_p}$ within ± 0.002 ($\pm 0.2\%$). The average value of $\overline{Y_p}$ for the bleed rates tested is 0.88 showing that most of the dynamic head available at inlet to the control volume is lost through the bleed system. This is a useful result because, given the stagnation pressure and dynamic head of the flow at inlet to the bleed system, the stagnation pressure loss through the bleed system can be predicted for different

bleed rates and operating points. It also provides a metric for comparing different bleed system designs.

5.4.4 Summary

A passage-averaged view of the flow provides a reasonable picture of the effect of uniform bleed rate on the downstream stage efficiency characteristic. However, a pitch-averaged analysis of the flow, where spanwise flow distributions are considered, is needed to capture the small change in stage efficiency with bleed. The overall efficiency of the compressor test rig reduces with increased bleed rate because the losses in the bleed system increase. A loss coefficient for the bleed system has been defined which normalises the stagnation pressure loss of the bleed flow by the dynamic head of the bleed flow before it is extracted from the main annulus. This loss coefficient is constant across the operating range of the compressor and at the different bleed rates tested for the large plenum chamber, four off-take duct case.

5.5 Conclusions

The following conclusions can be drawn from this chapter:

1. For bleed rates typical of a design operating point (i.e. between 0% and 6.23%), a passage-averaged analysis of the flow provides a useful simplification of the operation of a compressor stage with an upstream bleed slot and uniform bleed extraction. This works because the spanwise flow distributions are a similar shape for the bleed rates tested and therefore the flow can be characterised by just the passage average.
2. The small drop in stage pressure rise of up to 2.5% with increased bleed rate is due to a spanwise redistribution of flow caused by bleed extraction; a pitch-averaged analysis is required to capture this effect.
3. The test compressor stalls with a spike-type stall inception mechanism and this does not change for the bleed rates tested.
4. The stage operating range improves as bleed rate is increased. This is because bleed extraction causes a reduction in incidence of up to 1 degree at the rotor tip where spike-type stall is initiated.
5. The peak stage efficiency is slightly reduced as the bleed rate is increased (-0.3% points for a bleed rate of 6.23% compared to 0%). The change in stage efficiency with bleed is small because there is only a small spanwise redistribution with bleed at the bleed rates tested.

6. The reduction in efficiency due to losses in the bleed system increases with bleed rate. A loss coefficient has been defined which characterises the loss in the bleed system and is constant to within $\pm 1.1\%$ for the different operating points and bleed rates tested.

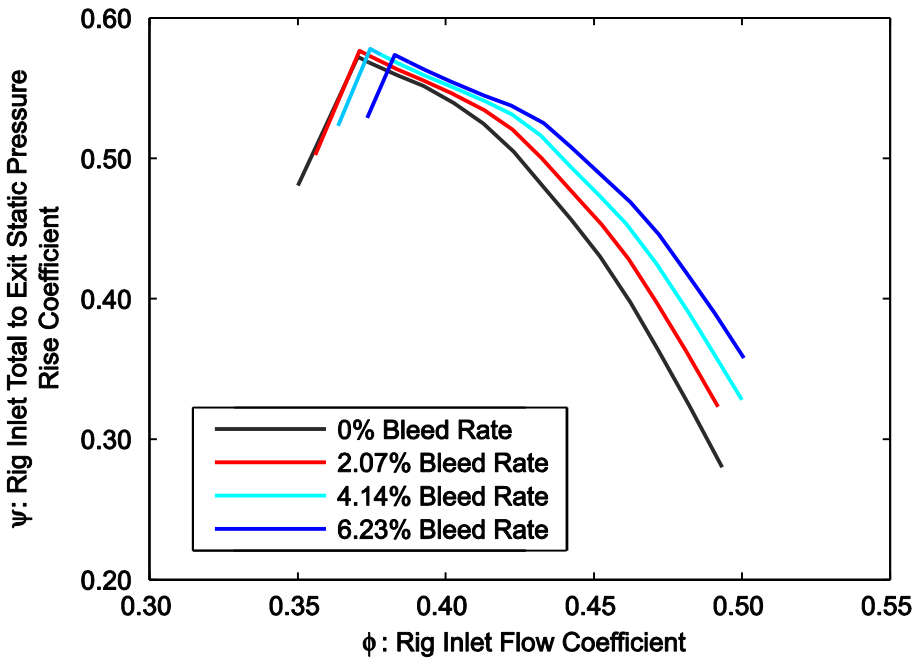


Figure 5.1: Rig inlet to stage exit total-to-static pressure rise against rig inlet flow coefficient for varying uniform bleed rate.

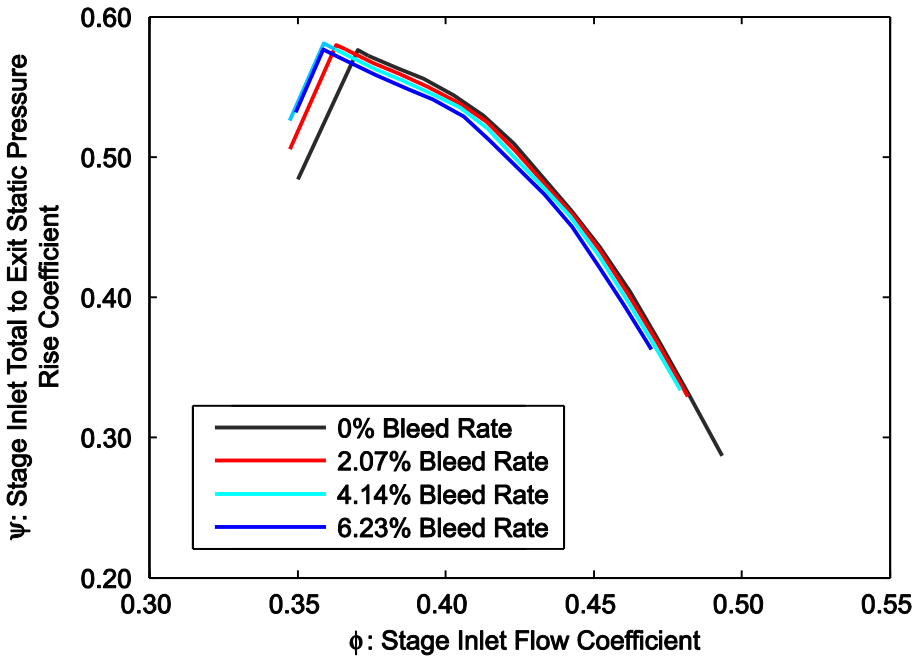


Figure 5.2: Stage inlet to stage exit total-to-static pressure rise against stage inlet flow coefficient for varying uniform bleed rate.

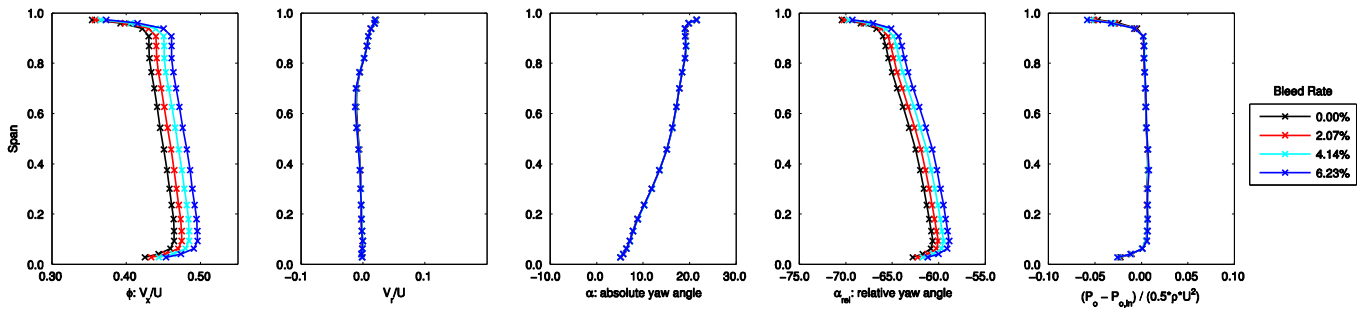


Figure 5.3: Rig inlet, pitch-averaged, spanwise distributions of flow for varying bleed rate. $\phi_{\text{stage}} = 0.43$.

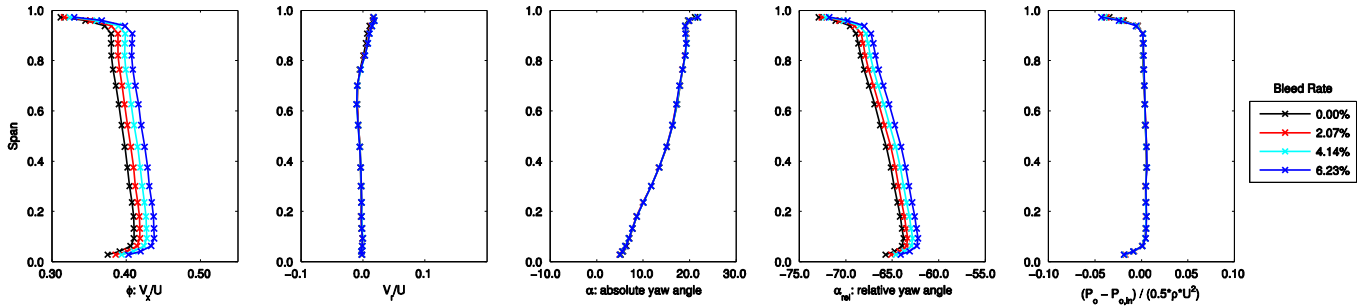


Figure 5.4: Rig inlet, pitch-averaged, spanwise distributions of flow for varying bleed rate. $\phi_{\text{stage}} = 0.38$.

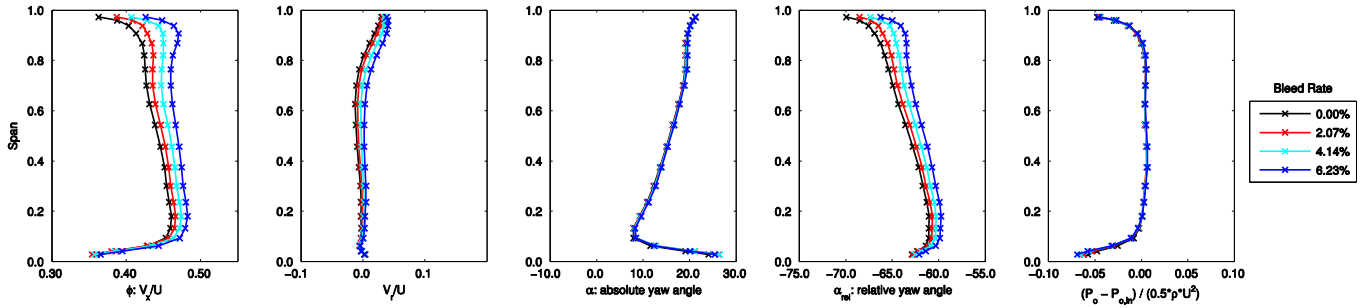


Figure 5.5: Upstream of slot, pitch-averaged, spanwise distributions of flow for varying bleed rate. $\phi_{\text{stage}} = 0.43$.

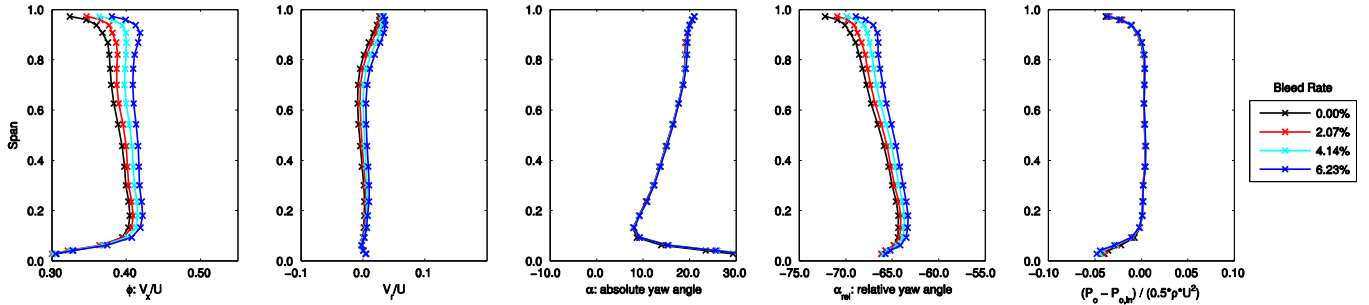


Figure 5.6: Upstream of slot, pitch-averaged, spanwise distributions of flow for varying bleed rate. $\phi_{\text{stage}} = 0.38$.

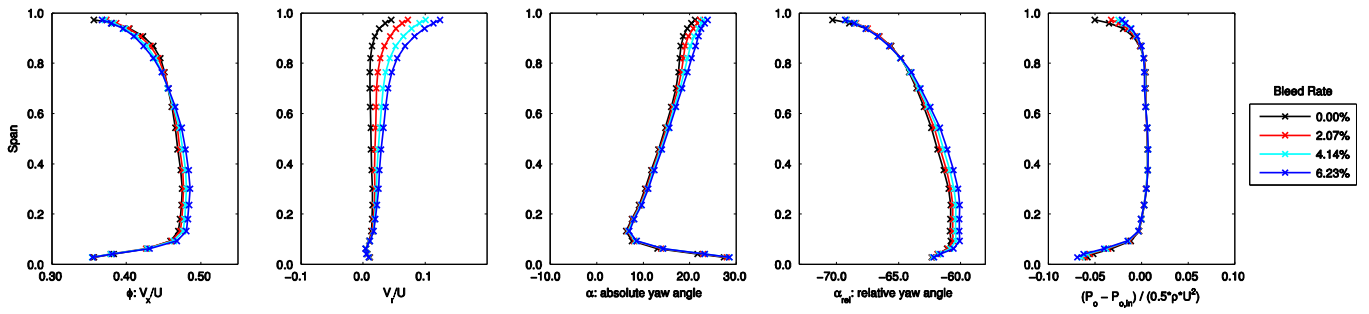


Figure 5.7: Stage inlet, pitch-averaged, spanwise distributions of flow for varying bleed rate. $\phi_{\text{stage}} = 0.43$.

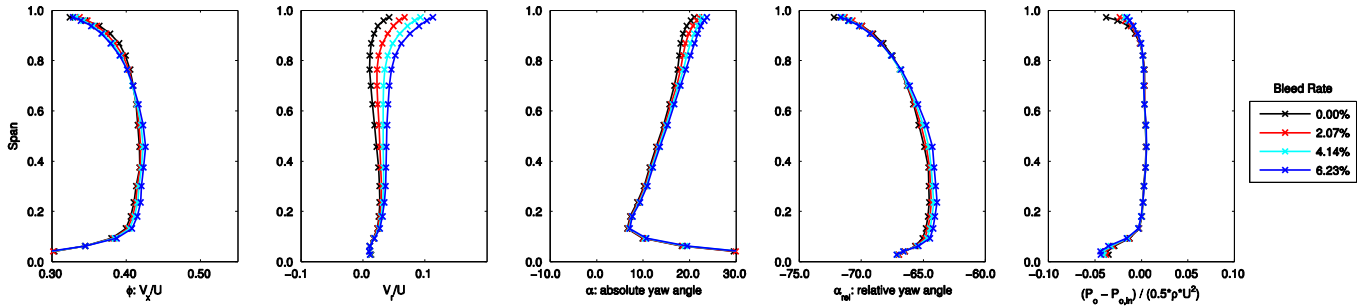


Figure 5.8: Stage inlet, pitch-averaged, spanwise distributions of flow for varying bleed rate. $\phi_{\text{stage}} = 0.38$.

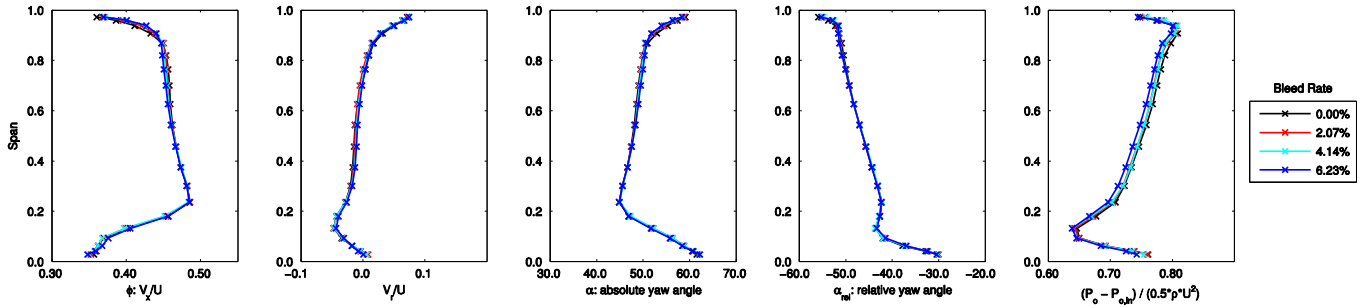


Figure 5.9: Downstream of rotor row, pitch-averaged, spanwise distributions of flow for varying bleed rate. $\phi_{\text{stage}} = 0.43$.

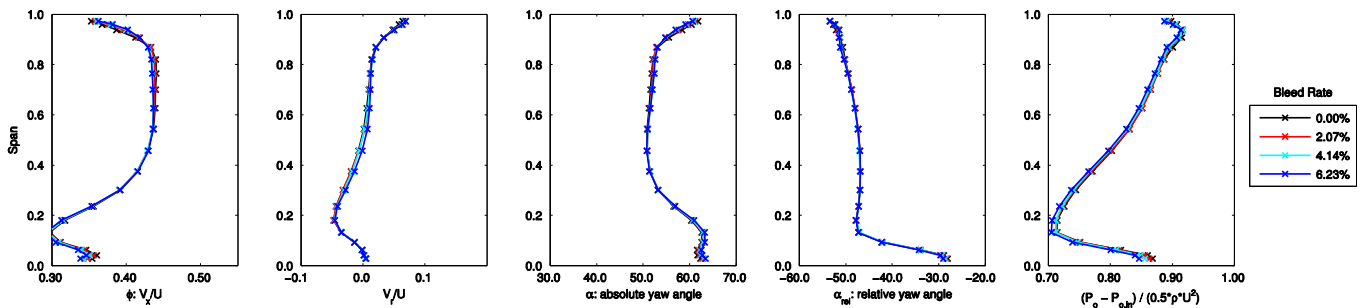


Figure 5.10: Downstream of rotor row, pitch-averaged, spanwise distributions of flow for varying bleed rate. $\phi_{\text{stage}} = 0.38$.

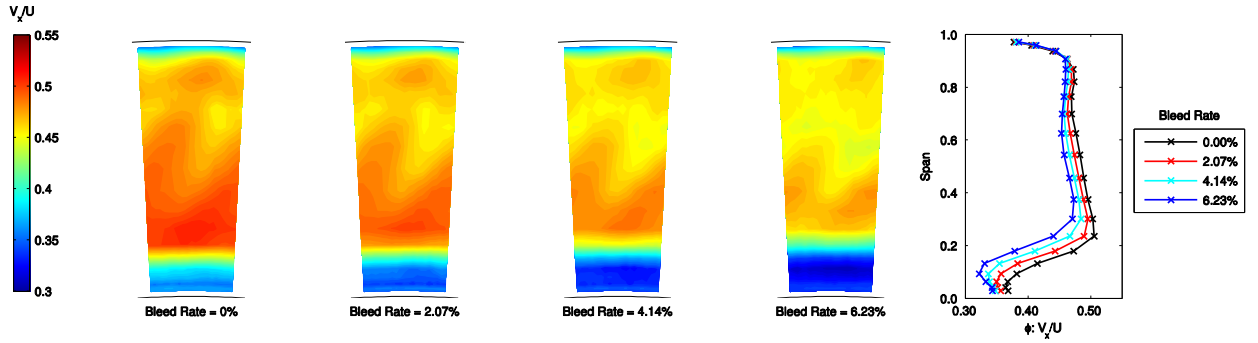


Figure 5.11: Downstream of rotor row, contours of flow coefficient and pitch-averaged, spanwise distributions of flow coefficient for varying bleed rate. Rig inlet flow coefficient fixed, $\phi_{rig} = 0.43$.

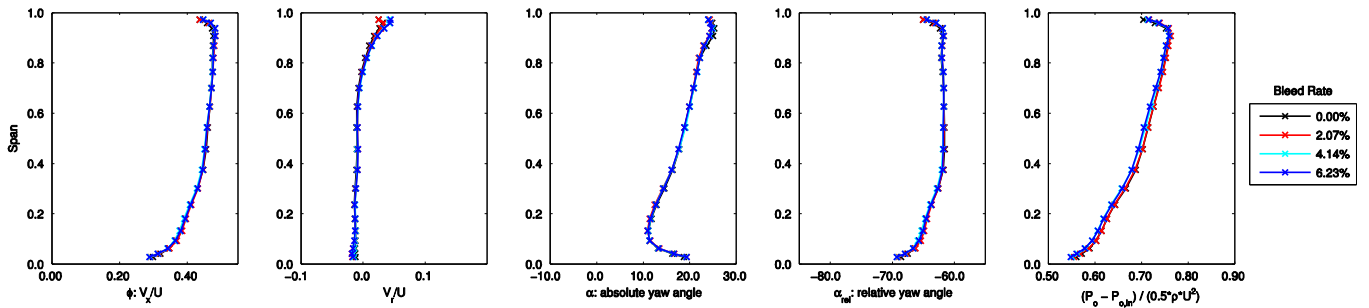


Figure 5.12: Downstream of stator row, pitch-averaged, spanwise distribution of flow for varying bleed rate. $\phi_{stage} = 0.43$.

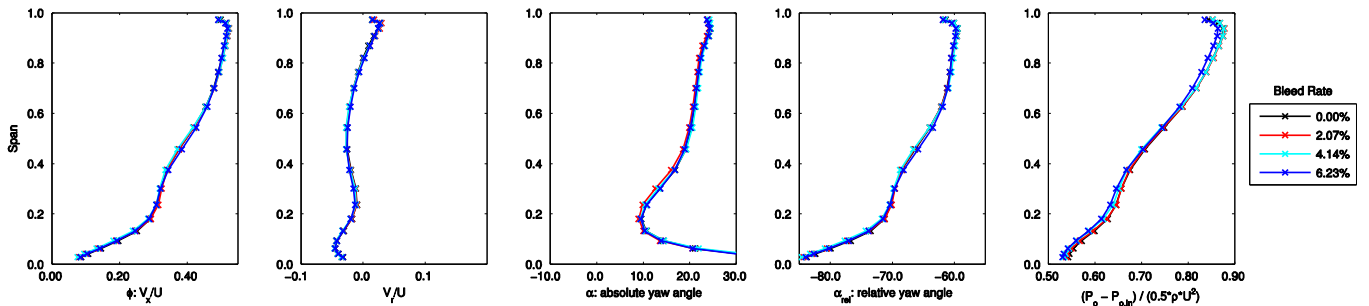


Figure 5.13: Downstream of stator row, pitch-averaged, spanwise distribution of flow for varying bleed rate. $\phi_{stage} = 0.38$.

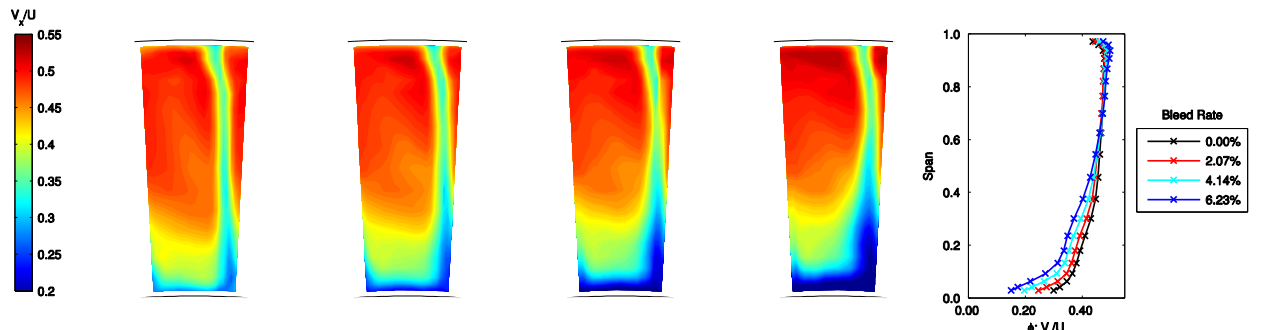


Figure 5.14: Downstream of stator row, contours of flow coefficient and pitch-averaged, spanwise distributions of flow coefficient for varying bleed rate. Rig inlet flow coefficient fixed, $\phi_{rig} = 0.43$.

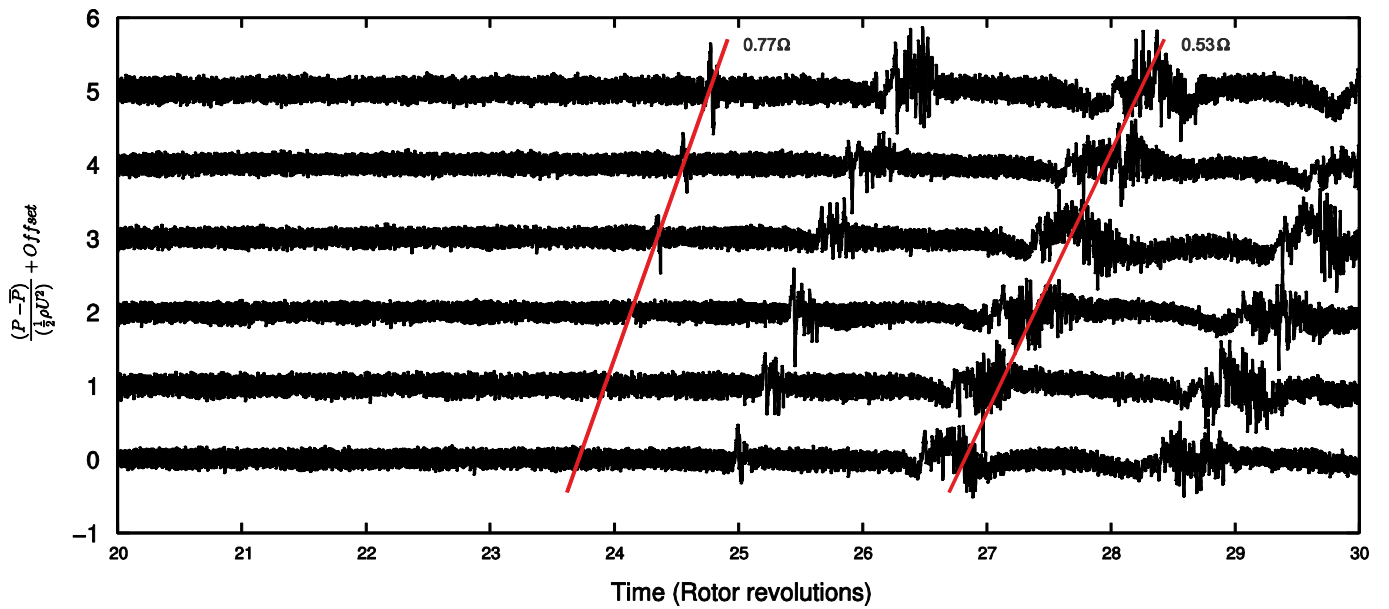


Figure 5.15: Unsteady static pressures at casing, just upstream of rotor leading edge, showing stall inception for case with bleed rate of 0%.

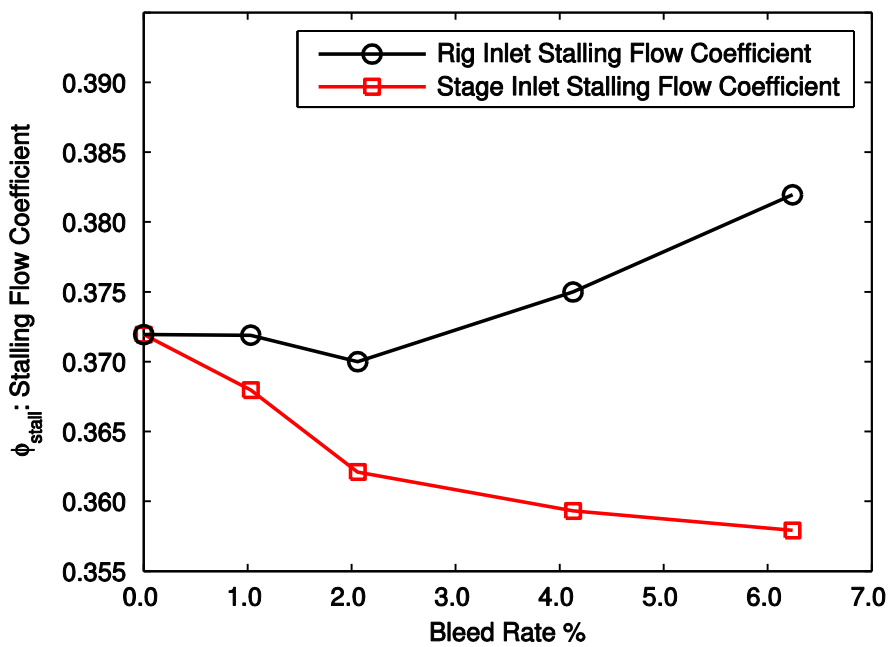


Figure 5.16: Rig and stage inlet flow coefficients at stall against bleed rate.

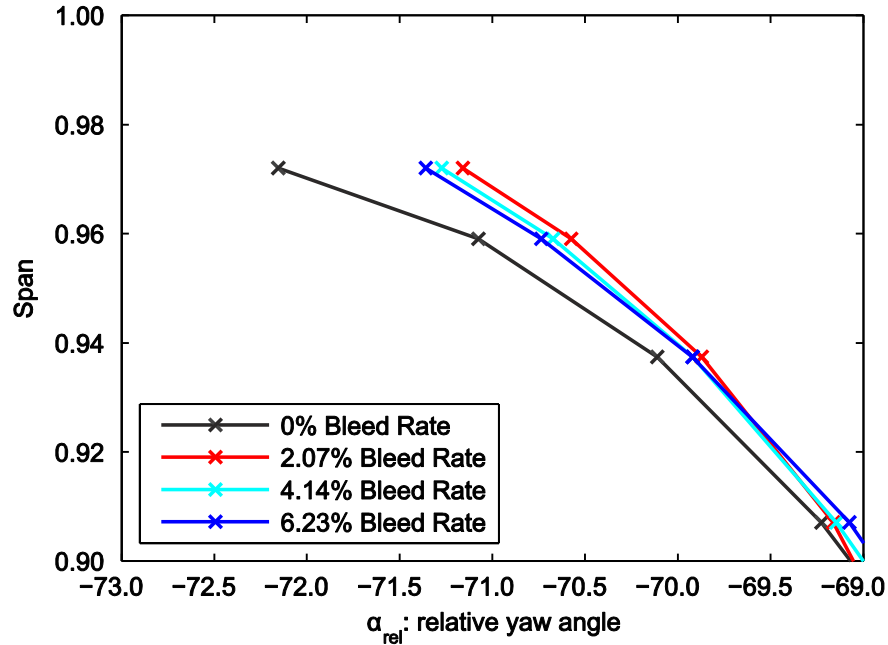


Figure 5.17: Stage inlet yaw angle in the rotor relative frame, from 90% to 100% of span. $\phi_{\text{stage}} = 0.38$.

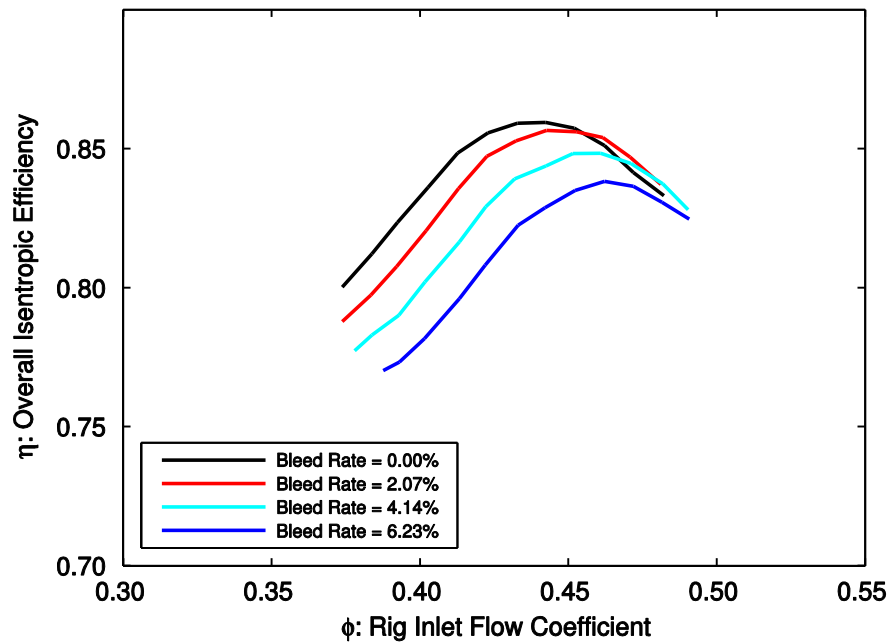


Figure 5.18: Overall efficiency against rig inlet flow coefficient for varying uniform bleed rate.

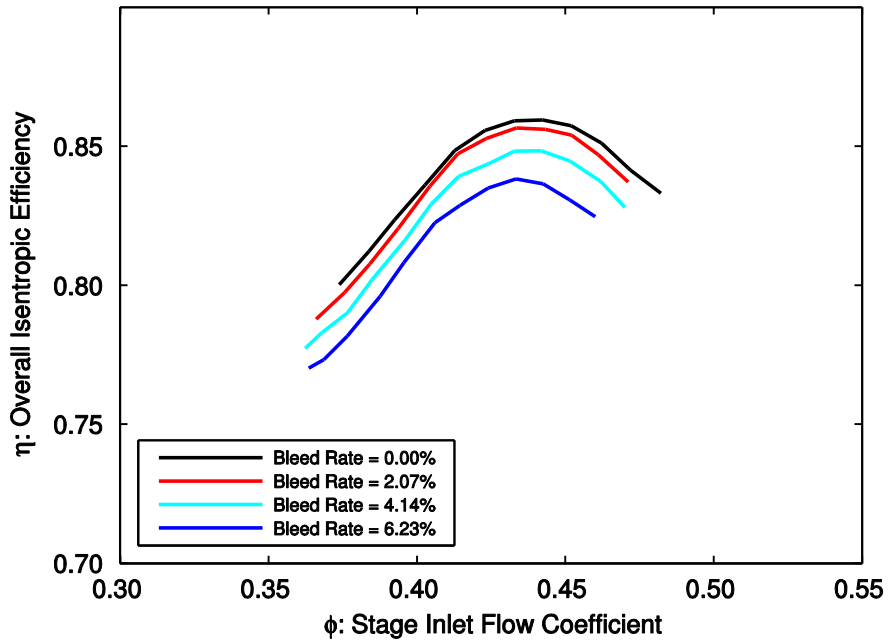


Figure 5.19: Overall efficiency against stage inlet flow coefficient for varying uniform bleed rate.

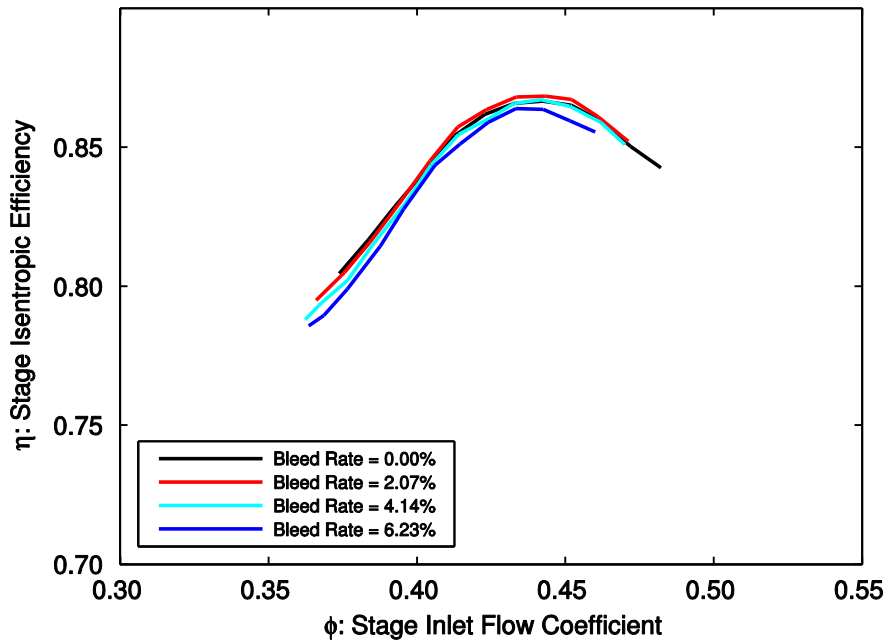


Figure 5.20: Stage efficiency against stage inlet flow coefficient for varying uniform bleed rate.

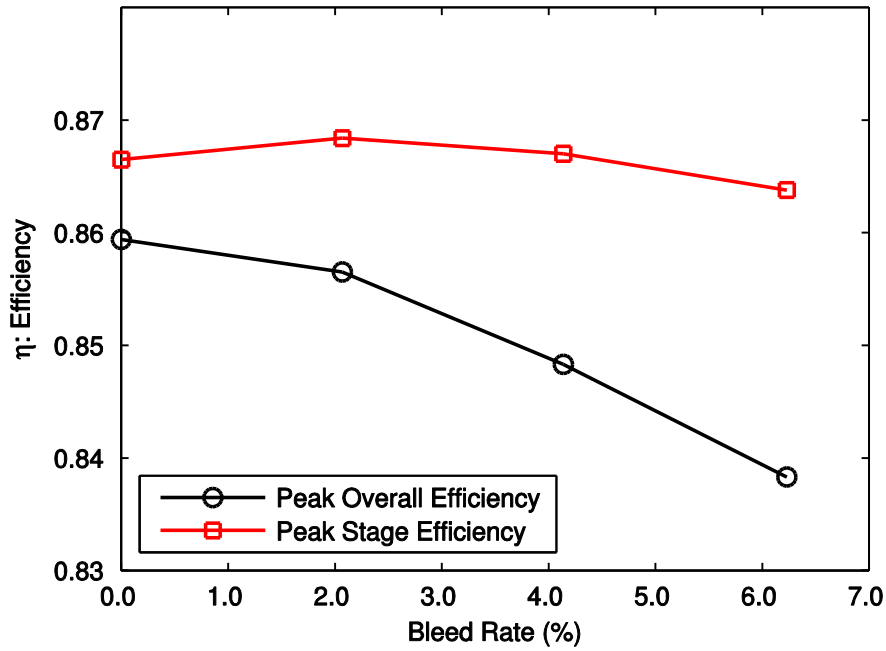


Figure 5.21: Peak overall and peak stage efficiency against bleed rate.

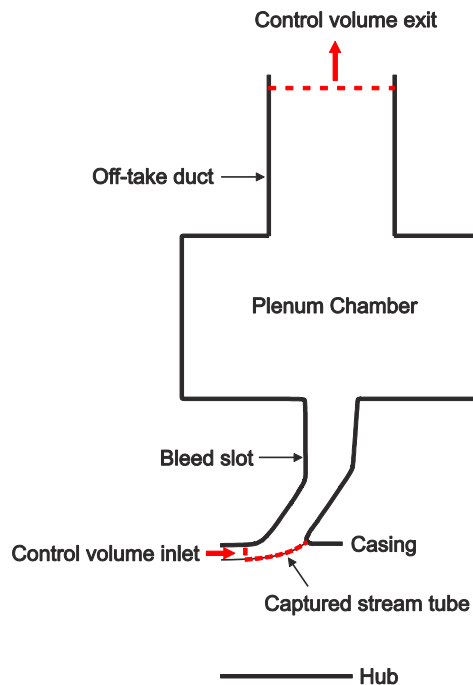


Figure 5.22: Control volume for bleed system flow.

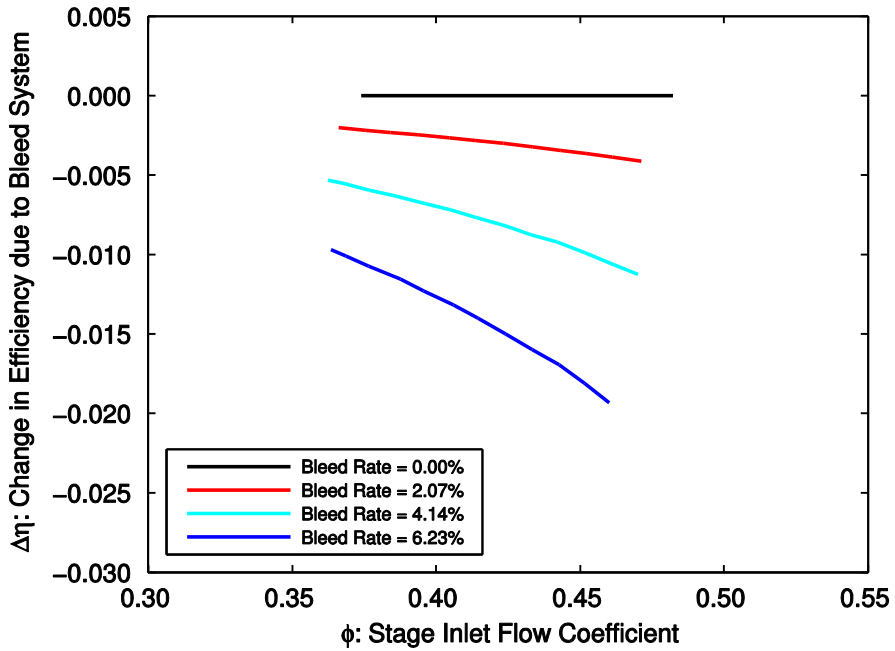


Figure 5.23: Change in efficiency due to bleed system against stage inlet flow coefficient for varying uniform bleed rate.

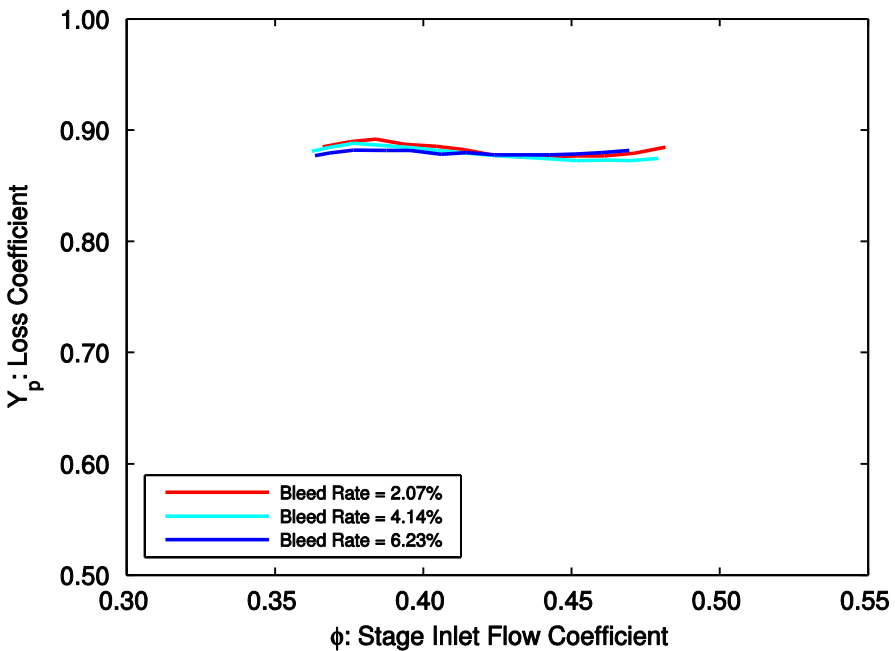


Figure 5.24: Bleed system loss coefficient against stage inlet flow coefficient.

Chapter 6

Non-uniform Bleed

6.1 Introduction

This chapter investigates the effect of circumferentially non-uniform bleed on the main annulus flow and the flow in the bleed system. In order to study the effect of non-uniform bleed extraction on operating range, a bleed system configuration with the small plenum chamber, one off-take duct and 4.14% bleed was chosen to be the test case. Figure 6.1 compares the stage inlet to stage exit total-to-static pressure rise characteristic for the test case and the uniform bleed case (at the same bleed rate). It shows that with non-uniform bleed the inlet stalling flow coefficient of the downstream compressor stage is increased by 3.0%. Figure 6.2 shows the local bleed rate distribution in the slot; the peak local bleed rate for this case is 22.9%.

The aim of the first two sections of this chapter is to show why circumferentially non-uniform bleed reduces the operating range of a downstream stage. To simplify the analysis, it is first assumed that there is no spanwise redistribution of the flow by the bleed extraction. This results in a passage-averaged analysis where the flow properties are non-uniform in the circumferential direction and the compressor stage operating point varies around the annulus. The full three-dimensional flow field is then studied. This provides a more detailed analysis of the effect of non-uniform bleed while showing that the assumptions used and the conclusions drawn from the passage-averaged analysis are valid. In both analyses particular attention is paid to the flow entering the downstream compressor stage as this determines whether the stage will stall and how the operating range is changed.

The final section of this chapter studies the effect of non-uniform bleed on compressor efficiency and loss in the bleed system. A variety of bleed system configurations are tested with different sizes of plenum chamber and number of off-take ducts.

6.2 Passage-averaged Analysis

In the previous chapter it was concluded that the passage-averaged analysis of the compressor flow provides a useful simplification of the operation of a compressor stage with an upstream bleed slot and uniform bleed extraction. A similar approach is adopted for non-uniform bleed extraction; spanwise redistribution of the flow by the bleed extraction is ignored and the changes in the flow due to circumferential non-uniformity are studied by passage-averaging area traverses at different locations around the annulus.

Area traverses are performed at five measurement stations and the off-take duct is moved relative to the traverse location so that the circumferentially non-uniform flow field can be measured around the whole annulus. Each area traverse is averaged in pitchwise and spanwise directions (“passage-averaged”). The passage-averaged flow property is then plotted against the circumferential position of the centre of the area traverse relative to the centre of the off-take duct to show the circumferential distribution of the flow around the annulus. For example, Figure 6.3 shows the passage-averaged flow coefficient against circumferential position relative to the off-take duct, at rig inlet. The operating point is set with annulus-averaged stage inlet flow coefficient of $\overline{\phi_{stage}} = 0.43$ and $\overline{\phi_{stage}} = 0.38$.

At rig inlet, and for both operating points, the annulus-averaged flow coefficient (i.e. the average of all the traverses) with an endwall boundary layer model applied (as described in Section 3.3.1) is within 0.7% of the expected flow coefficient found using the inlet calibration. However, the annulus-averaged flow coefficient at the other measurement stations differs from the expected flow coefficient by up to 3.1%. Upstream of the slot the annulus-averaged flow coefficients at $\overline{\phi_{stage}} = 0.43$ and $\overline{\phi_{stage}} = 0.38$ differ by -1.2% and -1.5% from the expected values. This difference is believed to be due to the endwall boundary layer model which becomes less realistic as the endwall boundary layers grow. At stage inlet the annulus-averaged flow coefficients differ by 3.1% and 2.4% from the expected values. There are two issues with this measurement station. First, the location of the traverse plane is upstream of the rear face of the bleed slot, as discussed in Section 3.2.2. A result of this is seen later in Figs. 6.19(b) and 6.20(b) where pitchwise-averaged V_r/U is still increasing at the measurement point closest to the casing as flow is drawn past the probe head into the slot. This suggests that more flow is extracted downstream of the traverse plane and hence there is more flow measured at this location than actually enters the downstream stage. The second issue is that the probe head is close to the rotors and will experience an unsteady pressure field. This is also an issue for the measurement station downstream of the rotors where annulus-averaged flow coefficient differs by 2.2% and 2.6% compared to the expected values. Downstream of the stators the annulus-averaged flow coefficient differs by 1.3% and 1.2% from the expected values. At this measurement station

there is a large region of low velocity flow associated with the stator hub corner separation and the probe calibration may not be reliable in this region since the calibration is performed at a Reynolds number which is representative of the mainstream flow.

Despite these issues the data is still useful because the relative differences in the flow properties around the annulus at each measurement station are more important than the absolute values. The flow distributions in the rest of this section are therefore plotted as the difference between the passage-averaged value (at a given circumferential location and operating point) and the annulus-averaged value for that measurement location and operating point.

Area traverses were performed at two operating points: a design operating point where $\overline{\phi_{stage}} = 0.43$ and an operating point close to stall where $\overline{\phi_{stage}} = 0.38$. It is shown below that the local bleed rate distribution does not change significantly with operating point; however, the flow measured in the main annulus varies significantly between the two operating points due to coupling between the bleed extraction, the main annulus flow, and the compressor stage. The rest of this section presents a passage-averaged analysis of the flow at each operating point. A conceptual description of the flow field is proposed which explains the observed flows, the differences seen at the different operating points, and why the compressor operating range is reduced by non-uniform bleed extraction.

6.2.1 Design operating point ($\overline{\phi_{stage}} = 0.43$)

Figure 6.4 shows the distribution of the passage-averaged flow coefficient upstream of the bleed slot, at stage inlet, downstream of the rotor row and downstream of the stator row at $\overline{\phi_{stage}} = 0.43$. Upstream of the bleed slot and close to the circumferential location of the off-take duct more flow is drawn through the main annulus due to the reduced pressure caused by non-uniform bleed extraction through the slot. At stage inlet the flow coefficient has an asymmetric distribution about the off-take duct location: there is reduced flow coefficient “before” the off-take duct location, i.e. at a negative circumferential position relative to off-take duct, and increased flow coefficient “after” the off-take duct, i.e. at a positive circumferential position relative to off-take duct. An asymmetric distribution similar to that observed at stage inlet is also present downstream of the rotor and stator rows.

The mass flow extracted by the bleed system is the difference in mass flow between the measurement stations upstream and downstream of the bleed slot. Figure 6.5 shows this difference in mass flow as a local bleed rate. Also plotted is the local bleed rate in the bleed slot measured using the stagnation pressure probe and static pressure tapping pairs. Compared to the bleed slot measurement the mass flow calculated from the area traverses has a lower, wider peak and there is a small amount

of bleed extraction even away from the off-take duct. This result indicates that the non-uniform static pressure field caused by the bleed decays away from the off-take duct resulting in a more circumferentially uniform bleed flow at the entrance to the bleed slot than at exit.

The pressure field generated by the non-uniform bleed extraction also affects the flow angle in the main annulus. The yaw angle distributions in the absolute frame, upstream of the bleed slot and at stage inlet, are plotted in Fig. 6.6. Upstream and downstream of the slot the yaw angle distributions are asymmetric about the off-take duct location: before the off-take duct location the angle is increased and after the off-take duct location the angle is reduced.

The results above can be explained by breaking the flow down into three parts: isolated bleed extraction with zero net main annulus flow, finite main annulus flow, and the downstream compressor stage. These elements are combined one by one to explain how they interact to produce the behaviour observed. In isolation (zero net main annulus flow), the bleed slot with non-uniform bleed will extract air from upstream and downstream of the slot. For incompressible flow, the axial velocity perturbations produced by the bleed will be equal and opposite upstream and downstream of the bleed slot. The streamlines also curve towards the peak in bleed extraction causing an asymmetric circumferential distribution of yaw angle. This is shown schematically in Fig. 6.7.

When the main annulus flow is included, bleed is no longer extracted from downstream of the slot but the symmetric distribution of the flow coefficient perturbation upstream and downstream of the slot will remain due to the superposition of the bleed slot and uniform annulus flow fields. If the mainstream flow has zero inlet swirl then the flow angle distribution will be asymmetric about the peak bleed close to the off-take duct but tend to zero away from this location. With inlet swirl, the flow coefficient distributions upstream and downstream of the bleed slot will become offset in the circumferential direction. The upstream peak occurs after the off-take duct position where the reduced yaw angle, caused by the curved streamlines, results in an increased axial velocity component. Downstream of the bleed slot the trough occurs before the off-take where increased yaw angle reduces the flow coefficient. The case with non-uniform bleed extraction and finite main annulus flow with swirl is shown in Fig. 6.8.

The coupling of the downstream compressor stage with the non-uniform bleed extraction acts to make the flow coefficient distribution at stage inlet more uniform. Figure 6.9(a) shows the measured distribution of stagnation pressure at stage inlet and Fig. 6.9(b) shows the measured static pressure at stage exit. Both of these pressure distributions are close to circumferentially uniform. The slight non-uniformity in the stage inlet stagnation pressure is due to varying amounts of the casing boundary layer being removed due to different rates of bleed extraction around the annulus. This is discussed further as part of the three-dimensional analysis in the next section. The exit static pressure is circumferentially uniform. Greitzer, Mazzawy & Fulkerson [52] show that this is because the stage

outlet flow is at a uniform absolute yaw angle, the downstream annulus is constant area and the throttle is sufficiently far downstream for it to be decoupled. Overall, Fig. 6.9 shows that the total-to-static pressure rise across the compressor stage does not vary around the annulus. However, Fig 6.4(b) shows that the stage inlet flow coefficient does change with circumferential position due to the non-uniform static pressure field created by the non-uniform bleed. This means that at stage inlet the compressor imposes its own non-uniform static pressure field on the flow. Specifically, in regions of relatively low inlet flow, the compressor will produce a relatively high static pressure rise so that the static pressure upstream of the stage is reduced and the axial velocity at rotor inlet is increased. This has the effect of reducing the flow coefficient non-uniformity entering the downstream stage. The trough in the flow coefficient distribution at stage inlet is therefore reduced compared to the case where there is no downstream compressor stage. The symmetry between the flow coefficient distributions upstream and downstream of the bleed slot, shown in Fig 6.8, is also broken and the peak in the flow coefficient distribution upstream of the slot is increased.

These effects can be seen in Figs. 6.4(a) and 6.4(b). The flow coefficient distribution upstream of the bleed slot has a peak like that shown schematically in Fig. 6.8 but the symmetry with the downstream flow coefficient distribution has been broken. Downstream of the slot the trough has been reduced by the interaction with the downstream stage. Also, where the yaw angle is increased by the non-uniform bleed extraction (shown in Fig. 6.8), the flow is less axial and the flow coefficient reduces. Where the yaw angle is reduced the flow is more axial and the flow coefficient is increased.

6.2.2 Near stall operating point ($\overline{\phi_{stage}} = 0.38$)

Figure 6.10 shows the distribution of the passage-averaged flow coefficient upstream of the bleed slot, at stage inlet, downstream of the rotor row and downstream of the stator row at $\overline{\phi_{stage}} = 0.38$. With this bleed system configuration (small plenum, one duct, 4.14% bleed rate) the stage inlet stalling flow coefficient is $\overline{\phi_{stage}} = 0.37$. Upstream of the bleed slot the distribution is similar to that observed in Fig. 6.4(a) where close to the circumferential location of the off-take duct there is a peak in the flow coefficient. However, at stage inlet the flow coefficient distribution is noticeably different to that shown in Fig 6.4(b). The distribution now has a trough with a minimum flow coefficient offset 11 degrees before the off-take duct location; the region of increased flow coefficient after the off-take location is not present. Downstream of the rotor and stator rows the distributions of passage-averaged flow coefficient are similar to those at stage inlet: they have a single trough offset just before the off-take duct position.

Figure 6.11 shows the difference in mass flow between the measurement stations upstream and downstream of the bleed slot as a local bleed rate at $\overline{\phi_{stage}} = 0.38$. Also plotted is the local bleed rate

in the bleed slot measured using the stagnation pressure probe and static pressure tapping pairs at $\overline{\phi_{stage}} = 0.38$. As in Fig. 6.5 the bleed mass flow calculated from the area traverses has a lower, wider peak and there is a small amount of bleed extraction even away from the off-take duct. Also the bleed rate distribution measured in the bleed slot in Fig. 6.11 is very similar to that shown in Fig. 6.5 at $\overline{\phi_{stage}} = 0.43$. The local bleed rate varies by 2% points at peak local bleed rate and by less than this for the rest of the distribution showing that the local bleed rate distribution measured in the slot is independent of the compressor operating point.

The yaw angle distributions in the absolute frame upstream of the bleed slot and at stage inlet are plotted in Fig. 6.12. These distributions are similar to those plotted in Fig. 6.6 at the design operating point and are again due to streamline curvature caused by the non-uniform static pressure field associated with the discrete off-take duct.

The schematic representations of the flow given in Fig. 6.7 for the isolated bleed slot and Fig. 6.8 for the bleed slot with main annulus flow are still valid as they are independent of the stage (or rig) inlet flow coefficient. This means that the change in the flow coefficient distribution at stage inlet is due to the coupling of the bleed slot and the main annulus flow with the downstream stage. Figure 6.13 shows the stage static-to-static pressure rise, defined in Equation 3.2, against stage inlet flow coefficient, for the uniform bleed case with a bleed rate of 4.14%. For the two-dimensional analysis it is assumed that the compressor operates locally on this characteristic around the annulus and the pressure rise is therefore set by the local flow coefficient. With a stage inlet flow coefficient, $\overline{\phi_{stage}} = 0.43$, reducing the flow coefficient results in an increased static-to-static pressure rise as described in the previous section. However with a stage inlet flow coefficient of 0.38 the characteristic is flat so that reduced flow coefficient does not result in increased pressure rise across the compressor. The compressor therefore cannot act to make the static pressure distribution at stage inlet more circumferentially uniform, as it does at the design operating point. At lower flow coefficients the trough seen in Fig. 6.8 is not reduced as much by the downstream compressor stage as at the design operating point and this results in an area of reduced local flow coefficient at stage inlet as observed in Fig. 6.10(b).

6.2.3 Rotor incidence and stall

Of interest is the stability of the stage immediately downstream of the bleed slot. The stability of this stage is governed by the flow coefficient and the yaw angle in the absolute frame at stage inlet. If the flow into the stage is reduced sufficiently the compressor will stall either via “modes” (if the stage reaches the peak of its total-to-static pressure rise characteristic) or “spikes” (if stall occurs, due to high rotor incidence, on the negative slope of the characteristic). In common with similar machines

in real applications, the test compressor in the present work exhibits spike-type stall inception so that, whatever happens upstream, incidence at rotor inlet will determine if the stage stalls or not.

Rotor incidence is determined by the yaw angle in the rotor-relative frame. Together the circumferentially non-uniform flow coefficient and absolute yaw angle distributions create a non-uniform relative yaw angle distribution at stage inlet. These distributions, at the two operating points, are plotted in Fig. 6.14. At the design operating point, away from stall, the average of the rotor incidence is well below the critical value at which the compressor stalls and so the distribution does not affect the stall point. It is interesting to note, however, that the relative yaw distribution is asymmetric about the off-take duct. Before the off-take duct location the angle is increased (rotor incidence reduces), largely due to the increase in this region of the absolute yaw angle. After the off-take duct location the relative yaw angle is reduced (rotor incidence increases), again, largely due to the reduction in absolute yaw angle in this region.

At $\overline{\phi_{stage}} = 0.38$ there is a reduction in relative yaw angle which corresponds to an increase in rotor incidence of up to 1.0 degree. The minimum relative yaw angle is offset by 34 degrees from the off-take duct location due to the asymmetric absolute yaw distribution. The relative yaw angle is reduced more at this operating point than at design because of the trough in the flow coefficient distribution combined with the reduced absolute yaw angle. As the compressor is throttled further the flow in this region of high incidence is more likely to separate from the rotor blade and cause the compressor to stall. This explains why circumferentially non-uniform bleed reduces the operating range of a downstream compressor stage.

6.2.4 Summary

The passage-averaged analysis has shown that non-uniform bleed extraction distorts the flow upstream and downstream of the bleed slot. Both flow coefficient and yaw angle in the absolute frame are affected as streamlines are drawn towards the region of low pressure caused by the discrete bleed off-take duct. At the design operating point, the coupling of the downstream compressor stage with the non-uniform flow caused by the bleed extraction acts to reduce the non-uniformity of the flow entering the stage. However at lower flow coefficients the compressor static-to-static pressure rise characteristic becomes flatter and the ability of the downstream stage to lessen the non-uniformity imposed by the non-uniform bleed extraction is reduced. Near stall, therefore, non-uniform bleed extraction results in a region of reduced flow coefficient and increased rotor incidence at stage inlet. This causes the rotors to stall due to high incidence at a higher overall flow coefficient and hence the operating range of the downstream stage is reduced.

6.3 Pitch-averaged Analysis

The passage-averaged analysis above connects non-uniform bleed extraction and a loss in operating range via the rotor incidence. This section studies the three-dimensional flow through the compressor rig by pitch-averaging the data from area traverses taken over 1 pitch \times 1 span at different locations around the annulus.

It is shown that the conceptual description of the flow presented in Section 6.2 is a useful simplification of the effect of circumferentially non-uniform bleed, while pointing out flow features which can only be understood by considering the spanwise redistribution of the flow. In particular, spanwise redistribution serves to exacerbate the effect of non-uniform bleed on operating range by increasing the rotor incidence further in the tip region.

6.3.1 Rig inlet

Figures 6.15(a) and 6.16(a) show contours of flow coefficient around the annulus at the rig inlet measurement station for $\overline{\phi_{stage}} = 0.43$ and $\overline{\phi_{stage}} = 0.38$. The figures show that close to the circumferential location of the off-take duct the flow coefficient is increased. Each area traverse is pitch-averaged and the spanwise distributions of the flow properties are plotted in Figs. 6.15(b) and 6.16(b). At this measurement station there is a non-uniform circumferential distribution of flow coefficient but the differences in flow coefficient around the annulus are uniform across the span. The radial velocity coefficient supports this conclusion: there is no variation around the annulus and it has a value close to zero across the entire span. This shows that there is very little radial redistribution of the flow occurring. The spanwise distribution of absolute yaw angle is also constant around the annulus so that at this location, although there is a non-uniform circumferential distribution of flow coefficient, the stream tubes are close to parallel. Finally, the figures also show that the stagnation pressure coefficient across the span is uniform around the annulus. These results are observed at both operating points so at this measurement station the compressor operating point does not affect the circumferential or spanwise distributions of the flow.

6.3.2 Upstream of the slot

The contours of flow coefficient in Figs. 6.17(a) and 6.18(a) show that close to the off-take duct position the flow through the annulus, just upstream of the slot, is increased. Figure 6.17(b) and 6.18(b) show the pitch-averaged flow properties at this location with stage inlet flow coefficients $\overline{\phi_{stage}} = 0.43$ and $\overline{\phi_{stage}} = 0.38$. Here there is a circumferentially non-uniform flow coefficient distribution across the entire span although the circumferential redistribution is felt more strongly in the outer 50% of span. The radial velocity coefficient shows that close to the off-take duct position the radial component of the flow increases across the entire span with peak $V_r/U = 0.066$ for

$\overline{\phi_{stage}} = 0.43$ and $V_r/U = 0.060$ for $\overline{\phi_{stage}} = 0.38$, i.e. 15% of $\overline{\phi_{rig}}$ at both operating points. This effect is caused by the flow curving upwards due to the bleed extraction through the slot. The absolute yaw plots in Figs. 6.17(b) and 6.18(b) show that a circumferential variation in yaw angle occurs across the entire passage but the change is more pronounced in the outer 30% of span with a variation of up to 11 degrees near the casing. The circumferential distribution of yaw angle is the same as in Figs. 6.6(a) and 6.12(a) with an asymmetric circumferential distribution of flow angle about the off-take duct location. The reason for the variation in yaw angle given in the two-dimensional analysis is still valid: the change in flow angle is due to streamlines curving towards the low pressure region created by the peak in bleed non-uniformity close to the off-take duct location. As with the rig inlet location, Figs 6.17(b) and 6.18(b) show that the stagnation pressure coefficient across the span is constant around the annulus. At both operating points the variation in spanwise and circumferential distributions are qualitatively similar so the operating point of the compressor stage has little effect on the flow at this location.

6.3.3 Stage inlet

Figure 6.19(a) shows contours of flow coefficient at stage inlet for $\overline{\phi_{stage}} = 0.43$. The contour plot shows that before the off-take duct (i.e. at a negative circumferential position relative to off-take duct circumferential position) flow coefficient is reduced and after the off-take duct (i.e. at a positive circumferential position relative to off-take duct circumferential position) it is increased. This asymmetric distribution is also shown in Fig. 6.4(b) in the passage-averaged analysis. Figure 6.19(b) shows that the circumferential redistribution of the flow affects the entire span. The spanwise distribution of flow coefficient shows that before the off-take duct location the flow coefficient is reduced across the whole span with the reduction being greatest in the outer 30% of span. After the off-take duct location the flow coefficient is reduced in the outer 30% of span but in the rest of the passage the flow coefficient is increased.

The spanwise distributions of radial velocity coefficient show that in the vicinity of the off-take duct position there is a component of radial velocity across the entire span. This component increases in the outer 30% of the span as the flow is drawn into the bleed slot. The spanwise distributions of yaw angle in the absolute frame show that before the off-take duct position the yaw angle is increased and after the off-take duct it is reduced. This is similar to the yaw angle plot in Fig. 6.17(b), upstream of the slot, but the spread in yaw angle has increased, particular in the outer 20% of the span: there is a variation in flow angle of up to 22 degrees near the casing. This is because at this location the streamlines have been curved further by the low pressure region created by the discrete off-take duct. The reduced yaw angle after the off-take duct position is the reason for the increased flow coefficient across 70% of the span at this location. However, close to the bleed slot (in the outer

30% of the span) the reduction in mass flow, due to the bleed extraction, dominates the local turning of the flow so the flow coefficient in this region is reduced.

The spanwise distribution of yaw angle in the rotor relative frame depends on the flow coefficient and the absolute yaw angle. The fourth plot in Fig. 6.19(b) shows how relative yaw changes with span and circumferential location relative to the off-take duct. At this operating point the circumferential variation in absolute yaw angle appears to be the dominant influence on the relative yaw angle: the passages with the lowest absolute yaw angle have the lowest relative yaw angle, even though these passages do not have the lowest flow coefficient. Figure 6.19(b) also shows that the stagnation pressure coefficient from about 10% to 80% of span is constant around the annulus. However, in the passages close to the off-take duct position the stagnation pressure coefficient is increased close to the casing and slightly reduced close to the hub. Close to the off-take duct, where the local bleed rate is highest, the casing boundary layer is drawn into the bleed slot so that the stagnation pressure coefficient is increased. At the hub, however, the streamline curvature means that there is an adverse pressure gradient which thickens the hub boundary layer.

Figure 6.20 shows the flow field at stage inlet for $\overline{\phi_{stage}} = 0.38$. The spanwise distributions of radial velocity coefficient, absolute yaw angle and stagnation pressure coefficient are qualitatively similar to those in Figure 6.19(b). However, the spanwise distribution of flow coefficient around the annulus has changed. The variation in flow coefficient is less asymmetric about the off-take duct location with the traverses close to the off-take duct having the greatest reduction in flow coefficient in the outer 50% of span. This change in circumferential flow coefficient distribution can be seen in Fig. 6.10(b) in the two-dimensional analysis. The reduced flow coefficient and reduced absolute yaw angle before the off-take duct result in a reduced relative yaw angle across the entire span. The reduction in relative yaw angle is greatest close to the casing and Figure 6.21 shows pitchwise-averaged relative yaw angle distribution at 97.6% of span (i.e. the last radial measurement location in the area traverse) against circumferential position relative to the off-take duct for $\overline{\phi_{stage}} = 0.38$. The peak change in relative yaw angle at the tip is 2.0 degrees, which is twice that measured using the passage-averaged values shown in Fig. 6.14(b) and re-plotted here with a dashed line. The reasons for the increase in rotor incidence at the tip are the same as those given in Section 6.2, i.e. near stall the non-uniform bleed causes a region of reduced flow coefficient and reduced absolute yaw angle which combine to create a region of increased rotor incidence. The three-dimensional analysis shows that the spanwise redistribution of the flow enhances these effects near the casing. This is particularly relevant when considering the effect of non-uniform bleed on stall because spike-type stall inception is initiated by an incidence-induced separation at the rotor tip leading edge [35].

6.3.4 Downstream of rotor row

Figure 6.22(a) shows contours of flow coefficient downstream of the rotor row at $\overline{\phi_{stage}} = 0.43$. There is an asymmetric circumferential distribution of flow coefficient which was observed in the two dimensional analysis in Fig. 6.4(c). Figure 6.22(b) shows this circumferential distribution of flow coefficient and also shows that the non-uniformity has been redistributed so that changes in the circumferential direction are close to uniform across the span. The spanwise distribution of radial velocity distribution is also uniform around the annulus. The yaw angle in the absolute and rotor relative frames vary circumferentially and the variation is constant across the span. A rotor passing around the annulus experiences an unsteady inlet flow due to the circumferential variation in the flow in the absolute frame at stage inlet. This unsteadiness is composed of high frequency changes due to the upstream IGV wakes (not important here) and a lower frequency variation due to the non-uniform bleed extraction. The reduced frequency is given by:

$$\kappa = \frac{c_x}{2\pi r_{mid}\phi_{stage}} \quad (6.1)$$

where c_x is axial rotor chord, r_{mid} is midspan radius and ϕ_{stage} is the stage flow coefficient. For the rotor at $\overline{\phi_{stage}} = 0.43$, $\kappa = 0.05$. This shows that the rotor response to changes in the upstream flow is quasi-steady and this explains why there is continues to be a circumferential variation in flow coefficient and rotor relative flow angle downstream of the rotor row.

At $\overline{\phi_{stage}} = 0.38$, Fig. 6.23 shows that there is a circumferential variation in flow coefficient and that the spanwise variation in flow coefficient is increased compared to the flow shown in Fig. 6.22 at the design operating point. The contour plot and spanwise flow coefficient distribution show that after the off-take duct location the (already large) rotor hub corner separation is increased and this leads to redistribution of the flow so that in the outer part of the span the flow coefficient is increased. This increased hub separation is due to the rotor incidence at stage inlet. The plot of relative yaw angle in Fig. 6.20 shows that, near the hub, rotor incidence just after the off-take duct location is increased. The increased rotor incidence in this region leads to an increased hub separation which is measured downstream of the rotor row. This result again demonstrates the quasi-steady response of the rotors, i.e. the increased hub separation only occurs in the region where upstream of the row there is increased rotor incidence, rather than being averaged around the entire annulus.

At both operating points there is a circumferential variation in stagnation pressure downstream of the rotor row because the region of flow with reduced flow coefficient operates further to the left on the rotor characteristic and therefore produces more total-to-total pressure rise.

6.3.5 Downstream of stator row

Downstream of the stator row at $\overline{\phi_{stage}} = 0.43$, Fig. 6.24 shows that there is still a circumferential variation in flow coefficient which has been evenly redistributed across the span. There is little variation in the radial velocity coefficient in either the spanwise or circumferential direction and its value is close to zero. As expected with a constant area downstream annulus and decoupled throttle the exit yaw angle in the absolute frame, shown in Fig. 6.24(b), is circumferentially uniform across the span. The circumferential variation in yaw angle in the relative frame is therefore due to the variation in flow coefficient around the annulus.

At $\overline{\phi_{stage}} = 0.38$ the contour plot and spanwise distribution of flow coefficient (note the change in scale on the x-axis) in Fig. 6.25 show that there is a large stator hub corner separation. Figure 6.25(b) shows that there is an increase in the radial velocity component in the outer 40% of span around the entire annulus. This is due to the streamlines curving around the large region of blockage created by the separation. Like the rotor hub corner separation discussed above, there is a circumferential variation in the size of the hub separation and this is created by the variation in incidence angle upstream of the stator row. As expected the largest stator hub corner separation occurs where the stator incidence near the hub is highest, in the region close to the off-take duct location (see plot of yaw angle in the absolute frame in Fig. 6.23(b)).

At both operating points a circumferential variation in stagnation pressure coefficient is still present downstream of the stator row. This can be seen by comparing Figs 6.22(b) and 6.24(b) and Figs 6.23(b) and 6.25(b) where the loss through the stator row, especially close to the hub, reduces the stagnation pressure coefficient but does not affect the circumferential distribution.

The variation in flow coefficient with circumferential position, and the near constant exit flow angle in the absolute frame, mean that downstream of the stator row there is a non-uniform distribution of yaw in the relative frame. Figure 6.25(b) shows that this circumferential variation varies across the span. The passages close to the off-take duct position have a reduced relative yaw angle of up to 4 degrees in the lower 70% of span and increased relative yaw angle of up to 2 degrees in the outer 30% of span. The performance of a stage downstream of the stator row would be affected by this circumferential and spanwise redistribution of rotor incidence. However, the downstream stage would also change the conditions at this point in the flow so it is not clear from these single-stage tests what affect non-uniform bleed has on further downstream stages. These results, however, suggest that the increase in rotor incidence for a further downstream stage will occur close to the hub, rather than near the rotor tip. This means that the operating range of the second stage will be less affected by circumferentially non-uniform flow than the first stage, assuming that stall in the second stage also originates from an incidence-induced separation near the rotor tip, i.e. it stalls with “spikes”. The

effect of the near hub increase in incidence could be important however, and further work is suggested on non-uniform bleed in a multistage environment.

6.3.6 Summary

This section shows that close to the bleed slot (upstream of the slot and at stage inlet) the bleed extraction results in a spanwise redistribution of the flow which is not captured by the passage-averaged analysis. However, the important interaction between the main annulus flow and the non-uniform bleed extraction, explained in Section 6.2 in terms of streamlines in a two-dimensional flow, is still the key mechanism driving the circumferential distribution of flow in three-dimensions.

The coupling of the downstream stage to the main annulus flow is more complicated in three-dimensions but the conclusion that non-uniform bleed extraction creates a region of increased rotor incidence at stage inlet, which then causes the stage to stall earlier, still holds. However, the pitch-averaged analysis shows that the effect of non-uniform bleed extraction on the flow at stage inlet is felt most strongly near to the casing. This exacerbates the effect of non-uniform bleed on operating range by increasing the rotor incidence in the tip region.

Downstream of the rotor and stator rows there is circumferential variation in the flow coefficient and relative yaw angle distributions. At the design operating point the circumferential redistribution is close to uniform across the span. However, near to stall, there are rotor and stator hub separations which vary in size around the annulus. This aspect of the flow is important in determining the effect of bleed on the next downstream stage and can only be captured by considering the three-dimensional flow with a pitch-averaged analysis.

6.4 Efficiency

The effect of non-uniform bleed on efficiency is investigated in this section. A number of different bleed system configurations are tested with different plenum chamber size, off-take duct number and (where relevant) off-take positions relative to each other. The peak overall efficiency is compared for these different cases and then the effect on stage efficiency and bleed system loss are studied separately.

6.4.1 Overall efficiency

Figure 6.26 shows the peak overall efficiency plotted against bleed rate, for cases with different bleed system configurations. Reducing the number of off-take ducts from four to one with the large plenum chamber has a negligible effect: the difference in peak overall efficiency between these two cases is less than 0.2% points for the bleed rates tested. For the cases with one off-take duct, Fig. 6.26 shows that reducing plenum size reduces the overall peak efficiency of the compressor and bleed

system. Efficiency is also reduced further as bleed rate is increased. With a bleed rate of 6.23% the case with one off-take duct and the small plenum chamber has a peak overall efficiency 8.8% points lower than the uniform bleed rate case at the same bleed rate.

6.4.2 Stage efficiency

As with the efficiency analysis in Chapter 5 on Uniform Bleed, it is helpful to separate compressor stage efficiency and the losses due to the flow through the bleed system. Figure 6.27 shows peak stage efficiency plotted against stage inlet flow coefficient for the same cases as above. Stage efficiency is calculated using Equation 3.14 with the annulus area-averaged values for \dot{m}_{in} , $\psi_{stage,t-s}$ and α_{exit} . These values would be better mass-averaged but this data is not available for the efficiency characteristics. The effect of reducing the number of off-take ducts from four to one, with the large plenum chamber, is negligible: the difference in peak stage efficiency is less than 0.1% for the bleed rates tested.

It is shown by Sections 6.2 and 6.3 that for the small plenum chamber, one off-take duct case, non-uniform extraction of bleed results in non-uniform flow entering the downstream stage. This means that the local operating point around the compressor varies and is moved away from the peak of the efficiency characteristic. The overall peak efficiency is therefore reduced as the flow entering the stage becomes more non-uniform. This effect can be seen Fig. 6.27; with a bleed rate of 6.23% the small plenum chamber, one off-take duct case has a peak efficiency 0.5% points lower than the uniform bleed rate case at the same bleed rate.

6.4.3 Bleed system loss

Although there is a small reduction in stage efficiency as the plenum size is reduced the large drop in overall efficiency is mainly due to increased loss in the bleed system. The change in efficiency due to the bleed system is defined for uniform bleed in Equations 5.1 and 5.2. These equations can still be used with the correction factors calculated for uniform bleed because Figs. 6.17(b) and 6.18(b) show that the stagnation pressure upstream of the slot does not vary around the annulus. Figure 6.28 shows the change in efficiency due to loss in the bleed system against stage inlet flow coefficient for different bleed system configurations with a bleed rate of 4.14%. As with the uniform bleed case throttling the compressor reduces the loss because the absolute bleed rate (in kg/s) through the bleed system is reduced. Reducing the number of bleed off-take ducts from four to one with the large plenum chamber only increases the loss in efficiency by 0.1% points at the operating point with peak overall efficiency. For the cases with one off-take duct, reducing the plenum chamber size significantly increases the loss due to the bleed system; for the small plenum chamber with one off-take duct and bleed rate of 4.14%, the loss in efficiency due to the bleed system is 3.4% points at the operating point with peak overall efficiency.

A loss coefficient for the bleed system, Y_p , is defined in Equation 5.3 for uniform bleed. The numerator in Y_p is the same as that in Equation 5.2, but negative, so the correction factors calculated for uniform bleed can be used. The denominator in Y_p is the dynamic head of the bleed flow just before it enters the bleed system. This value varies around the annulus due to the non-uniform static pressure field associated with the non-uniform bleed extraction. To simplify the analysis the annulus-average dynamic head is used and it is assumed that this is still given by the correction factors calculated for uniform bleed.

Figure 6.29 shows Y_p plotted against stage inlet flow coefficient for different bleed system configurations with a bleed rate of 4.14%. With the large plenum chamber, Y_p increases slightly as the number of ducts are reduced from four to one. It increases significantly as the plenum chamber size is reduced. Like the uniform bleed cases, Y_p is close to constant across the operating range of the compressor for each different configuration. Figure 6.30 shows the average loss coefficient across the compressor operating range, $\overline{Y_p}$, against bleed rate for different bleed system configurations. This shows that for all bleed rates tested the loss coefficient increases as the number of ducts or the plenum chamber size is reduced. It can also be seen that the increase in loss is greater as bleed rate increases.

Figure 6.2 shows that with the small plenum chamber and one off-take duct the local bleed rate in the bleed slot is highly non-uniform; the peak local bleed rate is 22.9% but in much of the bleed slot the local bleed rate is close to 0%. As the plenum chamber size and the number of off-take ducts are reduced, the velocities of the flow in the bleed system become more circumferentially non-uniform. The details of the flow in the bleed system are not studied experimentally in the current work. However, in Chapter 7, a full annulus CFD calculation is presented for the case with the small plenum chamber, one off-take duct and a bleed rate of 4.14%. This shows that the flow is complicated; there are large, separated vortices in the plenum chamber and bleed slot which get drawn, along with flow straight out of the bleed slot, into the off-take duct. Here, a simple model of the bleed system is required, however, and so the local velocity in the bleed slot is chosen to characterise the non-uniformity of the bleed flow. Assuming that specific loss is proportional to the characteristic velocity squared [53], the mass averaged specific loss is given by:

$$\text{Specific Bleed System Loss} \propto \frac{\int_0^{2\pi} 2\pi r \rho h V_s^3 d\theta}{\int_0^{2\pi} 2\pi r \rho h V_s d\theta} \quad (6.2)$$

where h is the height of the slot exit, r is the radius of the slot at exit and V_s is the local radial velocity in the bleed slot at a particular circumferential position, mass-averaged across the slot height. Equation 6.2 shows that loss increases non-linearly with the local slot velocity. This explains, qualitatively, why the loss increases as the bleed extraction becomes more non-uniform. V_s is not

measured in the current work, however it is assumed that V_s is proportional to the local bleed mass flow rate, $\dot{m}_{bl,loc}$. A parameter β can then be calculated from the experimental measurements:

$$V_s \propto \dot{m}_{bl,loc}$$

Therefore: $Specific\ Bleed\ System\ Loss \propto \frac{\int_0^{2\pi} \dot{m}_{bl,loc}^3 d\theta}{\dot{m}_{bl}}$

Also: $R_{bl,loc} = \frac{\dot{m}_{bl,loc}}{\dot{m}_{in}}$

And: $R_{bl} = \frac{\dot{m}_{bl}}{\dot{m}_{in}}$

So: $\beta = \frac{1}{R_{bl}} \int_0^{2\pi} R_{bl,loc}^3 d\theta \quad (6.3)$

where \dot{m}_{in} is the total mass flow at rig inlet and is assumed constant for a given $\overline{Y_p}$, \dot{m}_{bl} is the overall bleed mass flow rate, $R_{bl,loc}$ is the local percentage bleed rate in the slot, and R_{bl} is the overall percentage bleed rate.

Figure 6.31 shows β against $\overline{Y_p}$ for cases with different bleed rates, plenum chamber sizes, number of off-take ducts and for the two off-take duct cases, the circumferential separation between the ducts. As expected, the bleed system loss coefficient increases as the bleed extraction becomes more non-uniform. The best fit line provides a linear correlation between β and $\overline{Y_p}$ with a coefficient of determination, $R^2 = 0.91$.

This analysis of bleed system loss is constrained by the experimental data collected and this leads to two assumptions which may limit the accuracy of the analysis. First, the assumption that V_s is directly proportional to local bleed rate is an over simplification. The effective area of the bleed slot flow, and hence the slot velocity, depends on the size of the separation from the upstream wall of the slot. Leishman [15, Fig. 4.22] shows that the separation in an axisymmetric slot reduces in size as bleed rate is increased. This finding is reproduced in the current work with CFD and is presented in Chapter 7. A better correlation between $\overline{Y_p}$ and β might be achieved if V_s could be measured experimentally and used instead of local bleed rate. The second limiting assumption is that the change in loss is only due to change in the local bleed rate distribution in the bleed slot. This assumption is made because the velocities and losses in different parts of the bleed system cannot be split up given the experimental data available. An improved analysis might model the losses from different sources in the bleed system and correlate these to different characteristic velocities.

Despite these limitations the model described above is useful as it allows Y_p to be estimated with just the local bleed distribution in the slot. The loss through the bleed system can then be

estimated given Y_p and the annulus-averaged stagnation pressure and dynamic head at inlet to the bleed system control volume.

6.4.4 Summary

The overall efficiency of the compressor and bleed system is significantly affected by reduced plenum chamber size and off-take duct number. Non-uniform flow downstream of the bleed slot reduces the peak efficiency of the downstream stage by up to 0.5% points for the most non-uniform case tested, i.e. with the small plenum, one off-take duct and a bleed rate of 6.23%. More significant, however, is the increase in loss through the bleed system. For the most non-uniform case the bleed system loss is responsible for a drop of 8.3% points in peak overall efficiency. The reason for the increase in loss with increased bleed non-uniformity is that mass-averaged specific loss scales with velocity cubed. Loss, therefore, increases non-linearly as plenum chamber size and off-take duct number are reduced and the peak velocities in the bleed system increase. A model has been developed which allows the bleed system loss coefficient to be estimated given the local bleed rate distribution in the bleed slot.

6.5 Conclusions

Overall, this chapter has shown that non-uniform bleed has a negative impact on the operating range of the downstream stage and on the efficiency of the compressor and bleed system. The following conclusions can be drawn:

1. The non-uniform bleed extraction caused by a bleed system comprising of a small plenum chamber, one off-take duct and with a bleed rate of 4.14% increases stage inlet stalling flow coefficient by 3.0% compared to the uniform bleed case with the same bleed rate.
2. Non-uniform bleed extraction causes a circumferential redistribution of the main annulus flow upstream and downstream of the bleed slot. Non-uniform flow coefficient and yaw angle distributions occur due to the circumferentially non-uniform pressure field created by the bleed extraction.
3. The shape of the stage static-to-static pressure rise characteristic means that at the design operating point (and over much of its operating range) the compressor acts to reduce the non-uniformity of the flow at stage inlet.

4. At low flow coefficients (approaching stall) the stage static-to-static pressure rise coefficient is flat so the compressor cannot decrease the non-uniformity caused by the bleed extraction and at stage inlet there is a region of increased rotor incidence of up to 1.0 degree (passage-averaged). It is this region of increased rotor incidence which causes the downstream stage to stall at a higher annulus-averaged stage inlet flow coefficient.
5. A pitch-averaged analysis of the flow around the annulus, which captures variations in spanwise distribution of the flow, shows that the increase in rotor incidence close to the off-take duct position is up to 2.0 degrees near to the casing. This exacerbates the impact on operating range since incidence induced rotor tip separation is thought to initiate spike-type stall.
6. The non-uniform circumferential distribution of flow does not reduce the annulus-averaged pressure rise but the stage efficiency is reduced slightly; with a bleed rate of 6.23% the peak stage efficiency for the case with the small plenum chamber and one off-take duct is 0.5% points lower than the case with the large plenum chamber and four off-take ducts.
7. The reduction in efficiency due to loss in the bleed flow increases as the bleed flow becomes more non-uniform and the peak velocities increase; with the small plenum chamber, one off-take duct and a bleed rate of 4.14% the reduction in efficiency at $\phi_{stage} = 0.43$ is 3.3% points. A model has been developed which correlates the local bleed rate distribution with the bleed system loss coefficient.

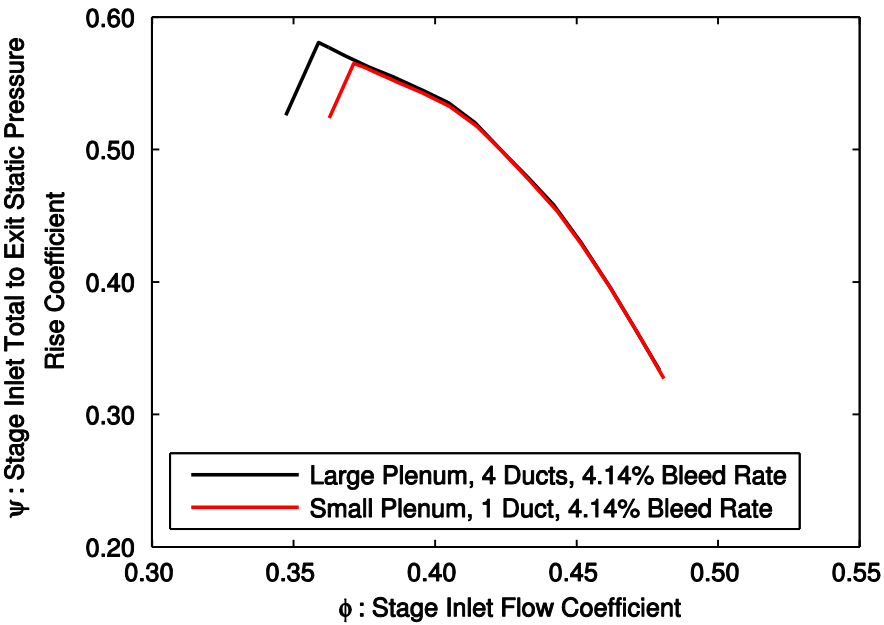


Figure 6.1: Stage inlet to stage exit total-to-static pressure rise characteristics for uniform and non-uniform bleed. The non-uniform bleed pressure-rise characteristic is obtained from the annulus-averaged flow quantities.

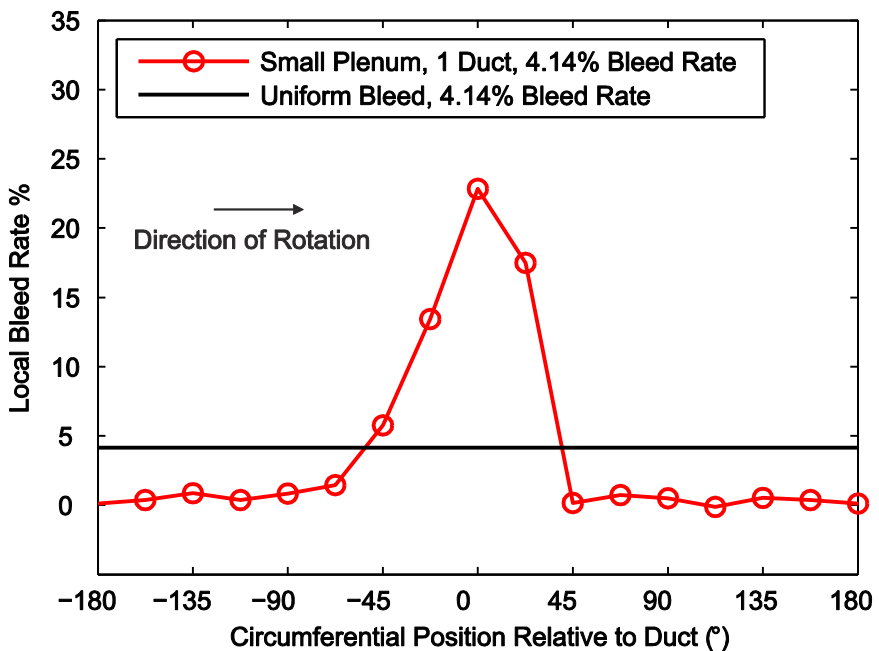


Figure 6.2: Local bleed rate distribution in bleed slot.

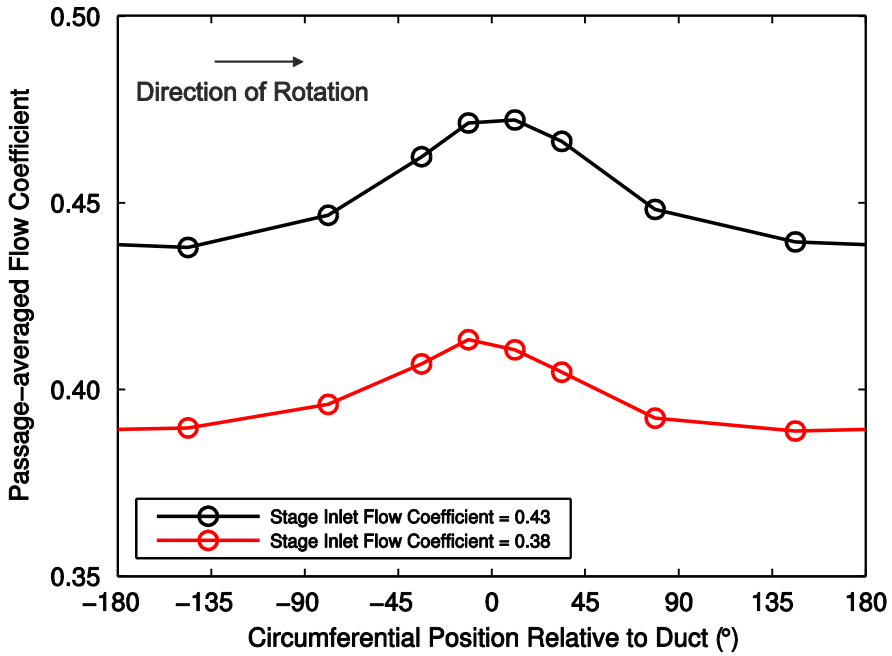


Figure 6.3: Circumferential distribution of passage-averaged flow coefficient at rig inlet.

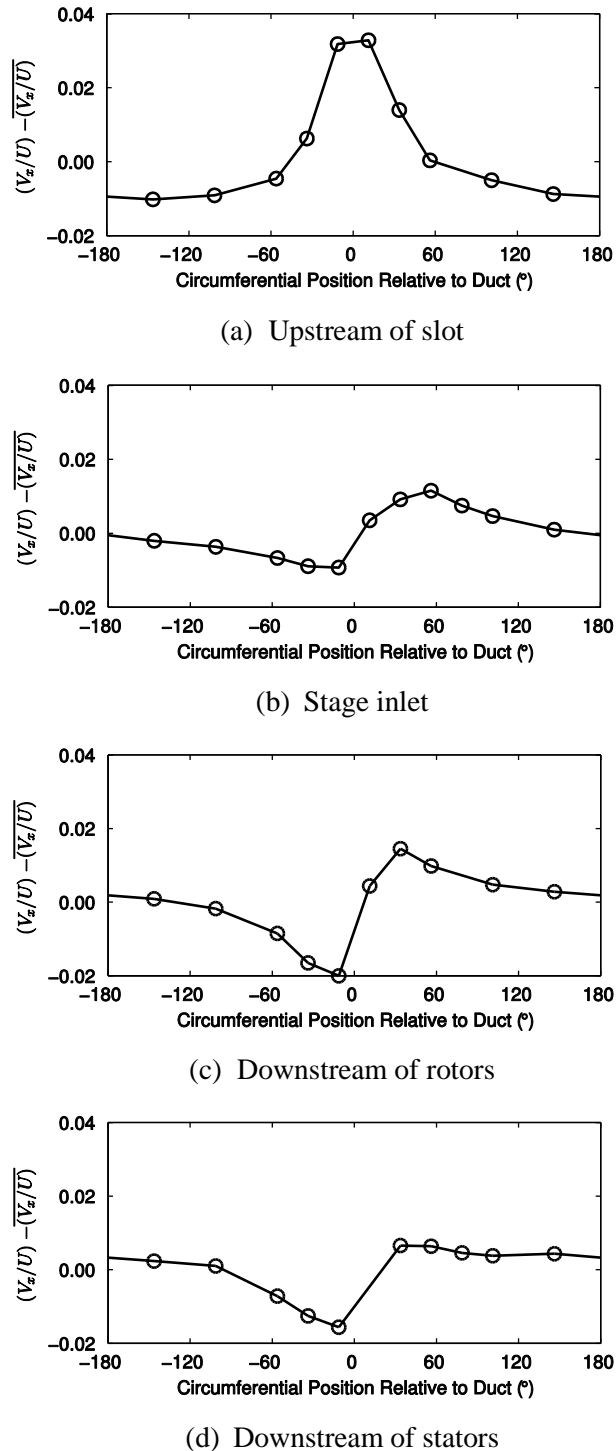


Figure 6.4: Change in passage-averaged flow coefficient compared to annulus-averaged value. $\overline{\phi_{stage}} = 0.43$.

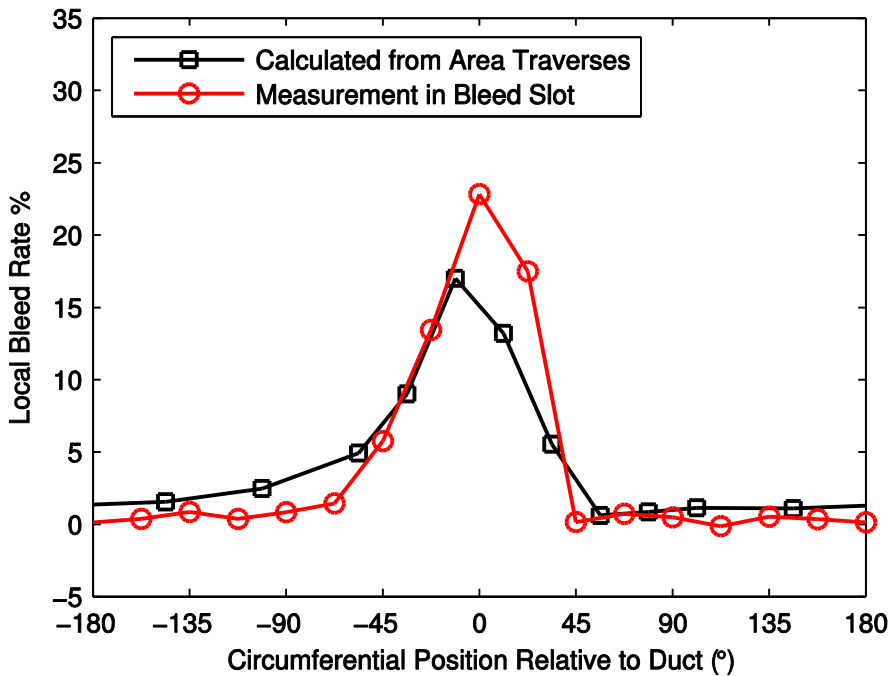
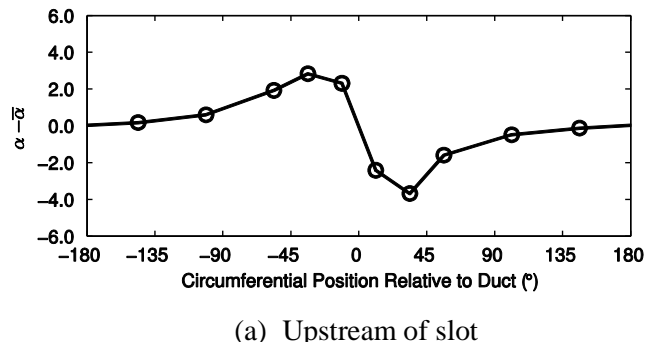
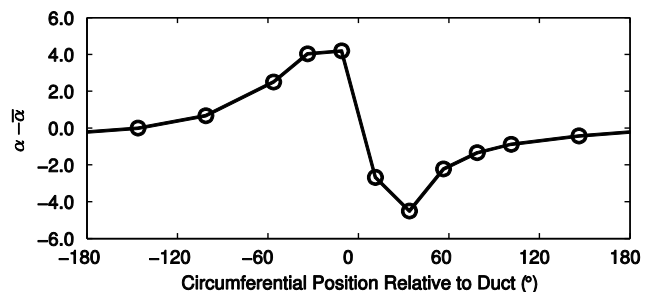


Figure 6.5: Comparison of bleed distribution measured in slot and derived from traverse data. $\overline{\phi_{stage}} = 0.43$.



(a) Upstream of slot



(b) Stage inlet

Figure 6.6: Change in passage-averaged yaw angle in the absolute frame compared to annulus-averaged value.

$$\overline{\phi_{stage}} = 0.43.$$

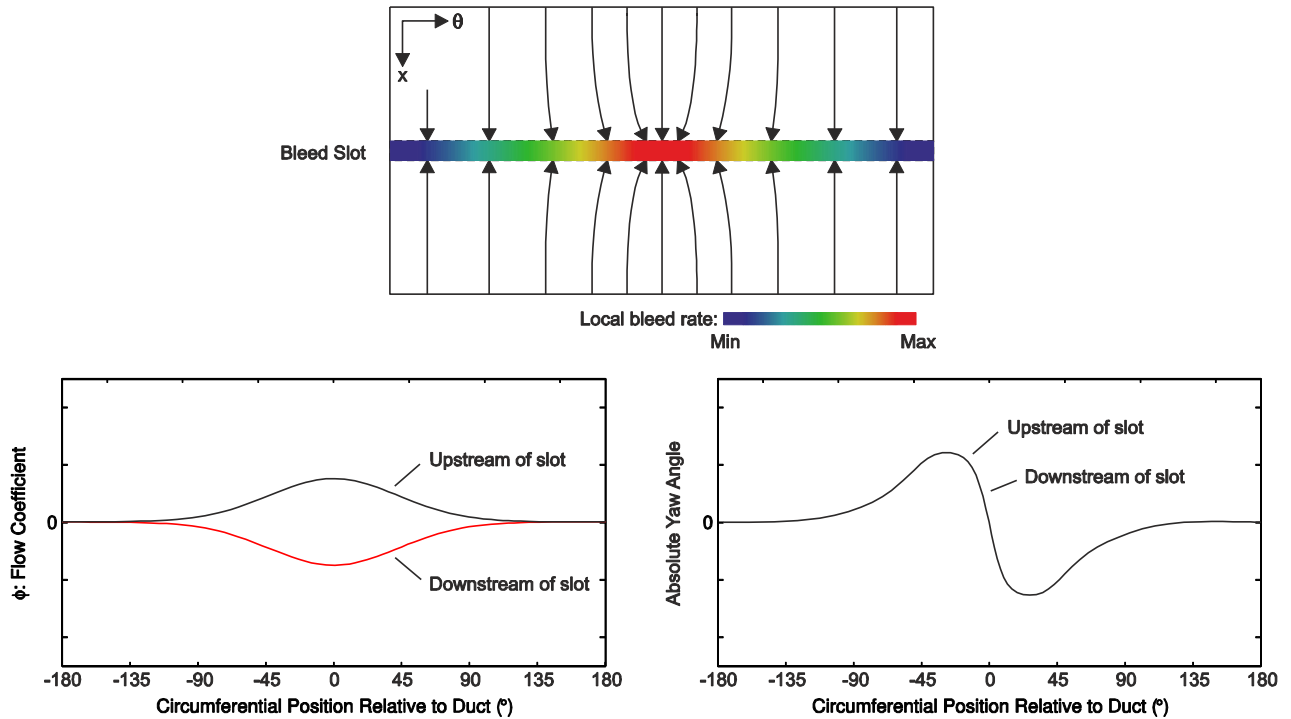


Figure 6.7: Flow schematic (top), flow coefficient distributions and absolute yaw angle distributions for isolated bleed extraction with no net main annulus flow.

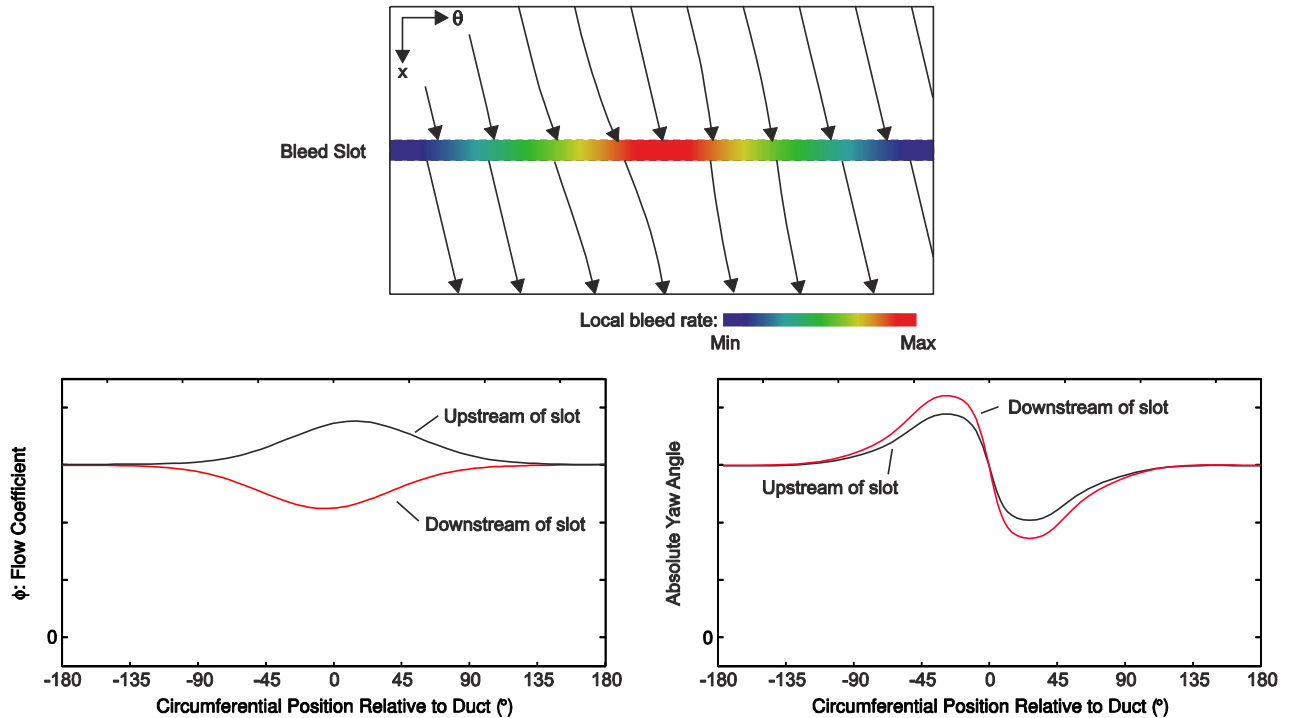
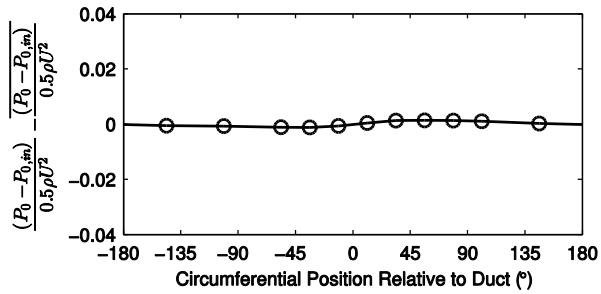
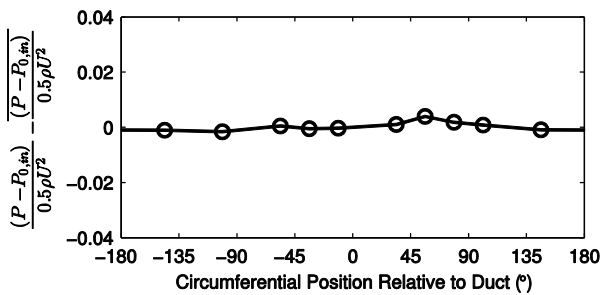


Figure 6.8: Flow schematic (top), flow coefficient distributions and absolute yaw angle distributions for bleed extraction with finite, swirling, main annulus flow.

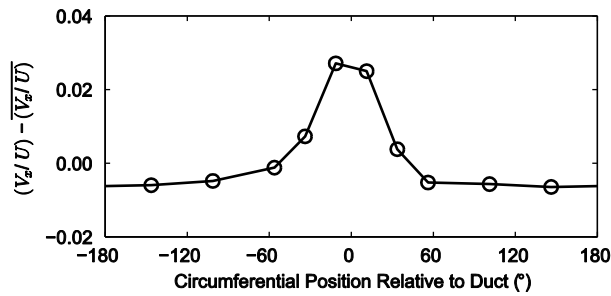


(a) Stagnation pressure at stage inlet

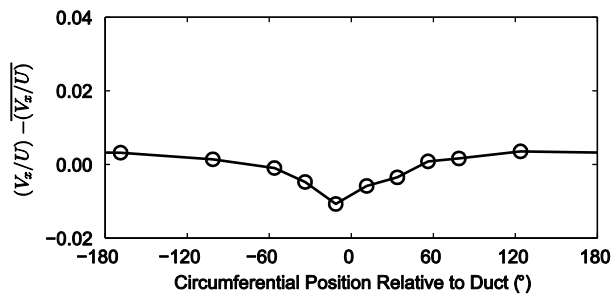


(b) Static pressure at stage exit

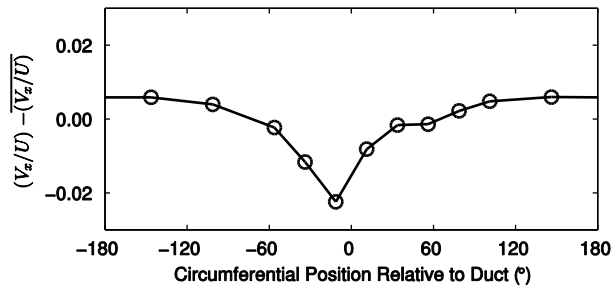
Figure 6.9: Change in passage-averaged pressure distribution compared to annulus-averaged value. $\overline{\phi_{stage}} = 0.43$.



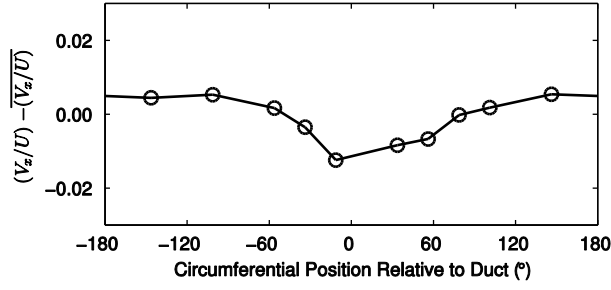
(a) Upstream of slot



(b) Downstream of slot



(c) Downstream of rotor



(d) Downstream of stator

Figure 6.10: Change in passage-averaged flow coefficient compared to annulus-averaged value. $\overline{\phi_{stage}} = 0.38$.

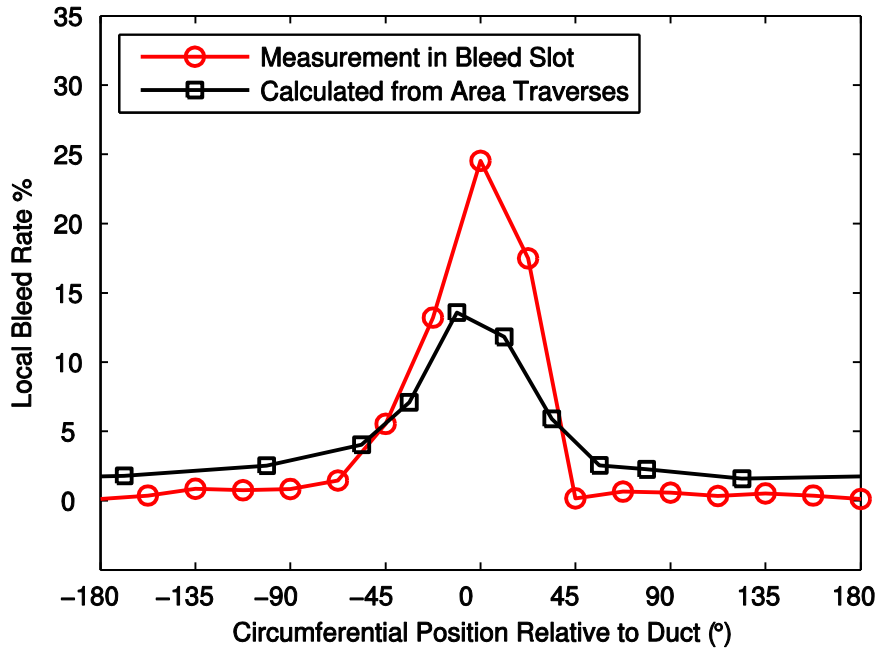
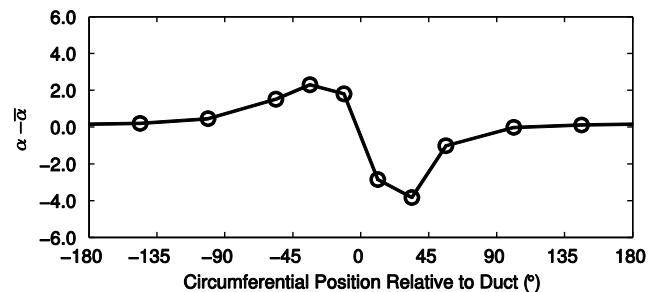
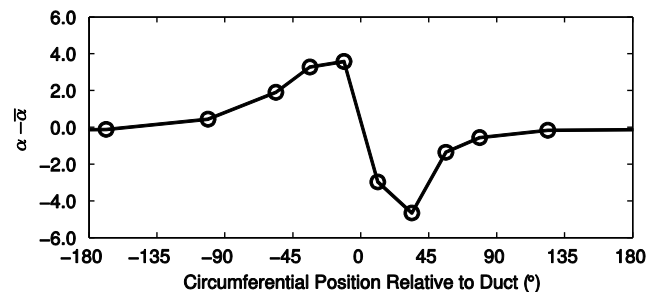


Figure 6.11: Comparison of bleed distribution measured in slot and derived from traverse data. $\overline{\phi_{stage}} = 0.38$.



(a) Upstream of slot



(b) Stage inlet

Figure 6.12: Change in passage-averaged yaw angle in the absolute frame compared to annulus-averaged value.

$$\overline{\phi_{stage}} = 0.38.$$

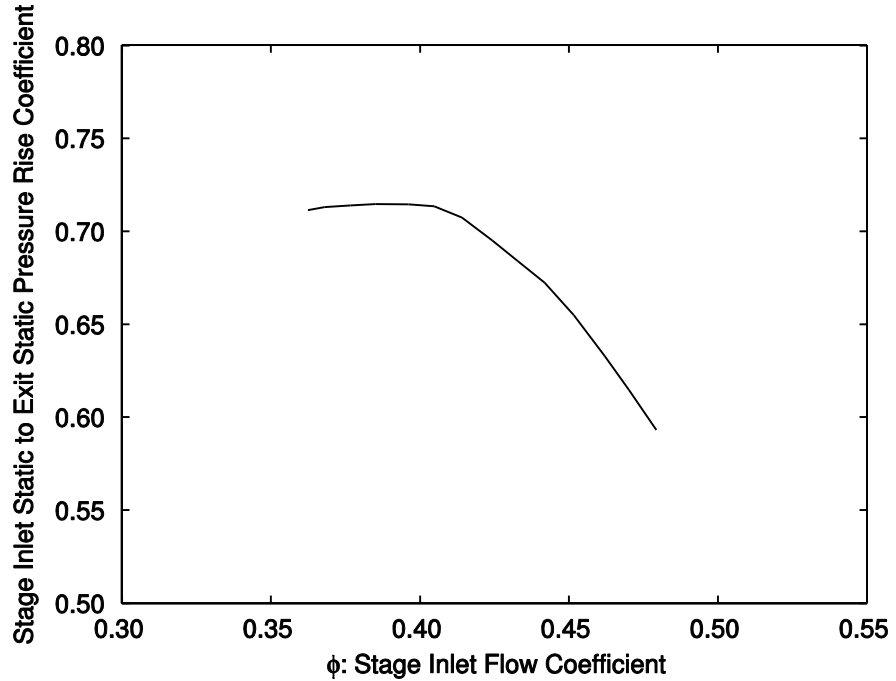
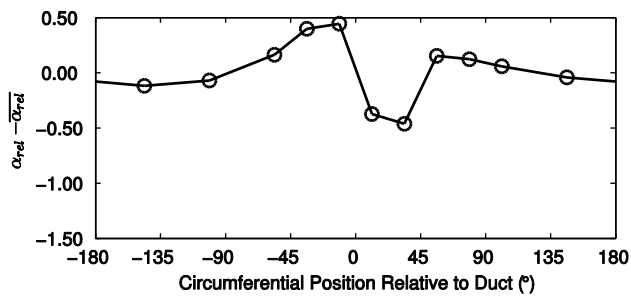
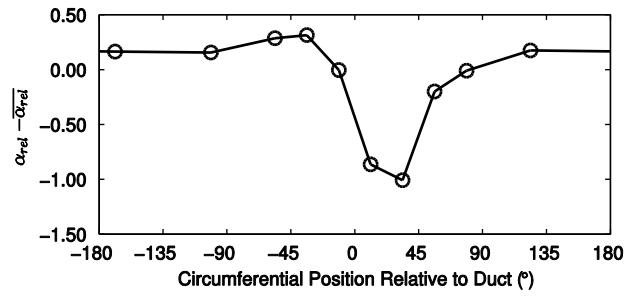


Figure 6.13: Stage inlet static-to-static pressure rise characteristic for uniform bleed case. Bleed rate = 4.14%.

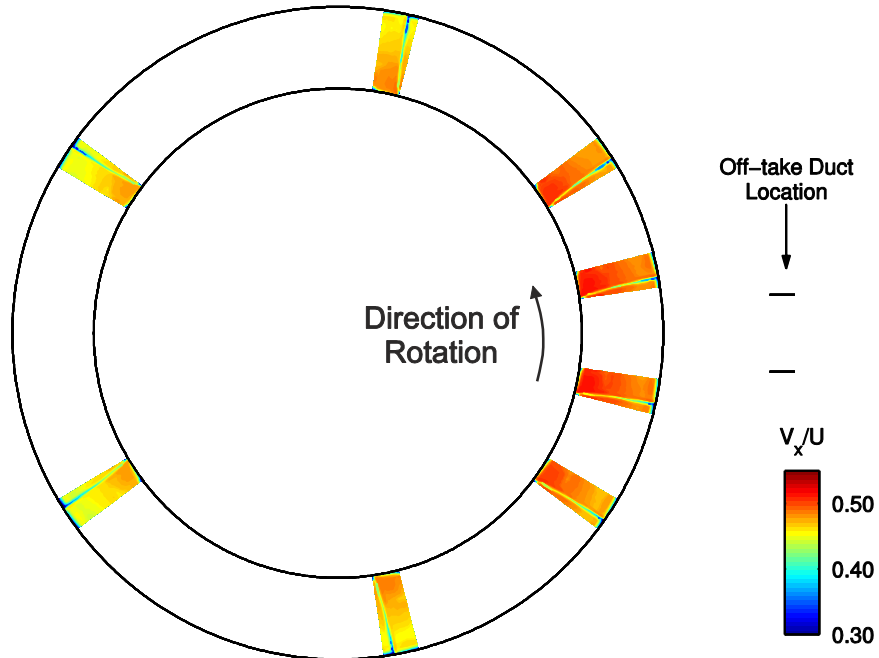


(a) Stage inlet flow coefficient, $\overline{\phi_{stage}} = 0.43$

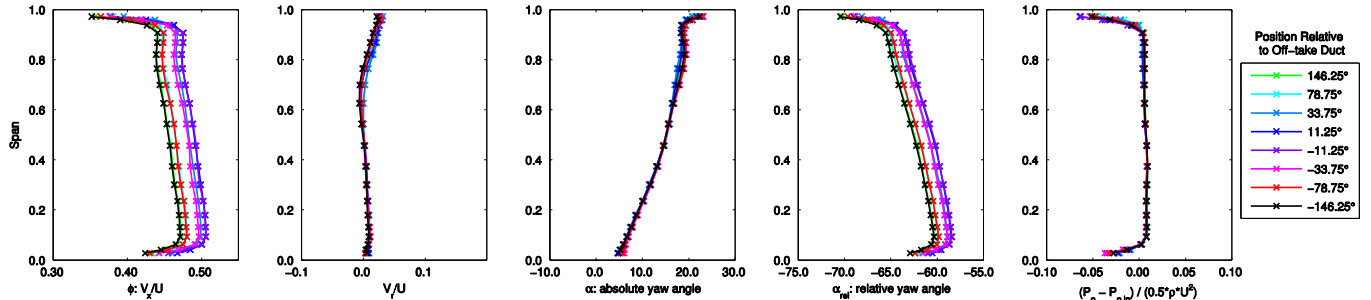


(b) Stage inlet flow coefficient, $\overline{\phi_{stage}} = 0.38$

Figure 6.14: Change in passage-averaged yaw angle in the rotor relative frame compared to the annulus-averaged value.

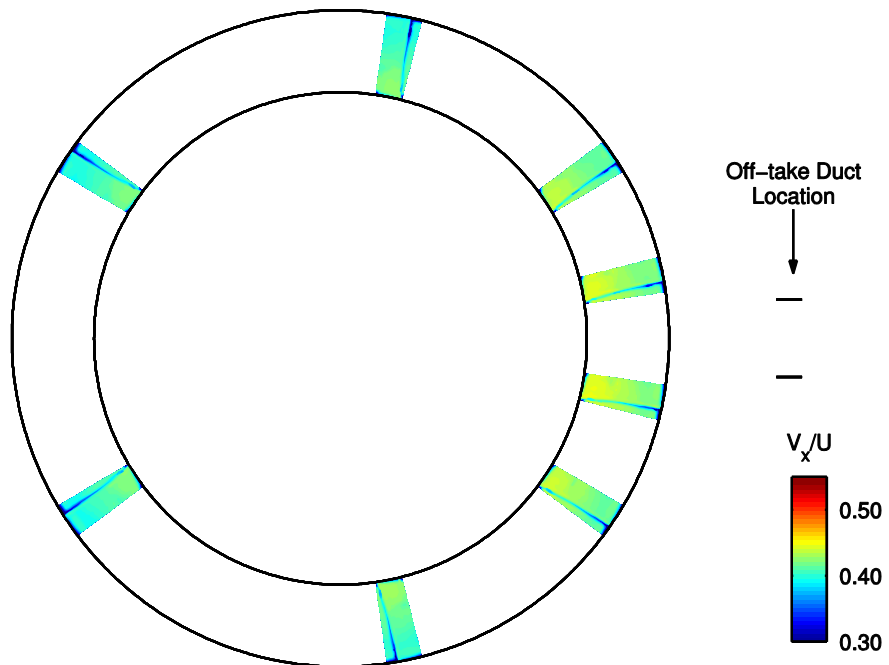


(a) Contours of flow coefficient

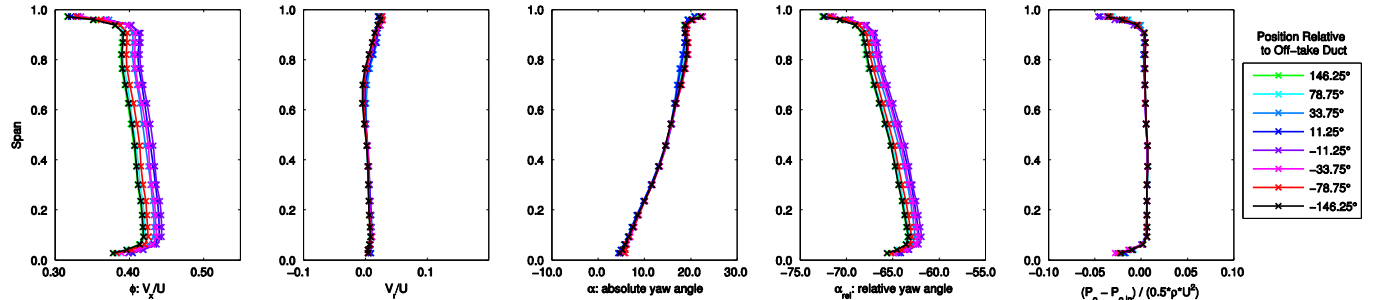


(b) Pitch-averaged, spanwise distributions

Figure 6.15: Flow field at rig inlet. $\overline{\phi}_{stage} = 0.43$.

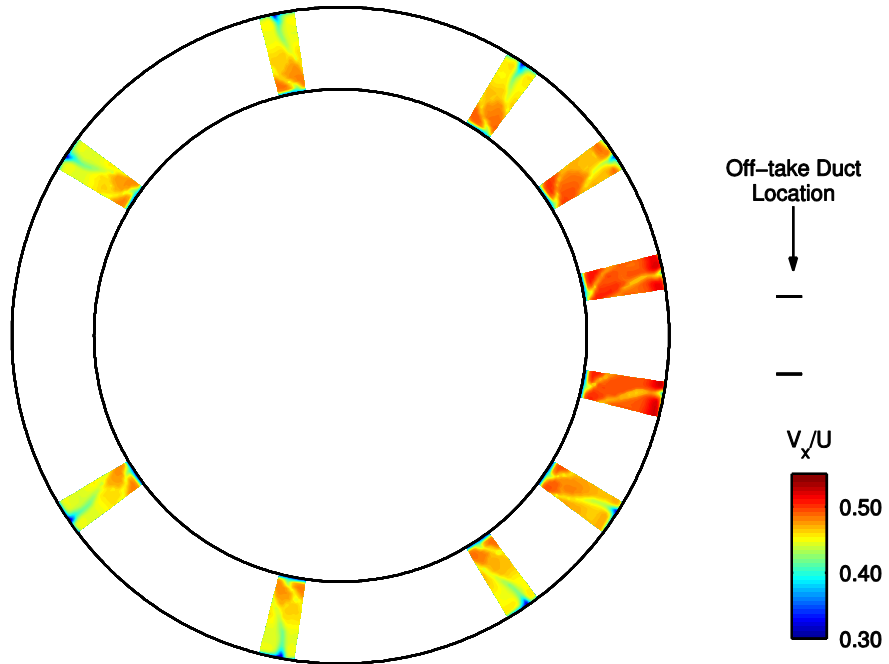


(a) Contours of flow coefficient

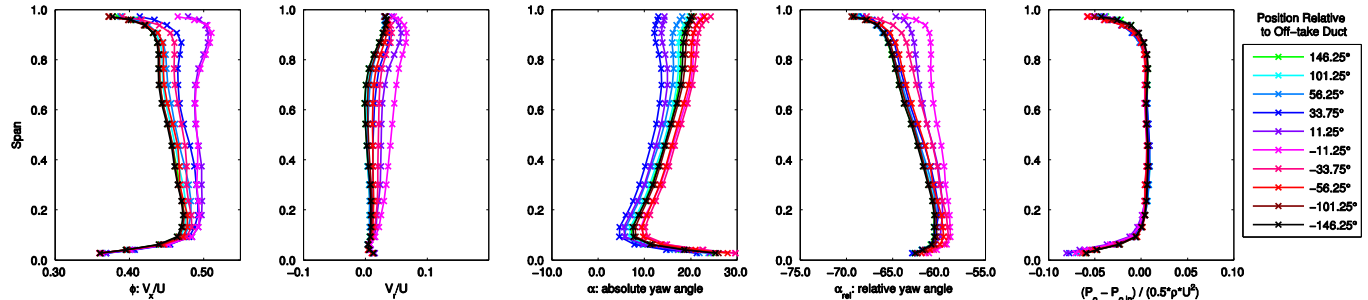


(b) Pitch-averaged, spanwise distributions

Figure 6.16: Flow field at rig inlet. $\overline{\phi_{stage}} = 0.38$.

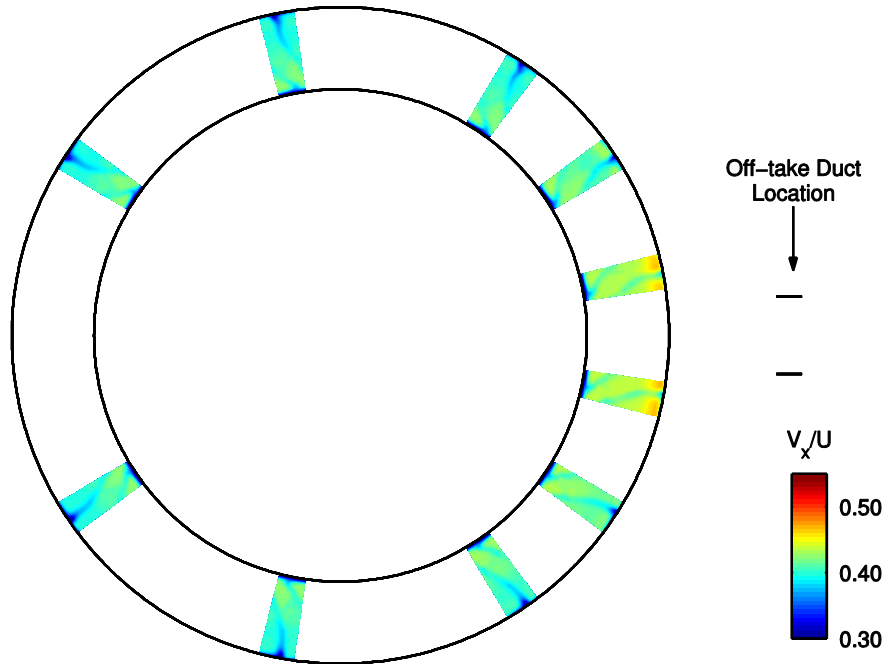


(a) Contours of flow coefficient

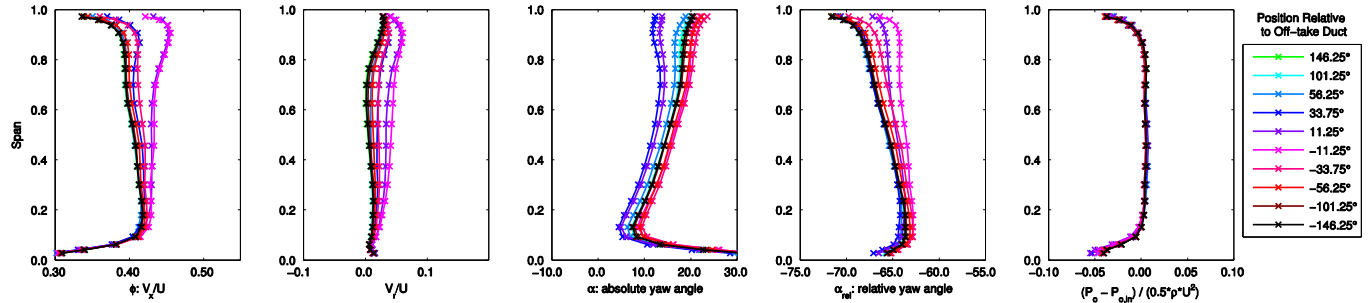


(b) Pitch-averaged, spanwise distributions

Figure 6.17: Flow field upstream of bleed slot. $\overline{\phi}_{stage} = 0.43$.

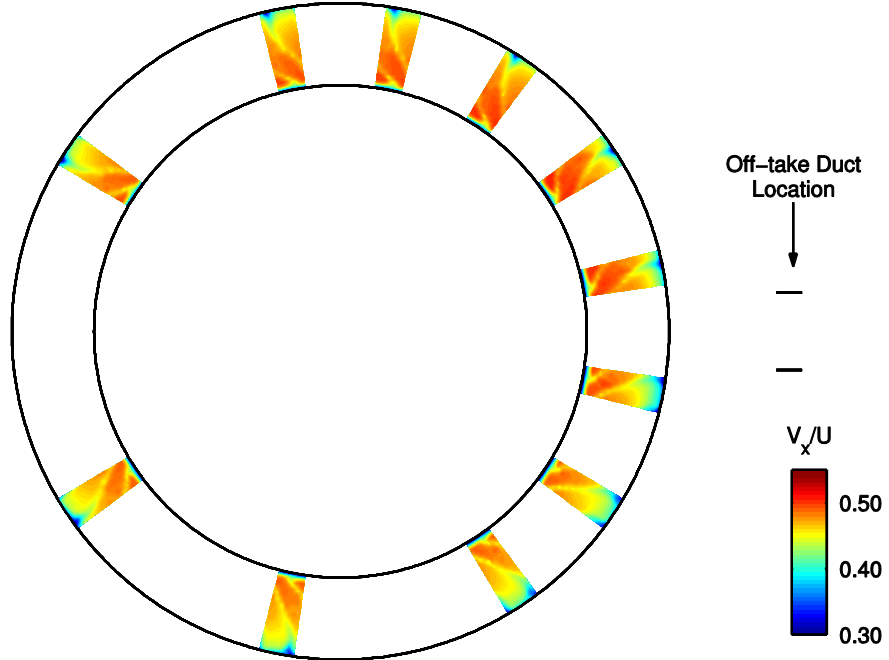


(a) Contours of flow coefficient

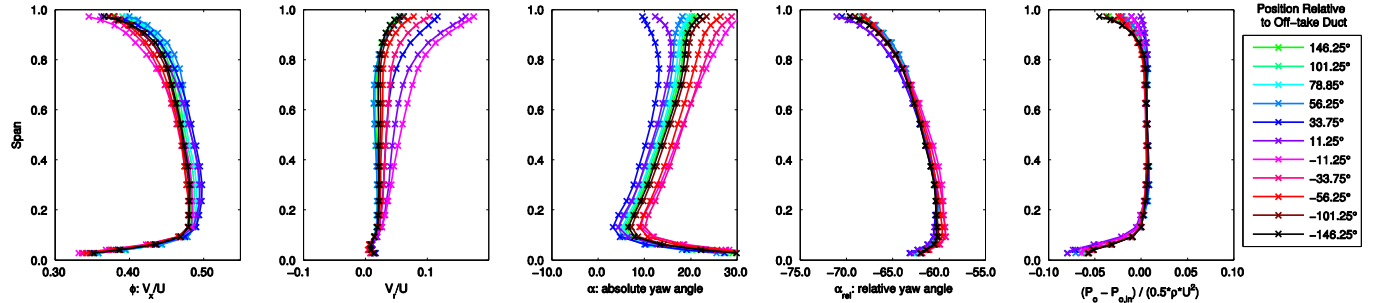


(b) Pitch-averaged, spanwise distributions

Figure 6.18: Flow field upstream of bleed slot. $\overline{\phi_{stage}} = 0.38$.



(a) Contours of flow coefficient



(b) Pitch-averaged, spanwise distributions

Figure 6.19: Flow field at stage inlet. $\overline{\phi}_{stage} = 0.43$.

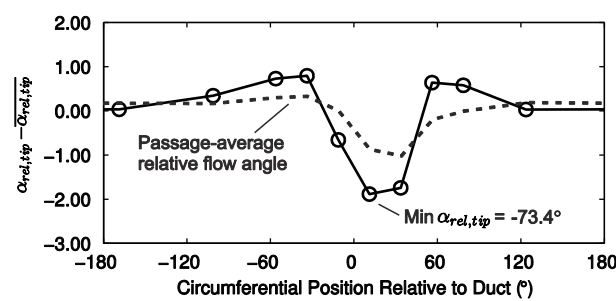
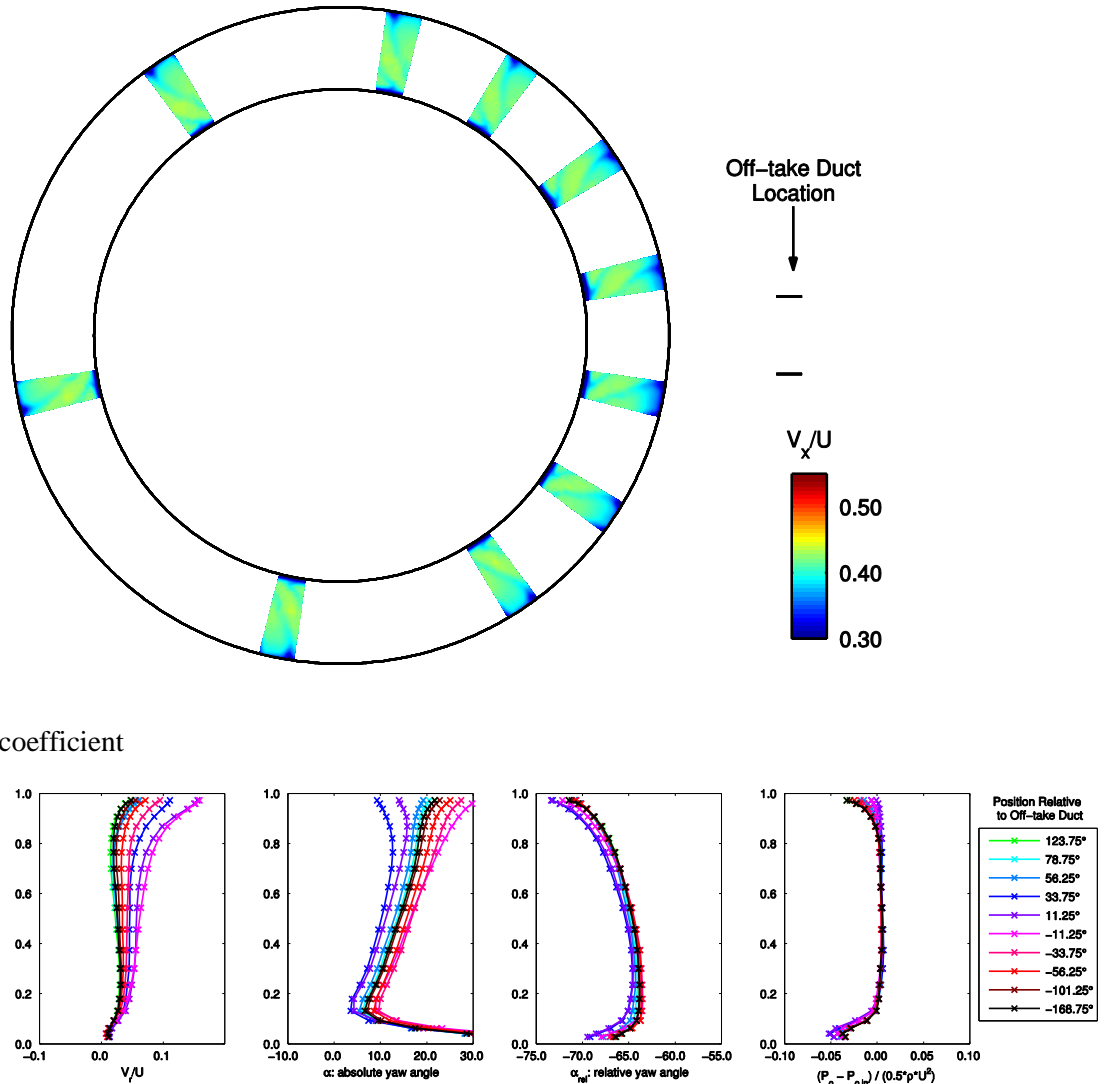
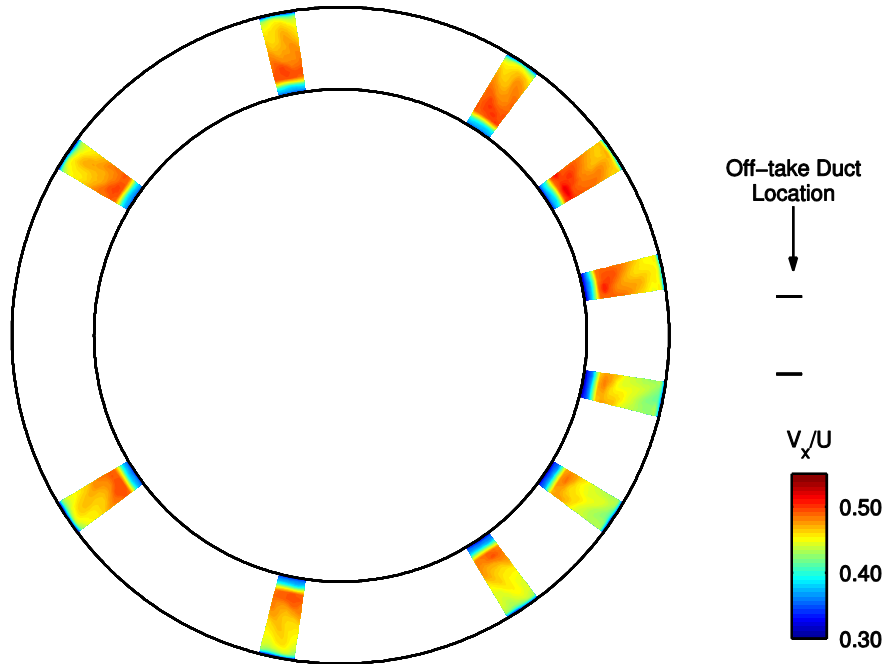
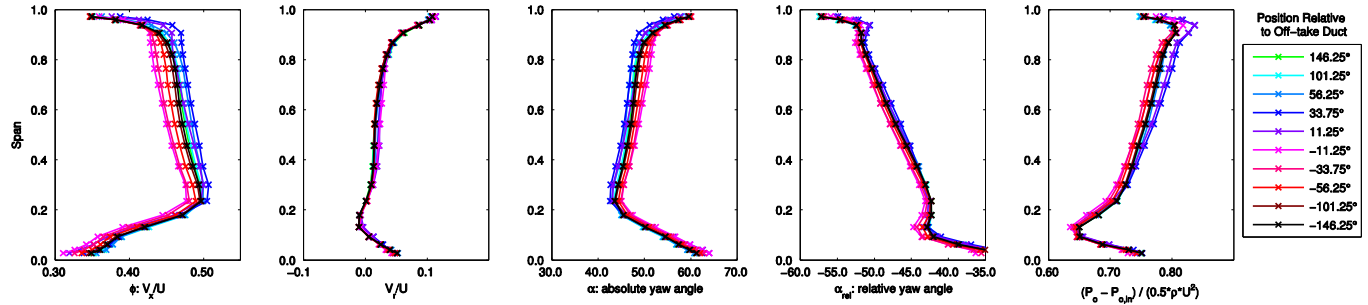


Figure 6.21: Change in pitch-averaged yaw angle in the relative frame at 97.2% of span compared to annulus-averaged value with $\overline{\phi_{stage}} = 0.38$.

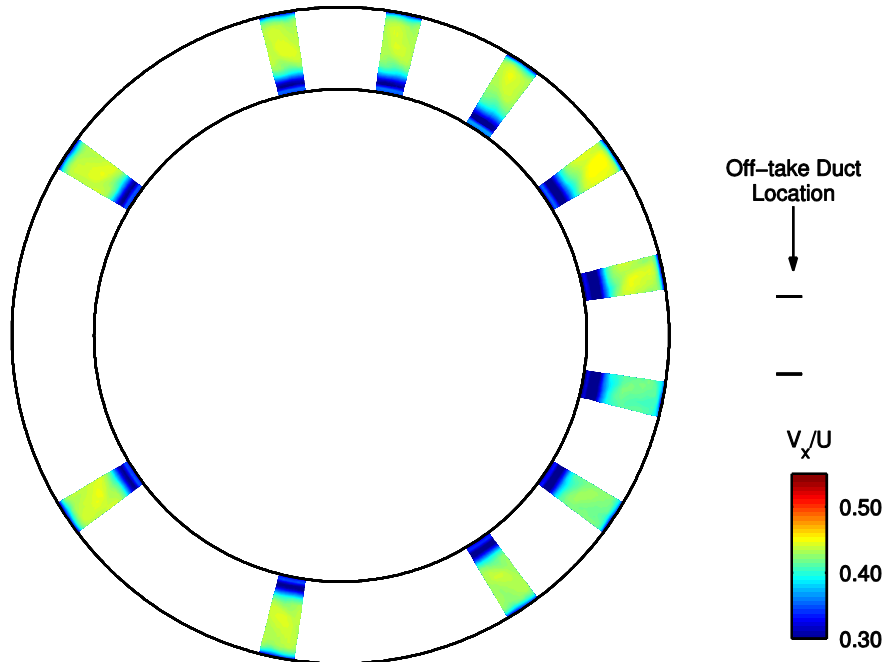


(a) Contours of flow coefficient

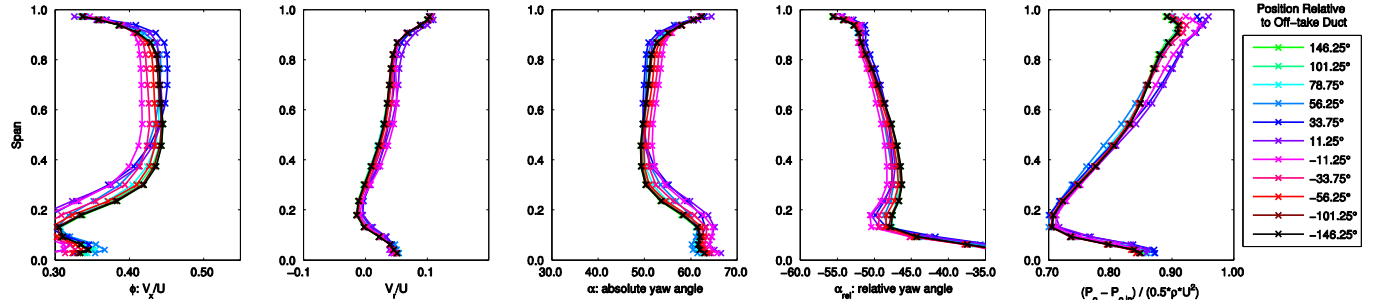


(b) Pitch-averaged, spanwise distributions

Figure 6.22: Flow field downstream of rotor row. $\overline{\phi}_{\text{stage}} = 0.43$.

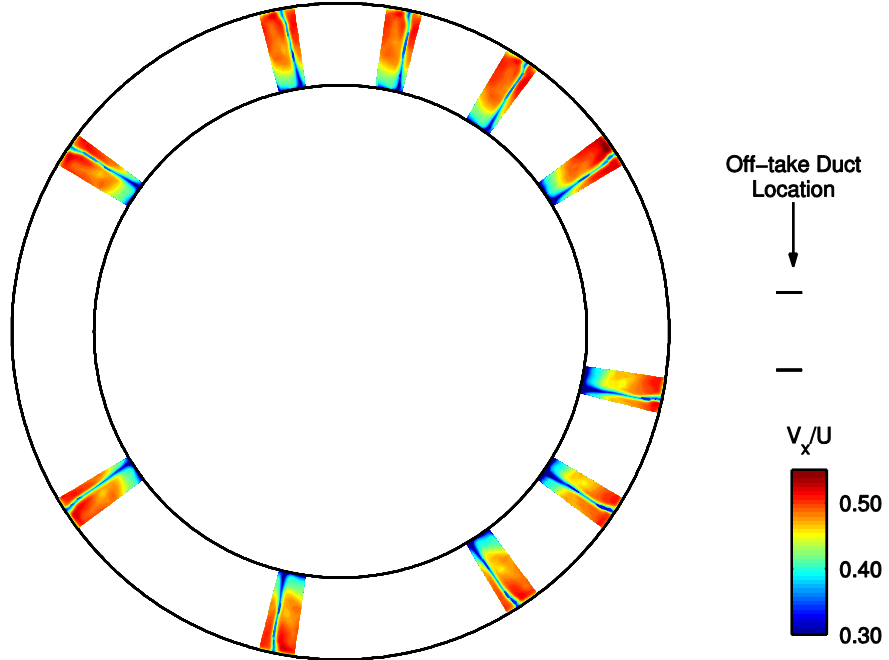


(a) Contours of flow coefficient

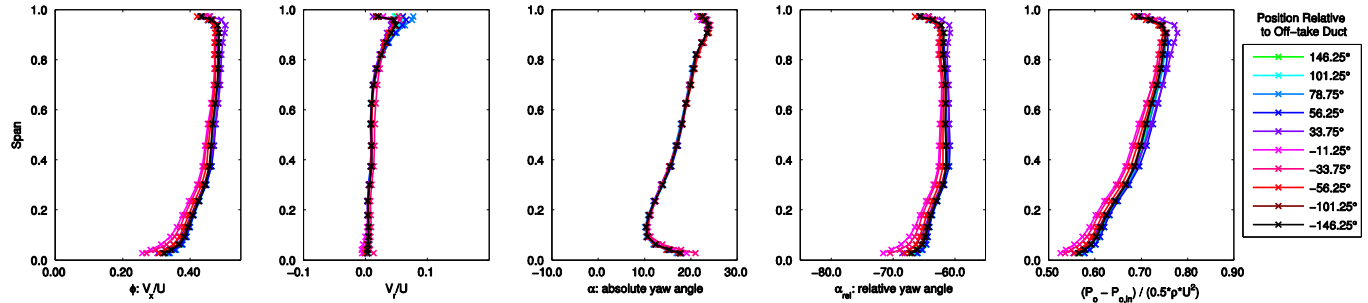


(b) Pitch-averaged, spanwise distributions

Figure 6.23: Flow field downstream of rotor row. $\overline{\phi_{stage}} = 0.38$.

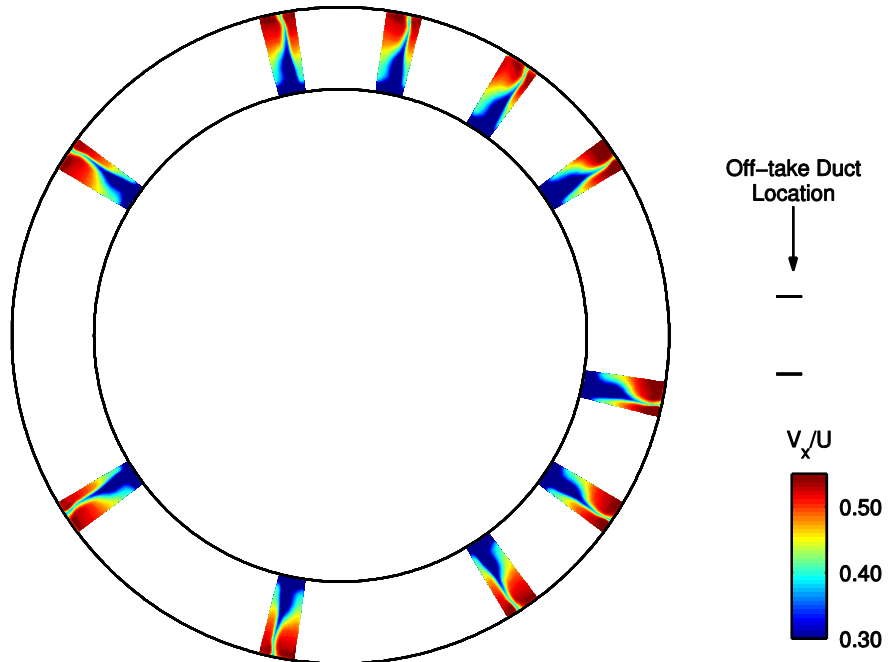


(a) Contours of flow coefficient

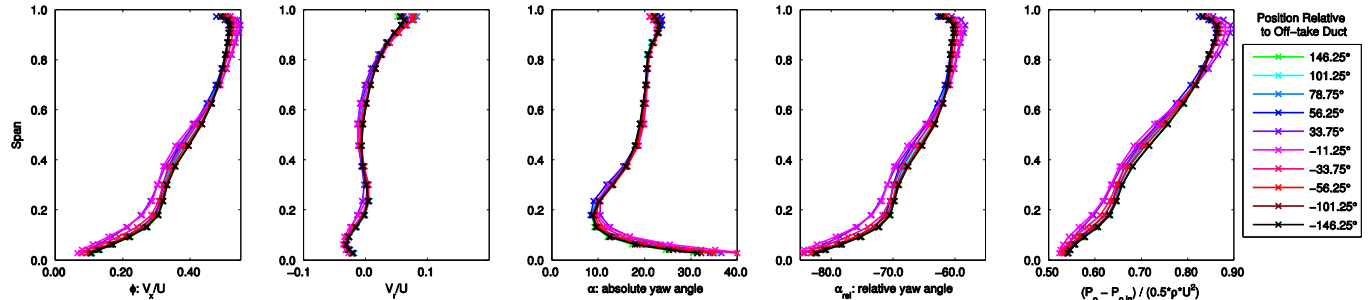


(b) Pitch-averaged, spanwise distributions

Figure 6.24: Flow field downstream of stator row. $\overline{\phi_{stage}} = 0.43$.



(a) Contours of flow coefficient



(b) Pitch-averaged, spanwise distributions

Figure 6.25: Flow field downstream of stator row. $\overline{\phi_{stage}} = 0.38$.

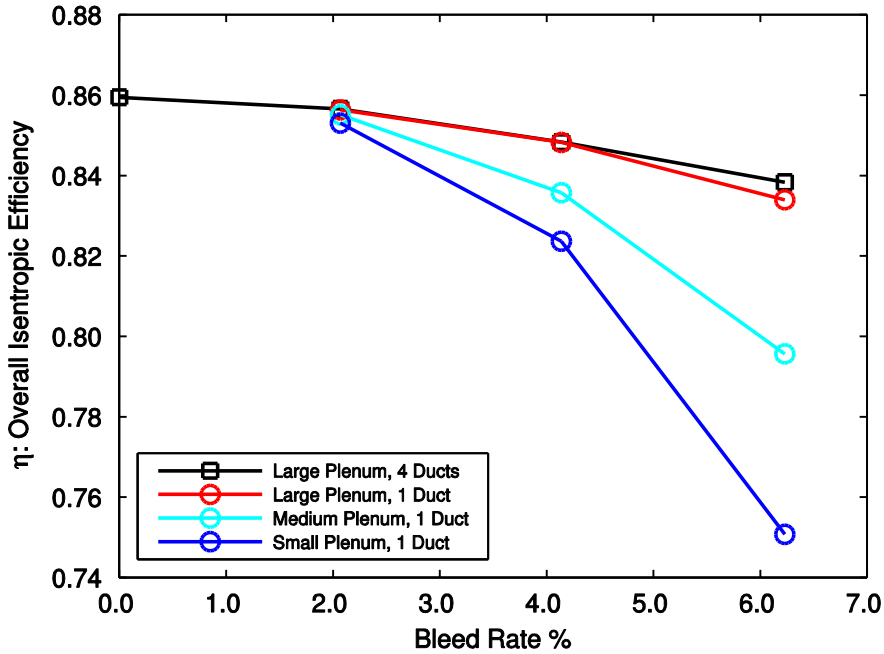


Figure 6.26: Peak overall efficiency of compressor and bleed system against bleed rate for different bleed system configurations.

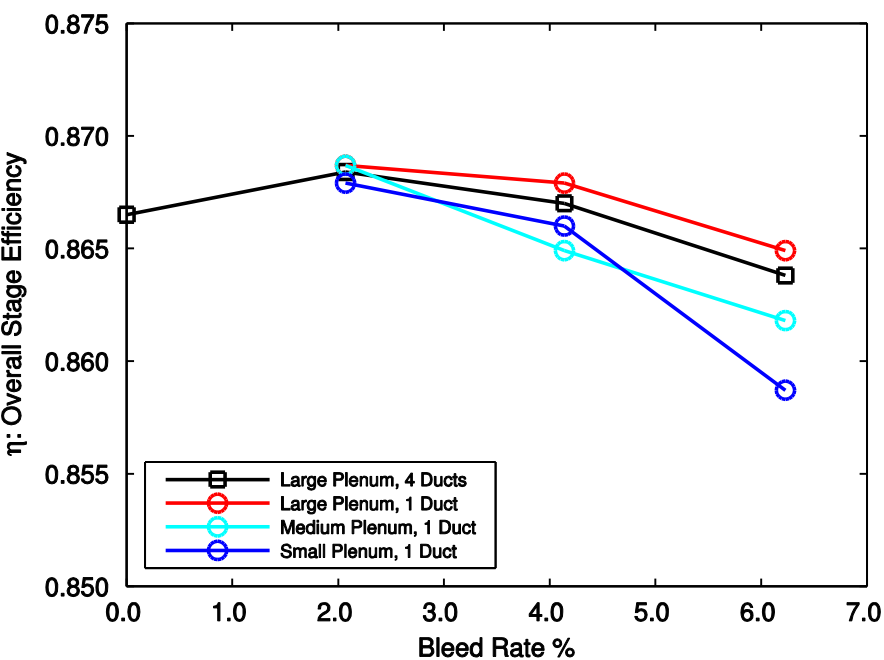


Figure 6.27: Peak stage efficiency against bleed rate for different bleed system configurations.

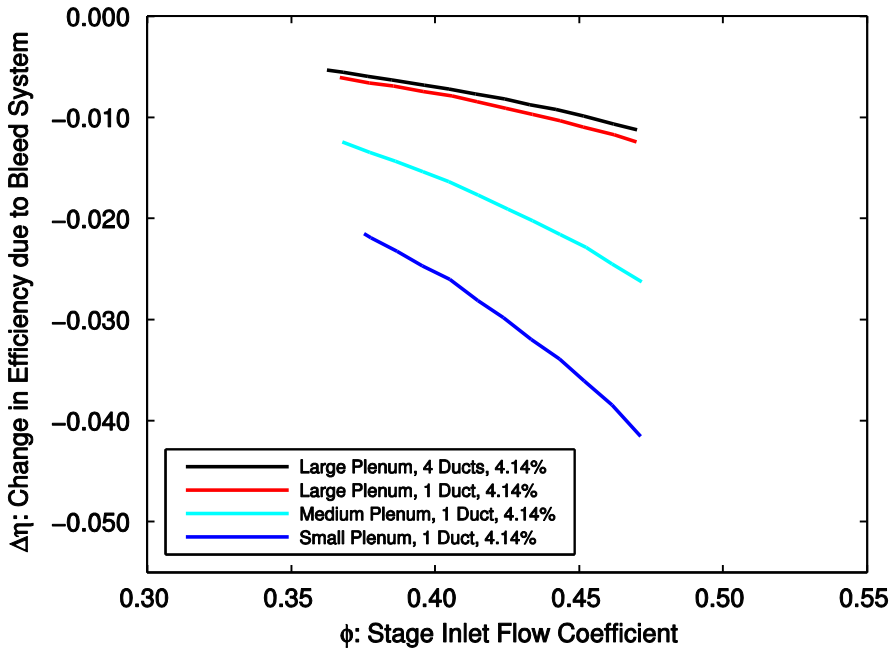


Figure 6.28: Change in efficiency due to bleed system against stage inlet flow coefficient for different bleed system configurations with bleed rate of 4.14%.

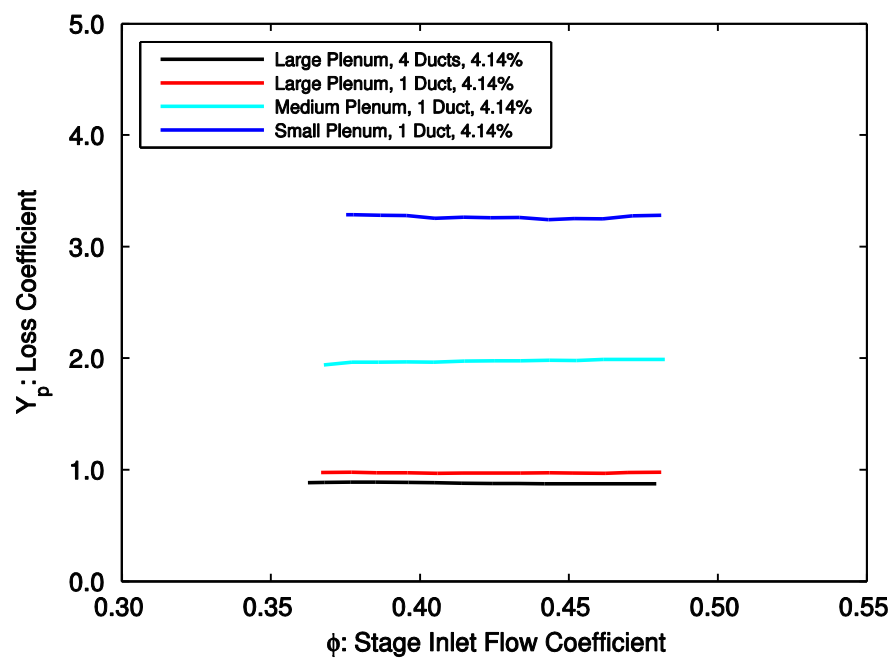


Figure 6.29: Bleed system loss coefficient against stage inlet flow coefficient for different bleed system configurations with bleed rate of 4.14%.

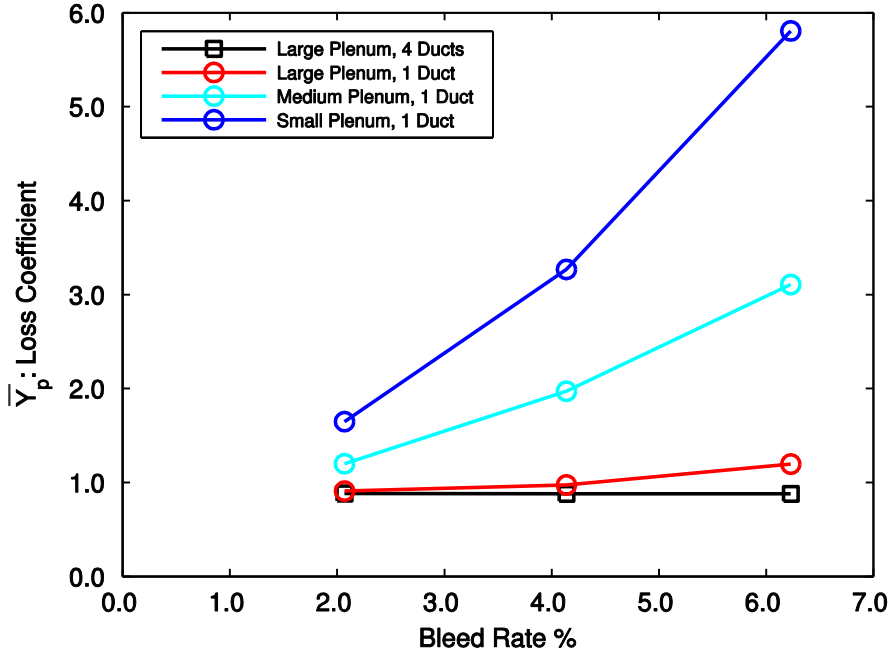


Figure 6.30: Average bleed system loss coefficient against bleed rate for various bleed system configurations.

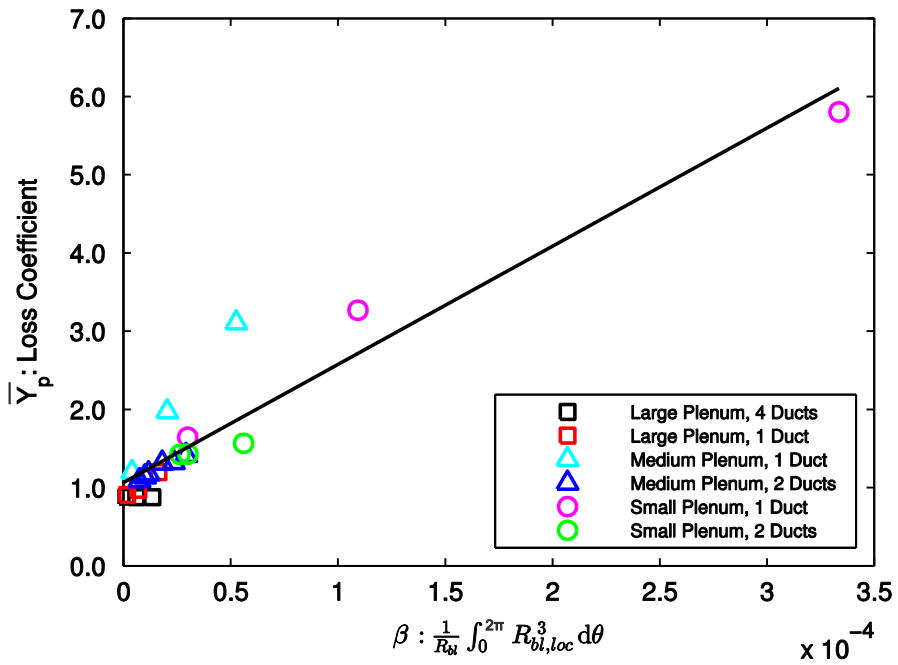


Figure 6.31: Average bleed system loss coefficient against β for various bleed system configurations.

Chapter 7

CFD Results

7.1 Introduction

The purpose of the CFD in the current work is twofold. First it is important to demonstrate the accuracy with which three-dimensional, unsteady, Reynolds averaged numerical simulations (URANS) can model both uniform and non-uniform bleed extraction and its effect on a downstream stage. Second, CFD results allow the compressor and bleed system to be investigated in more detail than was possible in the experiments.

The first section of this chapter investigates the effect of different rates of circumferentially uniform bleed on the main annulus flow and the flow in the bleed system. The second section studies a full annulus CFD solution for the compressor and bleed system configuration tested in Chapter 6, i.e. with the small plenum chamber, a single off-take duct, and a bleed rate of 4.1%.

7.2 Circumferentially Uniform Bleed

The effect of circumferentially uniform bleed is investigated using the two CFD meshes described in Sections 4.3.1 and 4.3.2. Single passage unsteady calculations, with bleed extraction from the top of the bleed slot, are used to study the effect of bleed rate on the main annulus flow distribution and on pressure rise and efficiency characteristics. The flow in the bleed system is then investigated with a quarter annulus unsteady calculation which includes the large plenum chamber, one off-take duct (i.e. four ducts per full annulus) and bleed rate of 4.1%.

7.2.1 Spanwise flow distribution

Rig inlet and upstream of bleed slot. Figure 7.1 shows computed pitchwise-averaged contours of radial velocity, with streamlines overlaid, at stage inlet flow coefficient, $\phi_{stage} = 0.43$ and varying bleed rates. The flow separates from the upstream face of the bleed slot and forms a region of recirculating flow. With a bleed rate of 0% the recirculating flow entirely blocks the bleed slot but as bleed rate increases the separation size reduces and bleed flow is extracted along the rear face of the bleed slot. At the rig inlet traverse location the streamlines in the main passage are close to parallel.

Just upstream of the slot the streamlines curve upwards as flow follows the curvature of the upstream face of the slot. This effect occurs with a bleed rate of 0% and increases as bleed rate is increased.

Figure 7.2 shows spanwise distributions at rig inlet for $\phi_{stage} = 0.43$ and $\phi_{stage} = 0.38$ with varying bleed rate. The increase in flow coefficient with increased bleed rate is uniform across the span because at this location there is no spanwise redistribution due to the bleed extraction. This is also shown in Fig. 7.1 where at rig inlet, the streamlines are parallel. Upstream of the bleed slot, Fig. 7.3 shows that the spanwise distribution is modified by the bleed extraction; the increase in flow coefficient due to bleed is greater above 70% span than in the rest of the passage and V_r/U is increased in this region. This is because bleed extraction causes the flow to be redistributed towards the bleed slot as is shown by the streamlines in Fig. 7.1. The plots of stagnation pressure coefficient in Figs 7.2 and 7.3 show no variation with bleed rate.

Stage inlet. Figure 7.4 shows that at stage inlet increased bleed rate changes the spanwise distribution of flow. In the outer 5% of span the flow coefficient increases with increased bleed rate; at 98% span the flow coefficient is 0.05 higher for 6.2% bleed rate compared to 0% bleed rate. This is because the low speed casing boundary layer flow is part of the flow extracted by the bleed slot. This effect can also be seen in the plots of stagnation pressure coefficient in Fig 7.4 where near the casing the stagnation pressure increases with increased bleed rate. From 65% to 95% of span increased bleed rate reduces the flow coefficient; at 88% span the flow coefficient is 0.02 lower for 6.2% bleed rate compared to 0%. For the rest of the span an increase in bleed rate results in slightly increased flow coefficient. These changes in spanwise flow occur because the flow is being redistributed following the extraction of the bleed flow. In the absolute frame the yaw angle of the flow above 70% of span increases as bleed rate is increased. This, combined with the change in flow coefficient distribution, results in the yaw angle in the rotor relative frame, in the outer 10% of span, increasing (becoming less negative) as bleed rate is increased. At 97% of span and with $\phi_{stage} = 0.38$, the relative yaw angle is 1.3 degrees greater at 6.2% bleed rate compared to 0% bleed rate and at 98% of span this has increased to 2.5 degrees. The rotor incidence in the rotor tip region is therefore reduced as bleed rate increases.

Downstream of rotor and stator rows. Figures 7.5 and 7.6 show that downstream of the rotor and stator rows, spanwise redistribution, due to bleed, is small; the difference in flow coefficient is everywhere less than 0.01. V_r/U is also unchanged by bleed rate because the spanwise redistribution of the flow due to the bleed extraction does not affect the flow at these traverse locations.

Comparison with experimental results. The effects of bleed on the spanwise flow distributions upstream of the bleed slot and at stage inlet agree closely with the measured data at both operating points investigated. The magnitude of the changes in velocity and angle of the flow are quantitatively similar, e.g. at stage inlet, at 97% of span, the change in rotor incidence between the

cases with 0% bleed rate and 6.2% bleed rate is measured experimentally as 1 degree and calculated by CFD to be 1.3 degrees. The spanwise extent of the changes also agree, e.g. at stage inlet, the spanwise location below which increased bleed rate increases flow coefficient and above which flow coefficient decreases, is shown to be 70% of span in both experimental measurements and CFD calculations (see Figs 5.7, 5.8 and 7.4). The major differences between the experimental results and the CFD calculations occur downstream of the rotor and stator rows near the hub and are present for all the cases, including bleed rate of 0%. These differences are due to the CFD not accurately capturing the flow through the blade rows, as discussed in Section 4.6.2 for the 0% bleed rate case. For the bleed rates studied, the changes in spanwise distribution at stage inlet have little impact on the rotor or stator hub corner separations.

7.2.2 Pressure rise characteristics

Rig inlet to stage exit total-to-static pressure rise characteristics, measured and computed for different rates of uniform bleed, are plotted in Fig. 7.7. At a given rig inlet flow coefficient the pressure rise increases as bleed rate is increased because the flow coefficient into the stage is being reduced. The CFD calculated characteristics match the experimental results well up to total-to-static pressure rise coefficient, $\psi_{t-s,rig} = 0.50$. Above this pressure rise the CFD calculated characteristics drop below the experimentally measured characteristics.

Figure 7.8 shows stage inlet to stage exit total-to-static pressure rise characteristics plotted against stage inlet flow coefficient. The CFD calculated characteristics collapse towards a single line in a similar way to the experimental measurements. A small reduction in pressure rise with increased bleed rate is observed for both the CFD calculations and experimental measurements and this is due to spanwise redistribution of the flow at stage inlet caused by bleed extraction. The pressure rise characteristics for all the bleed rates tested begin to drop below the measured characteristics for $\phi_{stage} < 0.41$. At $\phi_{stage} = 0.38$ the CFD calculated stage total-to-static pressure rise characteristic, for the case with a bleed rate of 0%, is 5.9% lower than the measured value. As explained in Section 4.6.2 for a bleed rate of 0%, this is because the rotor and stator hub corner separation sizes are exaggerated by the CFD and the stage pressure rise is therefore under predicted. The effect of the corner separations on the stage inlet characteristics is similar for different bleed rates because, for a given stage inlet flow coefficient, uniform bleed has little effect on the flow downstream of the rotor or stator rows.

Pullan et al. [35] observe that “a sufficient number of passages must be modelled in order to resolve the early stages of spike stall inception” and six passages are used in their work. The single passage unsteady calculations performed in this work are therefore not expected to predict the stall point of the compressor accurately. Also, the method described in Section 4.4 to obtain a stable operating point is implemented with “ramp-ups” in pressure of 100 Pa which result in changes in flow coefficient near the top of the characteristic of 0.012. Smaller changes in pressure (e.g. 20 Pa) should

be used to obtain a more accurate determination of the last stable operating point. The CFD calculations predict the stalling stage flow coefficient to within 0.01 (2.7%) of the experimental measurements but the limitations described above mean that the change in stage inlet stalling flow coefficient with bleed rate, measured experimentally, is not predicted by the CFD. However, the reduction in rotor incidence at the rotor tip, observed in Fig. 7.4, suggests that further work with multi-passage CFD and smaller changes in operating point near to stall may be able to reproduce this effect.

7.2.3 Efficiency

Overall efficiency characteristics, measured and computed for different bleed rates, are plotted in Fig. 7.9. The CFD calculations and experimental measurements do not match well. With a bleed rate of 0% this is because of differences in blade profile loss and rotor and stator hub separation size. This is discussed in more detail in Section 4.6.2. However, for the cases with bleed, the difference in loss in the bleed flow is also an important factor. The stage efficiency characteristics, plotted in Fig. 7.10, collapse towards a single line for both CFD calculations and experimental measurements. Figure 7.11 shows the measured and computed peak overall and peak stage efficiencies against bleed rate. The CFD calculated peak stage efficiency reduces by 0.22% points as bleed rate is increased from 0% to 6.2%; this agrees well with the measured change of 0.27% points. The CFD calculated peak overall efficiency reduces by 1.0% as bleed rates increase from 0% to 6.2%, however the measured peak overall efficiency reduces by 2.2%.

The difference between the measured and computed change in overall efficiency must therefore be due to differences in the bleed system loss. Figure 7.12 shows measured and computed change in efficiency due to bleed loss, $\Delta\eta_{bleed}$, plotted against stage inlet flow coefficient for varying uniform bleed rates. $\Delta\eta_{bleed}$ for the CFD calculations is defined as:

$$\Delta\eta_{bleed} = \frac{\dot{m}_{bl}U^2\Delta P_{0,CV,bl}}{\dot{m}_{exit}(h_{0,exit}-h_{0,in}) + \dot{m}_{bl}(h_{0,bleed}-h_{0,in})} \quad (7.1)$$

where $\Delta P_{0,CV,bl}$ is defined in Equation 5.2 and the other quantities are used for the overall efficiency (Equation 4.2). For a given stage inlet flow coefficient the losses in the bleed slot increase as percentage bleed rate increases and for a fixed percentage bleed rate the losses reduce as the compressor is throttled. The same qualitative trends are seen for the CFD calculations and experimental results. However, at $\phi_{stage} = 0.43$, with a bleed rate of 4.1%, the CFD calculated change in efficiency due to bleed loss is $\Delta\eta_{bleed} = 0.51\%$ points and the measured value at the same condition is $\Delta\eta_{bleed} = 0.82\%$ points.

The loss coefficient, Y_p , defined in Equation 5.3, is applied to the CFD calculations and plotted against stage inlet flow coefficient in Fig. 7.13. Like the experimental results, the loss coefficient is

close to constant across the operating range. However, the CFD calculated loss coefficient is significantly lower than the measured value; for a bleed rate of 2.1% the average loss coefficient across the operating range, $\overline{Y_p} = 0.63$ and this reduces to $\overline{Y_p} = 0.56$ for a bleed rate of 6.2%. In comparison the measured loss coefficient is constant for the bleed rates tested with $\overline{Y_p} = 0.88$. This explains why the overall efficiency reduces more quickly with bleed for the experimental measurements than the CFD calculations.

The most obvious limitation of the single passage CFD calculations is that the bleed flow is modelled only up to the top of the bleed slot. The losses which occur in the plenum chamber and off-take ducts are not included and hence the CFD calculated loss coefficient is expected to be lower than that measured experimentally. The next section uses a quarter annulus calculation, which includes the large plenum chamber and an off-take duct to investigate the flow and associated losses in the full bleed system.

7.2.4 Bleed system flow

The quarter annulus calculation with the large plenum chamber and one off-take duct (i.e. four ducts per annulus) is run with a bleed rate of 4.1% and $\phi_{stage} = 0.43$. Figure 7.14 shows contours of V_r/U in the bleed slot at 80% of slot height at a constant radius. In the circumferential direction, over the length scale of more than one pitch, the bleed flow is uniform. This supports the assumption made in Section 3.3.2 that bleed extraction is uniform for the bleed system with the large plenum chamber and four off-take ducts.

Gomes et al. [10,26] provide experimental measurements of the flow field in the bleed system and show that two counter rotating vortices are present in the plenum chamber of the test rig. However, these measurements do not provide a complete description of the bleed flow and in particular the interaction of the plenum chamber vortices with the off-take ducts is not explained. In this section the quarter annulus CFD is studied, a qualitative description of the flow through the bleed system is presented, and the breakdown of loss through the bleed system is analysed.

Figure 7.15 shows contours of tangential velocity coefficient, V_t/U , in the meridional plane at different circumferential locations relative to the off-take duct. Overlaid on the contours are projections of streamlines on to the same meridional plane as the contours. Figure 7.16 shows three-dimensional streamlines in the bleed system. 45 degrees away from the off-take duct (i.e. half way between the ducts) the flow has a positive tangential velocity. The flow leaving the bleed slot “rolls up” into two vortices similar to those observed by Gomes et al. [10,26]. Just before the off-take duct (at -10 degrees relative to the duct) the streamlines in Fig 7.15(b) have formed spirals because the flow is being drawn into the off-take duct and at this location the vortices are being stretched and bent

upwards. Directly underneath the off-take duct, as shown in Fig. 7.15(c), the streamlines and contours of V_t/U indicate that the vortices are no longer perpendicular to the meridional plane. This can be seen more clearly in Fig. 7.16(a) where the black streamlines, seeded in the off-take duct and traced backwards, have turned through 90 degrees and are being drawn into the off-take duct. The red streamlines, seeded in the bleed slot, show that air bled from the main annulus flow after 0 degrees, is not extracted by the off-take duct shown but is extracted further around the annulus.

To quantify the loss, the bleed system is divided into four control volumes, shown in Fig. 7.17. The loss coefficient from inlet to exit of each control volume is defined as:

$$Y_{p,CV} = \frac{P_{0,CV,in} - P_{0,CV,exit}}{(P_0 - P)_{CV1,in}} \quad (7.2)$$

where $P_{0,CV,in}$ is the mass-averaged stagnation pressure at inlet to the control volume, $P_{0,CV,exit}$ is the mass-averaged stagnation pressure at exit of the control volume, and $(P_0 - P)_{CV1,in}$ is the mass-averaged dynamic head at inlet to control volume 1. For the quarter annulus CFD calculation 54% of the loss occurs in the lower half of the bleed slot. The loss in this region is due to shearing at the edge of the separated region and in the boundary layer on the downstream face of the bleed slot. Figure 7.18 shows that the highest absolute velocities in the bleed system occur in the lower half of the bleed slot. This leads to steep velocity gradients and high shearing loss and this explains why this control volume has the largest loss coefficient. The single passage calculation gives almost the same value since the flow in this region is not greatly affected by the inclusion of the plenum chamber and off-take duct in the mesh. The upper half of the bleed slot contributes 13% of the loss. Figure 7.18 shows that the velocity of the flow in this control volume has decreased significantly. This is due to deceleration of the flow by the walls and the separated region and also due to diffusion caused by the increase in radius. Loss in this region is therefore reduced compared to the lower half of the slot. For this control volume the single passage value is 65% higher than the quarter annulus calculation. It is thought that this is due to the bleed being removed from the entire upper face of the bleed slot in the single passage calculations. This is an unrealistic boundary condition and Fig. 7.1(d) shows that this causes the streamlines near to the top of the slot to diverge, increasing the thickness of the boundary layer on the rear face of the slot. For the quarter annulus calculation 25% of the loss is generated in the plenum chamber. This is due to viscous losses associated with the jet of air leaving the bleed slot and mixing with the low velocity flow in the plenum chamber. 8% of the loss occurs in the fourth control volume whose exit is located at the same location as the Pitot rake in the experiment. This loss is again due to the shearing between the main flow and the separated region in the off-take duct.

The inclusion of the plenum chamber and off-take duct in the quarter annulus calculation increases the total loss coefficient compared to the single passage calculation by 30% so that the calculated value of loss coefficient is only 7.9% less than the measured value. The reason for this

discrepancy is not known. The CFD calculation may not accurately capture the large separated flow in the bleed slot or the low velocity, vortical flows in the plenum chamber. Further experimental work is needed to validate the CFD calculation of the flow inside the bleed system and if possible measure the stagnation pressure at bleed slot exit.

The quarter annulus CFD calculation provides useful information on how the bleed system can be improved. Reducing the size of the separation in the bleed slot, e.g. by redesigning the bleed slot shape, will lower velocities in the slot and hence reduce loss in control volumes one and two. Reducing the blockage in the bleed slot would also decrease the velocity of the jet of air that passes into the plenum chamber and this would reduce the mixing losses in control volume three. The separation in the off-take duct could also be reduced by rounding the duct inlet. The CFD calculation and the loss breakdown presented here can be used as a benchmark to assess the effectiveness of design changes before they are tested experimentally.

7.2.5 Summary

Single passage, unsteady calculations with bleed flow extracted from the top of the bleed slot are able to model the spanwise redistribution of flow, upstream of the slot and at stage inlet, caused by varying rates of bleed up to 6.2%. CFD calculated pressure rise characteristics agree well with measured characteristics for $\phi_{stage} > 0.41$. Below this flow coefficient the rotor and stator hub separations are not captured accurately, their size is exaggerated by the CFD, and this results in the pressure rise being under predicted.

The CFD calculations and experimental measurements of overall and stage efficiency characteristics do not match well. However, for stage efficiency, both the computations and measurements collapse towards a single line with the peak stage efficiency changing by only 0.22% and 0.27% respectively as bleed rate is increased from 0 to 6.2%. The change in overall efficiency with bleed agrees less well: as bleed rate is increased from 0% to 4.1% CFD calculations give a reduction in efficiency of 0.5% but the measured change in efficiency is 0.8%. This is because the single passage CFD calculations do not model the flow through the plenum chamber and off-take duct.

Including the plenum chamber and off-take duct in a quarter annulus CFD model with a bleed rate of 4.1% increases the bleed system loss coefficient to within 7.9% of the experimentally measured value. The loss in the bleed slot accounts for 67% of this loss, with losses in the plenum chamber totalling 25% and loss in the off-take duct accounting for the remaining 8%. The quarter annulus CFD calculations also show that two counter-rotating vortices are formed in the plenum chamber as the flow leaves the bleed slot. These vortices are then drawn into the off-take ducts causing strong secondary flows to be set up in the ducts.

7.3 Circumferentially Non-uniform Bleed

The full annulus CFD calculation with the small plenum chamber and one off-take duct is run at $\overline{\phi_{stage}} = 0.43$, with a bleed rate of 4.2%. The solution considered here is time-averaged over 29 rotor blade passings, i.e. half a revolution. In this section the main annulus flow is compared with experimental measurements and a qualitative description of the flow in the bleed system is provided.

7.3.1 Main passage flow

Rig inlet. Figure 7.19(a) shows CFD calculated contours of flow coefficient at rig inlet. The flow coefficient in the main passage is increased in the region close to the circumferential position of the off-take duct. Figure 7.19(b) shows that the circumferential redistribution of flow is uniform across the span and the change in yaw angle in the absolute frame is small. There is also no circumferential variation in stagnation pressure coefficient at this location. The CFD calculated changes in passage-averaged flow coefficient and flow angles around the circumference are compared with the experimental measurements in Fig. 7.19(c). The CFD calculated flow field matches the measurements well at this location.

Upstream of bleed slot. Contours of flow coefficient upstream of the bleed slot are shown in Fig. 7.20(a). The flow coefficient is increased close to the circumferential position of the off-take duct, and particularly in the outer 30% of span. This is also seen in the spanwise distribution of flow coefficient in Fig. 7.20(b). Close to the off-take duct position the radial velocity is increased as streamlines are turned up into the bleed slot. At this location, close to the bleed slot, the yaw angle in the absolute frame varies around the circumference. This behaviour, which is also measured experimentally, is explained in Section 6.2. Figure 7.20(b) shows that the stagnation pressure coefficient does not vary around the annulus. The CFD calculated passage-averaged flow field upstream of the bleed slot, in Fig. 7.20(c), matches the experimental results well. The CFD predicts a higher peak in flow coefficient but this is because the flow cannot be traversed experimentally at 0 degrees relative to the off-take duct.

Stage inlet. Figure 7.21 shows that before the off-take duct position (i.e. negative circumferential position relative to the duct) flow coefficient is reduced and after the duct (i.e. positive circumferential position relative to the duct) flow coefficient is increased. The computed passage-averaged flow coefficient distribution in Fig. 7.21(c) matches very well with the experimental measurements and shows that the circumferential variation in flow coefficient at stage inlet is more uniform than the distribution of flow coefficient upstream of the slot, shown in Fig. 7.20(c). This is because the variation in operating point around the annulus causes the downstream stage to impose its own non-uniform static pressure perturbation on the flow and at stage inlet this results in a more

uniform flow distribution. This is explained in more detail in Section 6.2. The close agreement between measurements and CFD is reliant on the response of the downstream stage to changes in local flow coefficient and flow angle being captured correctly. Fig. 7.8 shows that the CFD and measured stage characteristics for uniform bleed agree well for $\phi_{stage} > 0.41$. Therefore, for the non-uniform case at $\phi_{stage} = 0.43$, changes in flow coefficient around the annulus of ± 0.02 mean that the varying operating points all lie on the part of the characteristic that matches well with experiment. Calculations for the non-uniform case at reduced stage flow coefficient have not been performed in the current work. However, it is hypothesised that the agreement between measurements and CFD will be less good because the response of the stage, i.e. the match between the measured and computed pressure rise characteristics, is not as well predicted at stage inlet flow coefficients below $\phi_{stage} = 0.41$.

The spanwise distribution of flow coefficient in Fig. 7.21(b) shows that the circumferential non-uniformity is greatest in the outer 30% of span. The flow deficit caused by the bleed extraction near to the off-take duct causes the flow to redistribute towards the casing and the radial velocity coefficient is increased in this region.

Absolute yaw angle varies with circumferential position and Fig 7.21(c) shows that the CFD predicted passage-averaged distribution agrees well with the measured distribution. The reason for the shape of this distribution is explained in Section 6.2. Together, the flow coefficient and absolute yaw angle produce a variation in yaw angle in the relative frame which results in a region of passage-averaged relative yaw angle with a trough 0.49 degrees less than the mean. The experimentally measured value is 0.46 degrees. Reducing yaw angle in the rotor relative frame increases the rotor incidence and it is this effect which leads to a reduction in compressor operating range with non-uniform bleed. The spanwise distribution of relative yaw angle in Fig 7.21(b) shows that above 70% span the rotor incidence in the flow close to the off-take duct position is increased by up to 2.5 degrees compared to the flow away from the off-take duct position. The stagnation pressure coefficient in the outer 20% of span is increased in the region close to the off-take duct position because the high local bleed rate removes the upstream casing boundary layer.

Downstream of rotor row. The contour plot and spanwise distribution of flow coefficient in Figs. 7.22(a) and 7.22(b) show that the flow varies in the circumferential direction but that the change in flow coefficient is uniform across the span. The radial component of velocity is close to zero because there is no spanwise redistribution of the flow due to bleed extraction at this location. The yaw angle in the rotor relative frame is circumferentially uniform from 30% span to 90% but varies by up to 1.5 degrees near the hub and casing. This results in a passage-averaged relative yaw angle distribution which varies by less than ± 0.4 degrees. There is a circumferential variation in stagnation pressure downstream of the rotor row because the sector with reduced flow coefficient operates

further to the left on the rotor characteristic and therefore produces more total-to-total pressure rise. Figure 7.22(c) shows that the CFD calculated passage-averaged distributions match well with the experimental measurements.

Downstream of stator row. Figure 7.23 shows that downstream of the stator row there is circumferential variation in flow coefficient due to non-uniform bleed extraction. Close to the circumferential position of the off-take duct, the size of the stator hub corner separation is increased and the pitch-averaged flow coefficient up to 50% span is reduced. In the outer 30% of span flow coefficient is increased due to increased blockage near the hub. The increase in size of the hub corner separation is due to circumferentially non-uniform yaw angle in the absolute frame at inlet to the stator row as seen in Fig. 7.22(c). The experimental measurements in Fig. 6.24 also show this effect. A circumferential variation in stagnation pressure coefficient is still present downstream of the stator row. This can be seen by comparing Figs 7.22(b) and 7.23(b) where the loss through the stator row, especially close to the hub, reduces the stagnation pressure coefficient but does not change the circumferential distribution.

Downstream of the stator row, Fig. 7.23(b) shows that yaw angle is circumferentially uniform across the span and the passage-averaged value varies by less than ± 0.2 degrees. The yaw angle in the rotor relative frame of reference is circumferentially non-uniform due to the constant absolute yaw angle and circumferential variation in flow coefficient. The passage-averaged distribution in Fig. 7.23(c) shows a region where relative yaw angle is reduced by up to -1.23 degrees. This will result in a region of increased rotor incidence in the next rotor row. The effect that this has on the operating range of the next stage will be different to the current stage, however, because the variation in rotor incidence is more evenly distributed in a spanwise direction than at the stage inlet just downstream of the bleed slot. The effect of non-uniform bleed in a multistage compressor environment is an important area for further work.

7.3.2 Bleed system flow

Figure 7.24 shows CFD calculated local bleed rate in the slot at the same location as the stagnation pressure probes used to measure bleed rate in the experimental rig. The width of the peaks are in good agreement, however, the maximum local bleed rate calculated is 10% points higher than the experimental measurements. This is because the experimental measurements rely on a calibration, as described in Section 3.3.2, and at high local bleed rates an extrapolation from this calibration is required to calculate the bleed rate. It is an extrapolated value at the peak bleed rate which is significantly below the CFD predicted value in Fig. 7.24.

Figure 7.25 shows contours of radial velocity coefficient, V_r/U , in the meridional plane at different circumferential locations relative to the off-take duct. Overlaid on these contours are

streamlines constrained to be in the same meridional plane as the contours. Figure 7.25(a) shows that -90 degrees away from the off-take duct the bleed slot is almost completely blocked by the separation from the upstream face of the bleed slot and the radial velocity is close to zero. The streamlines in Fig. 7.25(a) and Fig. 7.26 show that any flow that is extracted from the main flow passes along the rear face of the slot and then through the small plenum chamber and the top of the bleed slot before being extracted through the off-take duct. At locations 10 degrees either side of the off-take duct the radial velocity in the bleed slot is high with V_r/U up to 0.60. At the top of the bleed slot two counter rotating vortices are formed; one of these is located in the small plenum chamber and the other in the top half of the bleed slot, near the upstream face. Figure 7.26 shows that these vortices are both drawn into the off-take duct. Underneath the off-take duct, Fig. 7.25(c) shows that there is no separation in the bleed slot due to the high local bleed rate. At the inlet to the off-take duct, however, a large separation blocks half of the diameter of duct causing high radial velocities of up to $V_r/U = 0.80$. This is due to the sharp turning of the flow from the plenum chamber into the off-take duct and is expected to be a region of high loss.

The full annulus CFD provides a way to study the flow in the bleed system which cannot be achieved with the current experimental rig. The comparison with the experimental measurements also gives confidence that the flow calculated is physically realistic. The full annulus CFD, with the bleed slot, plenum chamber and off-take duct modelled, can therefore be used to improve the design of the bleed system. For example, a non-axisymmetric bleed slot, designed to reduce bleed non-uniformity, could be investigated using CFD before being tested experimentally.

7.3.3 Summary

The key flow features observed experimentally in Chapter 6 are reproduced with the CFD calculation:

- Non-uniform bleed causes circumferentially non uniform main annulus flow upstream and downstream of the bleed slot.
- The compressor acts to reduce the non-uniformity at stage inlet.
- The reduction in flow coefficient and change in flow angle close to the off-take duct result in a region of increased rotor incidence at stage inlet.
- Bleed extraction changes the spanwise distribution of flow at stage inlet so that the circumferential non-uniformity is greatest near to the casing. This increases the rotor incidence at stage inlet in the rotor tip region.

The CFD calculated circumferential distribution of flow also quantitatively agrees well with the experimental measurements. This is because the mechanism driving the changes in the main annulus

flow is an inviscid, potential flow effect and the stage characteristic agrees closely with the experiment for the range of flow coefficients around the annulus at stage inlet. This type of CFD calculation can be used with confidence for future work to study, for example, different bleed system configurations, multi-stage compressors where the bleed slot is in an interstage gap, and real machine geometries at high speeds. The caveat to this is that the CFD calculation must be able to model the compressor with 0% bleed across enough of its operating range so that the coupling between the compressor and the non-uniform flow field created by the bleed extraction, is captured.

7.4 Conclusions

This chapter has shown that CFD is able to model uniform and non-uniform bleed and its effects on a downstream compressor stage. The following conclusions can be drawn:

1. Single passage, unsteady calculations with bleed flow extracted from the top of the bleed slot are able to model the spanwise redistribution of flow caused by varying bleed rate. CFD calculated pressure rise characteristics agree well with measured characteristics for $\phi_{stage} > 0.41$. Below this flow coefficient the rotor and stator hub separations are not captured accurately, their size is exaggerated by the CFD, and this results in the computed pressure rise characteristic dropping below the measured characteristic. At $\phi_{stage} = 0.38$ the CFD calculated stage total-to-static pressure rise characteristic, for the case with a bleed rate of 0%, is 5.9% lower than the measured value.
2. Single passage, unsteady CFD calculations and experimental measurements of overall and stage efficiency characteristics do not match well. There are two reasons for this. First, the CFD calculations of the stage efficiency do not match the experimental results. This is due to differences in blade profile loss and rotor and stator hub separation size. Second, for the single passage calculations, losses in the plenum chamber and off-take duct are not included so that the loss in efficiency due to bleed is 38% less than that measured experimentally.
3. Including the plenum chamber and off-take duct in a quarter annulus CFD model with a bleed rate of 4.1% increases the bleed system loss coefficient to within 7.9% of the experimentally measured value. The loss in the bleed slot accounts for 67% of this loss, with losses in the plenum chamber totalling 25% and loss in the off-take duct accounting for the remaining 8%.

4. The flow through the bleed system with the large plenum chamber is dominated by a separation from the upstream face of the bleed slot, two counter rotating vortices in the plenum chamber and a separation at inlet to the off-take duct. Improvements to the bleed system should focus on reducing the separation in the bleed slot. This will reduce loss in the slot and reduce the mixing losses in the plenum chamber as the velocity of the jet of air passing into the plenum will be reduced.
5. The effect of non-uniform bleed on the main annulus flow is modelled with a full annulus, unsteady CFD calculation which also includes the full bleed system geometry. At the design operating point, the circumferential distributions of flow coefficient and flow angles agree well with the experimental measurements. This is because the mechanism driving the changes in the main annulus flow is an inviscid, potential flow effect and the response of the coupled downstream stage is captured correctly by the CFD.
6. The CFD methods in the current work can be used with confidence to assess the effect, on either main annulus flow or the flow in a bleed system, of different bleed system designs, e.g. slot shape or plenum size, or compressor configurations, e.g. a multistage compressor with an interstage bleed slot.

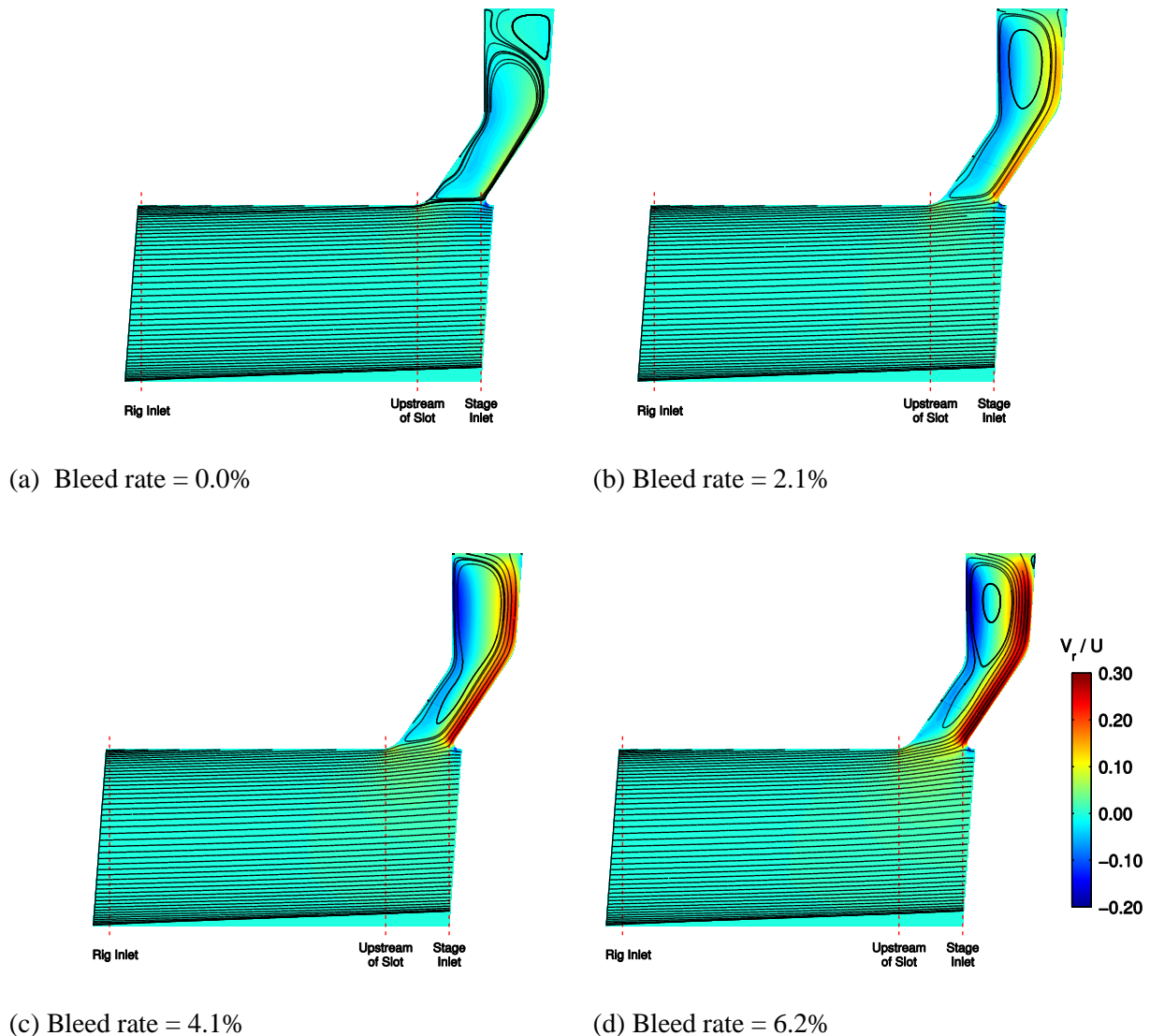
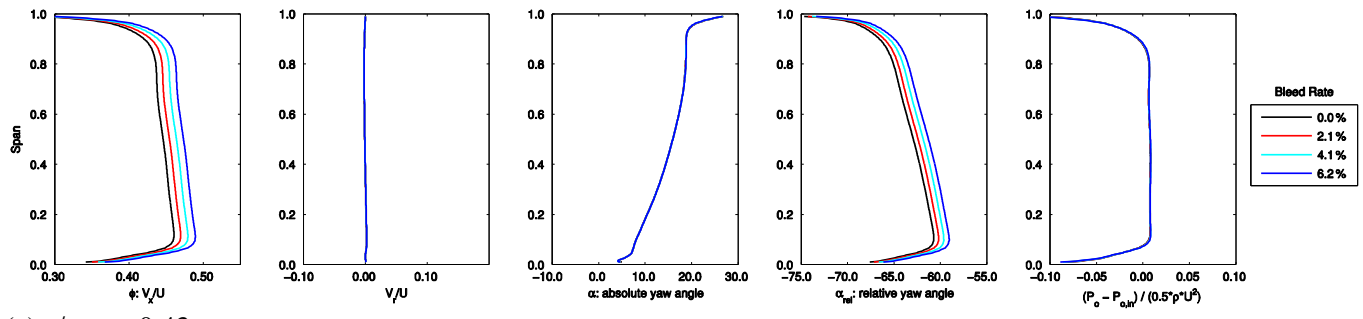
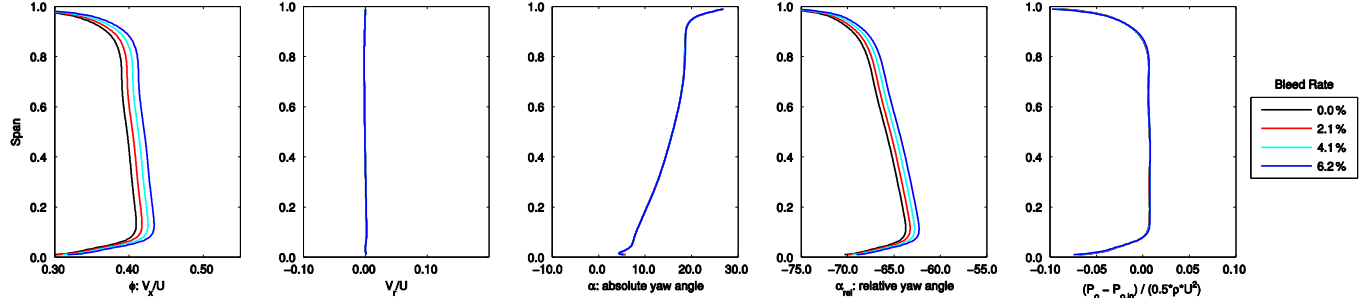


Figure 7.1: CFD calculated pitch-averaged contours of radial velocity coefficient at $\phi_{stage} = 0.43$ with varying bleed rate. Streamlines in the main passage are ‘seeded’ at rig inlet with additional streamlines seeded in the region of recirculating flow in the bleed slot.

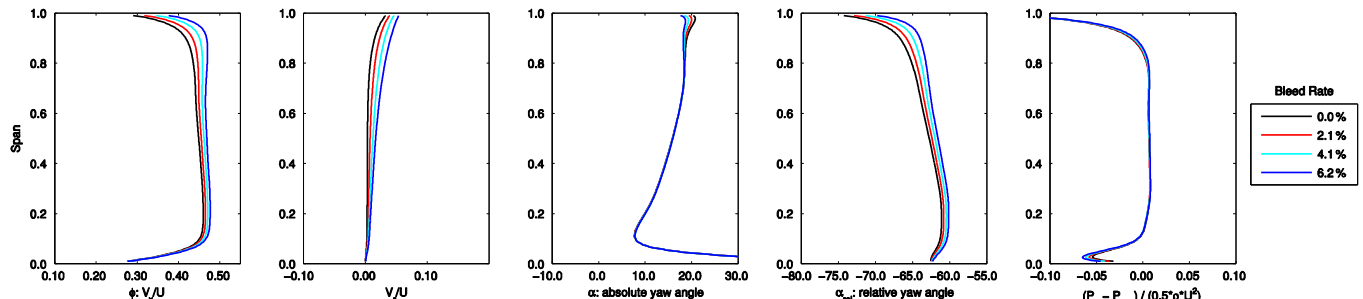


(a) $\phi_{stage} = 0.43$

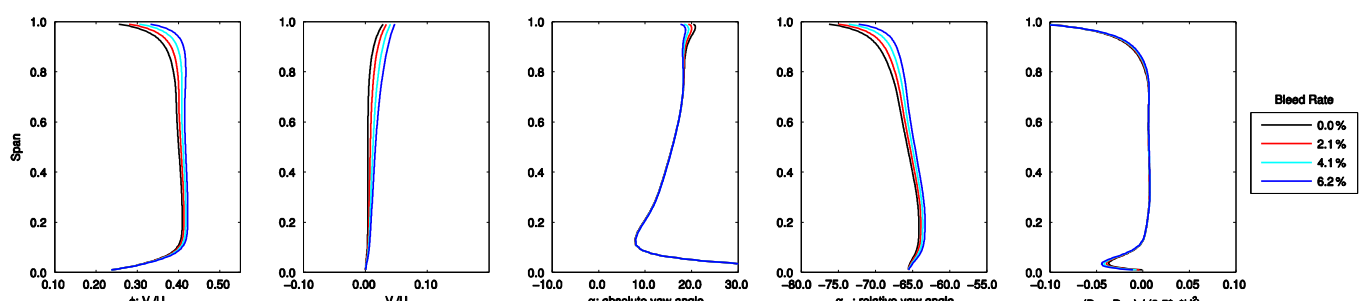


(b) $\phi_{stage} = 0.38$

Figure 7.2: Rig inlet, CFD calculated, pitch-averaged, spanwise distributions of flow for varying bleed rate.



(a) $\phi_{stage} = 0.43$



(b) $\phi_{stage} = 0.38$

Figure 7.3: Upstream of slot, CFD calculated, pitch-averaged, spanwise distributions of flow for varying bleed rate.

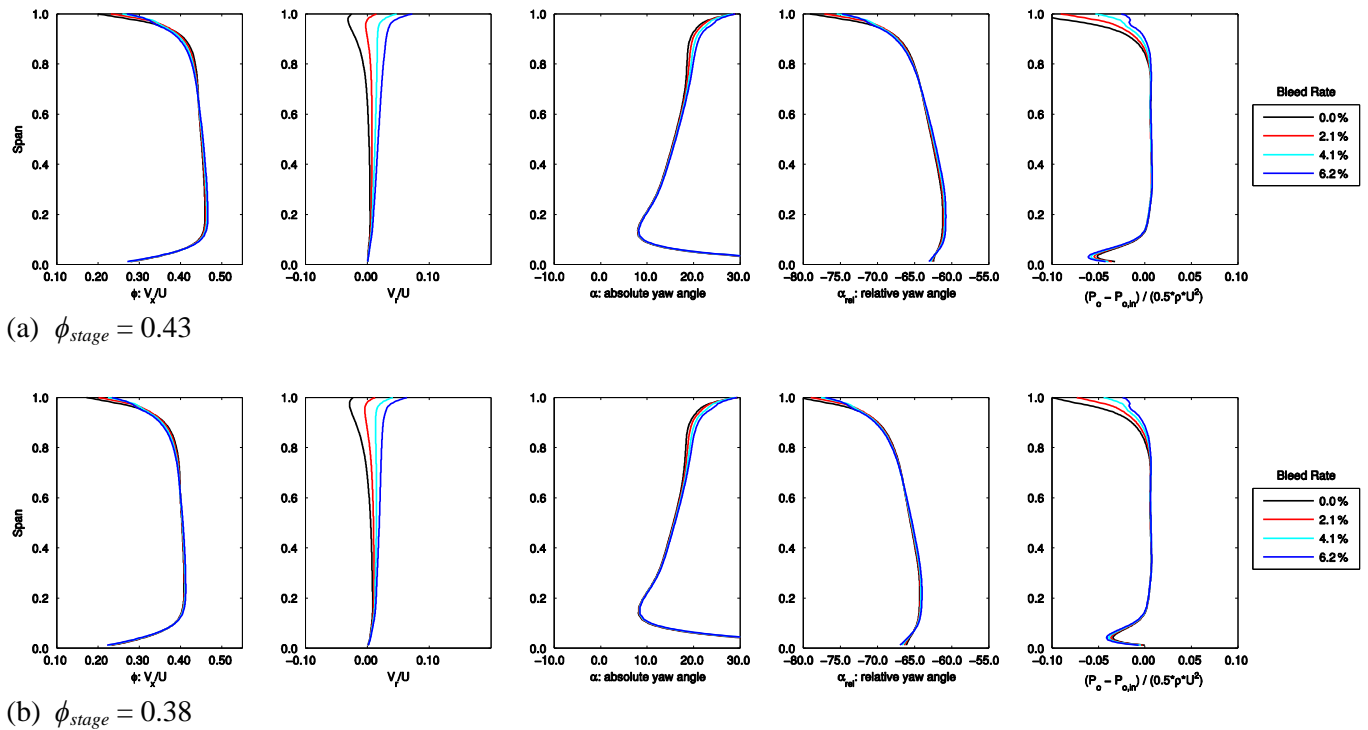


Figure 7.4: Stage inlet, CFD calculated, pitch-averaged, spanwise distributions of flow for varying bleed rate.

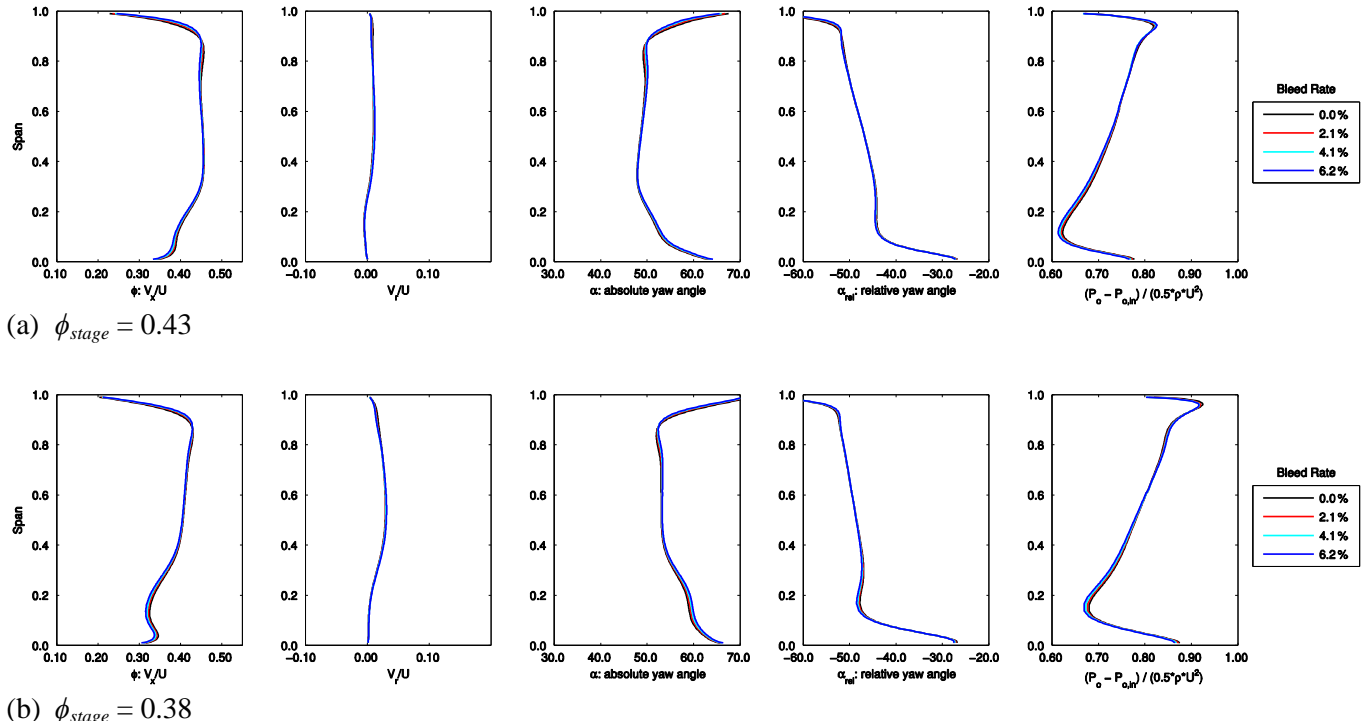
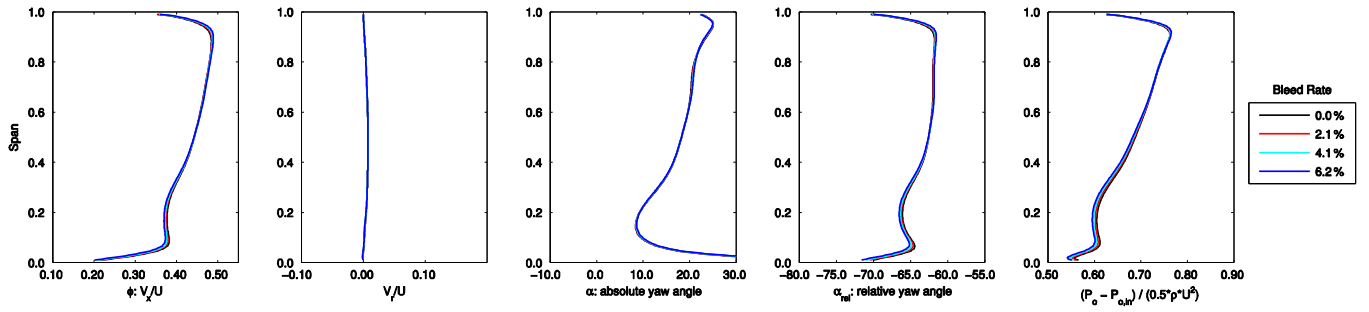
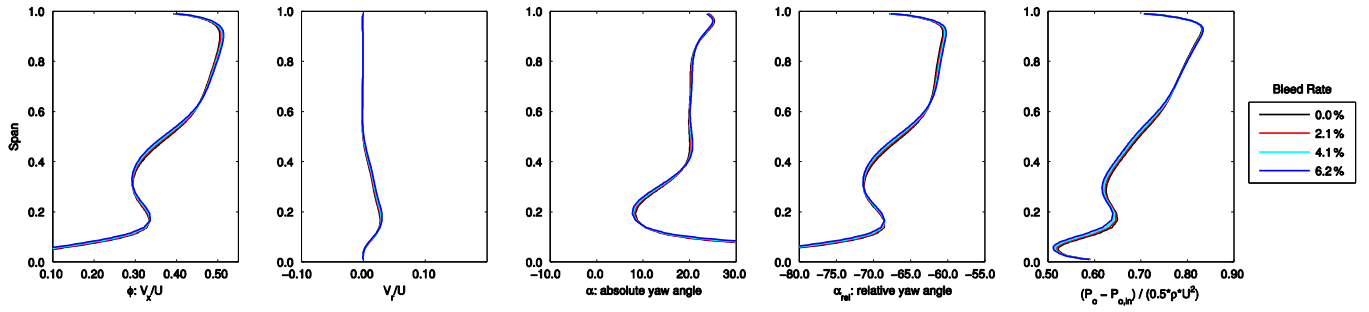
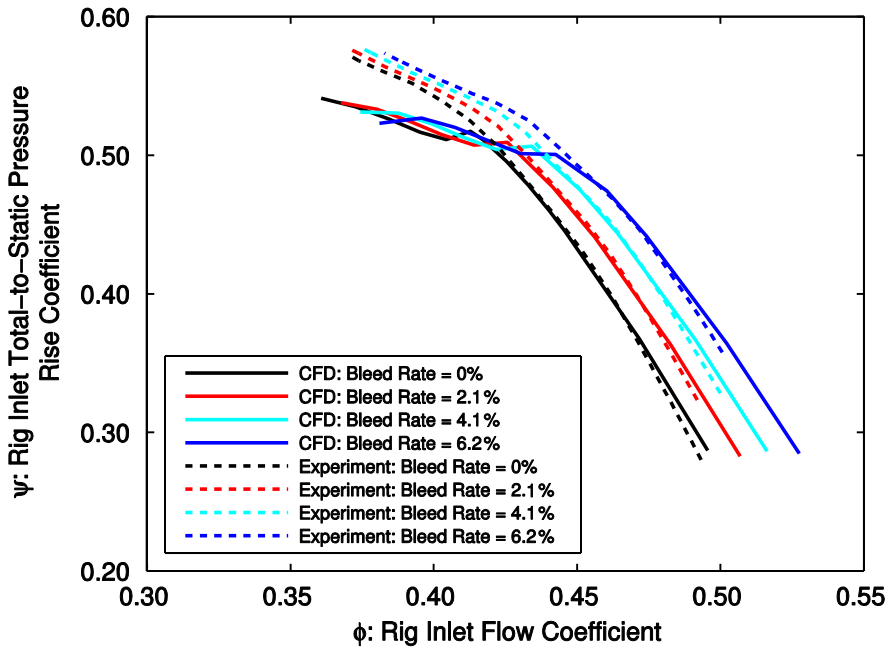


Figure 7.5: Downstream of rotor row, CFD calculated, pitch-averaged, spanwise distributions of flow for varying bleed rate.

(a) $\phi_{stage} = 0.43$ (b) $\phi_{stage} = 0.38$ **Figure 7.6:** Downstream of stator row, CFD calculated, pitch-averaged, spanwise distributions of flow for varying bleed rate.**Figure 7.7:** CFD calculated and experimentally measured rig inlet to stage exit total-to-static pressure rise coefficient against rig inlet flow coefficient for varying uniform bleed rate.

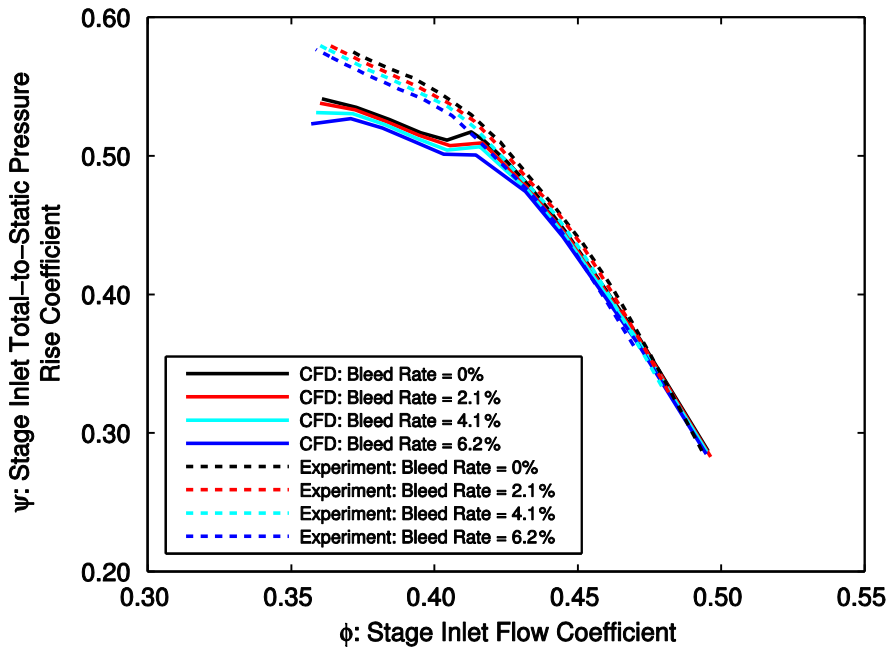


Figure 7.8: CFD calculated and experimentally measured stage inlet to stage exit total-to-static pressure rise against stage inlet flow coefficient for varying uniform bleed rate.

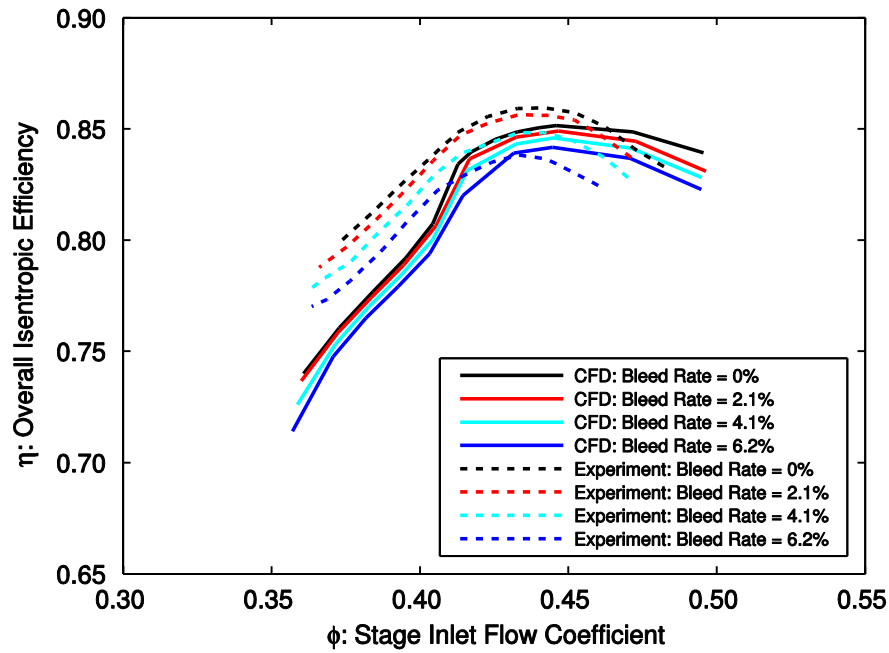


Figure 7.9: CFD calculated and experimentally measured overall efficiency against stage inlet flow coefficient for varying uniform bleed rate.

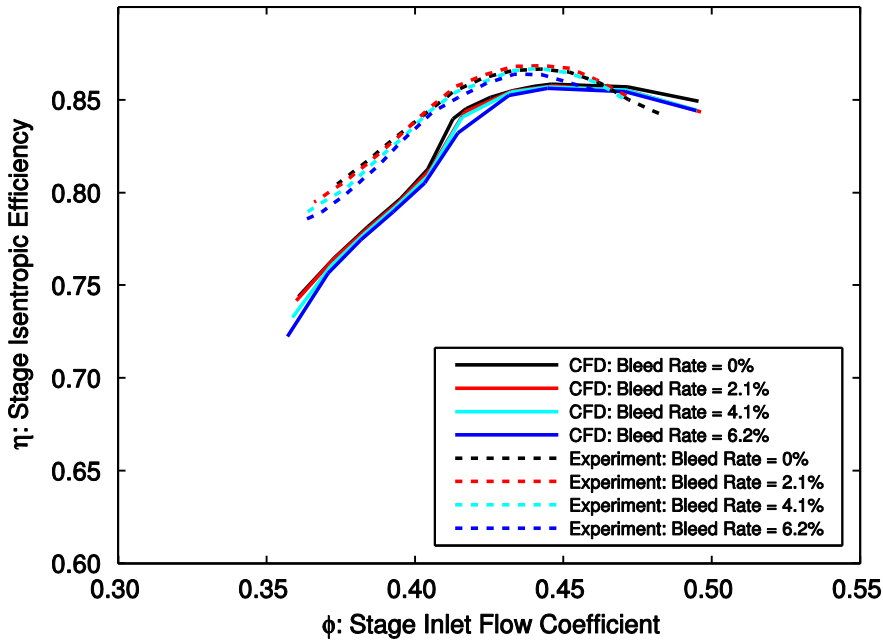


Figure 7.10: CFD calculated and experimentally measured stage efficiency against stage inlet flow coefficient for varying uniform bleed rate.

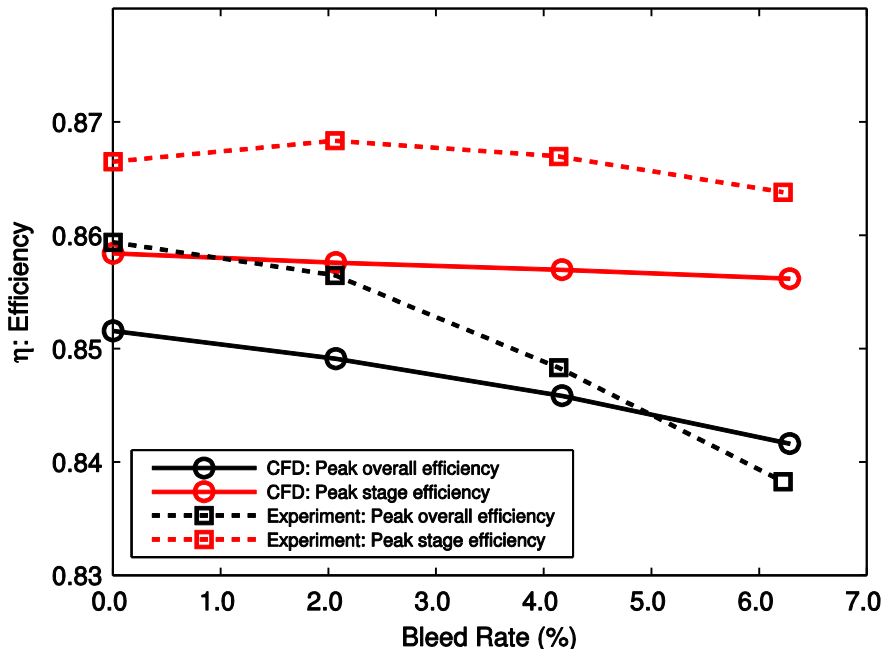


Figure 7.11: CFD calculated and experimentally measured peak overall and peak stage efficiency against bleed rate.

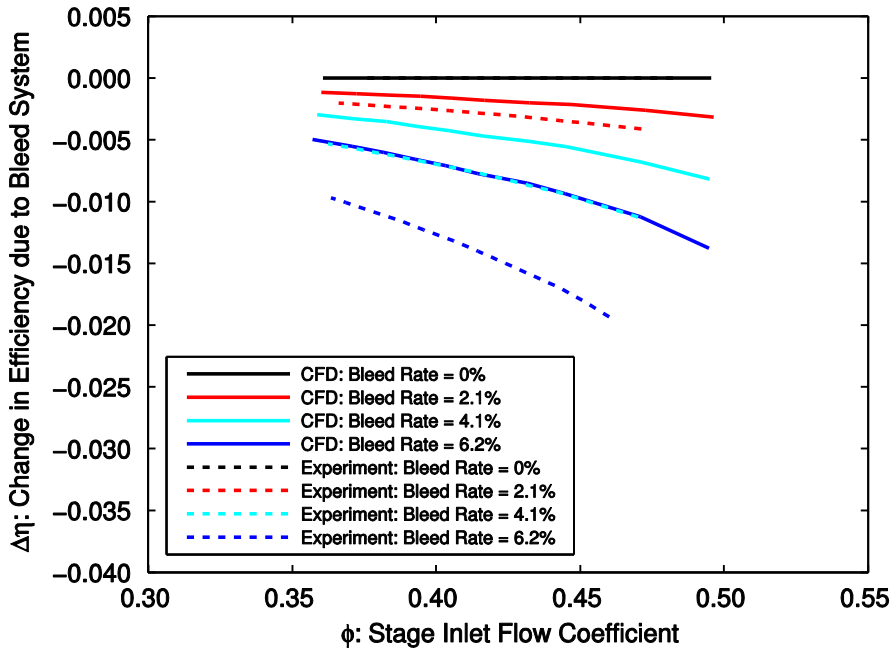


Figure 7.12: CFD calculated and experimentally measured change in efficiency due to bleed loss against stage inlet flow coefficient for varying uniform bleed rate.

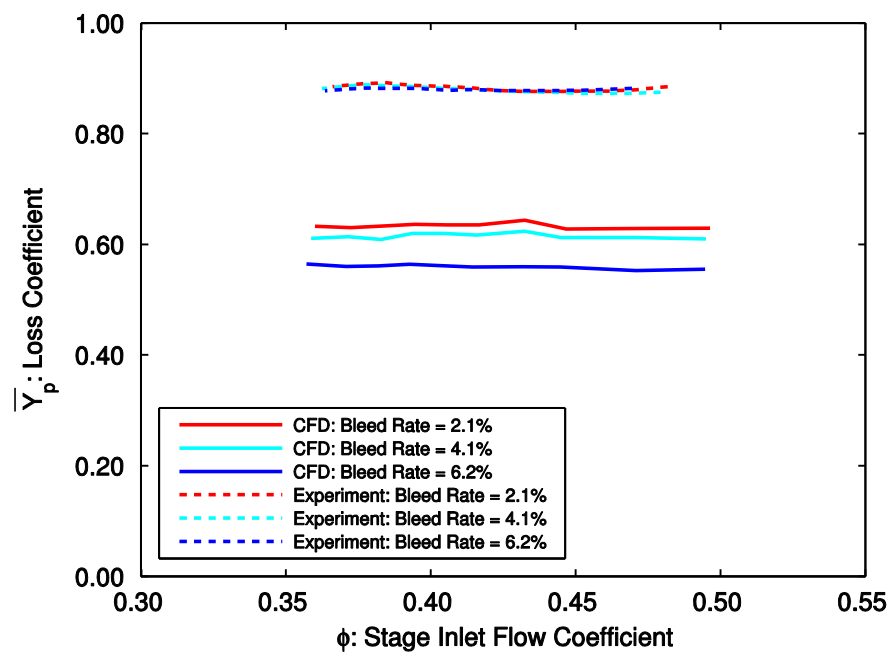


Figure 7.13: CFD calculated and experimentally measured bleed system loss coefficient against stage inlet flow coefficient for varying uniform bleed rate.

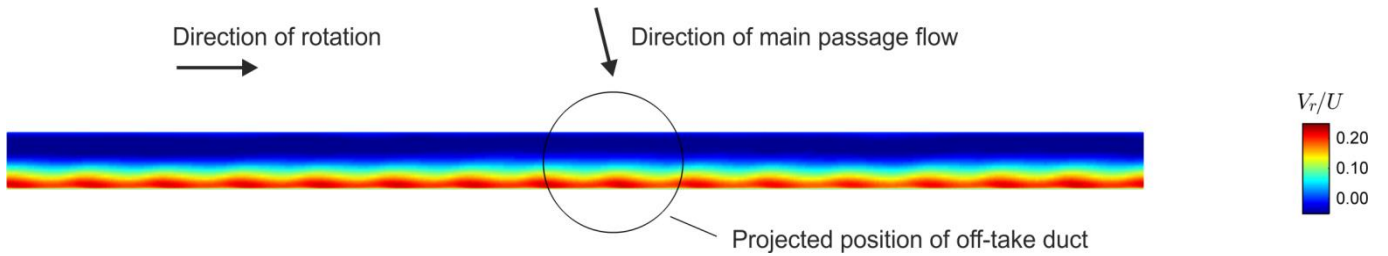


Figure 7.14: CFD calculated contours of radial velocity coefficient in bleed slot at 80% of slot height for quarter annulus section. $\phi_{stage} = 0.43$, bleed rate = 4.1%.

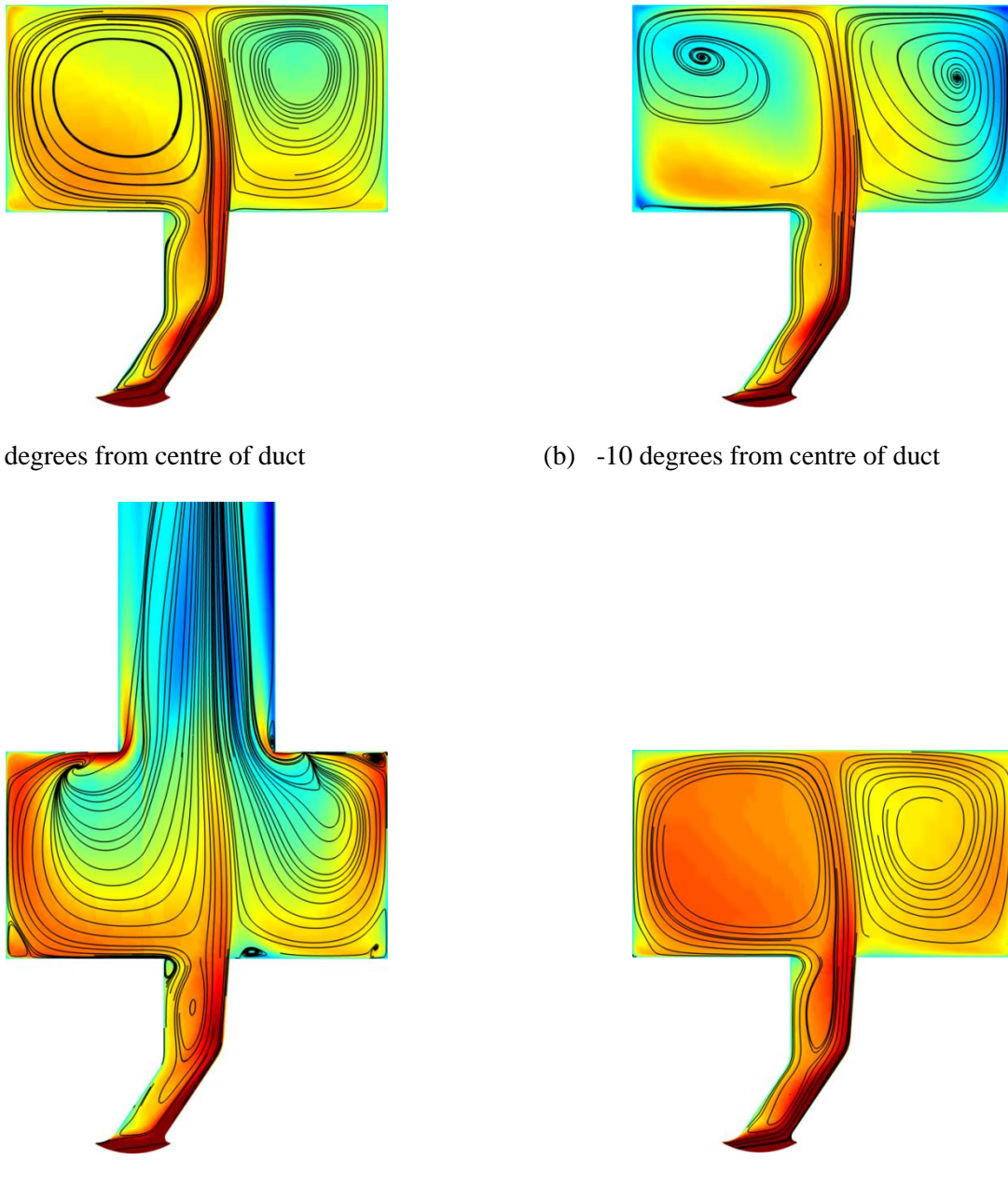
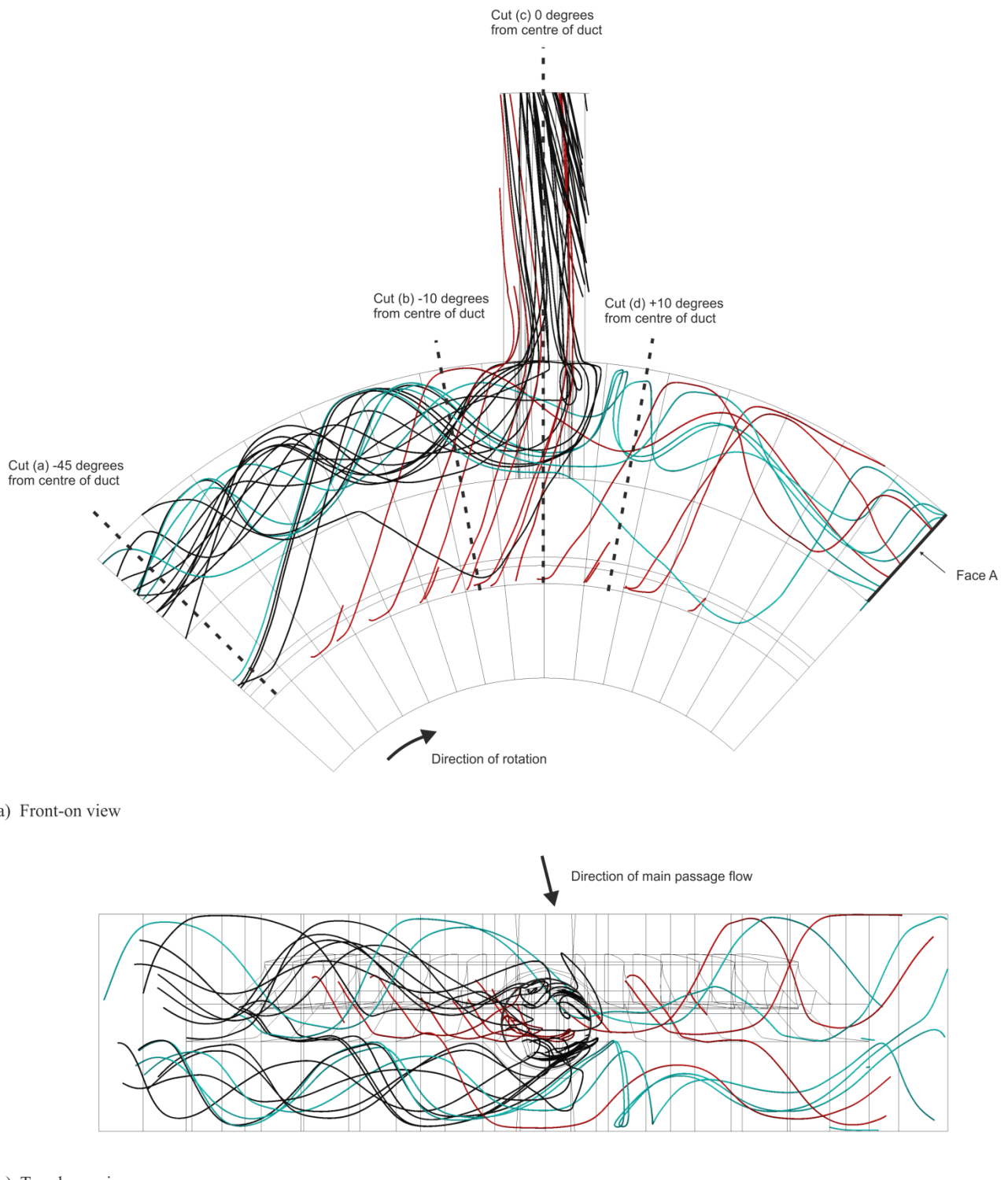


Figure 7.15: CFD calculated contours of tangential velocity coefficient at different circumferential locations. Overlaid are projections of streamlines on to the same plane as the contours. $\phi_{stage} = 0.43$, bleed rate = 4.1%.



(b) Top-down view

Figure 7.16: CFD calculated streamlines in bleed system. Black streamlines are seeded in the off-take duct and traced backward towards the plenum chamber. Red streamlines are seeded at the bottom of the bleed slot and are traced forwards. Blue streamlines are seeded on Face A and are traced backwards. $\phi_{stage} = 0.43$, bleed rate = 4.1%.

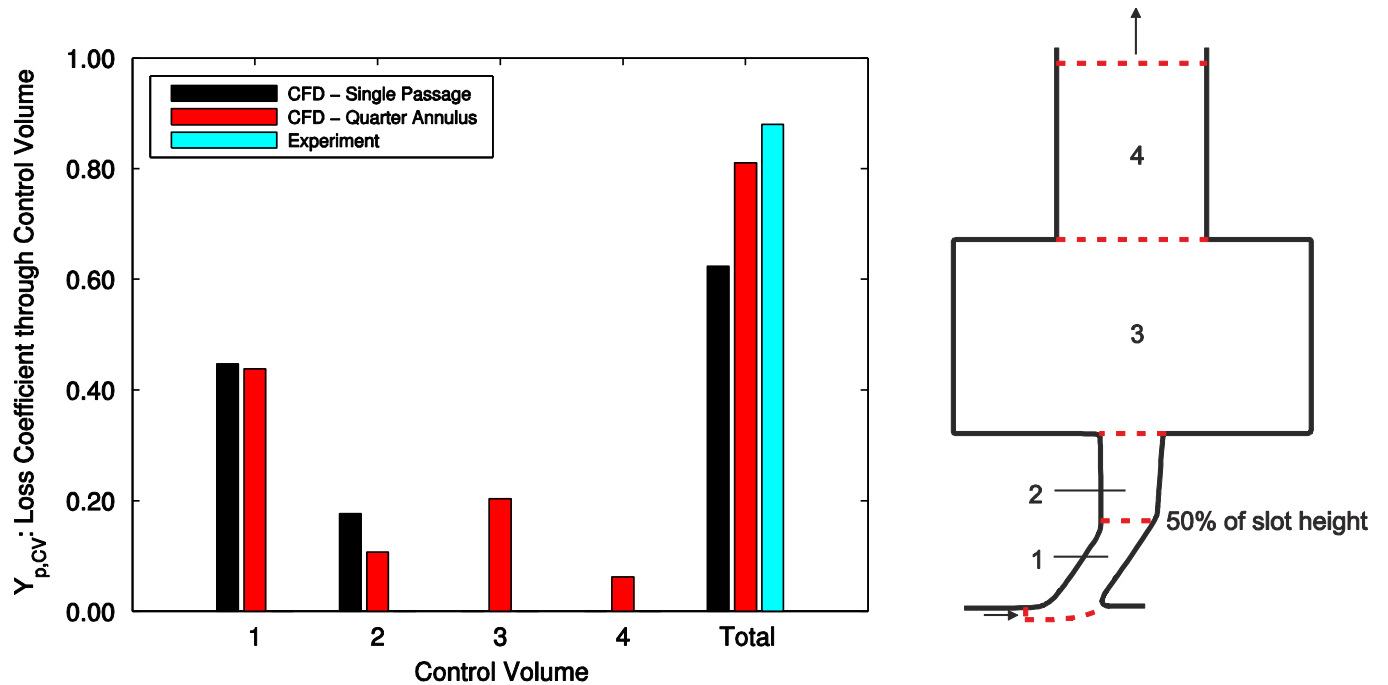


Figure 7.17: Loss coefficient between inlet and exit of control volumes in bleed system. $\phi_{stage} = 0.43$, bleed rate = 4.1%.

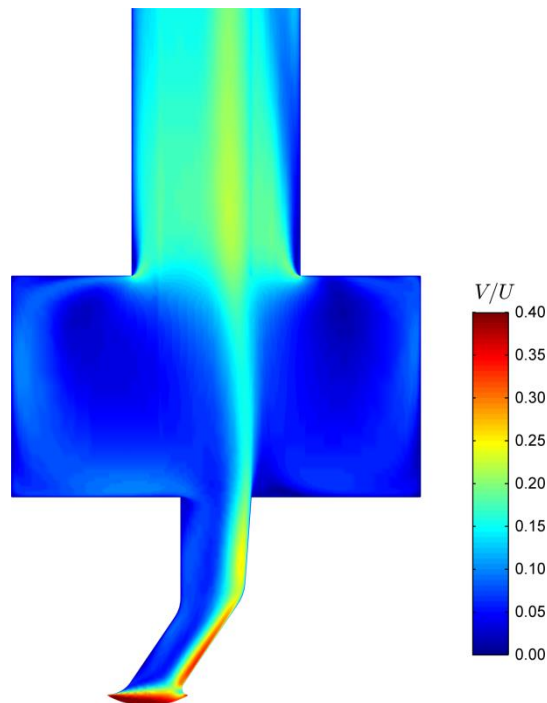
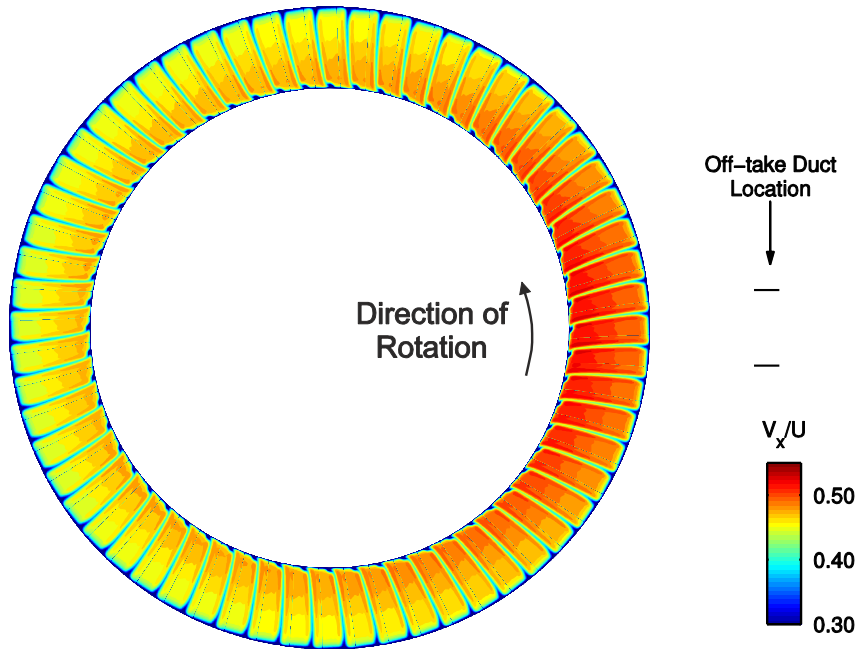
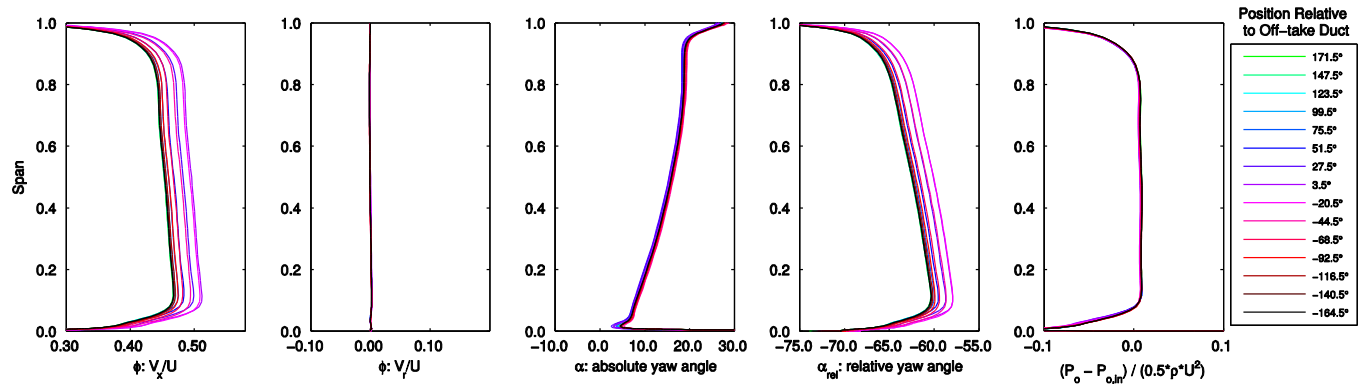


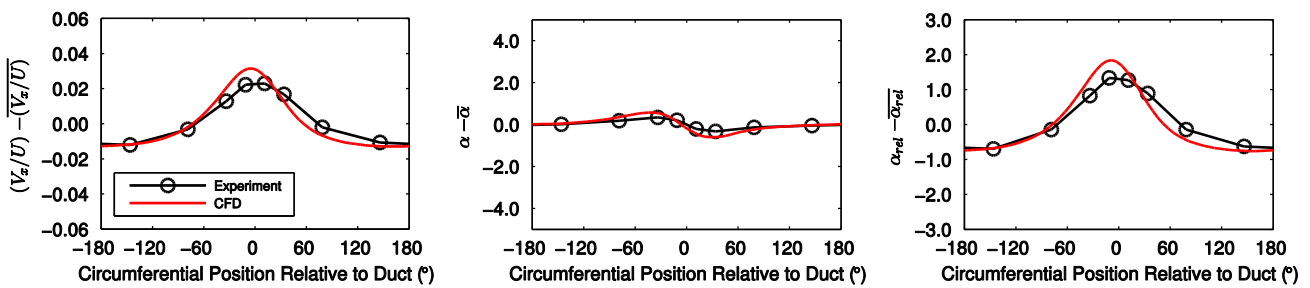
Figure 7.18: CFD calculated contours of absolute velocity coefficient. $\phi_{stage} = 0.43$, bleed rate = 4.1%



(a) Contours of flow coefficient

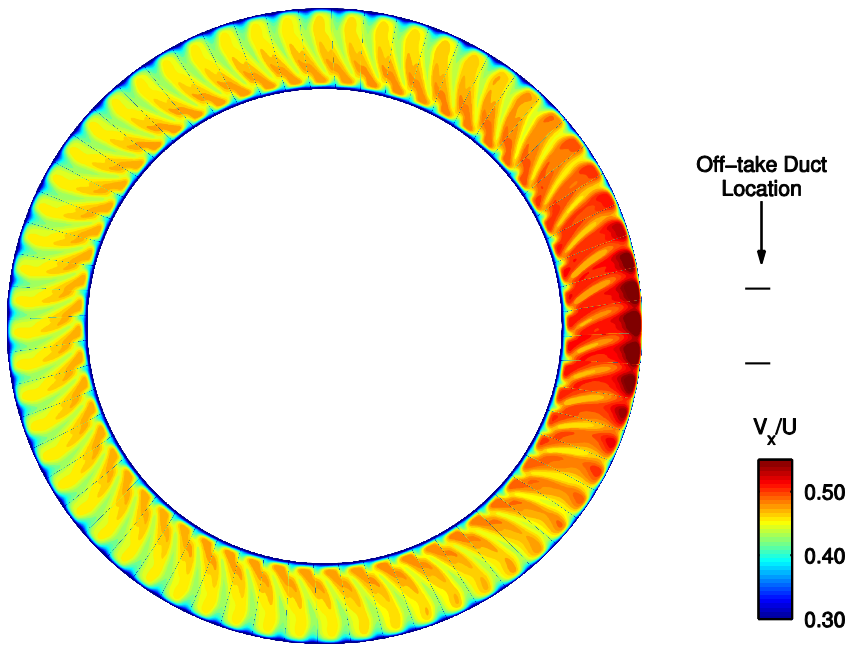


(b) Spanwise distributions. Each line shows the pitch-averaged values for a 6 degree sector

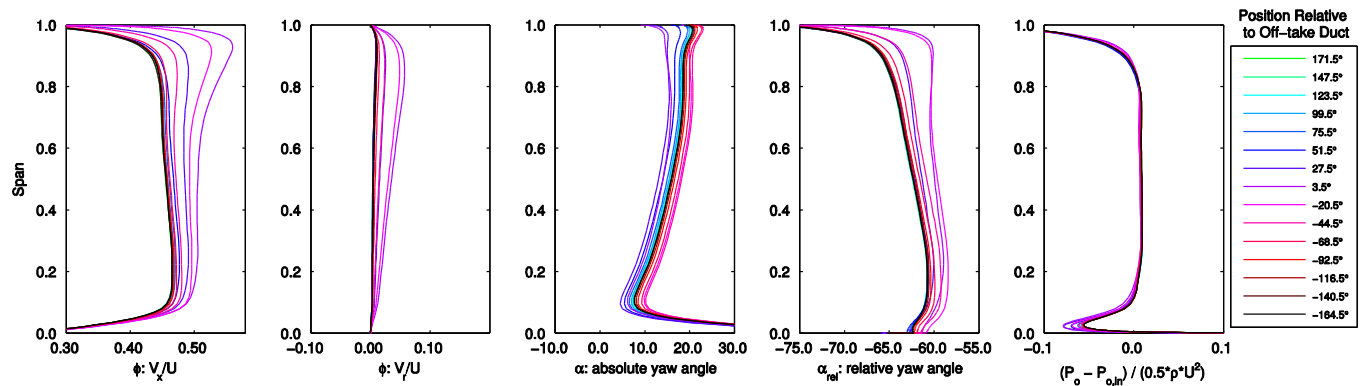


(c) Change in passage-averaged flow coefficient, absolute yaw angle and relative yaw angle compared to annulus-averaged value

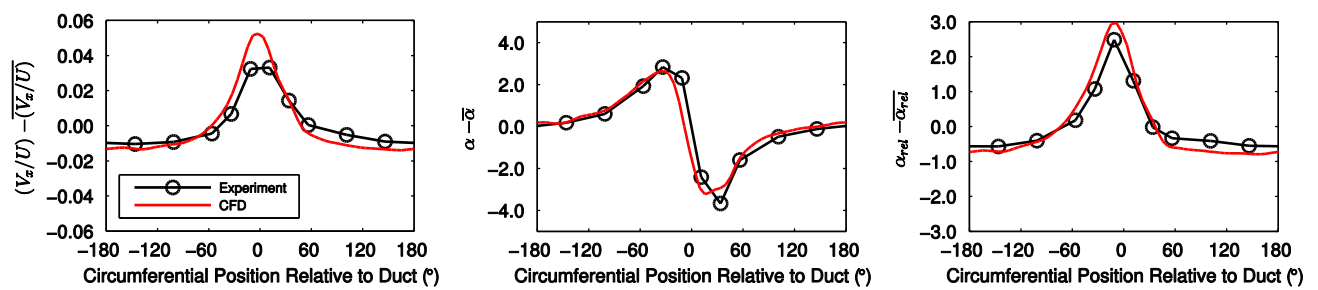
Figure 7.19: Rig inlet, CFD calculated flow field. $\phi_{stage} = 0.43$, bleed rate = 4.2%.



(a) Contours of flow coefficient

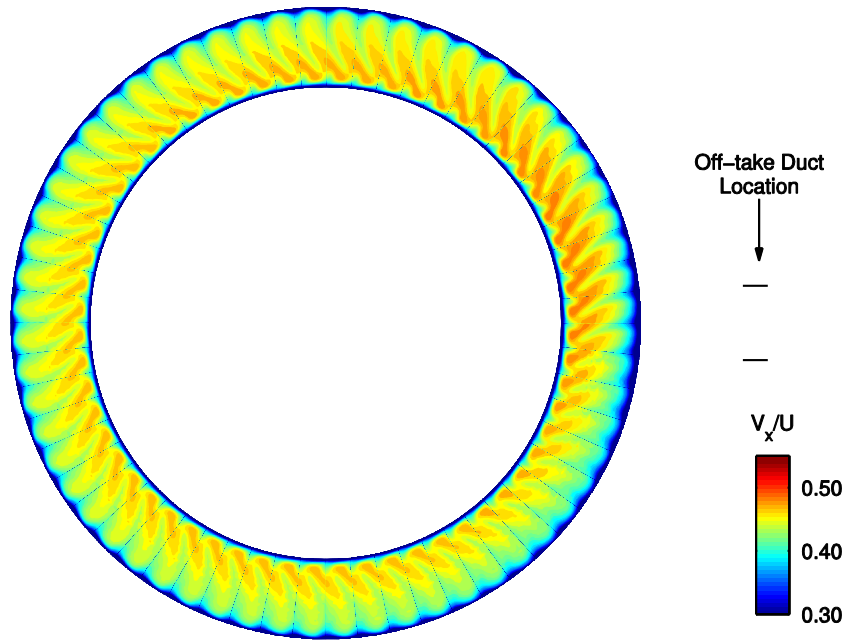


(b) Spanwise distributions. Each line shows the pitch-averaged values for a 6 degree sector

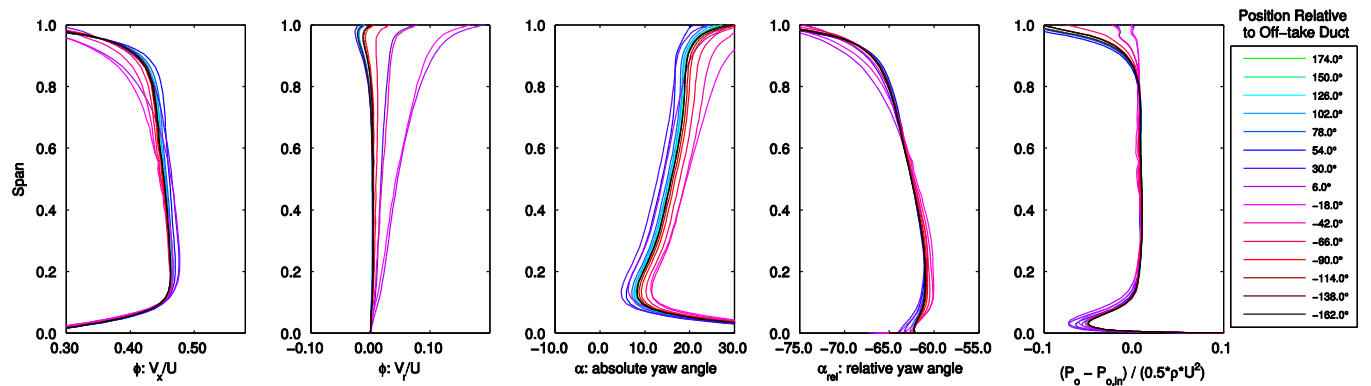


(c) Change in passage-averaged flow coefficient, absolute yaw angle and relative yaw angle compared to annulus-averaged value

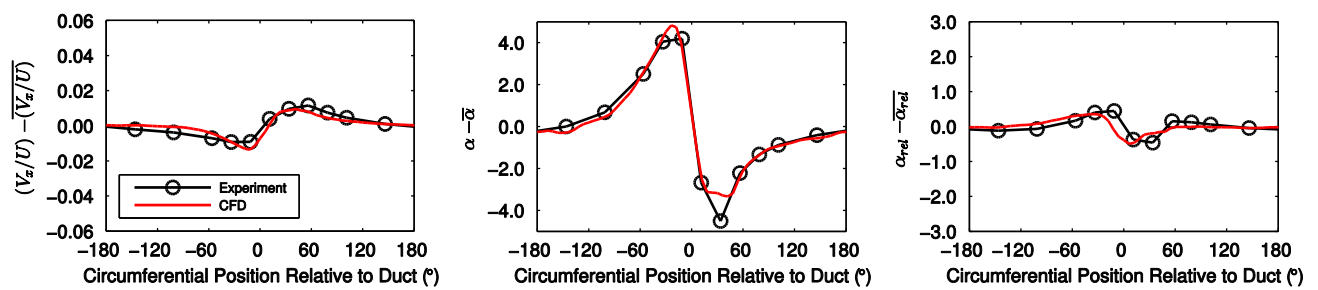
Figure 7.20: Upstream of slot, CFD calculated flow field. $\phi_{stage} = 0.43$, bleed rate = 4.2%.



(a) Contours of flow coefficient

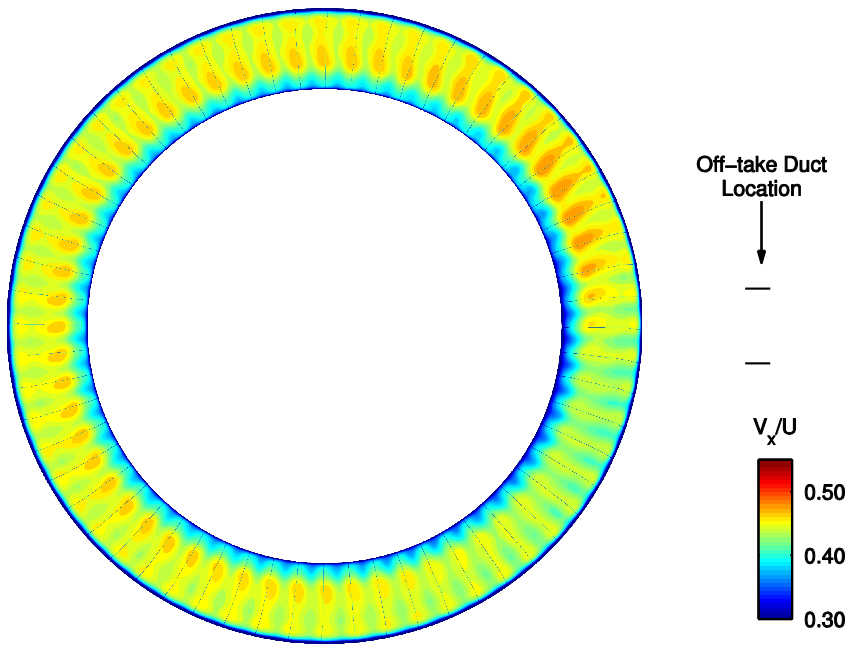


(b) Spanwise distributions. Each line shows the pitch-averaged values for a 6 degree sector

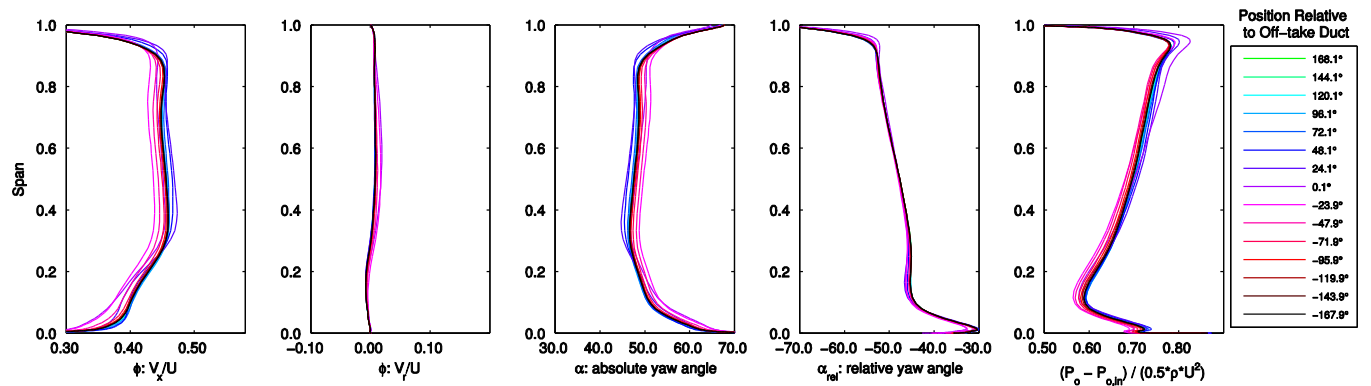


(c) Change in passage-averaged flow coefficient, absolute yaw angle and relative yaw angle compared to annulus-averaged value

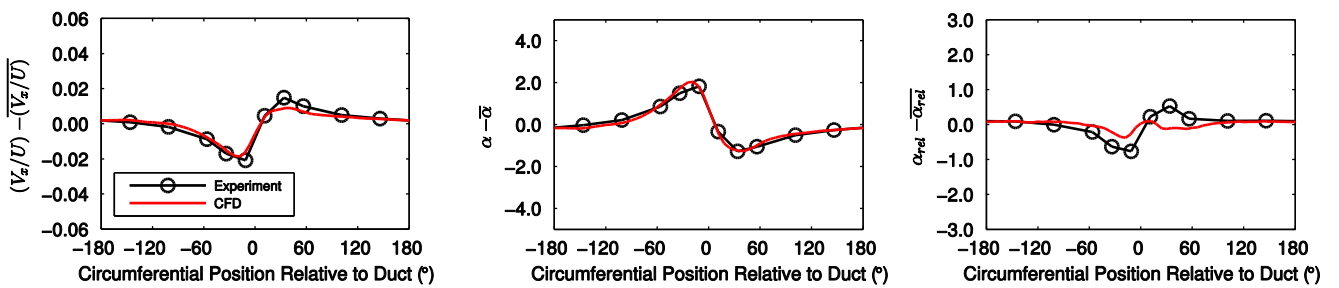
Figure 7.21: Stage inlet, CFD calculated flow field. $\phi_{stage} = 0.43$, bleed rate = 4.2%.



(a) Contours of flow coefficient

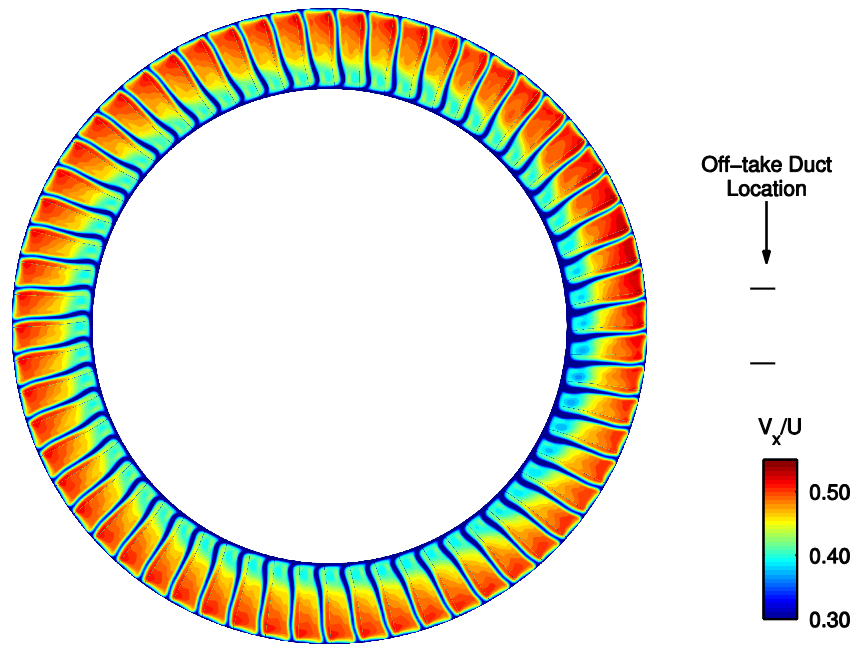


(b) Spanwise distributions. Each line shows the pitch-averaged values for a 6 degree sector

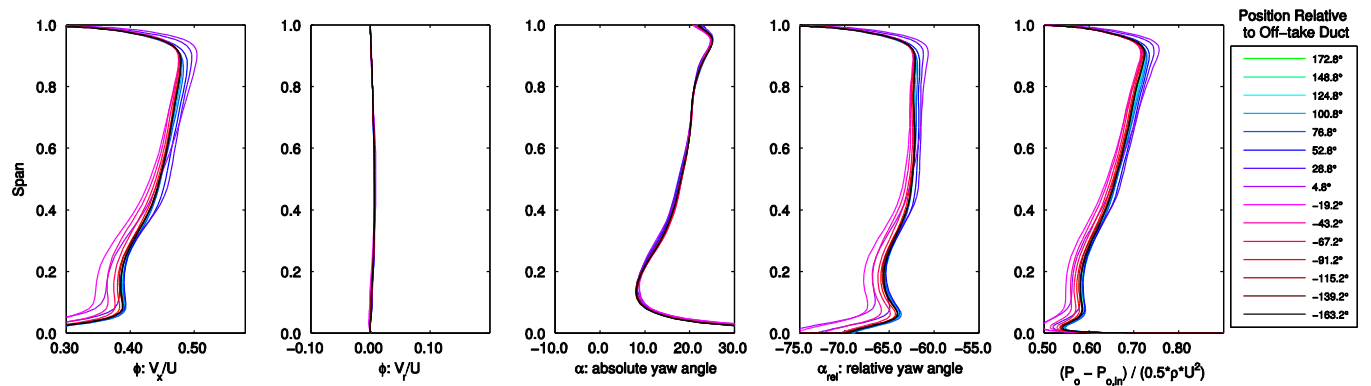


(c) Change in passageway-averaged flow coefficient, absolute yaw angle and relative yaw angle compared to annulus-averaged value

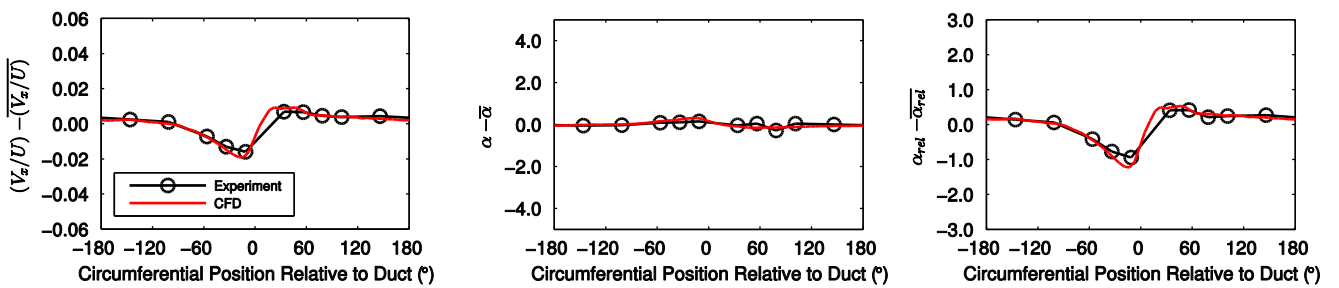
Figure 7.22: Downstream of rotor row, CFD calculated flow field. $\phi_{\text{stage}} = 0.43$, bleed rate = 4.2%.



(a) Contours of flow coefficient



(b) Spanwise distributions. Each line shows the pitch-averaged values for a 6 degree sector



(c) Change in passageway-averaged flow coefficient, absolute yaw angle and relative yaw angle compared to annulus-averaged value

Figure 7.23: Downstream of stator row, CFD calculated flow field. $\phi_{\text{stage}} = 0.43$, bleed rate = 4.2%.

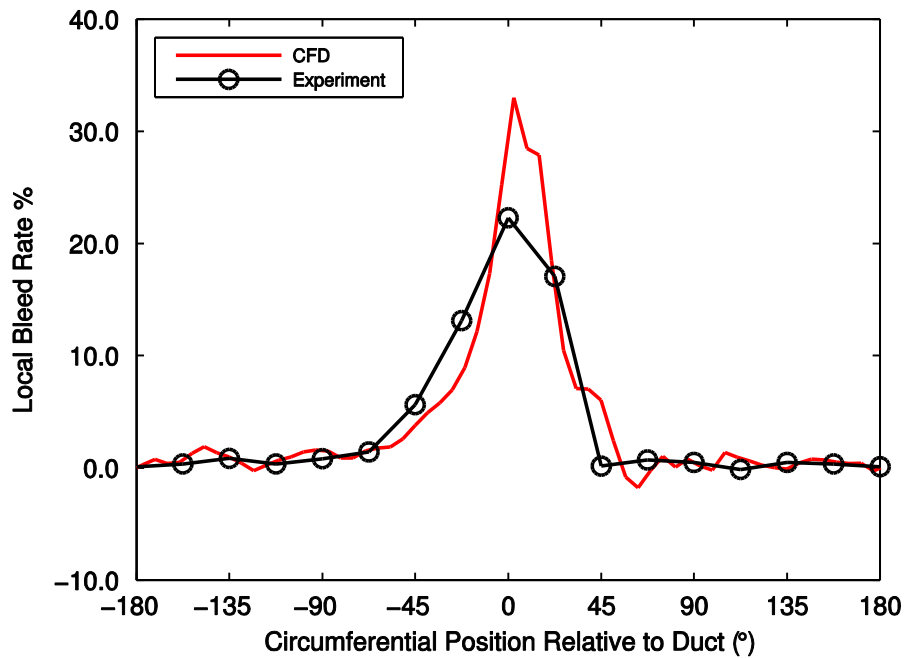
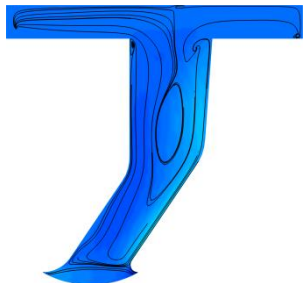
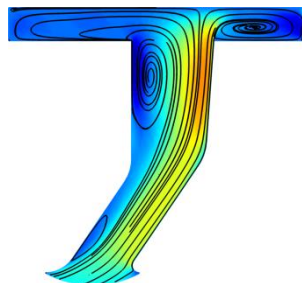


Figure 7.24: CFD calculated local bleed rate at 80% of slot height compared with experimental measurements.

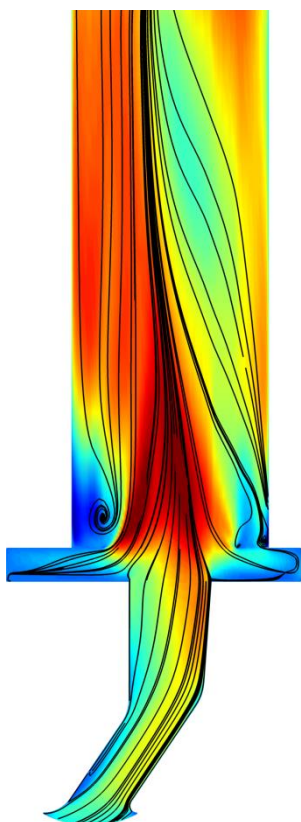
$\phi_{stage} = 0.43$, bleed rate = 4.2%. The CFD local bleed rate is averaged over 6 degree sections.



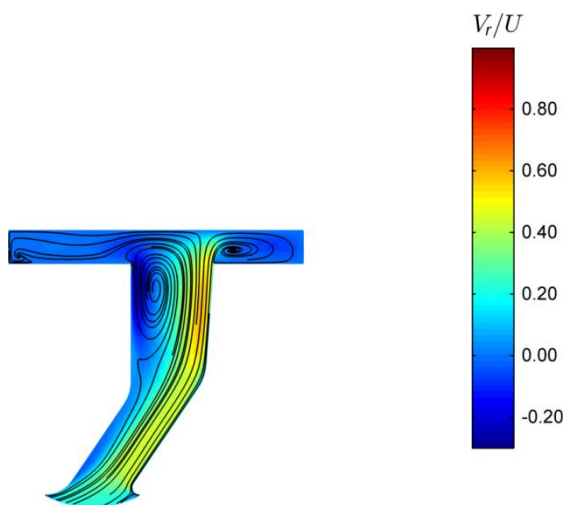
(a) -90 degrees from centre of duct



(b) -10 degrees from centre of duct

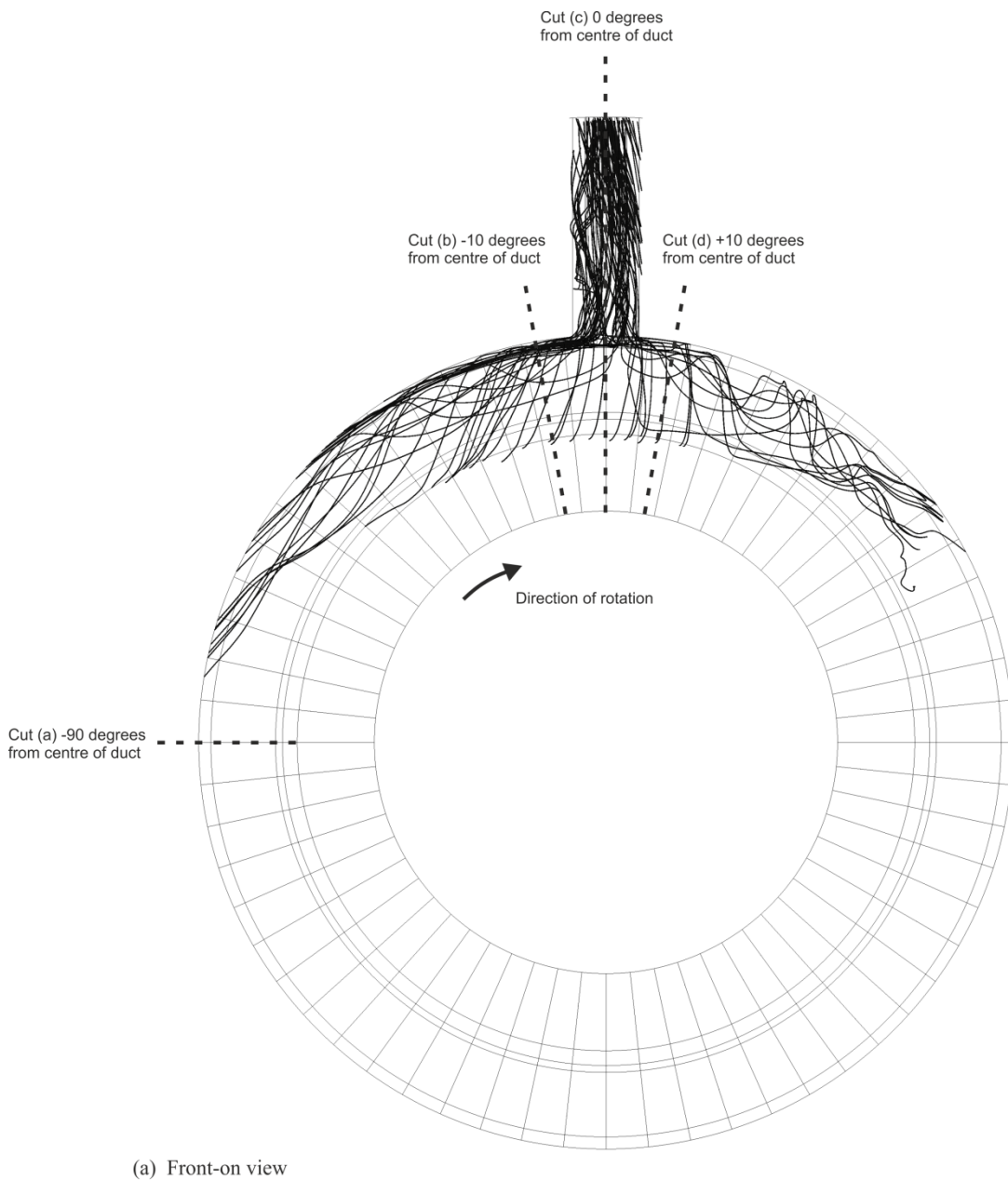


(c) 0 degrees from centre of duct

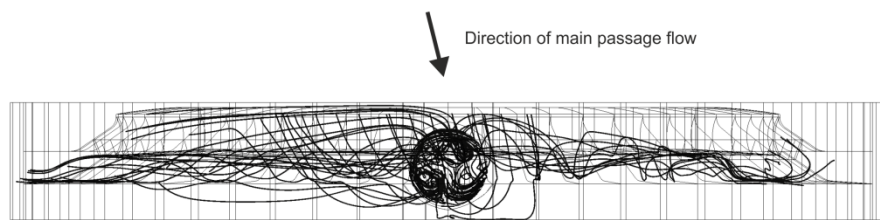


(d) +10 degrees from centre of duct

Figure 7.25: CFD calculated contours of radial velocity coefficient at different circumferential locations. Streamlines overlaid are constrained to the same meridional plane as the contours. $\phi_{stage} = 0.43$, bleed rate = 4.2%.



(a) Front-on view



(b) Top-down view

Figure 7.26: CFD calculated streamlines in bleed system. Streamlines are seeded in the off-take duct and traced backward towards the plenum chamber and bleed slot. $\phi_{stage} = 0.43$, bleed rate = 4.2%.

Chapter 8

Non-Uniform Bleed and Stall

8.1 Introduction

In this chapter the effect of circumferentially non-uniform bleed extraction on the operating range of the downstream stage is investigated. First, the change in stalling flow coefficient with different bleed system configurations is presented. Several measured bleed distributions from sample bleed system configurations are then studied. Finally, a critical sector approach, similar to that used in total pressure inlet distortion studies, is used to characterise the bleed non-uniformity. This produces a new parameter for bleed non-uniformity which is correlated with the reduction in the operating range of the downstream stage.

8.2 Flow Coefficient at Stall

Figure 8.1 shows the stage inlet stalling flow coefficient for a range of bleed system configurations against bleed rate. With a large plenum chamber and four off-take ducts (i.e. uniform bleed extraction), increased bleed reduces the stage inlet flow coefficient at which the compressor stalls. This effect is discussed in Section 5.3 in Chapter 5. For a given bleed rate the stage inlet stalling flow coefficient increases as the number of off-take ducts are reduced from four to one. The operating range, at a given bleed rate, is then further reduced as the plenum chamber size is reduced. These results can be explained by the increase in bleed non-uniformity caused by reducing the number of off-take ducts and reducing the plenum chamber size. Greater bleed non-uniformity increases the range of incidence angles that the downstream rotor blades move through as they rotate around the annulus.

The stage inlet flow coefficient at stall changes with bleed rate as well as with bleed system configuration. The change in stalling flow coefficient for different bleed system configurations should therefore be compared at the same bleed rate. For the rest of this chapter the change in operating range for a given bleed system configuration is defined as the difference between the stage inlet stalling flow coefficient with that configuration compared to the uniform bleed case (large plenum chamber, four off-take ducts) at the same bleed rate.

Figure 8.1 shows how the operating range of the downstream compressor stage is affected by the bleed non-uniformity generated by one off-take duct, i.e. the non-uniform bleed distribution has one peak. The effect of bleed non-uniformity produced by two off-take ducts is also of interest and this introduces another parameter: circumferential spacing between off-take ducts. Figure 8.2 shows the change in stage inlet stalling flow coefficient as the circumferential distance between the centres of the two off-take ducts is varied for bleed rates of 4.14% and 6.23%. As the off-take ducts are moved closer together, from a spacing of 180 degrees to 90 degrees, the change in stage inlet stalling flow coefficient is small: less than 0.001 for the 4.14% bleed rate case and only 0.0027 for the 6.23% bleed rate case. However, for a reduction in off-take duct spacing from 90 degrees to 22.5 degrees the change in stalling flow coefficient increases by 0.0067 with a bleed rate of 4.14% and by 0.0116 with a bleed rate of 6.23%. The change in stalling flow coefficient tends towards that of the one off-take duct cases, as expected. These experiments are reminiscent of the critical sector angle tests performed by Reid [38] in relation to inlet total pressure distortion. Reid tested the effect of changing the size of a stagnation pressure inlet distortion on compressor operating range. He showed that the loss in operating range suddenly increased when a critical sector angle was reached and that one large distorted sector caused a greater loss in operating range than several small sectors with the same total area. In the current work the effect of distortion caused by the individual off-take ducts increases when the ducts are close enough to generate one large distorted sector rather than two separate ones.

8.3 Circumferential Distribution of Bleed

Having measured the effect of different bleed system configurations on operating range, attention is turned to quantifying the effect that these different configurations have on the rate of bleed extraction around the circumference. Figure 8.3 shows the local bleed rate in the bleed slot against circumferential position for four cases that each have a total bleed rate of 4.14%. The uniform bleed rate distribution is also shown. The measurements are taken at $\overline{\phi_{stage}} = 0.43$. The bleed distribution close to stall is not expected to differ from these measurements since the local bleed distribution in the bleed slot is shown not to be affected by compressor operating point in Section 6.2. For the small plenum, one duct case, there is a clear peak in local bleed rate in the bleed slot close to the duct. The peak has a maximum local bleed rate of 22.9% and width of 135 degrees. With the small plenum chamber and two off-take ducts separated by 90 degrees the bleed distribution now has two peaks, in line with the two off-take ducts. The maximum local bleed rate is 14.2%. It can be seen that the two peaks are superimposed since the bleed rate does not drop to 0% between them. The width of the combined peaks is 200 degrees. The third example shown is the small plenum chamber with two off-take ducts separated by 180 degrees. The maximum bleed rate is 14.2% and the peaks in local bleed

rate are in line with the off-take ducts. Between these peaks the bleed rate falls to nearly zero and the width of each peak is 100 degrees. The fourth example shown is the large plenum chamber, one off-take duct configuration in which the non-uniformity in local bleed rate is much less pronounced and the peak bleed rate is 6.9%. In this case the local bleed rate drops to a minimum of 2.9% away from the duct and as expected the overall local bleed rate distribution is much less non-uniform than for the small plenum chamber cases.

8.4 Characterisation of Bleed Non-uniformity

Chapter 6 shows that non-uniform bleed extraction causes a circumferentially non-uniform main annulus flow to enter the downstream stage and a region of increased rotor incidence reduces compressor stability. Ideally the main annulus flow field would be measured for each bleed system configuration in the same way as it is for the case presented in Chapter 6. This data would then be used to characterise the non-uniformity of the flow entering the downstream stage and be correlated against the loss in operating range. In practice, however, these measurements were not possible in the current work and instead the local bleed rate distribution in the slot is used as a proxy for the non-uniformity of the main annulus flow entering the stage. The results in Chapter 6 showed that near stall the peak in bleed flow extraction coincided with a region of reduced flow coefficient and increased rotor incidence into the downstream stage. It is assumed that increasing the peak local bleed rate in the bleed slot reduces the flow coefficient and increases further the rotor incidence in the region close to the off-take duct at stage inlet. It is further assumed that changing the shape of the bleed extraction distribution, e.g. by including two off-take ducts, will be reflected in the non-uniform flow entering the downstream stage. In this way the local bleed rate in the slot is directly linked to the flow at stage inlet and is used in this section to characterise non-uniformity caused by non-uniform bleed extraction.

Figures 8.1 and 8.2 show that loss in operating range of the downstream stage is influenced by the level of bleed non-uniformity and, if there is more than one duct, the spacing between the off-take ducts. These observations point towards a critical sector angle approach and, in the spirit of the $DC(\theta_{crit})$ approach [40], a method to characterise bleed non-uniformity has been developed. Figure 8.4 helps to explain how the method is applied. The bleed distribution for the case with the small plenum chamber, two off-take ducts with 90 degree spacing and bleed rate of 4.14%, is shown along with the uniform bleed distribution. The first step is to calculate the deviation between the measured bleed distribution and the uniform bleed distribution. This is done to reflect how the change in operating range is calculated, i.e. as a difference between the stalling flow coefficients for non-uniform and uniform bleed cases, at the same bleed rate. The deviation from uniform bleed is then averaged over a

fixed sector. The averaging sector is swept through 360 degrees over the entire bleed distribution and the result is plotted in Fig. 8.4 as the “sector-averaged bleed distribution”. The peak value of this average, i.e. from the sector with the greatest local bleed extraction, provides a parameter for the non-uniformity of the bleed distribution called the “peak sector-averaged non-uniformity”. The use of the average sector allows the spacing between two off-take ducts to be included in the bleed non-uniformity characterisation, i.e. bleed from two off-take ducts separated by more than the sector size will result in a lower peak sector-averaged non-uniformity than bleed from two off-take ducts which are separated by less than the sector size.

8.5 Effect of Bleed Non-uniformity on Operating Range

Local bleed distribution measurements in the slot were taken for 32 different cases with varying bleed rates, plenum chamber sizes, number of off-take ducts and, where relevant, different circumferential spacing between the two off-take ducts. The peak sector-averaged non-uniformity is calculated for each of these cases with sector sizes of 1 to 180 degrees. The change in stage inlet flow coefficient at stall was also measured for each case. Figure 8.5 shows the relationship between the bleed non-uniformity and the change in stage inlet stalling flow coefficient for sector sizes of 1 degree, 90 degrees and 180 degrees. Figure 8.6 shows the coefficient of determination, R^2 , for the data best fit line for each of the sector sizes. This shows that the best linear fit for the data is found with an averaging sector of 90 degrees (though sector sizes of 60 degrees and 120 degrees give R^2 values within 4% of that obtained with the 90 degree sector).

Looking at Fig. 8.5(b) in more detail it can be seen that the method developed provides a linear relationship between bleed non-uniformity and loss in operating range for a wide range of different bleed system configurations. For the one off-take duct cases with large, medium or small plenum chambers the bleed non-uniformity increases with bleed rate and there is a subsequent increase in the change in stage inlet stalling flow coefficient. The two off-take duct cases are grouped so that each set has the same bleed rate and plenum chamber size but varying circumferential spacing between the off-take ducts. The figure shows that cases with off-take duct spacings of 180, 135 and 90 degrees have similar values of bleed non-uniformity and a similar reduction in operating range. Only with an off-take duct separation of 45 degrees is there a significant increase in bleed non-uniformity and a reduction in the operating range of the downstream stage.

The correlation shown in Fig. 8.5(b) is useful in an integrated compressor bleed system design process and could be used as follows:

- The impact of different bleed systems on compressor stability can be compared using the peak sector-averaged approach. For example, if one bleed configuration has a lower peak

sector-averaged bleed non-uniformity then it will have less of a negative impact on compressor operating range.

- The performance of bleed system design features which act to reduce bleed non-uniformity (such as non-axisymmetric slot design or a circumferentially varying plenum cross-section) can be quantified and compared using the peak sector-average approach.
- If the reduction in operating range caused by a particular distribution of non-uniform bleed is known then the bleed non-uniformity and change in stalling flow coefficient can be plotted for that particular case. Given that the uniform bleed rate case will have a bleed non-uniformity of zero and no change in stalling flow coefficient, a straight line can be plotted and the change in operating range caused by new bleed distributions can be predicted.

8.6 Conclusions

The following conclusions can be drawn from this chapter:

1. Changing the bleed system configuration so that the bleed distribution becomes more non-uniform reduces the operating range of a downstream stage.
2. For bleed systems with two off-take ducts the circumferential separation between the centres of the off-take ducts affects compressor stability. There is a critical off-take duct spacing (found in this work to be 90 degrees) above which downstream stage operating range is not significantly affected and below which the stalling flow coefficient increases as the ducts are moved closer together.
3. Whatever the configuration of bleed system, the non-uniform distribution of relative flow angle at inlet to the downstream rotor – the rotor incidence variation - determines the impact of the non-uniformity on the stability of the downstream stage. The local bleed rate distribution, measured in the bleed slot, provides a proxy which can be used to characterise the non-uniformity caused by the bleed system.
4. Non-uniform bleed can be characterised with the peak sector-averaged non-uniformity which takes inspiration from the $DC(\theta_{crit})$ method used to characterise stagnation pressure inlet distortion tests. This new parameter takes account of different bleed rates and bleed system configurations including the spacing between two off-take ducts.
5. For the compressor under test, and, it is inferred, for comparable compressors with similar hub-to-tip radius ratios, the change in flow coefficient at stall between cases with non-

uniform bleed and uniform bleed (at the same bleed rate) is found to correlate with the peak sector-averaged non-uniformity. This process allows any bleed system to be characterized in terms of its impact on compressor stability.

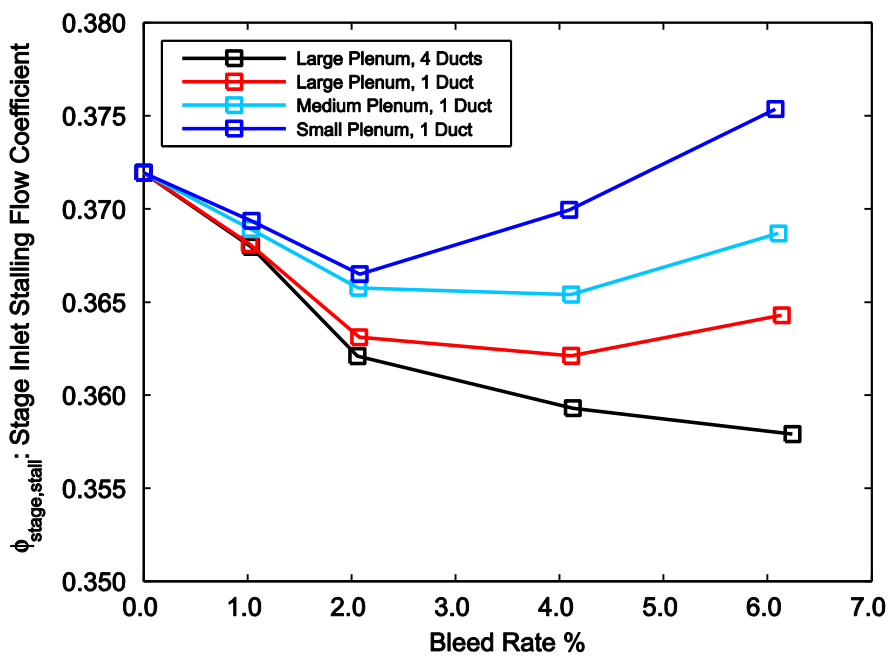


Figure 8.1: Stage inlet flow coefficient at stall against bleed rate for different bleed system configurations.

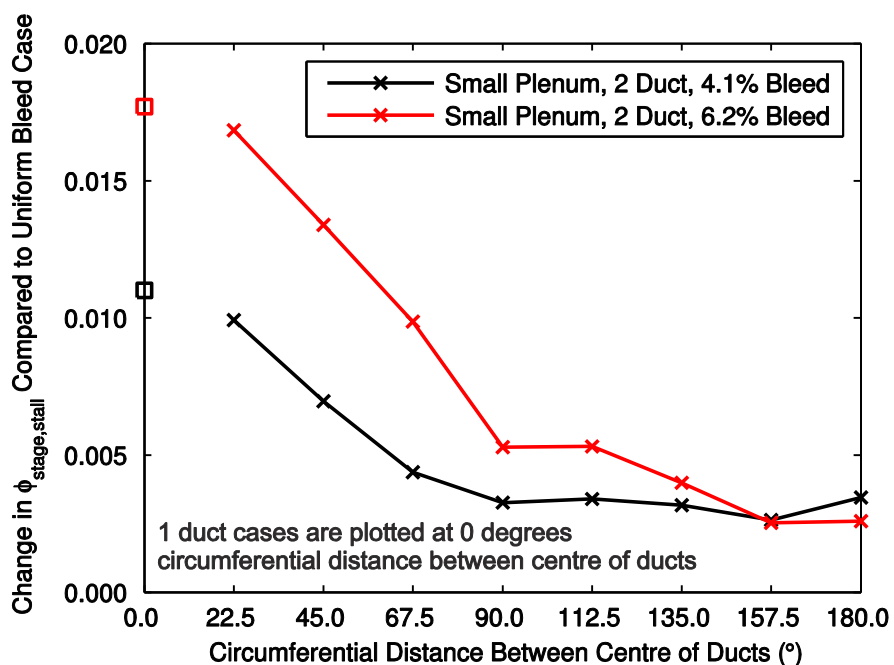


Figure 8.2: Variation of stage inlet flow coefficient at stall with angular separation of two off-take ducts.

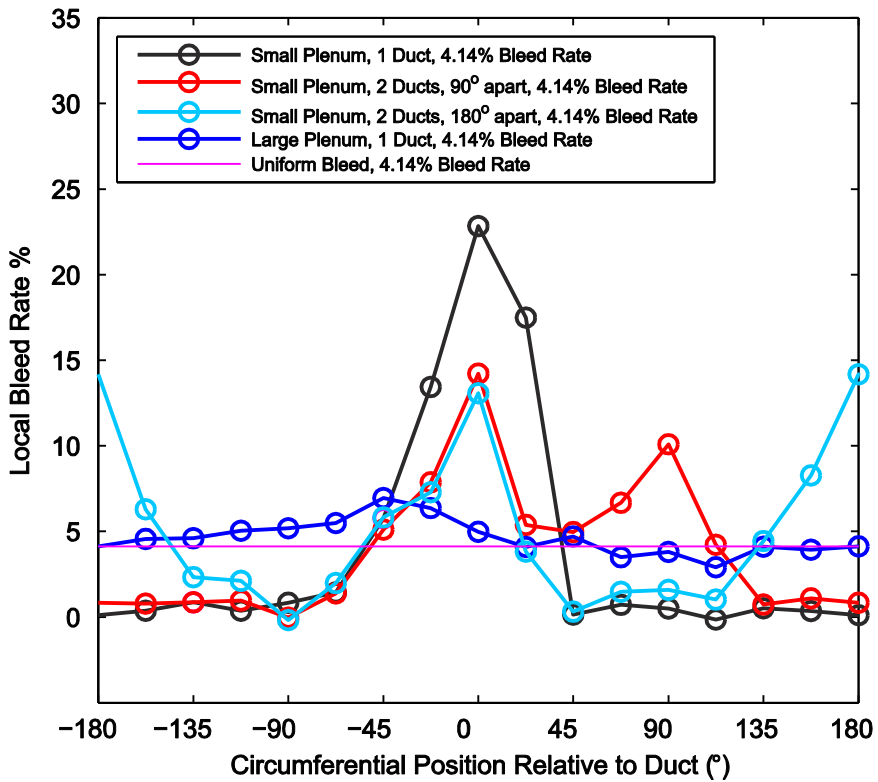


Figure 8.3: Variation of local bleed rate in slot with circumferential position relative to off-take duct.

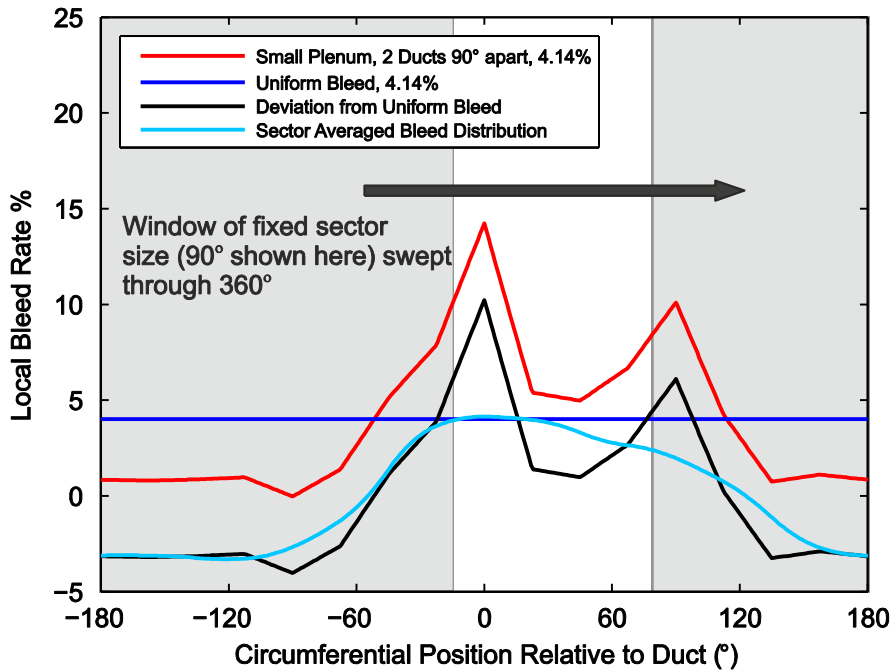
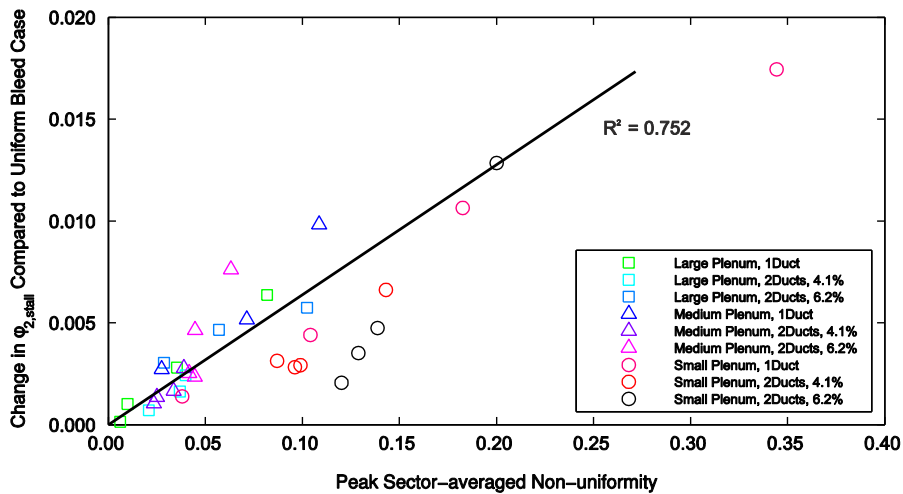
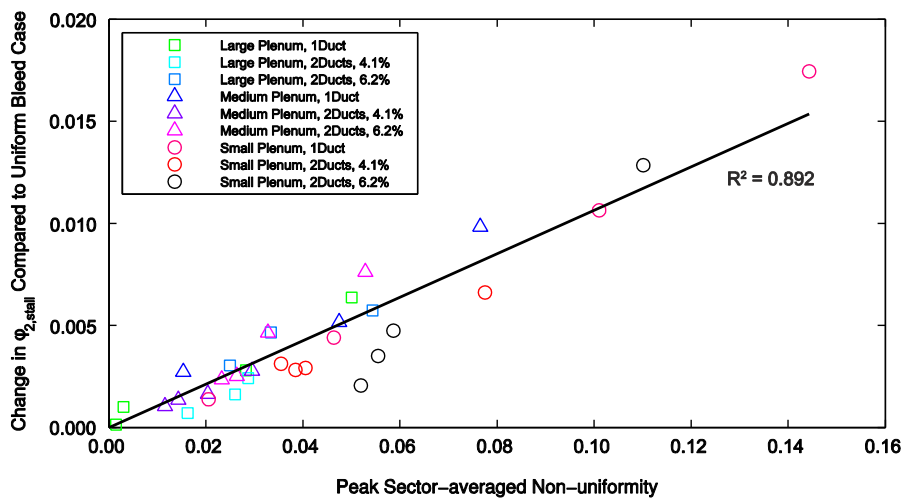


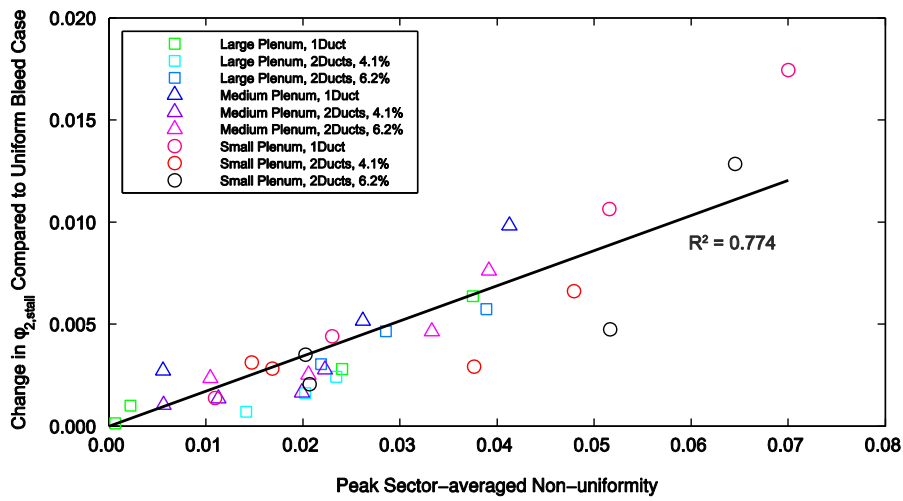
Figure 8.4: Method for obtaining the peak sector-averaged bleed non-uniformity.



(a) 1 degree sector



(b) 90 degree sector



(c) 150 degree sector

Figure 8.5: Change in stage inlet flow coefficient at stall with peak sector-averaged non-uniformity evaluated with different sector sizes.

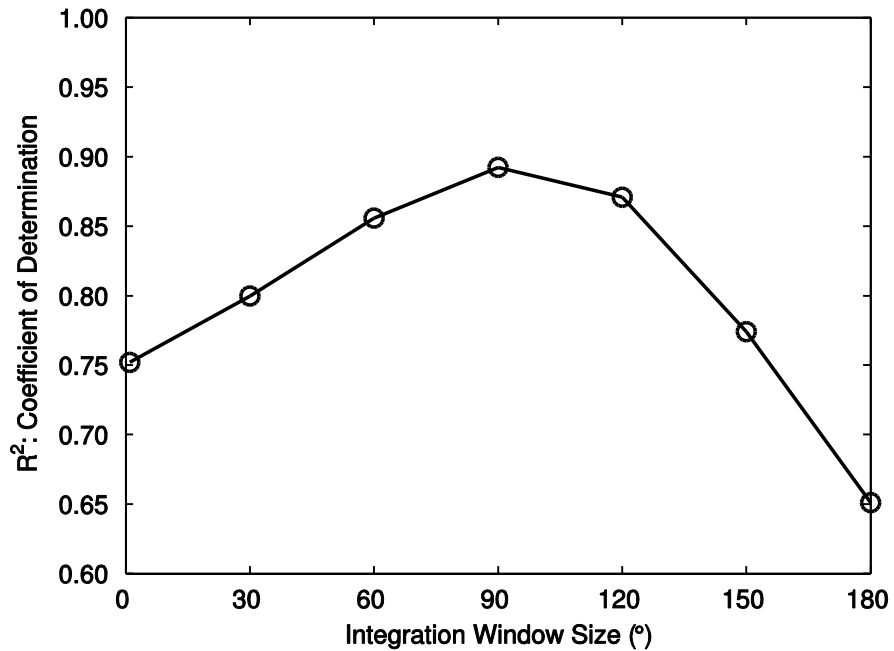


Figure 8.6: Variation of coefficient of determination, R^2 , with sector size.

Chapter 9

Conclusions and Suggestions for Future Work

9.1 Introduction

This dissertation presents a study of the effect of uniform and non-uniform axial compressor bleed on the performance of a single compressor stage downstream of an axisymmetric bleed slot, and on the flow through the bleed system. The key conclusions from the study are listed in three sections: Uniform Bleed, Non-uniform Bleed, and Non-uniform Bleed and Stall. A fourth section then provides suggestions for future work.

9.2 Uniform Bleed

Experimental tests and CFD calculations were performed to investigate the effect of circumferentially uniform bleed on the performance of the downstream stage. For bleed rates typical of a design operating point (i.e. between 0% and 6.23%) bleed extraction is shown to have a small effect on the spanwise distribution of flow upstream and downstream of the bleed slot, i.e. at stage inlet the flow coefficient does not change by more than 2.3% at any point across the span. With limited spanwise redistribution of the mainstream flow, pressure rise and efficiency characteristics collapse towards one line when plotted against stage inlet flow coefficient so that the reduction in stage total-to-static pressure rise at $\phi_{stage} = 0.43$ is 2.5% and the change in peak stage efficiency is 0.3% points for the case with a bleed rate of 6.23% compared with 0%.

The test compressor stalls with a “spike-type” stall inception mechanism and this does not change for any of the bleed rates and configurations tested in this work. It is found that the stage inlet stalling flow coefficient reduces by 3.8% as bleed rate is increased from 0% to 6.23%. This effect can only be understood by examining the spanwise redistribution of the flow due to bleed. At stage inlet, the experimental measurements and CFD calculations show that increasing bleed rate reduces the rotor incidence in the rotor tip region by up to 1 degree and hence stall inception is delayed to lower

flow coefficients. The changes in spanwise distribution also account for the small reduction in stage pressure rise and efficiency with bleed.

The experimental results show that the reduction in efficiency due to the bleed system increases with bleed rate and this results in a reduction in overall rig efficiency. A loss coefficient has been defined which characterises the loss in the bleed system and is constant to within $\pm 1.1\%$ for the different operating points and bleed rates tested.

Single passage, unsteady calculations with bleed flow extracted from the top of the bleed slot are able to model the spanwise redistribution of flow caused by varying bleed rate. The CFD calculations agree well with the experimental measurements for $\phi_{stage} > 0.41$. Below this flow coefficient the rotor and stator hub corner separation sizes are exaggerated by the CFD calculations so that the spanwise distributions do not agree with traverse data and the computed pressure rise characteristics drop below the measured characteristics. At $\phi_{stage} = 0.38$ the CFD calculated stage total-to-static pressure rise characteristic, for the case with a bleed rate of 0%, is 5.9% lower than the measured value.

The measured and computed overall and stage efficiency characteristics do not match well. For the stage efficiency this is because of differences in blade profile loss and rotor and stator hub separation size. For the overall efficiency the loss due to the bleed flow is also important. With the single passage calculations the losses in the plenum chamber and off-take duct are not included and the loss in efficiency due to bleed is 38% less than that measured experimentally. A quarter annulus CFD calculation which includes the bleed system with the large plenum chamber, one off-take duct (i.e. four ducts per annulus) and a bleed rate of 4.1% shows that 67% of the loss occurs in the bleed slot, 25% in the plenum chamber and 8% in the off-take duct. The overall bleed flow loss coefficient in the quarter annulus calculation is within 8% of the experimentally measured value.

9.3 Non-uniform Bleed

The bleed system configuration with the small plenum chamber, one off-take duct and a bleed rate of 4.14% was tested experimentally and modelled with a full annulus CFD calculation. Both the CFD and experimental results show that for this configuration the bleed extraction is strongly non-uniform with a measured peak local bleed rate of 22.9%. The experimental tests show that the annulus-averaged stage inlet stalling flow coefficient is increased by 3.0% compared to the uniform bleed case with the same bleed rate.

Experimental area traverses and the CFD calculation show that non-uniform bleed extraction causes a circumferential redistribution of the main annulus flow upstream and downstream of the

bleed slot. Non-uniform flow coefficient and yaw angle distributions are created by the circumferentially non-uniform pressure field associated with the discrete off-take duct. The shape of the stage static-to-static pressure rise characteristic means that at the design operating point (and over much of its operating range) the compressor acts to reduce the non-uniformity of the flow at stage inlet. The CFD calculation matches the measurements at this operating point because the mechanism driving the changes in the main annulus flow is an inviscid, potential flow effect and the response of the coupled downstream stage is modelled correctly by the CFD.

At reduced flow coefficients (approaching stall) the stage static-to-static pressure rise coefficient becomes flat so the compressor cannot reduce the non-uniformity caused by the bleed extraction. At stage inlet, therefore, there is a region of increased rotor incidence of up to 1.0 degree (passage-averaged). It is this region of increased rotor incidence which causes the downstream stage to stall at higher annulus-averaged stage inlet flow coefficient. A pitch-averaged analysis of the flow around the annulus, which captures variations in spanwise distribution of the flow, shows that the increase in rotor incidence close to the off-take duct position is up to 2.0 degrees near to the casing. This exacerbates the effect on operating range since incidence induced rotor tip separation is thought to initiate spike-type stall.

The non-uniform circumferential distribution of flow does not reduce the annulus-averaged pressure rise but the stage efficiency is reduced; with a bleed rate of 6.23% the peak stage efficiency for the case with the small plenum chamber and one off-take duct is 0.5% points lower than the case with the large plenum chamber and four off-take ducts.

The reduction in efficiency due to loss in the bleed flow increases as the bleed flow becomes more non-uniform and the peak velocities increase; with the small plenum chamber, one off-take duct and a bleed rate of 4.14% the reduction in efficiency at $\overline{\phi_{stage}} = 0.43$ is 3.3% points. A model has been developed which correlates the local bleed rate distribution with the bleed system loss coefficient.

CFD shows that the flow in the bleed system for the small plenum chamber, one off-take duct, 4.14% bleed rate case, includes a separation in the bleed slot which varies in size depending on the local bleed rate, counter rotating vortices in the plenum chamber and bleed slot which are drawn into the off-take duct, and a large separation at the inlet to the duct. Further CFD calculations with different bleed system configurations and bleed rates are required to understand and characterise the impact of these flow features on bleed system loss.

9.4 Non-uniform Bleed and Stall

Having shown that non-uniform bleed in one particular case reduces compressor operating range, the experimental rig is used to assess the effect of different bleed system configurations on stage inlet stalling flow coefficient. The results show that changing the bleed system configuration so that the bleed distribution becomes more non-uniform reduces the operating range of the downstream stage. For bleed systems with two off-take ducts the circumferential separation between the centres of the off-take ducts also affects compressor stability.

Whatever the configuration of bleed system, the non-uniform distribution of rotor incidence determines the stability of the downstream stage. The local bleed rate distribution, measured in the bleed slot, provides a proxy for the stage inlet rotor incidence distribution which can be characterised and correlated with the loss in operating range of the downstream stage.

Non-uniform bleed is characterised with the peak sector-averaged bleed non-uniformity which takes inspiration from the $DC(\theta_{crit})$ method used to characterise stagnation pressure inlet distortion. This new parameter takes account of different bleed rates and bleed system configurations including the spacing between two off-take ducts. For the compressor under test, and, it is inferred, for comparable compressors with similar hub-to-tip radius ratios, the change in flow coefficient at stall between cases with non-uniform bleed and uniform bleed (at the same bleed rate) is found to correlate with the peak sector-averaged bleed non-uniformity.

9.5 Suggestions for Future Work

This work has shown that a region of increased rotor incidence, caused by a non-uniform static pressure field associated with non-uniform bleed extraction, is responsible for reducing the operating range of a downstream compressor stage. The six unsteady pressure transducers located near the rotor tip are able to show that the compressor stalls with the spike-type stall inception mechanism. However, the unsteady pressure transducers are evenly spaced around the annulus and cannot locate where the spike is initially formed. The current rig can be modified to have the unsteady pressure transducers positioned close together so that they record the formation of the spike as it passes through the region of high rotor incidence. Capturing this event would strengthen the conclusion that reduced operating range is caused by a region of increased rotor incidence. The full annulus unsteady CFD could also be used to simulate the formation of the spike using a similar method to that employed by Pullan et al [35].

A link between non-uniform bleed distribution and a reduction in operating range of a downstream stage has been established for one specific compressor design. It is assumed that

compressors that stall with spikes and that have a high hub-to-tip ratio (~0.75) will respond to non-uniform bleed extraction in a similar manner to the test compressor. This assumption can be tested with the current rig by restaggering the rotor blades to provide a compressor with different loading and hence a different pressure rise characteristic. The pressure rise characteristic would also be changed by increasing the tip clearance. This might also, at tip clearances greater than 3% of rotor chord, change the stalling mechanism to modes [51]. For these different compressor configurations the effect of uniform and non-uniform bleed on operating range can be tested and the conclusions of this work assessed.

The current work has not investigated the effect of non-uniform bleed extraction on an upstream stage or what effect the upstream stage has on the distribution of the non-uniform flow entering the downstream stage. For example, the region of low static pressure associated with the non-uniform bleed extraction at the exit of the upstream stage will cause a non-uniform stagnation pressure to be delivered to the stage downstream of the bleed slot. The stators in the upstream stage will also constrain the yaw angle variation upstream of the bleed slot. The full annulus CFD calculation can be updated to include an upstream stage, allowing its effect on the flow field to be investigated. Similarly, an upstream stage can be added to the current experimental rig and area traverses performed to investigate the flow field.

For a handling bleed case, where mid stage bleed quantities can be much higher than those investigated here (up to 20%), the resulting stage matching can affect the stall margin of both upstream and downstream compressor stages. The change in stall margin of the downstream stage, reported in this work, is additional to that caused by the stage re-matching and should be taken into account if non-uniform bleed extraction is expected. Multi-passage, multi-stage CFD calculations with handling bleed rates and off design operating conditions could investigate this though the computational resource required would be extremely large. Alternatively a lower order model, validated against the current results could be developed and applied to investigate whether non-uniform handling bleed is a significant issue.

The idea of a non-axisymmetric bleed slot or plenum chamber which reduces the non-uniformity of the bleed extraction has been discussed throughout this project. The CFD methods developed in the current work can now be used to assess a redesigned bleed system for its ability to redistribute the flow in the bleed slot and reduce the non-uniformity of the flow entering the downstream stage. Once a promising geometry has been selected it can be tested in the experimental rig; its peak sector-averaged non-uniformity can be calculated and the improvement in operating range measured.

The work by Leishman [11,15,17,18] shows that pressure loss through the bleed system can be reduced by redesigning the bleed slot shape to minimise the size of the separation and decrease the

speed of the flow entering the plenum chamber. CFD can be used to assess different slot shapes and their effect on the flow through the bleed system. Once an improved slot design has been identified it can be tested in the experimental rig and the improvement in bleed system loss, and overall efficiency, can be measured.

References

- [1] International Energy Agency (IEA). World Energy Outlook 2011.
- [2] Intergovernmental Panel on Climate Change (IPCC). Climate Change 2013: The Physical Science Basis, Summary for Policymakers. Working Group 1 Contribution to the *Fifth Assessment Report of the Intergovernmental Panel on Climate Change*.
- [3] The United Kingdom's Climate Change Act of 2008, Chapter 27.
- [4] European Parliament and the Council of the European Union. Establishing a Scheme for Greenhouse Gas Emission Allowance Trading within the Community. *Directive 2003/87/EC*, October 2003
- [5] United Nations. Kyoto Protocol to the United Nations Framework Convention on Climate Change (UNFCCC), 1998.
- [6] US Energy Information Administration (EIA). Levelized Cost of New Generation Resources in the Annual Energy Outlook 2013, January 2013.
- [7] European Commission Joint Research Centre and Institute for Advanced Materials. Greenhouse Gas Emissions from Fossil Fuel Fired Power Generation Systems, 2001.
- [8] Eurelectric. Flexible Generation: Backing up Renewables, October 2011.
- [9] Grace, D. S. Combined-cycle Power Plant Maintenance Costs. Presented at *ASME Turbo Expo: Power for Land, Sea and Air, Berlin, Germany*, GT2008-51357, June 2008.
- [10] Gomes, R., Schwarz, C. & Pfitzner, M. Aerodynamic Investigations of a Compressor Bleed Air Configuration typical for Aeroengines. Presented at *XVII International Symposium on Air Breathing Engines, Munich, Germany*, ISABE-2005-1264, 2005.
- [11] Leishman, B. & Cumpsty, N. Mechanism of the Interaction of a Ramped Bleed Slot with the Primary Flow. *ASME Journal of Turbomachinery*, 129:669-678, October 2007.
- [12] Conan, F. & Savarese, S. Bleed Airflow CFD Modelling in Aerodynamic Simulations of Jet Engine Compressors. Presented at *ASME International Gas Turbine and Aeroengine Congress and Exhibition, New Orleans, LA*, 2001-GT-544, June 2001.
- [13] Wellborn, S. R. & Koir, M. Bleed Flow Interactions with an Axial-flow Compressor Powerstream. Presented at *AIAA/ASME Joint Propulsion Conference and Exhibit, Indianapolis, Indiana*, AIAA 2002-4057, July 2002.

- [14] Elmendorf, W., Mildner, F., Roper, R., Kruger, U. & Kluck, M. Three-dimensional Analysis of a Multistage Compressor Flow Field. Presented at *ASME International Gas Turbine and Aeroengine Congress and Exhibition, Stockholm, Sweden*, 98-GT-249, 1998.
- [15] Leishman, B. The Aerodynamic Behaviour and Design of Compressor Bleed Slots. *Ph.D. thesis, University of Cambridge, Department of Engineering*, 2003.
- [16] Bowman, R. Bleed Slot Efficiency Investigation. *M.Eng dissertation, University of Cambridge, Department of Engineering*, 1996.
- [17] Leishman, B., Cumpsty, N. A. & Denton, J. Effects of Bleed Rate and Endwall Location on the Aerodynamic Behaviour of a Circular Hole Bleed Off-take. *ASME Journal of Turbomachinery*, 129:645-658, October 2007.
- [18] Leishman, B., Cumpsty, N. A. & Denton, J. Effect of Inlet Ramp Surfaces on the Aerodynamic Behaviour of Bleed Hole and Bleed Slot Off-take Configurations. *ASME Journal of Turbomachinery*, 129:659-668, October 2007.
- [19] Wellborn, S.R. & Okiishi, T.H. The Influence of Shrouded Stator Cavity Flows on Multistage Compressor Performance. *ASME Journal of Turbomachinery*, 121:486-497, 1999.
- [20] Wellborn, S.R., Tolchinsky, I. & Okiishi, T.H. Modelling Shrouded Stator Cavity Flows in Axial-flow Compressors. *ASME Journal of Turbomachinery*, 122:55-61, January 2000.
- [21] Demargne, A. & Longley, J. Cavity and Protrusion Effects in a Single-stage Compressor. Presented at *International Gas Turbine and Aeroengine Congress and Exhibition, New Orleans, LA*, 2001-GT-433, June 2001.
- [22] Gummer, V., Goller, M. & Swoboda, M. Numerical Investigations of Endwall Boundary Layer Removal on Highly Loaded Axial Compressor Blade Rows. *ASME Journal of Turbomachinery*, 130:011015, January 2008.
- [23] Di Mare, L., Simpson, G., Mueck, B. & Sayma, A. Effect of Bleed Flows on Flutter and Forced Response of Core Compressors. Presented at *ASME Turbo Expo: Power for Land, Sea and Air, Barcelona, Spain*, GT2006-90683, May 2006.
- [24] Mossman, E. & Randall, L. An Experimental Investigation of the Design Variables for NACA Submerged Duct Entrances. *NACA Research Memorandum A7130*, 1948.
- [25] Dennard, J. A Transonic Investigation of the Mass-flow and Pressure Recovery Characteristics of several types of Auxiliary Air Inlets. *NACA Research Memorandum L57B07*, 1957.
- [26] Gomes, R. & Schwarz, C. Experimental Investigation of a Generic Compressor Bleed System. Presented at *ASME Turbo Expo: Power for Land, Sea and Air, Barcelona, Spain*, GT2006-

- 90458, May 2006.
- [27] Stenning, A. H. Rotating Stall and Surge. *ASME Journal of Fluids Engineering*, 102:14-20, March 1980.
 - [28] Emmons, H. W., Pearson, C. E. & Grant, H. P. Compressor Surge and Stall Propagation. *Transactions of the ASME*, 0:455–469, 1955.
 - [29] Day, I. J., Greitzer, E. M. & Cumpsty, N. A. Prediction of Compressor Performance in Rotating Stall. *ASME Journal of Engineering for Power*, 100(1):1-14, January 1978.
 - [30] Greitzer, E. M. Review - Axial Compressor Stall Phenomena. *ASME Journal of Fluids Engineering*, 102:134-151, June 1980.
 - [31] Moore, F. K. & Greitzer, E. M. A Theory of Post-stall Transients in Axial Compression Systems: Part i – development of equations. *ASME Journal of Engineering for Gas Turbines and Power*, 108:68-76, Jan 1986.
 - [32] McDougall, N. M. Stall Inception in Axial Compressors. *Ph.D. thesis, University of Cambridge*, March 1988.
 - [33] Day, I. J. Stall Inception in Axial Flow Compressors. *ASME Journal of Turbomachinery*, 115:1-9, January 1993.
 - [34] Camp, T. R. & Day, I. J. A Study of Spike and Modal Stall Inception in a Lowspeed Axial Compressor. *ASME Journal of Turbomachinery*, 120:393-401, July 1998.
 - [35] Pullan, G., Young, A. M., Day, I. J., Greitzer, E. M. & Spakovský, Z. S. Origins and Structure of Spike-type Rotating Stall. Presented at *ASME Turbo Expo, Copenhagen, Denmark*, GT2012-68707, June 2012.
 - [36] Dickens, A. M. J. Highly Loaded Compressors. *PhD thesis, University of Cambridge*, 2008.
 - [37] Simpson, A. K. & Longley, J. P. An Experimental Study of the Inception of Rotating Stall in a Single-stage Low-speed Axial Compressor. Presented at *ASME Turbo Expo, Montreal, Canada*, GT2007-27181, May 2007.
 - [38] Reid, C. The Response of Axial Flow Compressors to Intake Flow Distortion. *ASME Journal of Turbomachinery*, 90-GT-29, 1969.
 - [39] Pearson, H. & McKenzie, A. B. Wakes in Axial Compressors. *Journal of the Royal Aeronautical Society*, 415-416, 1959.
 - [40] Hercock, R. & Williams, D. D. Aerodynamic Response. *Distortion Induced Engine Instability, AGARD Lecture Series*, LS72-3, 1974.
 - [41] Gundy-Burlet, K. L. & Dorney, D. J. Physics of Airfoil Clocking in Axial Compressors.

- Presented at *ASME TurboExpo: Power for Land, Sea and Air*, 97-GT-44, 1997.
- [42] Dunkley, M. J. The Aerodynamics of Intermediate Pressure Turbines. *Ph.D. thesis, University of Cambridge, Department of Engineering*, 1998.
 - [43] Dominy, R. G. & Hodson, H. P. An Investigation of Factors Influencing the Calibration of Five-hole Probes for Three-dimensional Flow Measurements. *ASME Journal of Turbomachinery*, 115:513-519, July 1993.
 - [44] Denton, J. The Effects of Lean and Sweep on Transonic Fan Performance: a Computational Study. *TASK quarterly*, 6:7-23, 2002.
 - [45] Klostermeier, C. Investigation into the Capability of Large Eddy Simulations for Turbomachinery Design. *Ph.D. thesis, University of Cambridge, Department of Engineering*, 2009.
 - [46] Brandvik, T. & Pullan, G. An Accelerated 3D Navier-Stokes Solver for Flows in Turbomachines. *ASME Journal of Turbomachinery*, 133:021025, October 2010.
 - [47] Pullan, G. An Experimental and Computational Study of a Shed Vortex in a Turbine Stage. *Ph.D. thesis, University of Cambridge, Department of Engineering*, 2001.
 - [48] Spalart, P. R. & Allmaras, S. R. A One-equation Turbulence Model for Aerodynamic Flows. *La Recherche Aerospatiale*, 1:5-21, 1994.
 - [49] Vahdati, M., Sayma, A. I., Freeman, C. & Imregun, M. On the Use of Atmospheric Boundary Conditions for Axial-flow Compressor Stall Simulations. *ASME Journal of Turbomachinery*, 127:349-351, April 2005.
 - [50] Drela, M. MISES Implementation of Modified Abu-Ghannam/Shaw Transition Criterion. *Technical Report, MIT Aero/Astro*, 1998.
 - [51] Young, A. M. Tip Clearance Effects in Axial Compressors. *Ph.D. thesis, University of Cambridge, Department of Engineering*, 2012.
 - [52] Greitzer, E., Mazzawy, R., & Fulkerson, D., 1978. Flow Field Coupling between Compression System Components in Asymmetric Flow. *ASME Journal of Engineering for Power*, 100:66-72, January 1978.
 - [53] Denton, J. D., 1993. Loss Mechanisms in Turbomachines. *ASME Journal of Turbomachinery*, 115:621-656, October 1993.